University of Sussex

Computational Studies Of Manganese-Ligand Clusters In The Gas-Phase And Manganese Atoms In Graphene And Metal-Organic Frameworks

Jens Rydén

Submitted for the degree of Doctor of Philosophy
University of Sussex
September 2010

Declaration

I hereby declare that this thesis has not been and will not be submitted in whole or in part to another University for the award of any other degree.

Signature:

Jens Rydén

UNIVERSITY OF SUSSEX

JENS RYDÉN, THESIS SUBMITTED FOR THE DEGREE OF DOCTOR OF PHILOSOPHY

COMPUTATIONAL STUDIES OF MANGANESE-LIGAND CLUSTERS IN THE GAS-PHASE AND MANGANESE ATOMS IN GRAPHENE AND METAL-ORGANIC FRAMEWORKS

SUMMARY

The work in this thesis deals with computational studies of manganese ions and atoms in the gas-phase and in the solid phase. The results are divided into three chapters, and the theory and methods used are explained and discussed in a separate theory chapter. The first results on manganese and its coordination to water and methanol molecules in the gas-phase are discussed in the light of physical properties for different ligands including water and methanol. Preferred coordination of a specific ligand type, preferred complex or cluster size as well as coordination modes are thoroughly investigated. Also discussed is stability against proton-transfer reactions for a few manganese-water and manganese-methanol clusters. The work is carried out at the HF/6-31G(d), MP2/6-311G(d,p) and B3LYP/6-311(3df,3pd)-level of theory using the computer code Gaussian. The results presented here are in good agreement with experimental results and findings. It is concluded that mixing between 4s and 3d orbitals on the manganese atom is responsible for preference for a specific cluster size and that occupation of anti-bonding orbitals destabilizes the cluster, for a specific coordination mode. The next results are for manganese atoms in a double layer of graphite, using the computer code Aimpro. Different coordination modes are investigated as are magnetic properties upon adsorption and modification of the band structure compared to a pristine double layer of graphene. Only one case of a significantly high spin polarization is encountered, and the spin polarization on the manganese atom and the surrounding carbon atoms is investigated with Mulliken analysis. This study is in agreement with previous work in the same field, but provides a more realistic picture since a larger system is considered here. The final chapter deals with manganese atoms in metal-organic frameworks, MOFs, using the Aimpro code. Magnetic properties and binding energies for adsorption of selected molecules are discussed in this chapter. Magnetic properties are discussed using Mulliken analysis. Modification of the band structure upon coordination of these gas molecules is shown and investigated. Very few experimental results exist in this field for this structure, but its role as a potential candidate for hydrogen storage will specifically be discussed.

Acknowledgements

First of all, I want to thank the staff at the University who accepted me as a Ph.D-student. I also want to thank EPSRC and British Energy for the funding. Thanks to my supervisors Malcolm Heggie and Hazel Cox for helping me through these four years. Special thanks to Professor Sven Öberg at Luleå University of Technology for your help with Aimpro, for allowing me computational time at the supercomputer clusters Sarek and Akka and for your hospitality and very interesting discussions when visiting Luleå. I would not have made it without your help. Special thanks as well to Dr. John Turner at University of Sussex, for your suggestions of things to improve and change in the thesis. Thank you so much! Many thanks to past and present members of the Cox and Heggie groups; Ricardo, Caroline, Matt, Christo, Irene, Gemma, Calvin, James, Glen, Jean-Jo and Chris. Also thanks to than people in other research groups especially Giuseppe, Silvia, Marisian and of course Kayla. I also want to thank my parents (Christer, Inger, Björn and Cecilia) and family members for coming to Brighton and visit me (Tina, Dag, Andreas, Esse, Maja and Theo) and all other family members giving me support back in Sweden. I really appreciated your company and it helped me a lot! Finally I also want to thank all other friends from Sweden for visiting me here in Brighton especially Fredrik, Stefan, Ulrika and Annika. I really enjoyed it! Thanks to David Löf for encouraging me when coming to Sweden; annars är det slut på visslandet...

Contents

List of Tables

List of Figures

Chapter 1

Introduction to Thesis

The aims and the goals with this thesis is to shed some light over and explain more of some experimental results related to manganese and its chemical behaviour in both the gas phase and in the solid phase using computational methods. Manganese with a broad range of oxidation states ranging from -III to +VII[1], and with the possibility of adopting several spin states makes manganese a fascinating element to study, since this might give manganese containing compounds and molecules a permanent magnetic moment. Credit to the first isolation of manganese is normally given to the Swedish chemist Johan Gottlieb Gahn in 1774.[2] On an atomistic level, the outermost electron configuration can be descibed as: $4s^2$-$3d^5$. Removal of the 4s-electrons creates an ion with five unpaired electrons, although the number of unpaired electrons can be modified depending on the surrounding chemical environment/coordinating species, which in turn affects the overall geometry of the coordinating species.

Studies of metal atoms and ions and their chemical reactivity in the gas phase are very similar to, and in many ways mimics the coordination to ligands in human and plant cells, due to the limited amount of surrounding water or other ligand molecules. Thus, these studies are extremely important to reveal physical and chemical information about the role of different metal atoms in human or plant cells. Manganese ions are present in a large numbers of proteins with various oxidation states, ranging from II to IV.[3] One example would be the Mn-superoxidase dismutase in mitochondria, chloroplasts and prokaryotes, but the most well known example would possibly be photosystem II, which is important for the release of oxygen in green algea and plants. In order to create systems for artificial photosynthtesis, a lot of effort have been made both experimentally and theoretically trying to understand the chemistry and mechanisms of photosystem II. This is only one example of ongoing investigations that deals with systems with conditions similar to those in the cells. Since in vivo experiments in this area of research are difficult to carry out, gas phase

experiments of metal ions together with theoretical investigations can reveal a lot of information about the subtle interplay between a metal ion and different types of coordinating species. Chapter 3 covers some questions regarding manganese atoms in the gas-phase. What different research groups normally have studied include for example binding energies and free energies of ligands to alkaline and first row transition metal ions as well as geometry of complexes. Since the geometry of complexes is not revealed through experiments, computer simulations constitute a tool to add additional information to experimental results. Due to problems in generating doubly charged metal ions, early work in this area mainly dealt with singly charged metal ions. Since a lot of metal ions occurs as M^{2+} in biological systems, later work focused more on doubly charged metal ions. Similarly, most previous work have dealt with "one ligand type only" and very little work have been published concerning mixed ligand systems. This is where and why the current work is unique; a mixed ligand system with a doubly charged metal ion. There are several ways of generating charged metal-ion ligand clusters, one of the will be described here. This method to generate multiple charged metal ions is the so-called pick-up technique developed by Stace and co-workers at University of Sussex. The basic idea is to pass a neutral solvent/argon gas mixture of molecules through a vapour of metal atoms at approximately 10-13 mbar, in which the argon gas acts as a carrier gas. Neutral solvent clusters are formed by adiabatic expansion through a supersonic nozzle. Solvation of the metal atom occurs when encounter the solvent molecules and then by electron impact at approximately 100eV, the resulting complexes are ionized. Thus, a metal-ion complex with a specific number of ligands will be derived through excess evaporation of solvent molecules, this method has proven to be a very successful way of creating multiply charged metal-ion complexes. Analysis of the complex is done by mass spectrometry. The requirement for this technique is that the solvent/ligand has a vapour pressure high enough to generate gas-phase complexes. Although this method is successful in generating complexes with ligands that have not formed stable complexes with other methods, and displaying the size of the cluster, it is not possible to determine the shape or geometry of the cluster. To be more precise, a complex can be revealed to have four ligands, but it is not possible to determine if the complex is tetrahedral or square-planar. Different fragmentation pathways can also be determined by collision of complexes with gas molecules, normally air is used for this purpose, and called Mass analysed Ion Kinetic Energy Spectroscopy (MIKES). With this method it is possible to detect fragmentation products and hence determine different fragmentation pathways for a complex. The back ground for the results in chapter 3, lies the studies from Stace *et al.* which have revealed interesting results regarding a Mn^{2+}-ion and its ability for coordination to water and methanol molecules. Very few studies in this field have dealt with mixed solvents i.e. solvents with two or more components,

and preferential coordination/take-up of ligands will reflect many interesting physical properties of ligands and the metal ion.

The second area dealt with in chapter 4 is adsorption of a manganese atom to a double layer of graphene. Adsorption of transition metal atoms on graphene have gained interest due to the possibility of modifying the electronic properties of graphene and expected usage in spintronics and gas-sensors. Promising transition metal atoms for this purpose is for example Co, Cr and Mn. Despite the fact that several publications exist in this field, more work needs to be done, since much of the work published have been performed only for small systems. When employing larger and more realistic systems, diverging result and conclusions appear for different coordination modes. The aim with the current study is to investigate a number of adsorption modes of Mn on a double layer of graphene and investigate electronic and magnetic properties. Finally, another field that also has received a lot of attention recently, is porous metal-organic frameworks, MOF:s, which are best described as inorganic clusters connected by organic molecules, so called linkers, in a one- two- or three-dimensional network. By changing the metal in the inorganic part or changing the organic linking molecule, the basic topology of the MOF can be maintained, while the physical properties of the MOF structure can be altered widely. The reason for the attention is due to their expected use in gas purification, gas storage and as chemical catalysts, just to mention a few areas. This is the topic in chapter 5. These new materials are readily synthesised in the lab and can be tailor-made with different properties suitable for a broad range of applications. Up to date, a large number of experimental studies have appeared in the literature, whereas the number of theoretical studies are quite low. Research groups usually report new successfully synthesized structures, sometimes accompanied with gas-adsorption studies for that particular structure. But due to the large number of atoms in a realistic MOF system and the presence of heavier elements such as transition metals, theoretical studies of MOF systems are still a challenge to carry out. That is why the current work in chapter 5 is unique. With the increasing computational power and with more efficient and robust programs, theoretical studies in all areas of chemistry becomes more important and reliably. Calculations can act as a strong support for experimental findings. Furthermore, different chemical systems and reactions can now be investigated in detail and depth, and information that is difficult or even impossible to get from experiments, can be obtained from theoretical calculations.

Chapter 2

Theoretical Overview

Introduction *In this chapter, the fundamentals of quantum mechanics and the various theoretical methods used in the the different projects, will be presented. The chapter begins with the birth of quantum mechanics, and how this later evolved into Hartree-Fock theory. In addition, the MP2 method, which was developed from the Hartree-Fock method will also be considered. The third computational method that will be discussed here is the Density Functional Theory (DFT) which is a major method used in this work. DFT has been applied both for single isolated molecules and for solid state calculations. A section dealing with techniques of solid state calculations is also included.*

2.1 Schrödinger equation

A number of experimental findings at the end of the 19th century led to contradictions with the predictions of classical physics. The failure of classical physics to explain these new findings ultimately led to the development of quantum mechanics. One such important findings is the photoelectric effect, the release or emission of electron from a metal surface when subjected to ultraviolet light. The emission of electrons occurred no matter how low the intensity of the incident light was as long as the frequency of the light was higher than a threshold value. Incident light with frequency below this threshold value did not cause any emission of light regardless of the intensity. Also, the kinetic energy of the emitted electrons changes linearly with the frequency of the incident light. The explanation was provided by Albert Einstein[4] in 1905, who proposed that the incident light was quantized, consisting of discrete packets of energy (photons) with the magnitude $h\nu$. By considering the photons as particles colliding with electrons on the metal surface, the photoelectric effect could be explained since the instantaneous emission of electrons and the linear relationship with the incident frequency of light was taken into account.

Incident photons with the energy $h\nu$ minus a minimum value for the electron emission, normally called threshold value and denoted Φ, gives the kinetic energy E_K for the emitted electrons according to:

$$E_K = h\nu - \Phi \tag{2.1.1}$$

Considering photons as particles, a linear momentum p should be associated with them. This linear momentum was detected as a change in wave-lengths of photons when colliding with electrons in a scattering experiment performed by Compton[5] in 1923. Another set of experimental observations that could not be explained by classical physics was the emission of light from atoms, which occurred as discrete lines in the observed spectra and not as a continuous band of all wavelengths. The spectrum for hydrogen had been investigated by J. Balmer[6] in 1885, with the suggestion that the emitted light expressed as wave-numbers ν did match the expression:

$$\tilde{\nu} = R_H \left(\frac{1}{2^2} - \frac{1}{n^2} \right) \tag{2.1.2}$$

where are integers n=1,2,3..., $\tilde{\nu} = \nu/c$ and R_H is the Rydberg[7] constant. The failure of classical physics was due to the observation of discrete lines in the spectra instead of a continuous spectra. In 1913, Niels Bohr[8] tried to combine earlier conclusions and observations into one formula for the hydrogen atom, in which the electrons were assumed to move in circular orbits around the nucleus with only certain values allowed for the orbit.

$$E_n = -\frac{\mu e^4}{8h^2\varepsilon_0^2} \cdot \frac{1}{n^2}, \tag{2.1.3}$$

where n takes the values 1,2,3..., m_e and m_p is the rest mass of the electron and proton respectively, μ represents the reduced mass $\frac{1}{\mu} = \frac{1}{m_e} + \frac{1}{m_p}$, ε_0 is the vacuum permittivity and finally h is the Planck constant. Although equation 2.1.3 could account for all spectral lines in the hydrogen spectra(known at that time),also contains incorrect assumptions, such as the electrons are moving in circular orbits around the nucleus. However, equation 2.1.3 was an important step towards the development of quantum mechanics as it can predict spectral lines with high accuracy and the includes the primary quantum number n.

If photons are considered to be particles they must possess a linear momentum:

$$p = \frac{h\nu}{c} = \frac{h}{\lambda} \tag{2.1.4}$$

The idea that all particles could be considered as waves, i.e. have an associated wave length, was first proposed by de Broglie[9], and is normally referred to as the wave particle duality. Between

1925 and 1926 two different and complete theories about quantum mechanics were published; matrix mechanics was proposed by W. Heisenberg, Born and Jordan,[10–12] and independently of their work, Erwin Schrödinger[13] published the other formalism of quantum mechanics known as *wave-mechanics* which followed from the de Broglie relationship. In this approach, a wave function ψ describes the distribution of a particle and all relevant physical information can be calculated from the wave function. For a stationary state, where ψ is not a function of t, the eigenequation

$$\hat{H}\psi = E_{tot}\psi \tag{2.1.5}$$

can be used to calculate the energy E_{tot}, the eigenvalue, from the eigenfunction ψ using a variation of the classical Hamiltonian, $\hat{H}$. The Hamiltonian has the general form:

$$\hat{H} = T + V, \tag{2.1.6}$$

where T is the kinetic energy and V represents the potential energy. For a molecular system, the nuclear potential is assumed to be invariant over the transformations or motions of the electrons. The constant nuclear configuration is described by the Born-Oppenheimer approximation.[14] This state that as a consequence of the nuclei being much heavier than the electrons, the nuclei therefore move much slower compared to the electrons. Because of this, all the electrons are considered to follow any movement of the nuclei instantly or in other words, the nuclei can be considered to be fixed for the equations of motions of the electrons. In quantum mechanics, measurable quantities are obtained as integrals over all space of the wave function, ψ, when an $operator$ operating on the wave function and multiplied by the complex conjugate of the wave function $\psi^{*\cdot}$. For the energy this can be expressed as:

$$E = \int \psi^* \hat{H} \psi d\tau \tag{2.1.7}$$

Then, if the wave function is an eigenfunction of that operator, the Schrödinger equation gives an $eigenvalue$ times the wave function. Furthermore, according to equation 2.1.6, the Hamiltonian consists of two parts, one kinetic and one potential. When written more specifically, the Schrödinger equation for a one particle system becomes:

$$\frac{\hbar^2}{2\mu}\nabla^2 + V\psi = E\psi \tag{2.1.8}$$

The first part is the kinetic energy, and the second part is the potential contribution. $\hbar$ is the Planck's constant h which is divided by 2π, μ the reduced mass of the particles and ∇ is the Laplacian operator which describes the energy of motion of the particle in three dimensions. The Laplacian operator can for example be expressed in Cartesian coordinates:

$$\nabla^2 \equiv \left(\frac{\partial^2}{\partial x^2} + \frac{\partial^2}{\partial y^2} + \frac{\partial^2}{\partial z^2}\right) \tag{2.1.9}$$

Instead of using Cartesian coordinates as in equation 2.1.9, the wave function ψ can be expressed in polar coordinates r, θ and ϕ , a mathematical technique which makes it easier to consider atomic (and spherical) systems since:

$$r = \sqrt{(x^2 + y^2 + z^2)} \tag{2.1.10}$$

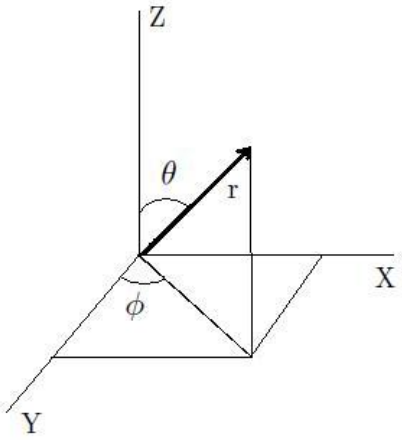

Figure 2.1: Polar coordinates with the angular dependence θ, ϕ and r.

Using polar coordinates, equation 2.1.9 re-arranges into:

$$\nabla^2 = \left(\frac{\partial^2}{\partial r^2}\right) + \left(\frac{2}{r}\right)\left(\frac{\partial}{\partial r}\right) + \left(\frac{1}{r^2}\right)\Lambda^2 \tag{2.1.11}$$

where 2.1.11, Λ^2 is a shortening of the expression:

$$\Lambda^2 = \left[\left(\frac{1}{\sin^2\theta}\right)\left(\frac{\partial^2}{\partial\phi^2}\right) + \left(\frac{\cos\theta}{\sin\theta}\right)\left(\frac{\partial}{\partial\theta}\right) + \left(\frac{\partial^2}{\partial\theta^2}\right)\right] \tag{2.1.12}$$

The wave function can now be considered in three parts, one radial and two angular parts:

$$\psi(r,\theta,\phi) = R(r)\Theta(\theta)\Phi(\phi) \tag{2.1.13}$$

The radial function $|R(r)|^2$ defines the probability (wave function) at various distances from the nucleus, and the two angular components Θ and Φ are needed to specify how the angular motion varies from point to point in space, i.e. it gives both the shape and the orientation of the wave function.

After the discoveries of de Broglie and Shrödinger, the electrons are described through the wave function ψ when bound in a system. The wave function has no physical meaning but according to the Born interpretation, the probability of finding the electron at the point r in a volume element dτ is proportional $\int |\psi|^2 d\tau$ Two observables that can not be determined simultaneously with arbitrarily precision are denoted complementary observables. Examples of such pair of observables are the linear momentum and the position of a particle. According to Heisenberg's uncertainty principle[15] it is impossible to describe both the momentum and the location of a particle like an electron, with an arbitrarily precision. For a particle moving in the x-direction there is a relation between the uncertainty in the position of the particle, Δx and the uncertainty of the momentum of the particle, Δp_x, according to:

$$\Delta x \Delta p_x \geq \frac{h}{4\pi} \tag{2.1.14}$$

The same discussion can be extended describing a particle in three dimensions. The uncertainty principle reveals a very important aspect of the Schrödinger equation; the electrons are best described as *orbitals*, regions with a high probability of finding the electron.

Considering a one-electron system, such as the hydrogen atom, the electron-nucleus interaction can be written as:

$$\frac{\hbar^2}{2m}\nabla^2\psi - \frac{e^2}{4\pi\varepsilon_0 r}\psi = E\psi \tag{2.1.15}$$

where *e* is the charge of the electron, ε_0 is the vacuum permittivity and r the distance of the electron from the nucleus. The second term in equation 2.1.15 is the Coulomb interaction between the electron and the proton in the nucleus. The problem will be more complex for systems with more than one electron, due to the electron-electron interaction. For a two-electron system like the helium atom, the potential energy term in equation 2.1.8 turns out to be:

$$V = -\frac{e^2}{4\pi\varepsilon_0 r}\left[\frac{Z}{r_1} + \frac{Z}{r_2} - \frac{1}{r_{12}}\right] \tag{2.1.16}$$

The first two terms in the bracket of equation 2.1.16 describe the interaction between electrons and the nucleus, and the last term describes the electronic repulsion between the electrons. Thus, the total wave function consists of coordinates of two electrons and is a second order differential equation with six independent variables. This equation is impossible to solve exactly and so approximate methods are necessary for quantitative predictions. One such approximation is to ignore the interaction between the electrons; this is known as the one-electron or orbital approximation. Each electron is occupying one orbital, which is considered to be hydrogen like, and the total wave function becomes:

$$\psi\left(1, 2...N\right) = \phi\left(1\right)\phi\left(2\right)...\phi\left(N\right) \tag{2.1.17}$$

where $\phi(1)$ is the the function for electron 1, $\phi(2)$ is the function for electron 2 and so on. The problem is now to find the eigenvalues to the Schrödinger equation that give the lowest energy of the system. This is achieved by applying the *variational principle* which states that for any trial wave function, the expectation value of the energy can never be less than the true ground state energy E_0. The variational principle is expressed mathematically by:

$$E_0 \leq \frac{\int \phi^* \hat{H} \phi d\tau}{\int \phi^* \phi d\tau}, \tag{2.1.18}$$

where $\int \phi^* \phi d\tau$ represents the normalized wave function. As a result of a very famous experiment done by Stern and Gerlach in 1922[16], not only was space quantization discovered, but the intrinsic electron spin as well, which was then explained by Goudsmit and Uhlenbeck.[17]

The electron spin has consequences for the way the electrons are distributed in different orbitals. The spin constitutes the fourth quantum number and has quantum mechanical origin, due the electron-electron interaction, and two rules referring to the spin have to be obeyed:

1.**The Pauli exclusion principle**,[18] an experimental observation based on symmetry which states that no two electrons can occupy the same quantum state simultaneously. The Hamiltonian in equation 2.1.8 expressed for two electrons:

$$\hat{H}(1,2) = \frac{\hat{p}_1^2}{2m} + \frac{\hat{p}_2^2}{2m} + V(q_1, q_2) \tag{2.1.19}$$

where q_1 and q_2 are the three-dimensional spatial coordinates and spin coordinates of electron 1 and 2 respectively. Since electrons are not distinguishable, the Hamiltonian must be symmetric with respect to interchange of the particles, which for two electrons 1 and 2 can be written as:

$$\hat{H}(1,2) = \hat{H}(2,1) \tag{2.1.20}$$

If the Hamiltonian was not symmetric, the corresponding eigenvalues would differ between different electron configurations and the particles would thus be distinguishable. By using a linear hermitian operator, which normally is denoted permutation operator $\hat{P}$, the symmetric requirement for the Hamiltonian can be preserved:

$$\hat{P}f(1,2) = f(2,1) \tag{2.1.21}$$

where $f(1,2)$ is a function of the spatial and spin coordinates q_1 and q_2. Furthermore, $\hat{P}$ commutes with the Hamiltonian such that:

$$\left[\hat{P}, H\right] = 0 \tag{2.1.22}$$

Performing a new permutation on equation 2.1.21 brings back the original function according to $\hat{P}f(2,1) = f(1,2)$ which implies that:

$$\hat{P}^2 = 1 \tag{2.1.23}$$

with the eigenvalues ε $\pm$=1

Wave functions that have the eigenvalue ε =1 as well as the eigenvalue E are denoted symmetric wave functions. Particles that possess this type of wave function such as photons are called bosons. Accordingly, ε =-1 corresponds to antisymmetric wave functions and these particles are called

fermions. Electrons belong to this group of particles. For fermions this implies that when two electrons are interchanged, the total wave function must change sign, that is:

$$\psi(1,2) = -\psi(2,1) \tag{2.1.24}$$

This reflects the antisymmetric behaviour of the wave function and is a fundamental consequence of the spin properties of the electrons.

2. **Hund's rule of maximum multiplicity**,[19] states that the maximum number of unpaired electrons are obtained due to the Coulombic repulsion Π_c between electrons. In addition to this rule, there is also an exchange energy Π_e associated with the number of ways the electrons can be paired. The more possibilities to arrange the electrons, the lower the energy.

Suggested by Hartree and then refined by Fock,[20,21] the total wave function of a *N* electron system can be expressed as a *Slater determinant*[22,23] which takes into account the antisymmetric behaviour of the wave function as a consequence of the Pauli exclusion principle:

$$\psi = \frac{1}{\sqrt{N!}} \begin{vmatrix} \phi_1(1)\alpha(1) & \phi_1(1)\beta(1).. & \phi_N(1)\alpha(1) & \phi_N(1)\beta(1) \\ \phi_1(2)\alpha(2) & \phi_1(2)\beta(2).. & \phi_N(2)\alpha(2) & \phi_N(2)\beta(2) \\ \vdots & & & \\ \phi_1(N)\alpha(N) & \phi_1(N)\beta(N).. & \phi_N(N)\alpha(N) & \phi_N(N)\beta(N) \end{vmatrix} \tag{2.1.25}$$

In the Slater determinant, every term can be considered to be a hydrogenic wave function multiplied by a spin function. α(i) and β(i) represents the electron spin eigenfunction of the electron. This way of describing the total wave function ensures the antisymmetric behaviour, since an exchange of spin and spatial coordinates of two particles $\phi(1)$ and $\phi(2)$ is equivalent to changing two rows so that the wave function changes sign.

2.2 The Hartree-Fock Method

At the heart of the Hartree-Fock method is the assumption that the electrons in the system of interest can be expressed as a Slater determinant. Each electron is occupying a spin orbital which takes into account the electronic spin. Spin orbitals can be considered to be products of the spatial orbitals and a spin function. The exclusion principle is thus obeyed since electrons with the same spin are contained in different orbitals. The main advantage with the Hartree-Fock equation is that it expresses the many electron Schrödinger equation as many one-electron wave functions where each electron is subject to the net field of all the other electrons.
The Hartree-Fock equation for finding the total energy can be expressed as:

$$\hat{F\varphi}_i = \varepsilon_i \varphi_i \tag{2.2.1}$$

where $i = 1, 2, 3...n$.

$\hat{F}$ is the so-called Fock operator which gives the energy ε_i when operating on the ith spin orbital, φ_i. More specifically, the one-electron Fock operator holding *N* electrons in *N* orbitals can be written as:

$$\hat{F} = h_1 + \sum_{j=1}^{N} \left[\hat{J}_j(1) - \hat{K}_j(1) \right], \tag{2.2.2}$$

It can also be expressed in the closed shell form as with *N* electrons in $\frac{N}{2}$ orbitals:

$$\hat{F} = h_1 + \sum_{j=1}^{N/2} \left[2\hat{J}_j(1) - \hat{K}_j(1) \right], \tag{2.2.3}$$

where the first term, h_1, in equation 2.2.2 defines the kinetic energy of the electron and the second term is the potential between the electron and the nucleus. Two more contributions to the total energy have been taken into account in equation 2.2.2, $\hat{J}_j(1)$ that involves the Coulombic and $\hat{K}_j(1)$ that involves the exchange energy. These are defined as:

$$\hat{J}(1)\varphi_i(1) = \varphi_i(1) \int |\varphi_j(2)|^2 \frac{1}{r_{12}} dv_2 \tag{2.2.4}$$

and

$$\hat{K}(1)\varphi_i(1) = \varphi_j(1) \int \frac{\varphi_j^*(2)\varphi_i(2)}{r_{12}} dv_2 \tag{2.2.5}$$

Equation 2.2.4 can be interpreted as the repulsion between electron 1 in orbital φ_i and electron 2 in orbital φ_j separated by the distance r_{12}. Similarly, the exchange operator 2.2.5 appears as a result from the antisymmetric requirement of the wave function. This operator can be considered to be a correction to the Coulomb term and reduces the effects of repulsion. The corresponding eigenvalues of the Fock operator ε_i can be obtained from equation 2.2.2:

$$\varepsilon_i = E_{ii} + \sum_{j=1}^{N}(J_{ij} - K_{ij}) \tag{2.2.6}$$

Just adding the sum of the eigenvalues will not give the correct total energy, since each electron-electron interaction will be counted twice, a second term that corrects for the double counting of the electrons must be included:

$$E_{HF} = \sum_{i=1}^{N}\varepsilon_i - \frac{1}{2}\sum_{i=1}^{N}\sum_{j=1}^{N}(J_{ij} - K_{ij}) \tag{2.2.7}$$

Roothaan[24] and Hall[25] suggested that the Hartree-Fock orbitals could be expressed as a linear combination of a complete set of *basis functions*, which are known. Through an iterative process applying the variational principle (equation 2.1.18), the energy and molecular coefficients can be calculated to an arbitrary accuracy within the given size of the basis function.

From the exchange operator, equation 2.2.5, electron correlation between electrons with the same spin are included in the Hartree-Fock method, whereas electron correlation E_c between electrons of opposite spins are neglected. This is one of the most important approximations in the Hartree-Fock method. In this way, electrons are not repelled as efficiently as they are in reality. Hartree-Fock energy accounts for 99 percent of the true energy in a system, but for chemical systems this difference can have a crucial impact of the accuracy of chemical properties. When a molecular system increases in size, the number of electron pairs in inter-molecular orbitals increases faster than electron pairs in a single molecular orbital.[26] Electron correlation between opposite spins has both intra- and intermolecular origin, and will therefore grow larger than electron correlation of the same spin. As the molecular system increases in size this electron correlation discrepancy gets larger. Usually, results from Hartree-Fock calculations need to be improved, and one way of obtaining a more accurate result is to include more than one Slater determinant, which is the scope of *electron correlation methods*. One advantage with the HF-method is that it is a relatively cheap computational method that accounts for $\sim$ 99 percent of the true energy and can act as a point from where improvements can be made.

2.3 Perturbation theory and the MP2-method

One of the most important methods that includes electron correlation has its roots in the *pertubation theory*, and was suggested by Møller and Plesset.[27] A new Hamiltonian operator H is defined, which consists of the original Hamiltonian H_0 as a *reference operator* plus a small perturbation $\lambda H^{'}$:

$$H = H_0 + \lambda H^{'} \tag{2.3.1}$$

Furthermore, the solution to the original Hamiltonian is considered to be known:

$$H_0\Phi_i = E_i\Phi_i, i = 0, 1, 2...\infty \tag{2.3.2}$$

In the case where $\lambda = 0$, it means that $H = H_0$, $\Phi_i = \Phi_0$ and $E_i = E_0$. When $\lambda \neq 0$, the wave function and energy and can be expressed as a Taylor expansion series:

$$\Phi_i = \Phi_i^0 + \lambda\Phi_i^1 + \lambda^2\Phi_i^2 + \lambda^3\Phi_i^3 + ... \tag{2.3.3}$$

$$E_i = E_i^0 + \lambda E_i^1 + \lambda^2 E_i^2 + \lambda^3 E_i^3 + ... \tag{2.3.4}$$

The sum of Fock operators is usually chosen as the Hamiltonian for the zeroth-order of perturbation i.e. with no perturbation present:

$$H_0 = \sum_{i=1}^{N} \hat{F}_i = \sum_{i=1}^{N} h_0 + \sum_{i=1}^{N} (\hat{J}_{ij} - \hat{K}_{ij}) \tag{2.3.5}$$

One reason for making this choice is that the Hartree-Fock determinants are known and easy to calculate. In addition, the perturbation can be considered to be small which is one of the main requirements in perturbation theory. Accordingly, the unperturbed energy E_{MP}^0 is the sum of the eigenvalues of all occupied states from the Fock operators, which is the sum of energy from all the occupied molecular orbitals with ε_i defined in 2.2.6:

$$E_{MP}^0 = \sum_{i=1}^{N} \varepsilon_i \tag{2.3.6}$$

All electronic interactions are ignored except putting more than two electrons into an orbital in the unperturbed system. Differently to the one particle Fock operator, the perturbation $\lambda H^{'}$ can be expressed as a two-particle operator where the term $\upsilon_i(i,j)$ is the Coulomb repulsion between two electrons. Equation 2.3.7 corresponds to the first order of perturbation:

$$\lambda H' = \frac{1}{2}\sum_{i\neq j}\upsilon_i(i,j) - \sum_{ij}(\hat{J}_{ij} - \hat{K}_{ij}) \tag{2.3.7}$$

The unperturbed energy E^0_{MP} plus the first order of correction E^1_{MP} corresponds to the Hartree-Fock energy, since the first order correction compensates for the overestimation (double counting) of electron-electron repulsion in the unperturbed system just like the correction term in equation 2.2.6:

$$E_{MP1} = E^0_{MP} + E^1_{MP} = E(HF) \tag{2.3.8}$$

At the second order of correction, electron correlation enters the equation. This is done by including additional excited Slater determinants. These additional Slater determinants are "constructed" through promoting two electrons from occupied orbitals k and l with energies ε_k and ε_l to excited or virtual orbitals a and b with energies ε_a and ε_b. Since the perturbation operator 2.3.7 is a two-particle operator only double excitation determinants are considered. Thus, the Slater determinant $\psi^{a,b}_{k,l}$ incorporates excitations from orbitals k and l to virtual orbitals a and b. Determinants for single, triple and higher excitations are zero and do not contribute to the final energy. The expression for the MP2 energy can ultimately be written as:

$$E^2_{MP} = \sum_{k,l}^{occ}\sum_{a,b}^{vir}\frac{|<\psi_{HF}|\lambda\hat{H}|\psi^{a,b}_{k,l}>|^2}{\epsilon_k + \epsilon_l - \epsilon_a - \epsilon_b} \tag{2.3.9}$$

2.4 Density Functional Theory

Approximately at the time of birth for the wave-function based approach to quantum mechanics, several ideas and attempts to express the total energy as a function of the electron density, ρ, were developed. One of them was the *Thomas-Fermi* model,[28] which was developed by Thomas (1927) and Fermi (1928). This model deals with the kinetic energy of the electrons based on a system with a uniform electron gas, electron-nucleus attraction and electron-electron repulsion are treated in a classical way whereas electron correlation and exchange are ignored. The Thomas-Fermi model was mostly used in solid state physics but less successful for molecular systems. Considering only the expression for the kinetic energy, the Thomas-Fermi model can be expressed as:

$$T_{TF}\left[\rho(\vec{r})\right] = \frac{3}{10}(3\pi^2)^{2/3}\int \rho^{5/3}(\vec{r})d\vec{r} \tag{2.4.1}$$

The importance of 2.4.1 is reflected in the sense that the energy of the system is completely expressed as a function of the electron density, although the model provides a crude description of the kinetic energy. No actual *proof* of the connection between the electron density and the ground state energy was presented. In 1964 Hohenberg and Kohn[29] proved that the ground state energy for an electronic system could be entirely described by the electron density.

$$E = E[\rho\left(\vec{r}\right)] \tag{2.4.2}$$

In equation 2.4.2, the brackets means the the energy is a function of the energy which itself can be described as a set of functions, which normally is denoted *functional*. The total number of electrons N is defined through the electron density:

$$N = \int \rho(\vec{r})d\vec{r} \tag{2.4.3}$$

This first theorem just proves the existence of a "true" electron density $E[\rho(\vec{r})]$ and hence a functional that describes that density, but it does not give the specific form for such a functional. The second theorem from Hohenberg and Kohn states that the electron density is variational just like the wave-function problem. It means that once a trial-density $E[\rho^{'}(\vec{r})]$ is provided, it is possible to calculate a better electron density in an iterative process such that:

$$E[\rho^{'}(\vec{r})] \geqslant E[\rho(\vec{r})] \tag{2.4.4}$$

It was not until 1965 when Kohn and Sham[30] published a set of equations that made calculations from electron density possible. A system of non-interacting electrons can be perfectly well described by a set of one-electron orbitals that makes up a Slater determinant.

It is possible to obtain the kinetic energy for the electrons from this determinant, in a similar fashion to the Hartree-Fock theory. In this approach, the total kinetic energy constitutes the sum of the contributions from all the one-electron orbitals. Using orbitals similarly to the wave-function methods, the total energy for the system can be expressed as:

$$E[\rho(r)] = \sum_{i}^{N} \left(\left\langle \phi_i | -\frac{1}{2}\nabla_i^2 | \phi_i \right\rangle - \left\langle \phi_i | \sum_{k}^{nucl} \frac{Z_k}{|r_i - r_k|} | \phi_i \right\rangle \right) + \sum_{i}^{N} \left\langle \phi_i | \frac{1}{2} \int \frac{\rho(r')}{|r_i - r'|} dr' | \phi_i \right\rangle + E_{xc}[\rho(r)] \tag{2.4.5}$$

The first term in equation 2.4.5 on the right side, represents the kinetic energy of a system containing N electrons, the second term represents the electron-nucleus interaction. The third term is the Hartree-term which describes the electrostatic energy which depends on the charge density ρ, and finally the fourth term is the contribution from electron-electron exchange and correlation. It is also a correction for the self-interaction energy and the difference in kinetic energy between a non-interacting system of electrons and a real system with interacting electrons. Applying the scheme from the Hartree-Fock theory when finding the minimum energy, the pseudo-eigenvalue equations becomes:

$$h_i^{KS} \phi_i = \varepsilon_i \phi_i \tag{2.4.6}$$

h_i^{KS} is the so called Kohn-Sham operator (one-electron) which is defined as:

$$h_i^{KS} = -\frac{1}{2}\nabla_i^2 - \sum_{k}^{nucl} \frac{Z_k}{|r_i - r_k|} + \int \frac{\rho(r')}{|r_i - r'|} dr' + V_{xc} \tag{2.4.7}$$

where V_{xc} is the exchange-correlation potential defined as the derivative of the energy with respect to the density:

$$V_{xc} = \frac{\partial E_{xc}[\rho]}{\partial \rho(r)} \tag{2.4.8}$$

Similarly to the Hartree-Fock method, the Kohn-Sham equations can be solved in an iteratively manner until self-consistency is reached. The initial electron density gives an initial potential which then is used again to produce a new set of density and potential energy. A very common way of writing the expression for the DFT-energy is as follows:

$$E_{DFT}[\rho] = T_s[\rho] + E_{ne}[\rho] + J[\rho] + E_{xc}[\rho] \tag{2.4.9}$$

where $T_s[\rho]$ is the kinetic energy of the electrons, $E_{ne}[\rho]$ is the electron-nucleus attraction, $J[\rho]$ is the electron-electron repulsion term and finally $E_{xc}[\rho]$ is the exchange-correlation term

that deals with the exchange-correlation energy between the electrons.

Further approximations are needed for expressing the exchange-correlation potential. Two of them are the Local Density Approximation, LDA,[31] and the Generalized Gradient Approximation, GGA.[32,33]

In the Local Density Approximation the electron density is treated as a uniform gas, or put in another way, as a slowly varying function. The exchange energy in the case of a uniform electron gas can be written as:

$$E_x^{LDA}[\rho] = -C_x \int \rho^{4/3}(r) dr \tag{2.4.10}$$

An extended version of LDA that takes spin densities into account is the Local Spin Density Approximation, LSDA, which gives the total energy as a sum of the individual spin-densities:

$$E_x^{LSDA}[\rho] = -2^{1/3} C_x \int \left[\rho_\alpha^{4/3} + \rho_\beta^{4/3}\right] dr \tag{2.4.11}$$

One way of improving the LDA-results is to add derivatives of the electron density to the LDA-functional. This takes into account differences in the electron density that may be present in a system. This constitutes the basic idea of the Generalized Gradient Approximation. A general expression for the exchange-correlation energy can be written as:

$$E_{xc}[\rho] = \int \rho(r) \varepsilon_{xc}[\rho(r)] F_{xc}[\rho(r), \nabla\rho(r), \nabla^2\rho(r), ..] dr \tag{2.4.12}$$

where F_{xc} is a dimensionless factor and $\nabla\rho(r)$ is the gradient of the density. GGA-functionals in general improve binding energies, atomic energies, bond lengths and angles for many systems, but in other cases it fails over LDA to make an accurate description. Both of the methods have limitations when it comes to describing long-range interactions. The challenge of DFT theory is to develop suitable expressions for the correct exchange and correlation energies. Although the existence of such expression has been proven by Hohenberg and Kohn, no explicit form has been given.

A large variety of functionals exist, and the development of new, more accurate functionals is one of the biggest areas in computational chemistry. One functional that has been used in this work for evaluation of methods is the GGA-functional BP86 with correlation and exchange energy proposed by Perdew[33] and Becke.[34] This functional can serve as an example of how different correction terms enter the expression for the LSDA-functional.

Perdew added a correction term to the LSDA-functional defined as:

$$\varepsilon_c^{P86} = \varepsilon_c^{LDA} + \Delta\varepsilon_c^{P86} \tag{2.4.13}$$

where the last term on the right hand side is defined as:

$$\Delta\varepsilon_c^{P86} = \frac{e^{\Phi}\mathbf{C}(\rho)|\nabla\rho|^2}{f(\zeta)\rho^{7/3}} \tag{2.4.14}$$

and with $f(\zeta)$, Φ and $C(\rho)$:

$$f(\zeta) = 2^{1/3}\sqrt{\left(\frac{1+\zeta}{2}\right)^{5/3} + \left(\frac{1-\zeta}{2}\right)^{5/3}} \tag{2.4.15}$$

$$\Phi = a\frac{C(\infty)|\nabla\rho|}{C(\rho)\rho^{7/6}} \tag{2.4.16}$$

$$C(\rho) = \xi_1 + \frac{\xi_2 + \xi_3 r_s + \xi_4 r_s^2}{1 + \xi_5 r_s + \xi_6 r_s^2 + \xi_7 r_s^3} \tag{2.4.17}$$

In equation 2.4.16 and 2.4.17, a and $C(\rho)_{1-7}$ denotes numerical constants.
Becke added the exchange energy correction term to the LSDA functional:

$$\varepsilon_x^{B88} = \varepsilon_x^{LDA} + \Delta\varepsilon_x^{B88} \tag{2.4.18}$$

$$\Delta_x^{B88} = -\beta\rho^{1/3}\frac{x^2}{1 + 6\beta x \sinh^{-1} x} \tag{2.4.19}$$

where x is defined through:

$$x = \frac{|\nabla\rho|}{\rho^{4/3}} \tag{2.4.20}$$

and β is a parameter which is set to fit atomic data. Other functionals used in this work is the hybrid B3LYP[35]-functional which consists of a 3 parameter correction term for the exchange-correlation energy (B3)[34] in combination with a gradient corrected correlation functional (LYP)[36] and the LDA functional PW92[37], which was employed for the double layer of graphene as well as the project with metal-organic frameworks. Cramer[38] presents a detailed analysis over different functionals and conclude that the BP86 functional should be avoided due to its large mean absolute errors and maximum errors when employed for calculating atomization energies.

2.5 Basis sets

Independent of the methods used, i.e. Hartree-Fock, post Hartree-Fock or DFT, a mathematical way of representing the orbitals or wave functions is necessary in order to solve the electronic problem. For this purpose, a linear combination of functions that constitute a *basis set* are chosen according to:

$$\varphi_i(r) = \sum_{\alpha=1}^{M} c_{i\alpha}\phi_\alpha(r), \tag{2.5.1}$$

where the sum spans all the basis functions up to the size of the basis set M, and $c_{i\alpha}$ are expansion coefficients that govern their participation in each function. A complete basis set would contain an infinite number of basis functions which, of course, is impossible in any real calculation. Hence, only a limited number of basis functions can be taken into account. The basis functions are related to the radial function R_{lm} and a spherical function Y_{lm} according to:

$$\phi(r) = R_{lm}(r)Y_{lm}(\Theta, \Phi) \tag{2.5.2}$$

where r, Θ and Φ are spherical coordinates with respect to the atom. Usually the basis functions are centred at the origin of an atom. For molecular systems the two most common basis functions are the Slater and Gaussian type, STO and GTO, respectively. A Slater type orbital has the mathematical form:

$$\phi_{\zeta,n,l,m}(r, \Theta, \Phi) = NY_{l,m}(\Theta, \Phi)r^{n-1}e^{-\zeta r} \tag{2.5.3}$$

where N is a normalization constant and $e^{-\zeta r}$ is an exponential radial part which displays the exact behaviour for a hydrogen atom. Gaussian orbitals are expressed in a similar but slightly different way:

$$\phi_{\zeta,n,l,m}(r, \Theta, \Phi) = NY_{l,m}(\Theta, \Phi)r^{(2n-2-l)}e^{-\zeta r^2} \tag{2.5.4}$$

The r^2 term in the Gaussian orbital introduces two very important differences between STOs and GTOs. A Gaussian type orbital does not have a proper and correct shape at the centre of the atomic nucleus; it has a derivative which is zero, while Slater type orbitals have a discontinuous derivative, a so-called "cusp". Gaussian type of orbitals also decreases too rapidly far away from the nucleus compared to Slater type orbitals which tailor off in a more appropriate way. As a consequence, more Gaussian functions are needed to represent the total orbital. Mathematically, it is more difficult to find an analytical expression for the integrals that follow from a Slater type orbital, and analytical methods have to be used instead.

This is computationally very expensive and STOs are therefore mainly limited and used for small systems.

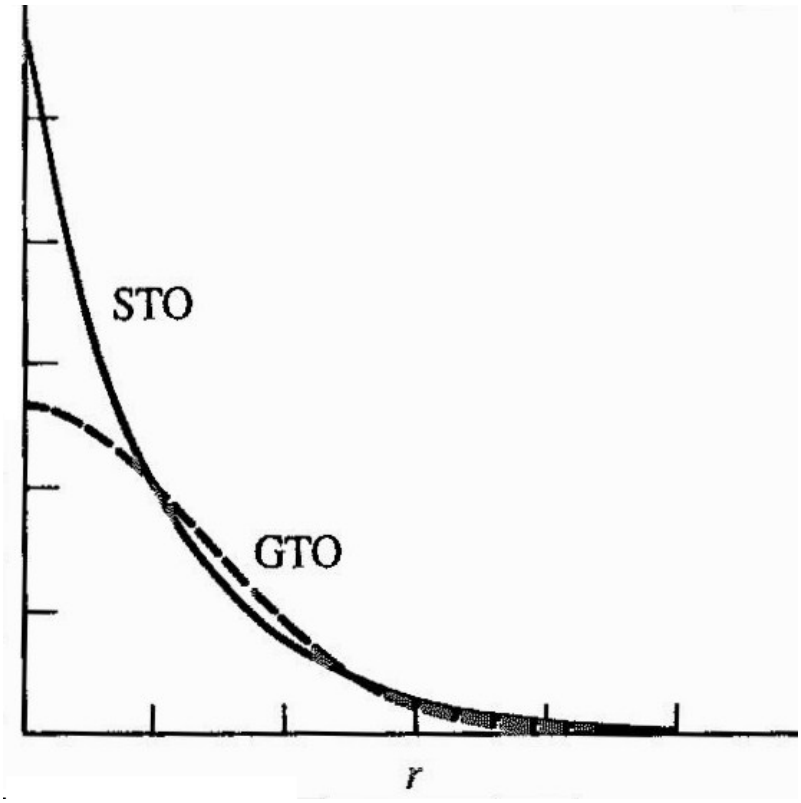

Figure 2.2: The decline of Slater and Gaussian type of orbitals when the distance r from the centre of the nucleus increases. From reference 39 .

Since Gaussian functions mathematically are added in a very simple way according to the *Gaussian rule*, and the integrals are evaluated more easily than in a STO-calculation, GTOs are in general preferred over STOs. The smallest number of basis functions that is required to describe all electrons in a neutral atom or molecule is called a *minimum basis set*. With a minimum basis set, the hydrogen and the helium atom are represented with one s-orbital, the first row in the periodic table are represented by two s-orbitals and three p-orbitals etc. Clearly this is not enough in order to give a good description of the electrons in an atom or a molecular system. Therefore, increasing the number of basis functions for each orbital to the double, triple (or even higher) amount is usually required to obtain a reliable result. A *polarized basis set* can be created by adding functions of higher angular momentum to an atom in the ground state. This gives the electrons more flexibility and includes a possibility to distort the electron cloud, which gives a better description for polarized systems. Another way of giving the electrons more flexibility in loosely bonded regions is to include *diffuse functions*, which usually is helpful when dealing with hydrogen bonds or radicals and are a must for calculating anions.

2.6 Periodic structures

When considering condensed phases such as liquids and solids, a different simulation technique is required. For a solid, a collection of atoms are repeated periodically in one, two or three directions. The smallest possible collection of atoms constitutes a *unit cell* and together with a set of predefined vectors it is possible to replicate the whole crystal structure. Due to the periodicity of the crystal structure, other properties such as the electron density and a wave function are also periodic at equivalent points in the structure. As proven in Bloch's theorem[40], a wave function $\psi_k(\mathbf{r})$ (in this case an electronic wave function) under the influence of an external potential $v(r) = v(r+a_i)$ such as atomic nuclei obeys the following:

$$\psi_k(\mathbf{r}) = e^{i\mathbf{k}\cdot\mathbf{r}} u_k(\mathbf{r}), \tag{2.6.1}$$

where $u_k(\mathbf{r}) = u_k(\mathbf{r} + \mathbf{a}_i)$ is a function with the same periodicity as the crystal. $e^{i\mathbf{k}\cdot\mathbf{r}}$ is the so-called phase factor that follows from the translational symmetry. In the expression for the phase factor, **k** represents the wave vector which determines the magnitude and the direction of propagation. When the position r is changed by the unit vector $\mathbf{a}_i$ the wave function can be expressed as

$$\psi_k(\mathbf{r} + \mathbf{a}_i) = e^{i\mathbf{k}\cdot\mathbf{a}_i} \psi_k(\mathbf{r}) \tag{2.6.2}$$

The electron density that follows with the periodicity can be expressed in the regular way as the square of the wave function:

$$\rho_k(\mathbf{r}) = |\psi_k(\mathbf{r})|^2 \tag{2.6.3}$$

When the condition $e^{i\mathbf{k}\cdot\mathbf{r}} = 1$ is met, the wave function is in phase in all its neighbouring cells. From the smallest set of vectors that fulfils this condition, it is possible to determine the smallest *reciprocal lattice vectors*, defined by $\mathbf{a}_i \cdot \mathbf{b}_j = 2\pi\delta_i j$

Just like the three primitive lattice vectors in real space that make up the unit cell, three primitive lattice vectors in reciprocal space constitutes the smallest possible cell, normally called first Brillouin zone. Higher orders of the Brillouin zone are also possible to consider, using other reciprocal lattice vectors. Different values of **k** generate different points in the reciprocal cell that are defined by the lattice reciprocal vectors. When calculating the wave function and the energy in the solid state, the **k**-points needs to be restricted to one cell in the reciprocal space, and usually the first Brillouin zone is that choice.

Both Hartree-Fock and the DFT-method are possible for the solid state calculations, but since the DFT-method is used in this work, focus will now be on the electron density which can be expressed in a more general way:

$$\rho(\mathbf{r}) = \sum_{\mathbf{k} \in BZ} \omega_{\mathbf{k}} |\psi_{\mathbf{k}}(\mathbf{r})|^2 \tag{2.6.4}$$

The density is summed over all **k**-vectors in the Brillouin zone and ω_k have the role of weight factors that depends on the cell symmetry. In reality, only a limited number of **k**-points are possible to consider, the more **k**-points the closer approximation to the true value. Furthermore, specific properties of the system determine the number of suitable points. A small cell in real space usually requires a large number of **k**-points for correct sampling compared to a big cell. If the cell is big enough, only sampling from the origin in the reciprocal cell, the Γ-point, might be necessary to obtain a good approximation to the true energy.

2.7 Optimization Techniques

Many different techniques for finding a stationary point at the potential energy surface are available in modern chemistry software packages. Which one to use is depending on reliability, speed, performance, computational resources and the type of problems considered. A few of the methods used in the projects in this thesis will be described here. Localizing minima and saddle points can be put as finding stationary points of a multidimensional function. A simple but illustrative picture can be seen in figure 2.3. The reaction proceeds in the direction of a reaction coordinate, where a saddle point has to be passed when going from the minimum of the reactant to the minimum of the product.

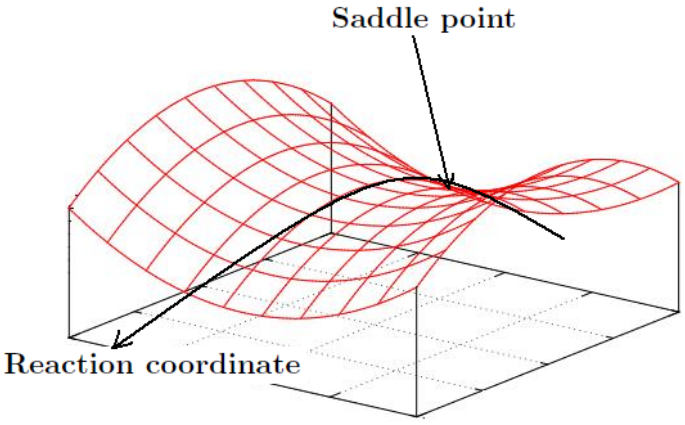

Figure 2.3: Saddle point on a potential energy surface.

Since the potential energy is dependent on many nuclear coordinates q_i for a polyatomic molecule, the gradient g_i

$$g_i = -\frac{\partial E}{\partial q_i} = 0 \tag{2.7.1}$$

During a geometry optimization the geometry of the molecule is varied until all forces on the molecule are arbitrarily close to zero. The first derivative of the potential energy gives information of existing stationary points, but it does not reveal if the stationary point is a minimum, maximum or saddle point. Therefore, the second derivative of the potential energy with respect to nuclear coordinates must be calculated as well. The collection of all the second derivatives constitutes what is normally referred to as the Hessian matrix H. All the eigenvalues of the Hessian matrix show what type of stationary point that is found. When all values are positive in all directions along the potential energy surface (PES) they correspond to a minimum, all values negative indicates a maximum and finally all values positive except one negative is a proof of a first order saddle point. If n negative number of values are found it is an n^{th} order of saddle point. The gas-phase project described in chapter 3 used the Gaussian03[41] package which by default employs the Berny algorithm[42] which involves the Newton-Raphson method. During the optimization process, a number of procedures are performed in order to optimize in the right direction with respect to the gradient g. The first one involves the creation of the Hessian matrix when the first optimization step is taken, or an update of the Hessian if it is a later step in question. Using Taylor expansion at the point x_0, the potential energy function $f\,(x)$ is expanded to the second order:

$$f(x) \simeq f(x_0) + g^t(x - x_0) + 1/2(x - x_0)^t H(x - x_0) \tag{2.7.2}$$

One of the problems that occurs is to keep the size of the step taken in the optimization within the region where equation 2.7.2 is valid. This region is usually referred to as the *trust radius*. In Gaussian, the scheme defining the maximum trust radius follows the method of Fletcher.[43–45] The second problem is to choose in which direction to move. If the geometry of the molecule is close to a minimum, all the eigenvalues of the Hessian should be positive and the direction for the step to be taken is opposite to the gradient direction. If not all values of the Hessian are positive the step will be taken along the gradient direction and possibly end up at a first order saddle point. The step in the Newton-Raphson procedure can be written as:

$$\Delta x_i^{'} = -\frac{f_i}{\epsilon_i - \lambda} \tag{2.7.3}$$

where f_i is the projection of the gradient in the eigenvector direction with the eigenvalue ϵ_i. λ is introduced as a *shift parameter* which can be chosen for the specific optimization task i.e.

minimum or saddle point. If an optimization to a minimum is requested, a linear search between the two latest points is performed. When second derivatives are available at both points, a quintic polynomial fit between these points is tried first. If this fit is not successful, a lower polynomial fit will be employed. The step is accepted if the latest step taken is the lowest in energy.

The Berny algorithm can be used for optimizations towards transitions states as well, but it generally requires a good initial guess for the starting structure in order for the optimization to be successful. Instead of the Berny algorithm, the *Synchronous Transit-Guided Quasi Newton* (QSTN) method was used for locating transition states. This method requires a specification of the reactant(s), the products(s) and an initial guess of the transition state. Having specified the initial and final structures, the transition state is considered to somewhere "in between" these points and is located with interpolation techniques. The QSTN method uses a circle for interpolation between the points, and when the region of the transition state is found, another algorithm (quasi-Newton-Raphson, equation 2.7.3) is used to locate the actual transition state. When the switch occurs is determined by the presence of exactly one negative eigenvalue in the Hessian and if the corresponding eigenvector points in the correct direction.

The Aimpro code uses the conjugate gradient method as a default algorithm, in which steps are taken along a line that consists of a mixture of the negative gradient and the previous search direction. Conjugate gradient methods are only capable of locating minima, so another method, Nudged Elastic Band, NEB is employed when locating saddle points. A series of images are generated between an initial and a final structure and the structures are optimized through calculation of forces, which are used to proceed in the "uphill" direction. However, no saddle point search was performed in the current work.

2.8 Vibrational Modes

Calculation of the vibrational frequencies are often wanted not only as they give the IR frequencies, they also provide information of which stationary point that has been found in the optimization, i.e a minimum, saddle point or maximum. The process includes calculation of the normal modes. These can be considered to be simple vibrational modes which in combination make up all the complex vibrations for a molecule. If a minimum is found, all the normal mode force constants are positive. A saddle point is characterized by just one imaginary/negative frequency since on normal mode is pointing downward from the hill in the direction of the reaction coordinate. More than one imaginary frequency means that a maximum of *n*t order has been found. Vibrational modes in a molecule can be treated in the harmonic oscillator approximation, in which the displacement $r = x - x_0$ of atoms from an equilibrium position can be expressed with a Taylor expansion.

For a diatomic molecule:

$$V(r) = V(0) + \left(\frac{dV}{dr}\right) r + \frac{1}{2}\left(\frac{d^2V}{dr^2}\right) r^2 + ... \tag{2.8.1}$$

Since the first point is a stationary state, the potential energy at this point can be set to zero i.e. $V(0) = 0$, and the first derivative at that point is also zero. If the displacement from equilibrium is small, all terms beyond the second order can be ignored. Only the term proportional to r^2 is left and this corresponds to the harmonic approximation:

$$V(r) = \frac{1}{2}kr^2, k = \left(\frac{d^2V}{dr^2}\right) \tag{2.8.2}$$

k is the force constant of the bond. The Hamiltonian for vibration in a two-atom system can be written as:

$$H = -\frac{\hbar^2}{2\mu}\frac{d^2}{dr^2} + \frac{1}{2}kr^2 \tag{2.8.3}$$

where μ is the *reduced* or *effective*-mass of the two atom-system:

$$\frac{1}{\mu} = \frac{1}{m_1} + \frac{1}{m_2} \tag{2.8.4}$$

In a polyatomic molecule all the atoms are vibrating like a harmonic oscillator, which makes the situation much more difficult. The total vibration for a molecule can be expressed as a linear combination of a number of *normal vibrations*. If the displacement of each nucleus is expressed in a coordinate system with the origin of each vibrating system at the equilibrium position r_0 for each nucleus, the total kinetic energy T will be:

$$T = \frac{1}{2}\sum_N m_N \left[\left(\frac{d\Delta x_N}{dt}\right)^2 + \left(\frac{d\Delta y_N}{dt}\right)^2 + \left(\frac{d\Delta z_N}{dt}\right)^2\right] \tag{2.8.5}$$

For convenience mass weighted or generalized coordinates are used:

$$q_1 = \sqrt{m_1}\Delta x_1, q_2 = \sqrt{m_1}\Delta y_1, q_1 = \sqrt{m_1}\Delta z_1 ... \tag{2.8.6}$$

Then, the kinetic energy can be simplified to:

$$T = \frac{1}{2}\sum_i^{3N} \dot{q}_i^2 \tag{2.8.7}$$

Using equation 2.8.2 for a polyatomic system and neglecting higher order terms than the second order, the equation becomes:

$$V(r) = \frac{1}{2}\sum_{i,j} K_{ij} q_i q_j \; K_{ij} = \left(\frac{\partial^2 V}{\partial q_i \partial q_j}\right) \tag{2.8.8}$$

Thus, the total energy for the vibrations become the sum of equation 2.8.7 and 2.8.8. The eigenvalues and the eigenvectors are obtained through diagonalizing via a unitary transformation. Separation of the 3N-dimensional Shrödinger equation to 3N one dimensional Shrödinger equations gives the expression for the normal harmonic oscillators:

$$v_i = \frac{1}{2\pi}\sqrt{\varepsilon_i} \tag{2.8.9}$$

Chapter 3

Preferential Coordination Of Manganese Ions In The Gas Phase

Introduction *Many metal ions play a very important role in biological systems and since the number of coordinating species in such systems varies to a large extent, gas-phase studies of metal ions can reveal information of how metal ions and coordinating ligands behave in those systems. Manganese, an element with a wide range of oxidation states from -III to +VII, is found to a large extent in biological systems, usually in the oxidation state of +III and +II, in which it has been suggested that manganese can act as a Lewis acid in enzymes as well as an oxidation catalyst. One purpose of this study is to investigate if there is any preferential coordination of water or methanol molecules to a doubly charged Mn-ion and examine coordination structures and bonding properties of these manganese complexes. Another purpose was to investigate the stability and proton transfer reactions are compared between* $[MnH_2O]^{2+}$ *and* $[MnCH_3OH]^{2+}$ *complexes. The first part of the chapter will cover some basic coordination chemistry relevant for the current study as well as a short section on how these complexes are made experimentally. The second part of the chapter will deal with the methods used and the results from the theoretical study. Many of the results in this chapter can be found in reference 46.*

3.1 Crystal Field Theory and Ligand Field Theory

Proposed by Griffith and Orgel,[47] ligand field theory combines the previously developed crystal field theory[48] with molecular orbital theory[49] into a more complete picture for metal-ligand complexes, where bonding and antibonding orbitals are considered. Figure 3.1 shows the principal distribution of ligands in an octahedral complex and the coordinate axes.

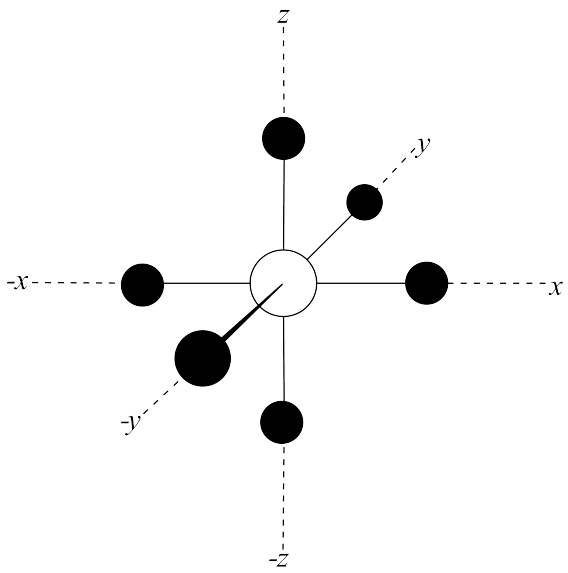

Figure 3.1: Structural disposition of ligands (black) around the central metal (white) and the coordinate axis frame for O_h-symmetry metal complex. Made with help from 50.

Crystal field theory was originally developed for metal atoms in crystals[48] and depending on the crystal structure, the d-orbitals of the metal ion are interacting to an unequal extent with the anions. No covalent bonding is taken into account at this stage, just the energetics of the d-orbitals of the metal ion. The potential energy between a single electron on the metal ion and a ligand can be expressed as the sum of the interaction between the orbitals on the metal ion and all the ligands:

$$V = \sum_{i}^{n} \frac{ze}{|\mathbf{r}_j - \mathbf{r}_i|} \tag{3.1.1}$$

where $\mathbf{r}_i$ is the distance from the *i*th ligand to the centre of the metal ions, and $\mathbf{r}_j$ is the distance to a general point in space, ze is the charge on the ligand and n is the number of anions. Figure 3.2 shows the five different d-orbitals of a transition metal atom and their orientation in space.

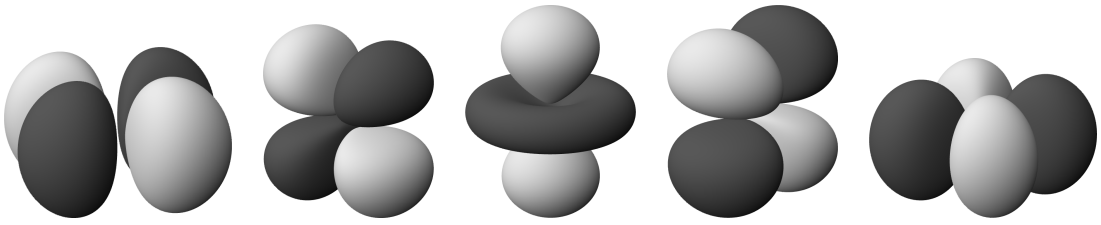

Figure 3.2: Hydrogenic $3d$ orbitals. Made with help of 50 .

A total number of six d-orbitals exist; $d_{x^2-y^2}$, $d_{z^2-y^2}$, $d_{z^2-x^2}$, d_{xy}, d_{xz} and d_{yz}, but only five of them can be written as linearly independent of each other, and in a non-spherical form.[51–53] By convention the two orbitals $d_{z^2-x^2}$ and $d_{z^2-y^2}$ form the linear combination $d_{2z^2-y^2-x^2}$ which is abbreviated to d_{z^2}. As can be seen from figure 3.2, the d_{z^2} and $d_{x^2-y^2}$ orbitals have lobes that points in the direction of the coordinate axes, whereas the lobes of the three remaining d-orbitals points between the coordinate axis, which in turn affects the metal ion-ligand bonding.

3.2 Octahedral Crystal Field

For an octahedral complex, the six ligands can interact strongly with the d_{z^2} and $d_{x^2-y^2}$ orbitals, and as a result these orbitals are raised in energy compared to the free metal ion. On the other hand, the d_{xy}, d_{xz} and d_{yz} orbitals are affected to a much smaller extent. The energy difference between these two sets of orbitals is usually denoted as Δ_o. In crystal field theory, the d-orbitals of the metal ion are split or raised in energy by the electrostatic field created by the surrounding ligands. Figure 3.3 shows how the five d-orbitals all are affected by the ligands considered as point charges and how these five orbitals are split into two energy levels as a consequence of their different interaction with the point charges.

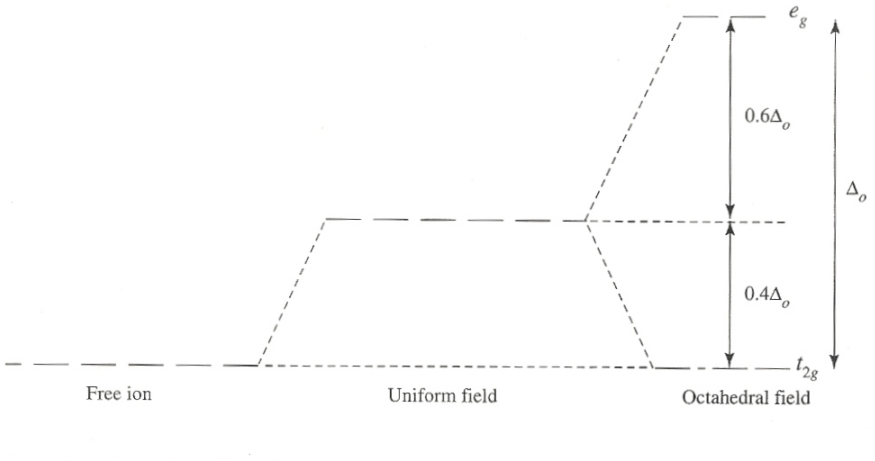

Figure 3.3: Splitting of d-orbitals in an octahedral crystal field. From reference 54.

Group theory will reveal the existence of a splitting between the five d-orbitals, but it does not predict the magnitude of the splitting. Nevertheless, group theory can be an extremely useful tool for a discussion of orbitals involved in bonding between a metal ion and a set of ligands, which will be shown later in the chapter.

If equation 2.1.5 is written as:

$$\hat{H}\psi_i = E_{tot}\psi_i, \tag{3.2.1}$$

where *i* takes the values from 1 to *n*, which in the case of d-orbitals will be 1 to 5, it is possible to examine the result of an external potential. By employing the perturbation theory, it is possible to calculate the magnitude of the splitting. A new term $H^{'}$ will thus enter the unperturbed Hamiltonian H_0:

$$\left(H_0 + H^{'}\right)\psi_j^{'} = E_j^{'}\psi_j \tag{3.2.2}$$

Similarly to equation 3.2.1, *j* takes the values from 1 to *n* which in this case is 1 to 5. In this particular case when dealing with crystal field splitting, the unperturbed Hamiltonian, H_0, is the Hamiltonian for a one-electron system (equation 2.2.7) and $H^{'}$ is the perturbation in equation 3.2.2. The perturbed wave function $\psi_j^{'}$ can be expressed as a linear combination of the original unperturbed wave function ψ_i:

$$\psi_j^{'} = c_{1j}\psi_1 + c_{2j}\psi_2 + ...c_{nj}\psi_n = \sum_{i=1}^{n} c_{ij}\psi_i \tag{3.2.3}$$

c_{ij} represents the combinations of all the coefficients associated with the unperturbed and perturbed wave functions. By expressing the d-orbitals as spherical harmonics, the splitting between different orbitals can be derived. As stated in Chapter 2, the spherical harmonics consists of a radial part and an angular part 2.1.13. Tables of spherical harmonics for different quantum numbers l and m_l can be found in the literature;[55,56] it can be shown that only a few of the spherical harmonics are needed for investigating the effect of ligand field splitting. Common notations for spherical harmonics are Y_l^m or alternatively $Y_{l,m}$, where *l* is the orbital or angular momentum quantum number and *m* the magnetic or azimuthal quantum number. The energy of the perturbed system $E_j^{'}$ can be minimized with respect to the wave functions.[22,23] However, in this case, electron spin is not included. When the determinant is diagonalized, it gives the eigenvalues and the eigenvectors. The eigenvectors provide the perturbed wave functions, $\psi_j^{'}$, as a series of linear combinations of the original unperturbed wave function, ψ_i, which consist of the d-orbitals.

$$0 = \begin{vmatrix} & \psi_1 & \psi_2 & .. & \psi_N \\ \psi_1 & H_{11}^{'} - E^{'} & H_{12}^{'} & .. & H_{1N}^{'} \\ \psi_2 & H_{21}^{'} & H_{21}^{'} - E^{'} & .. & H_{2N}^{'} \\ : & & & & \\ \psi_N & H_{N1}^{'} & H_{N2}^{'} & .. & H_{NN}^{'} - E^{'} \end{vmatrix} \tag{3.2.4}$$

In 3.2.4, the wave functions are defined as in equation 2.1.13 and the matrix elements are defined as:

$$H_{ij}^{'} = \int \psi_i^* H^{'} \psi_j d\tau \tag{3.2.5}$$

When evaluating the integral, it can be shown that many terms can be ignored; for example the only spherical harmonics needed for describing the splitting are Y_4^0 and $Y_4^{\pm 4}$. With the solutions from 3.2.5, a new secular determinant can be set up yielding the eigenvalues (energies) of the orbitals. From the energies it is also possible to obtain the eigenfunctions. By convention the "center of gravity" should not be changed from the uniform field, therefore the doubly degenerate d_{z^2} and $d_{x^2-y^2}$ orbitals, denoted e_g, are raised by 0.6 Δ_o compared to the uniform field. For the same reason the triply degenerate d_{xy}, d_{xz} and d_{yz} orbitals, denoted t_{2g}, are lowered by 0.4 Δ_o compared to the uniform field.[54,57] Even if crystal field theory does not take bonding into account, some basic ideas are very useful for further discussion of the d-orbital splitting. As a starting point for a more sophisticated ligand field approach, only sigma bonding is considered. Molecular orbitals are discussed in the light of Symmetry Adapted Linear Combinations of Atomic Orbitals, SALC-AO.

3.3 Sigma-bonding

With the powerful technique of group theory, it is possible to determine which atomic orbitals are participating in bonding of a particular kind. For a $3d$-transition metal ion, bonding can occur if the $4s$, $4p_x$, $4p_y$, $4p_z$, $3d_{z^2}$ or $3d_{x^2-y^2}$ orbitals match ligand orbitals with σ-symmetry. Using figure 3.1, ligands 1-4 occupy the sites in the x-y-plane, ligands 5 and 6 occupy the last two sites in the z-direction. According to group theory, the six ligand p-orbitals forms the irreducible representation: $\Gamma = A_{1g} + T_{1u} + E_g$. The spherical symmetric A_{1g}-orbital on the metal ion interacts to an equal extent with all the ligand p-orbitals. For the metal ion, the d_{xy}, d_{xz} and d_{yz} orbitals with T_{2g} symmetry do not match any of the ligand orbitals, and hence, are non-bonding when only considering sigma-bonding is considered. As a result, six bonding and six anti bonding molecular orbitals of a_{1g}, e_g and t_{1u} symmetry will be formed.[54] Electrons from the ligands occupy the bonding molecular orbitals, whereas the electrons from the metal ion end up in one of the non-bonding t_{2g} or anti bonding e_g orbitals. Different types of ligands interact to different extents with the orbitals on the metal ion; some ligands cause a large energy splitting between the t_{2g} and the e_g orbitals, and these ligands are called "strong field ligands." Similarly, "weak field ligands" are ligands that interact weakly with the metal orbitals and cause a small energy difference between the t_{2g} and e_g orbitals.[54,57] Many of the interesting features of metal-complexes such as magnetic

properties, structure and electronic spectra come from the occupation of the t_{2g} and higher orbitals.[54] For metal ions d^0 to d^3 and d^8 to d^{10} only one electron configuration for the d-electrons is possible, but for metal ions d^4 to d^7, two different configurations are available for each. This is very important since some of these configurations affect the total magnetic spin for the molecule. Strong field ligands cause the electrons in the d-orbitals to be paired, creating a low-spin complex, while weak field ligands allow the d-electrons to be unpaired, resulting in a high-spin complex. To summarize; strong field ligands lead to a low-spin complex with a high Δ_o, and weak field ligands lead to high-spin complexes with a small Δ_o.[54,57]

3.4 Ligand Field Stabilisation Energy

The total energy required to pair two electrons, usually called spin pairing energy, is dependant on the Coulomb repulsion Π_c and the exchange energy Π_e. The Coulomb repulsion results in destabilisation and the exchange energy in stabilisation of the complex. Thus, there is a subtle interplay between Δ_o, Π_c and Π_e. If the total spin pairing energy is larger than the Δ_o, then a high-spin complex is favoured, the reverse situation is true when the Δ_o is larger than the spin pairing energy. In the latter case, putting two paired electrons in one orbital is favoured over having electrons in separate d-orbitals. The difference in energy for a complex is denoted the ligand field stabilization energy, LFSE. This is the stabilization that is gained by the presence of the ligands. For a high-spin octahedral complex, one electron in the t_{2g} set of orbitals, results in a stabilization of the complex by $\frac{2}{5}\ \Delta_o$. Similarly, an electron in the e_g set, implies a destabilization of $\frac{3}{5}\ \Delta_o$. In total, for a high-spin octahedral complex with r number of electrons in the t_{2g} orbitals and s electrons in the set of e_g orbitals, the net stabilization energy will be; $(2r/5 - 3s/5)\Delta_o$. Table 3.1 and 3.2 shows the ligand field stabilization energy for both high-spin and low-spin octahedral complexes. All the values are taken from reference 54. It is important to remember that these values are approximate, since they only take σ-bonding into account, even though a significant amount of Π-interaction might be present. In some cases, there is no ligand stabilization energy present at all. For a high spin d^5-ion like the Mn^{2+}-ion, no ligand field stabilization energy occurs in the high-spin octahedral case, which also is true for d^0 and d^{10} -ions.

Number of d-electrons	Weak-field t_{2g}	e_g	LFSE (Δ_0)
1	↑		-2/5
2	↑↑		-4/5
3	↑↑↑		-6/5
4	↑↑↑	↑	-3/5
5	↑↑↑	↑↑	0
6	↑↓↑↑	↑↑	-2/5
7	↑↓↑↓↑	↑↑	-4/5
8	↑↓↑↓↑↓	↑↑	-6/5
9	↑↓↑↓↑↓	↑↓↑	-3/5
10	↑↓↑↓↑↓	↑↓↑↓	0

Table 3.1: LFSE for weak-field arrangements. From reference 54.

Number of d-electrons	Strong-field t_{2g}	e_g	LFSE (Δ_0)
1	↑		-2/5
2	↑↑		-4/5
3	↑↑↑		-6/5
4	↑↓↑↑		-8/5
5	↑↓↑↓↑		-10/5
6	↑↓↑↓↑↓		-12/5
7	↑↓↑↓↑↓	↑	-9/5
8	↑↓↑↓↑↓	↑↑	-6/5
9	↑↓↑↓↑↓	↑↓↑	-3/5
10	↑↓↑↓↑↓	↑↓↑↓	0

Table 3.2: LFSE for strong-field arrangements. From reference 54.

This can be shown by the hydration process for a doubly charged metal ion according to the reaction:

$$\mathrm{M}^{2+}_{(g)} + 6\,\mathrm{H_2O}_{(l)} \longrightarrow [\mathrm{M(H_2O)_6}]^{2+}_{(aq)} \tag{3.4.1}$$

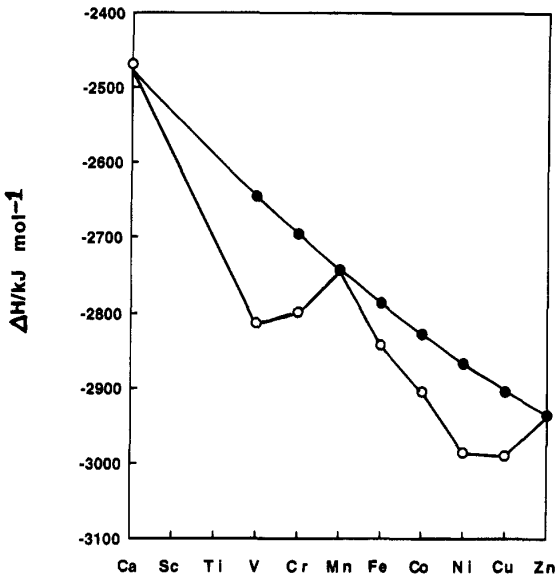

Figure 3.4: Experimentally obtained hydration energy for a number of doubly charged third row transition metal ions, according to reaction 3.4.1. Taken from reference 58.

Figure 3.4 shows the experimentally obtained values for enthalpies of the hydration, which are shown as open white circles, and the filled black circles are the values for the enthalpies of hydration when the ligand field stabilization energy is subtracted (in addition with small corrections for the spin-orbit splitting and the inter electronic repulsion energy). The black circles lie on a smooth curve, which is the expected behaviour for spherically symmetric ions with decreasing radius due to the increased nuclear charge. Accordingly, values for ΔH should decrease continuously, but as a consequence of the ligand field stabilization energy they do not, but instead display a double-humped curve.[58,59]

3.5 Pi-bonding

When there are atomic p or molecular π^*-orbitals available on the ligands, there is an additional possibility for π-bonding to the metal-ion occurs. For an octahedral complex, there will be a total number of 12 ligand orbitals in the π system. For any coordinate system chosen in a consistent way, the reducible representation of these 12 orbitals are: $\Gamma_\pi = T_{1g} + T_{2g} + T_{1u} + T_{2u}$. From these four reducible representations, only T_{2g} and T_{1u} can overlap with the metal orbitals. Orbitals with T_{2g} representation can overlap with the metal T_{2g} set of orbitals, whereas the T_{1u} matches the symmetry of p-orbitals on the metal atom. In an octahedral complex, the T_{1u} set made up of p-orbitals on the metal atom are already occupied via σ-bonding to the ligands and do not overlap well with the ligand orbitals to form π-bonds. The remaining T_{2g} set on the metal atom are the most likely to form bonding and antibonding orbitals with the six ligands. Due to the extent of occupation of these orbitals, a few consequences arise. The most important case, with the strongest bonding interaction comes from the fact that the π^*-orbitals are empty like in the CN^- ion. These ligands are usually called π-acceptor ligands, since electron density from the metal T_{2g}-orbitals can occupy these antibonding ligand orbitals.[54,57] If they do, the new bonding orbitals are lower in energy than the original T_{2g}-orbitals and the new antibonding orbitals are higher than the E_g orbitals on the metal ion. Furthermore, the value for Δ_o gets larger resulting in an increased bonding strength. This is commonly known as the Dewar-Chatt-Duncanson model or π-backbonding, and can result in significant energy stabilization of the metal-ligand bond. When electron density is carried away from the metal ion to the π-orbitals on the ligands, the overall stability of the complex is enhanced. Ligands that can take part in this type of interaction are very important in chemistry.[54,57]

The other case involving metal-ligand π-bonding is when ligand p-orbitals are already occupied. These electrons will occupy bonding π-orbitals with the following consequences; the t_{2g} set, primarily of ligand character, become bonding orbitals and strength the metal-ligand interaction,

whereas the antibonding t_{2g}^* set primarily with metal character, are raised in energy. Overall, Δ_o is lowered and the previously empty t_{2g}^* set is now occupied. This process is known as ligand-to-metal π-bonding, where electron density is pushed from the ligand to the metal.[54,57] Examples of such ligands involves the negatively charged F^- and Cl^- ions and they are sometimes called π-donating ligands. A consequence of ligand-to-metal interaction is that the combination of σ and π donation from the ligands will result in a larger negative charge on the metal ion and hence a larger repulsion between the metal ion and the ligands. Thus, ligand-to-metal interactions are less favourable than metal-to-ligand interactions.[54,57]

3.6 Tetrahedral Crystal Field

One common way of describing a tetrahedral complex is to think of the ligands as occupying four corners of a cube, with the metal ion placed at the centre of the cube, which can be seen in figure 3.5.

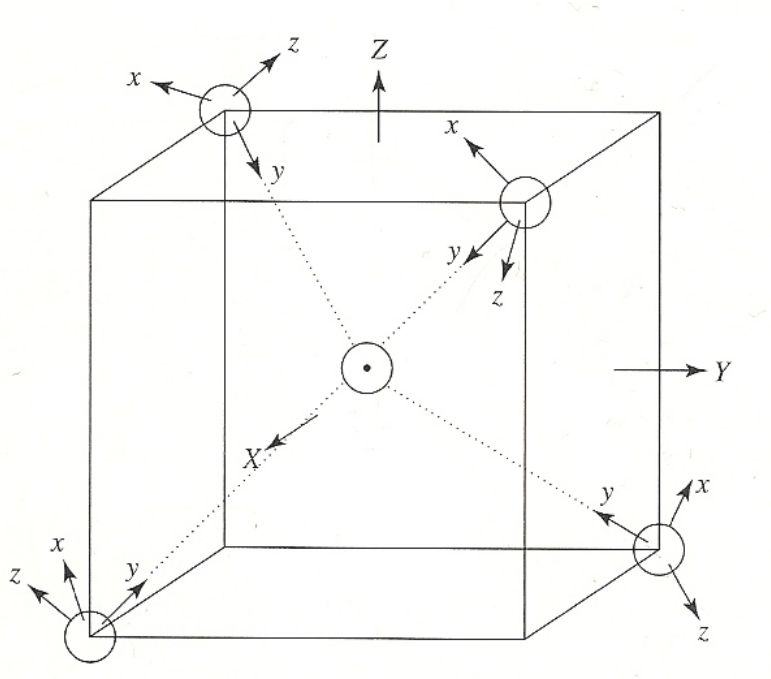

Figure 3.5: Ligand interaction with central metal ion in a tetrahedral complex. Image taken from reference 54.

In a tetrahedral complex, the d-orbital splitting is reversed with respect to the octahedral case, and the splitting parameter, Δ_t, is smaller than the corresponding parameter, Δ_o.

The strongest ligand interaction with the metal d-orbitals will occur for the three d_{xy}, d_{xz} and d_{yz} orbitals of T_2 symmetry which are raised in energy by 0.4 Δ_t, whereas ligand interaction between the two d_{z^2} and $d_{x^2-y^2}$ making up the E set are much smaller. As a consequence, the E set is lowered in energy by 0.6 Δ_t. Overall, Δ_t is 4/9 of the value for Δ_o The orbital splitting can be seen in figure 3.6.

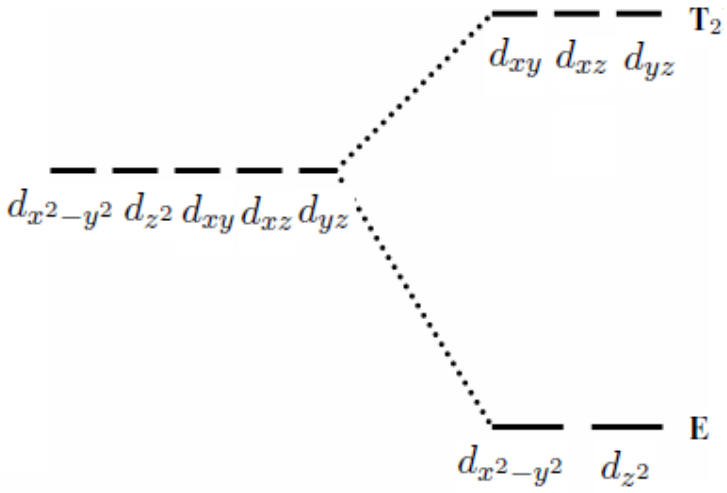

Figure 3.6: Splitting of d-orbitals in a tetrahedral complex.

3.7 Sigma-bonding

Adopting the same symmetry principle as in the octahedral case, the irreducible representation for sigma bonding includes the T_2 and the spherical symmetric A_1 representation. The interaction between the ligand orbitals with T_2 symmetry occurs with the d_{xy}, d_{xz} and d_{yz} orbitals, which make up the T_2 set on the metal ion.[54,57]

3.8 Pi-bonding

Irreducible representations for the ligand orbitals that can participate in π-bonding include the E, T_1 and T_2 representations. The T_1 set do not have any matching orbitals on the metal ion, whereas E can form bonding and anti bonding orbitals with the E set on the metal made up of the d_{z^2} and $d_{x^2-y^2}$ orbitals. Similarly, ligand orbitals with T_2 symmetry can interact with the T_2 set on the metal ion composed of the d_{xy}, d_{xz} and d_{yz} orbitals in order to form π-bonds.[54,57]

3.9 Angular Overlap Model

The octahedral and tetrahedral case described so far can be extended in a similar way for square planar complexes, although square planar complexes are not considered in this work. For complexes with geometries other than octahedral, square planar or tetrahedral, it is more difficult to use the ligand field model to predict energy change or orbital interaction.

An alternative way of describing other geometries is the angular overlap model,[60,61] which takes into account both σ and π-interactions with respect to the angular overlap between ligand orbitals and metal d-orbitals. Some ligand orbitals will have a strong interaction with a specific metal d-orbital, other ligand orbitals will only interact to a small extent or not at all, depending on their relative position to the metal orbitals. By considering both σ and π-interactions from each ligand in turn, a total energetic picture for the complex can be obtained.[54]

3.10 Spectrochemical Series

It should be pointed out that the splitting parameter is strongly dependant on the ligands and on the metal atom/ion itself, in comparison to the total spin pairing energy Π. Different types of ligands can be arranged in a series which reflects their ability to form low-spin and high-spin complexes as well as their σ and π-bonding abilities. This series is more well known as the spectrochemical series;[54,57] examples of the series are collected in Table 3.3

$CO, CN^-, phen > NO_2^- > NH_3 > NCS^- > H_2O > F^- > RCO_2^- > OH^- > Cl^-, Br^-, I^-$	
Low Spin	High Spin
Large Δ	Small Δ
π-acceptors	π-donors

Table 3.3: Representative members of the spectrochemical series.

3.11 Previous Experimental And Computational Results

Metal ion and neutral ligand complexes have been under investigation for the last two decades, and a lot of insight has been gained regarding the structures and physical properties that make a metal ion-ligand complex stable.[62–110] Several different research groups have investigated binding energies, free energies, geometry of complexes, spectroscopic data, transition states and detailed information about population of orbitals and metal ion-ligand interactions. Initial work focused on singly charged metal ions, but later work considered doubly charged species, due to the fact that a lot of alkaline earth metals and first row transition metals occurs as M^{2+}, especially in biological systems. One thing which has interested both experimental and theoretical groups is why a specific metal ion complex is stable, and the minimum number of ligands that are required to stabilize the complex. In one experimental study made by Stace and co-workers[87] based on mass-spectrometry, the aim was to investigate the different physical properties of oxygen- and nitrogen-coordinating ligands with the Mg^{2+}-ion. In this study, Stace performed studies for the gas phase stability of $[Mg(L)_n]^{2+}$ complexes using the pick-up technique described earlier. By varying the type of ligand, the stability of the complex could be investigated thoroughly with ligands possessing a large variety of physical properties in terms of polarizability, dipole moment and ionization potential. In order to explain the experimental results, a simple electrostatic model was employed:[111]

$$V(r) = -\frac{\alpha z^2}{2r^4} - \frac{z\mu_D}{r^2}\cos(\theta) \tag{3.11.1}$$

where z is the charge of the ion, r is the distance between ion and ligand, α is the polarizability of the ligand, μ_D is the dipole moment of the ligand and finally θ is the angle between the dipole and the line of bonding. The interaction from the dipole moment varies with z/r^2, which has importance at long range distances, and the polarizability term varies with z^2/r^4 which dominates at short distances. This model does not take bonding into consideration and makes a number of other assumptions:

a) The distance r between the metal ion M^{n+} and the ligand L is a scalar quantity.

b) All energetic interactions are represented by point interactions.

c) No ligand interaction is taken into account.

d) There is no difference in polarizabilities of the metal ions M^+ and M^{2+}.

e) There is no difference in polarizabilities and dipole moment of L and L^+.

Previous computational studies include Asthagiri[112] and co-workers, who investigated the hydration structure and free energy of alkaline earth metals and first row transition metals using DFT

at the B3LYP/6-31+G(d,p) level. The goal was to examine the hydration structure and the free energy of hydration of Mg_2^+, Ca_2^+ and the transition metal ions Sc^{2+}, Ti^{2+}, V^{2+}, Cr^{2+}, Mn^{2+}, Fe^{2+}, Co^{2+}, Ni^{2+}, and Cu^{2+}. This group found a strong contribution from the ligand field effect on the free energy hydration. Siegbahn[113] and co-workers performed DFT-calculations of the hydration of Be^{2+}, Mg^{2+}, Ca^{2+} and Zn^{2+} ions at the B3LYP/6-311+G(2d,2p)-level. It was found that in order to obtain accurate binding energies, the dipole moment and polarizability of water have to be well described. Geometry optimizations, binding energies and electronic structures of $[CuH_2O]^{2+}$, $[CuNH_3]^{2+}$, $[CuH_2O]^{+}$, $[CuNH_3]^{+}$ and other monohydrated metal-ion complexes were investigated by El-Nahas with the ab initio methods (CCSD(T)), as well as DFT-calculations, B3LYP, using 6-311+G(d,p)- and LANL2DZ-basis set.[79–81] One purpose of these studies was to investigate the stability of monohydrated metal-ion complexes, and the results strongly indicate stable $[CuH_2O]^{+}$ and $[CuNH_3]^{+}$ complexes. Extensive studies of most transition metal-ions and main group metal-ions and their interaction with water using the ab initio methods MP2 and CCSD(T) were performed by Bock, Glusker and co-workers, for example calculation of the hydration of zinc-ions where performed.[71] The purpose of this study was to compare Zn^{2+} hydration with hydration of Mg^{2+} and Be^{2+} ions. One finding in this study was a smaller energy difference for Zn^{2+} ions having water molecules hydrogen bonded in a second solvation shell, than the corresponding difference for Mg^{2+} and Be^{2+} ions. The same group also investigated the charge distribution in orbitals, bonding enthalpies and vibrational frequencies of metal-ion monohydrates.[72] One of the main findings from this study was that the negative charge on the coordinated oxygen-atom of the water molecule increased, followed by a decrease of negative charge on the hydrogen atoms compared to an uncoordinated water molecule.[72] Bock and co-workers also investigated the hydration structure and binding enthalpies of the first and second coordination shell of Mg^{2+} ions at the MP2/6-311++G(d,p) level and at the B3LYP/6-311++(3df,3dp) level of theory.[73] Different structures with up to six water molecules in a first coordination shell and 12 water molecules in a second were considered in order to investigate the energy difference of having water molecules in the first as opposed to the second shell. The results indicated a preference for having water molecules in a first shell, and that this preference is larger for MP2 calculations than for the corresponding B3LYP calculations. In another study[74] of Bock and co-workers, the linear relationship between acidity and stability in mono- and hexa-hydrated metal-ion complexes were examined for a large range of alkaline earth metals and first row transition metal ions at the MP2(Full)/6-311++G(d,p) level of theory. This group found a linear relationship between the calculated enthalpies, ΔH^0_{298}, of dissociation of the mono- and hexahydrates and the experimentally determined pKa values of metal-ions. Several papers have also combined experimental and computational studies, for

example Cox, Stace and co-workers[91] presented experiments and ab initio, MP4, calculations of Cu^{2+}, Ag^{2+}, Au^{2+} and Ar complexes in which the unexpected stability of these metal-ion argon complexes were reported. Their results show that the stability of the complexes is due to strong electrostatic interactions and the high ionization energy of argon. The same group performed DFT calculations and experiments in order to investigate the requirement of alcohols to stabilize the Pb^{2+} ion.[98] Increasing the chain length of the alcohols resulted in more stable complexes, a result due to a softer ligand. In another experimental and ab initio study by Cox et al. the Pb^{2+}, Hg^{2+}, Sn^{2+} along with their interaction with water and especially proton transfer reactions were investigated.[92] The calculations and experiments showed all three metal-ions displayed proton transfer reactions. No stable metal-ion water complex was found. Finally, Cox et al. investigated both experimentally and computationally the requirement for a ligand to stabilize the Al^{3+} ion using both DFT and post Hartree-Fock calculations.[93] MP2 was employed for geometry optimization and frequency calculations, and single point CCSD(T)-calculations were used to include electron correlation. Ligands such as acetonitrile, which can act as strong σ donors as well as electron acceptor were successful in stabilizing the Al^{3+} ion.

3.12 Experimental considerations of ionization energy difference

It has been a well-known fact that the difference between the ionization energy of a metal ion and a ligand is a crucial factor in the stabilization of a complex against charge transfer, and Marcus[114] has given a detailed analysis of charge transfer processes in solution. Possible charge transfer processes that can occur in the gas phase by a single molecule and a doubly charged metal ion have been suggested in later work.[115,116] The difference between the second ionization energy of the metal ion, M^{2+}, and the first ionization energy of the ligand, has been given as the reason for proton transfer reactions to occur. The magnitude of this difference determines if a charge transfer reaction will be energetically favourable or not. If the difference is large, it will occur spontaneously at contact between a doubly charged metal ion and a neutral ligand.

The reactions[87] that can occur between a metal-ion M^{2+} and neutral ligands, for example water, are the charge transfer reaction 3.12.1:

$$M^{2+} + H_2O \longrightarrow M^+ + H_2O^+ \tag{3.12.1}$$

and proton transfer reaction 3.12.2:

$$M^{2+} + 2\,H_2O \longrightarrow MOH^+ + H_3O^+ \tag{3.12.2}$$

Table 3.4 shows the main results from Stace and co-workers.[87] Mass spectrometry was employed in order to determine the minimum size of the complex n_{min}, which indicates the lowest number of ligands that is needed to stabilize the complex, and n_{max} which is the number of ligands at which maximum intensity occurs i.e. the size of the most stable complex. Ionization energy for different ligands is given in electron volts, polarizability in $\mathring{A}^3$ and dipole moment μ_D in Debye. The conclusions from the study were that the stable complexes can be divided into three different categories:

1. Ligands with high first ionization energy (IE >12 eV): The critical n_{min} in this group is 1 or 2. Water, carbon dioxide and acetonitrile belong to this group. The difference between the ionization energy of the ligand and the second ionization energy of the metal ion is small (for example ΔE between H_2O and Mg^{2+} is 2.4 eV) which does not lead to a big stabilization energy for the complex and charge transfer products i.e. the gain in energy for reaction 3.12.1 or 3.12.2 is small.

2. Ligands with a quite small IE, but with sufficiently large polarizability: The minimum value for stabilization of a complex is 2. Members of this group are pyridine, diethyl ether and butylamine.

3. In the last group comes ligands which display a combination of the different physical properties that taken together can stabilize the complex, and the minimum size in this group is 3.

Ligand	n_{min}	n_{max}	α (Å^3)	μ (D)	IE (eV)
CO_2	2	4	2.63	0	13.8
H_2O	2	4-6	1.48	1.85	12.6
Acetonitrile	1	4(6)	4.40	3.92	12.2
Methanol	2	5-10	3.23	1.71	10.8
Ammonia	3	4	2.26	1.47	10.7
Ethanol	3	4(6,8)	5.41	1.69	10.47
n-Propanol	3	4	6.74	1.58	10.2
Acetone	3	4(6)	6.39	2.88	9.7
2-Butanone	2	4	8.13	2.78	9.51
Diethyl Ether	2	3	8.73	1.15	9.51
THF	2	4	6	1.75	9.41
Butylamine	2	4	13.5	1.0	9
2-Pentanone	2	4	9.93	-	9.38
Pyridine	2	4	9.5	2.2	9.3
Penta-2,4-Dione	1	2	10.5	-	8.85
Pyrrole	2	4	9.27	4.22	8.64
Nitric Oxide	X	X	1.70	0.16	9.26
Dimethyl Sulfoxide	X	X	-	3.96	9.1
Ethylene Diamine	X	X	-	-	7.6

Table 3.4: Physical properties and minimum size n_{min} of a stable cluster which is the minimum size required to result in a stable cluster. Also shown is the maximum size n_{max}, which is the size of the most stable cluster found in experiments. Number within parenthesis in this column indicates a secondary maximum. X=No stable complex observed. From reference 87.

When looking at n_{max}, one trend can be seen as the function of complex size. Smaller ligands like water and methanol can adopt two or three possible coordination structures with 4, 5 and 6 ligands. The interpretation of Stace and co-workers was that in many cases, these sizes correspond to the optimum coordination of the metal ion, although several factors contribute to this coordination. There were also three ligands that failed to stabilize the Mg^{2+} ion, and no stable structures could be found at all in these three cases. Their low ionization energy in combination with low values for the other two physical properties given in table 3.4 might be an explanation to this failure. Stace and co-workers also points out that for both Mg^{+} and Mg^{2+}, the main contribution to the bonding in the magnesium ion-ligand complex is electrostatic ion-dipole and polarization or induced dipole interaction. There is also a possibility for a covalent interaction through charge transfer from ligand orbitals to the $3s$ or $3p$ orbitals in Mg^{2+} and Mg^{+} ions. Hence the magnitude of this interaction will be important for the overall bonding interaction and the data presented in table 3.4. In a later study made by Shvartsburg and Siu[62], the number of water molecules required to stabilize various metal dications was explored. The minimum size was investigated, this time by changing the metal ions with the same type of ligand. The goal was to see if there is a minimum size below which metal ion complex dissociation occurs spontaneously through charge transfer, shown in reaction 3.12.3, or through proton transfer, 3.12.4. In addition, neutral ligand loss as in reaction, 3.12.5, might also occur:

$$[\mathrm{M(H_2O)_n}]^{2+} \longrightarrow [\mathrm{M(H_2O)_{n-1}}]^{+} + \mathrm{H_2O}^{+} \tag{3.12.3}$$

$$[\mathrm{M(H_2O)_n}]^{2+} \longrightarrow [\mathrm{MOH(H_2O)_{n-k-2}}]^{+} + \mathrm{H_3O}^{+}\mathrm{(H_2O)_k} \tag{3.12.4}$$

$$[\mathrm{M(H_2O)_n}]^{2+} \longrightarrow [\mathrm{M(H_2O)_{n-1}}]^{2+} + \mathrm{H_2O} \tag{3.12.5}$$

Experimental results from this investigation are shown in table 3.5. Interestingly, the number of water molecules required to stabilize Mg^{2+} is only 1, which is lower than found by Stace and co-workers.[87] Minimum n_{min} values for the number of ligands to stabilize the metal-water complex against reaction 3.12.3 and reaction 3.12.4 and critical n_{max} values for the largest number of H_2O molecules at which reaction 3.12.4 was observed, are shown in table 3.5. As can be seen from table 3.5, the minimum size in all cases except Be^{2+}, is 1 and as pointed out from Shvartsburg et al this is very surprising since in their study, the difference in ionization energy between a metal ion M^{2+} and the water molecule can be as high as 8 eV.

This is in contrast to the results shown in table 3.4, which indicate that the difference between the ionization energy of Mg^{2+} (15.0 eV), and ligands such as ethanol or n-propanol with a difference of approximately 4.5-5 eV, requires 2 or 3 ligands respectively. The conclusions from these two studies was that the overall stability and charge transfer reactions could be explained at a semi-quantitative level that does not take bonding into account. Critical factors for the stability are the second ionization potential of the metal and the first ionization potential of the ligand. As earlier mentioned, the electrostatic model (equation 3.11.1) only considers electrostatic interactions, so no knowledge about electron transfer into specific orbitals can be revealed. Furthermore, no information of the complex geometry other than the number of ligands coordinated to the metal ion can be found in the experimental data. Most of the studies in this area have dealt with single component systems i.e. only one type of ligand, but a few of them have investigated the behaviour and preferential solvation of multi-component systems, those with more than one type of ligand. Preferential take-up of methanol over water was observed experimentally and theoretically by Kebarle et al[63] when studying singly charged alkaline metal ions, and by Yamashita and Fenn[117] when investigating the same ions. A decrease in the preferential take-up for methanol was also observed when going from Li^+ to Cs^+. This was explained by the increasing ion radius, where the distance from the metal ion to the coordinating oxygen atom in the ligand became larger and, hence, made the polarizability less important according to equation 3.11.1.

Element	Second IE eV	n_{min}	n_{max}
Ba	10.0	1	2
Sr	11.0	1	2
Ca	11.9	1	2
Mg	15.0	1	4
Mn	15.6	1	4
Fe	16.2	1	5
Cd	16.8	1	4
Co	17.1	1	5
Zn	18.0	1	6
Ni	18.2	1	5
Be	18.2	2	8
Cu	20.3	1	6

Table 3.5: Second ionization energy and minimum size of stable cluster for different metals taken from 62. n_{max} is the maximum value for which reaction 3.12.4 was observed.

3.13 Validation of dipole moment and polarizability importance in this work

Since a lot of interaction in isolated gas-phase molecules have been suggested to consist of dipole and polarizability interactions, these quantities have to be defined. Two charges q^- and q^+ separated by a distance r constitute a dipole where the dipole moment, μ, which is a vector, can in classical terms be expressed as $\vec{\mu} = rq$. In a molecule, the sum from individual electrons makes up the total dipole moment:[55]

$$\vec{\mu} = \sum_i q_i r_i \tag{3.13.1}$$

where r_i is the location of particle i. An applied external, electrical field can distort the electron cloud in a molecule and create an induced dipole moment. The extent to which the electrons are distorted is a measure of the polarizability, α, of the molecule. In most cases, the induced dipole moment, $\vec{\mu}$, is proportional to the applied field, ε:

$$\vec{\mu} = \alpha\varepsilon \tag{3.13.2}$$

The importance of polarizability and dipole moment in the context of distance dependence can be shown when the difference between the two terms in equation 3.11.1 is calculated for different values of r. Since the dipole moment is similar for water and methanol, whereas the polarizability differs significantly for these two molecules, the first term in equation 3.11.1 can be expected to be of greater importance at shorter distances from the metal ion, than the second term. Due to the smaller polarizability of water, the dipole moment becomes more important at shorter distances from the metal ion than for methanol. This is shown in figure 3.7, where the curve for water displays a stronger and more enhanced dip than the corresponding curve for methanol. For comparison, ethanol (μ_D=1.69 D, α=5.41 Å) and ammonia (μ_D=1.47 D, α=2.26 Å) are also included in the graph. The graph clearly shows the counterbalance between the dipole moment and polarizability when comparing the water and ethanol molecules. For ethanol, the dipole moment term becomes important further away from the metal ion compared to the water molecule and a smoother curve is obtained for ethanol.

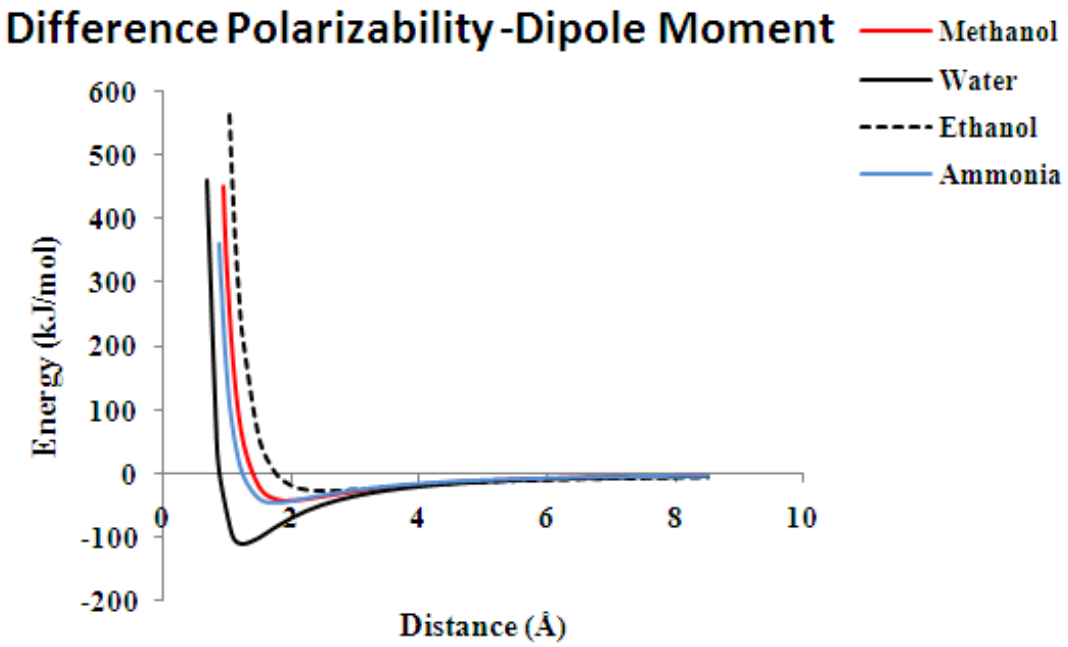

Figure 3.7: Energy difference between polarizability and dipole moment as a function of distance between a ligand and a doubly charged particle representing a doubly charged metal ion according to equation 3.11.1.

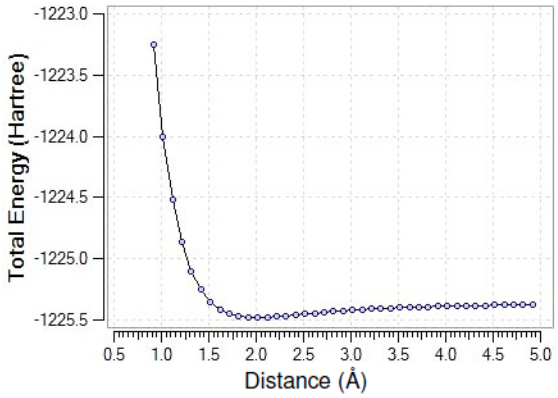

Figure 3.8: Scan of the $Mn^{2+}-H_2O$ system.

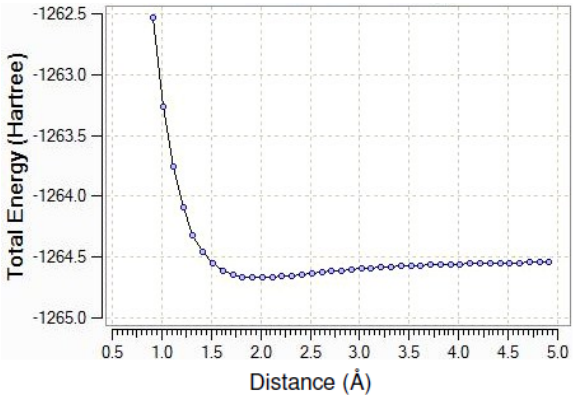

Figure 3.9: Scan of the $Mn^{2+}-CH_3OH$ system.

3.14 Computational studies of physical properties in this work

In order to validate equation 3.11.1, scan calculations were performed for the manganese-water and manganese-methanol systems, where the distance between the manganese-ion and a water/methanol molecule was increased in 30 steps of 0.25 Å each. The calculations were performed using the Gaussian03[41] software package, at the MP2/6-311G(d,p) level of theory. As can be seen from the graphs, the manganese-methanol system displays a stronger interaction which implies a lower total energy than the corresponding manganese-water system. A stronger binding energy for methanol molecules to a doubly charged manganese ion is observed in comparison to water molecules. On the other hand, both curves behaves in a similar way with a minimum at a distance of approximately 2 Å. This minimum represents the most favourable distance between the Mn^{2+} ion and a single water/methanol molecule i.e. bond distance. However, when more ligands are coordinated to a transition metal ion, the bond distance will be affected by orbital-mixing on the metal-ion and electrostatic repulsion/interaction between the ligands. Mixing of the $3d$-$4s$ orbitals will be discussed later in this chapter, and will prove to have a crucial influence of the binding energies and bond lengths.

3.15 Preferential coordination of H_2O or ROH to a Mn^{2+}-ion

One previous solvation study of water or alcohol with the doubly charged manganese ion, were made by Stace and co-workers.[88] In this study, which was supported by DFT calculations, stable structures of $[Mn(H_2O)_4]^{2+}$ and $[Mn(ROH)_4]^{2+}$ were found. Figure 3.10 to 3.14 shows the ion intensity distribution for $[Mn(H_2O)_N]^{2+}$ and $[Mn(ROH)_N]^{2+}$ complexes. In all cases a sharp peak for N=4 can be seen. This is a strong indication that a complex with four ligands is particularly stable. Furthermore, for all ligands, the intensity curves show a anomalous behaviour for $N \gg 5$ which is believed to be caused by larger hydrogen bonded network structures. (n in the figure correspond to N in the text).

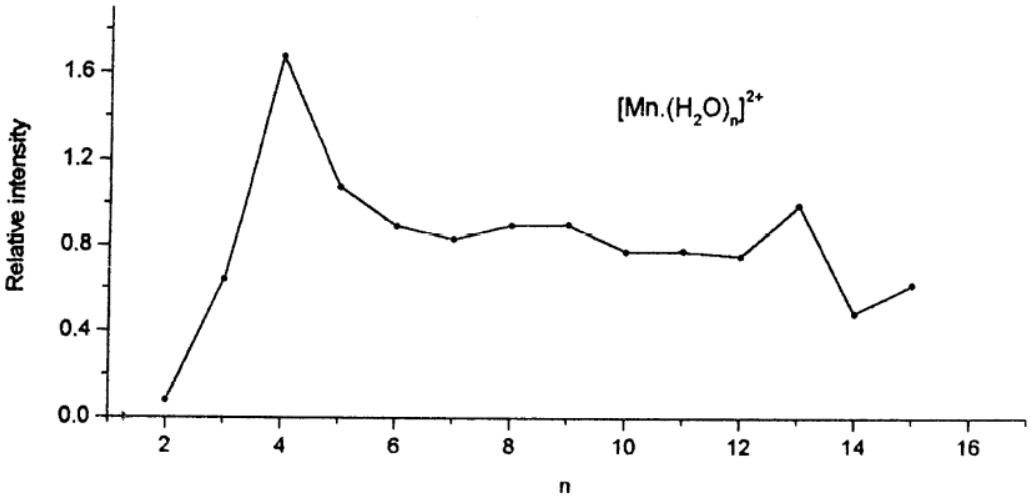

Figure 3.10: Ion intensity distribution for $[M(H_2O)_N]^{2+}$. Image taken from reference 88.

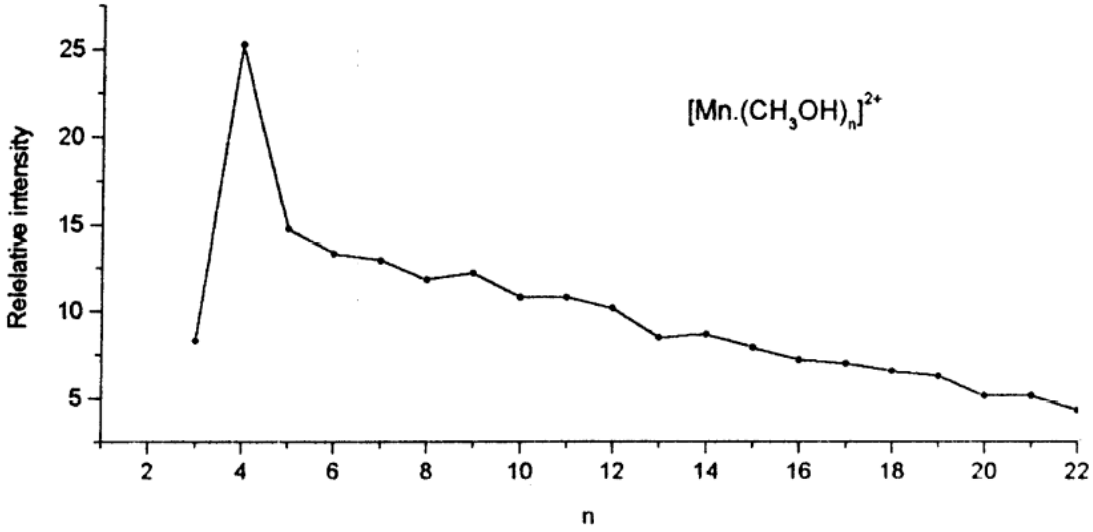

Figure 3.11: Ion intensity distribution for $[Mn(CH_3OH)_N]^{2+}$. Image taken from reference 88.

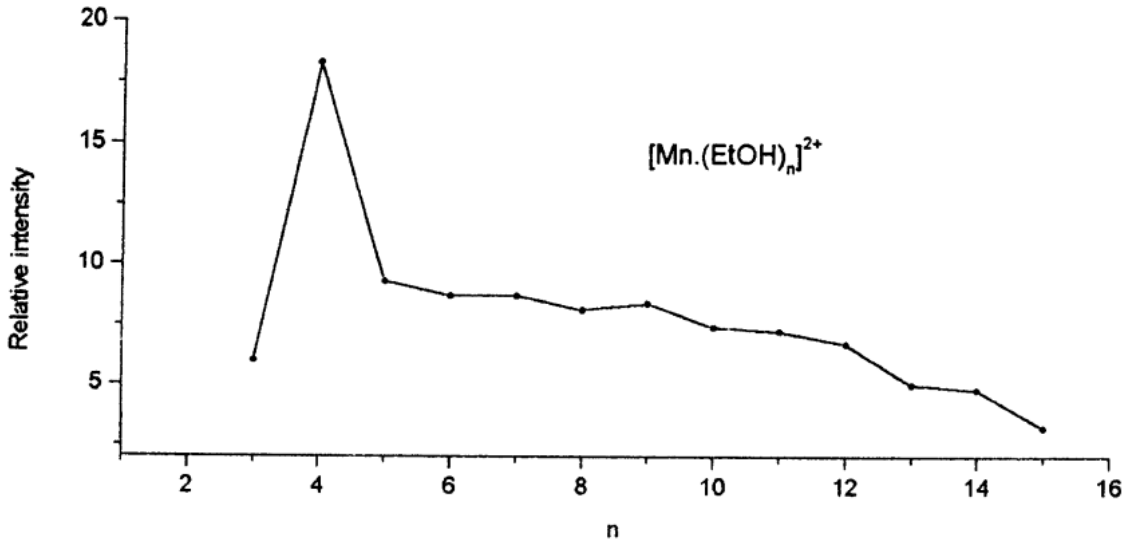

Figure 3.12: Ion intensity distribution for $[Mn(EtOH)_N]^{2+}$. Image taken from reference 88.

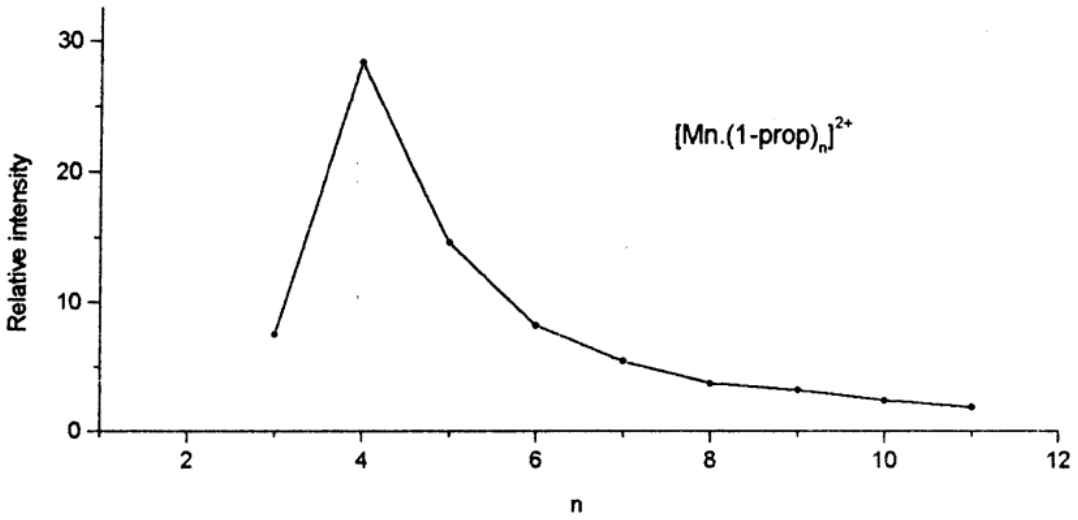

Figure 3.13: Ion intensity distribution for $[\mathrm{Mn}(1-\mathrm{prop})_N]^{2+}$. Image taken from reference 88.

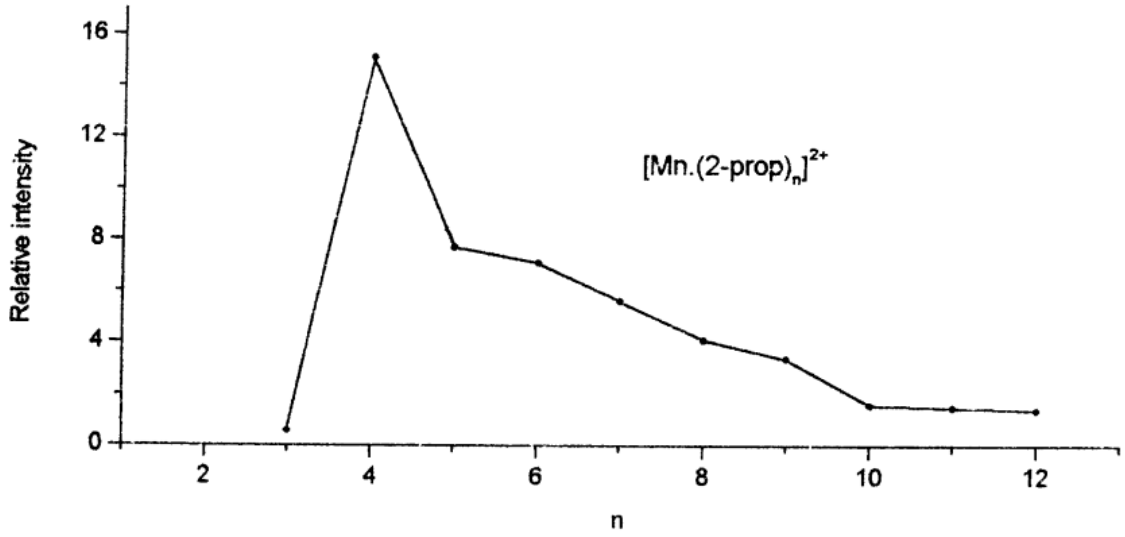

Figure 3.14: Ion intensity distribution for $[\mathrm{Mn}(2-\mathrm{prop})_N]^{2+}$-complexes. Image taken from reference 88.

Experimental results from the same group when dealing with a solvent mixture of methanol and water indicates that a complex with 4 and 6 ligands are stable.[46] Figure 3.15 shows the precursor ion distribution for a complex of the form $[Mn(CH_3OH)_N(H_2O)]^{2+}$. Two sharp peaks can be seen where N=3 and 5 which correspond to the $[Mn(CH_3OH)_3(H_2O)]^{2+}$ and the $[Mn(CH_3OH)_5(H_2O)]^{2+}$ complexes respectively. Obviously, this is a difference from the "single" solvent case were only one peak could be observed. Different fragmentation pathways were studied using the MIKES technique described earlier in the introduction. For the complexes under investigation in this study, two different types of neutral fragmentation pathways are possible:

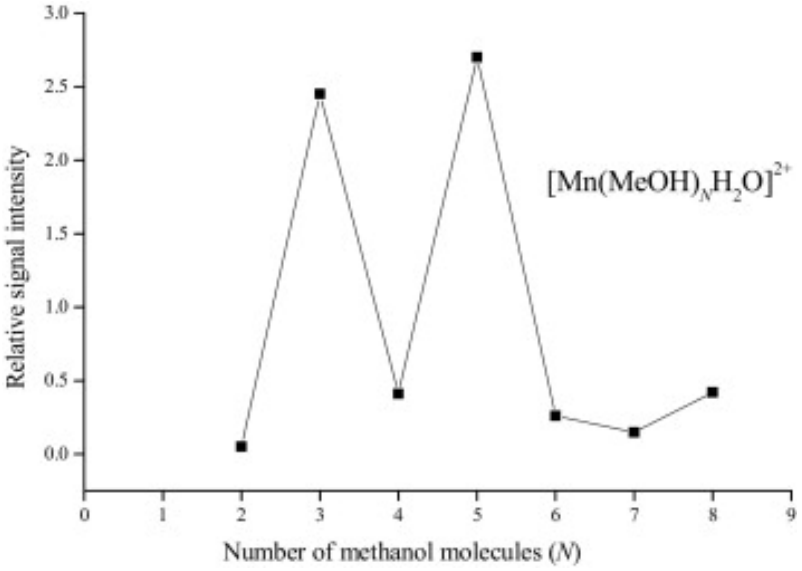

Figure 3.15: Ion intensity distribution for complexes of the form $[Mn(CH_3OH)_N(H_2O)]^{2+}$. Image taken from reference 46.

$$[\mathrm{Mn(CH_3OH)_N(H_2O)}]^{2+} \longrightarrow [\mathrm{Mn(CH_3OH)_N}]^{2+} + \mathrm{H_2O} \tag{3.15.1}$$

$$[\mathrm{Mn(CH_3OH)_N(H_2O)}]^{2+} \longrightarrow [\mathrm{Mn(CH_3OH)_{N-1}(H_2O)}]^{2+} + \mathrm{CH_3OH} \tag{3.15.2}$$

If there are two possible reaction routes like 3.15.1 and 3.15.2 with different reaction energies, the reaction with the lower activation energy will occur. Any difference in the physical properties will reveal if one of the reactions is possible, or in other words if one of the two ligands is more strongly bound to the metal ion.

The kinetic shift that arises from competing reactions can act as a tool for probing these relative binding energies,[89,90] and has been used for both unimolecular decay and for collision activation. In the first series of complexes $[Mn(CH_3OH)_N(H_2O)]^{2+}$, N was varied between 3-5. With just one water molecule it is possible to detect which one of the two ligand type falls off more readily, and hence, is more loosely bound to the metal di-cation. Figure 3.16 shows the CID (Collision Induced Dissociation) and unimolecular fragmentation results which were recorded for the $[Mn(CH_3OH)_4(H_2O)]^{2+}$ complex. In both the CID experiment and from the unimolecular fragmentation it can be seen that the most prominent peaks come from the loss of one neutral water molecules. When the loss of a neutral methanol molecule occurs in the CID spectrum, it is also followed by a loss of a water molecule. CID spectra and unimolecular fragmentation pathways were also recorded for complexes of the form $[Mn(CH_3OH)_N(H_2O)_2]^{2+}$ when N=3 and 4. Figure 3.17 shows the CID and unimolecular fragmentation when N=4. The same pattern can be seen; loss of a neutral water molecule is still the most dominant reaction. In addition, a peak which implies loss of two molecules can be seen.

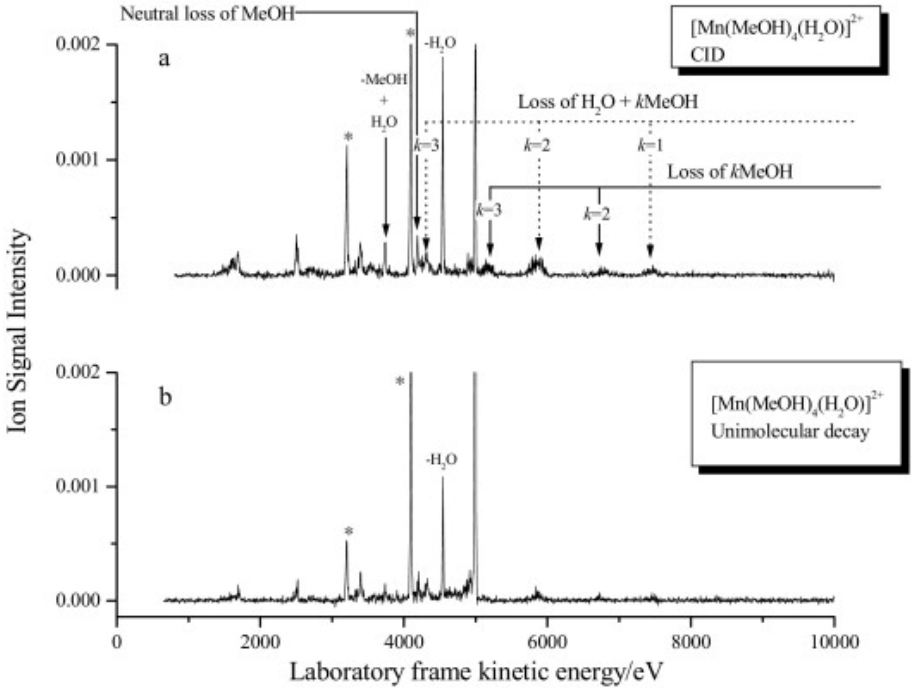

Figure 3.16: CID (a) and unimolecular (b) fragmentation for a $[Mn(CH_3OH)_4(H_2O)]^{2+}$-complex. Image taken from reference 46.

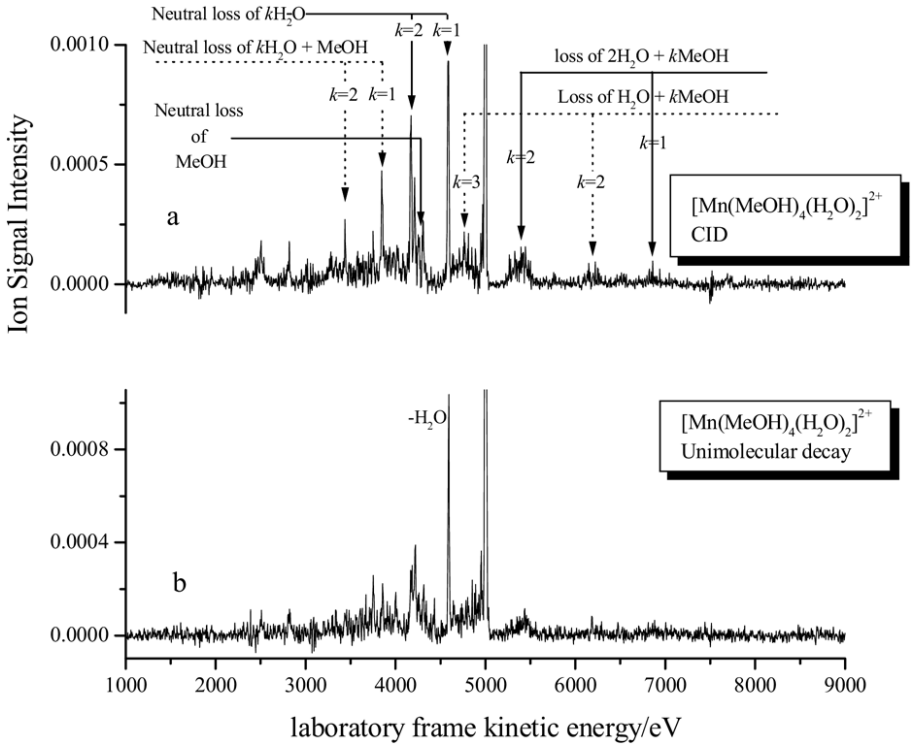

Figure 3.17: CID (a) and unimolecular (b) fragmentation for a $[Mn(CH_3OH)_N(H_2O)_2]^{2+}$-complex. Image taken from reference 46.

3.16 Computational Details

Earlier calculations[88] with manganese ions and water molecules performed using the BP86 functional with triple-ζ Slater Type Orbital basis set on manganese and double-ζ Slater Type Orbital for oxygen, carbon and hydrogen, showed that additional molecules coordinated to a $[Mn(L)_4]^{2+}$ complex forms a secondary solvation shell, where the additional molecules are hydrogen-bonded to the molecules in the first shell, which are directly coordinated to the manganese ion. It was also established in this study that a high-spin treatment of the complexes best replicated the experimental results. However, in a later paper from Rotzinger,[118] coordination to a transition metal ion was investigated using both Hartree-Fock and DFT methods. It was concluded that DFT has limitations, especially the metal-ligand interaction and hydrogen-bonding is not correctly treated. For metal ions with a charge higher than two, well established functionals appear to favour a low coordination number of the first shell i.e. coordination of all ligands directly to the first shell might be less favourable compared to having some ligands hydrogen bonded in a second solvation shell. For example, a ligand number of six in total, results in having four ligands in the first shell and the remaining two in a second solvation shell hydrogen bonded to the first shell ligands. Expressed in another way, DFT as a method would overestimate hydrogen-bonding and make structures contai-

Method/ Functional	Δ E (4+0)-(3+1)	Δ E (6+0)-(4+2) Trans	Δ E (6+0)-(4+2) Cis	Δ E (6+0)-(5+1)
BP86	-42.3	30.6	17.0	22.0
B3LYP	-51.7	11.8	-1.5	11.2
HF	-68	-37.0	-48.5	-15.5
MP2	-60	-18.6	-31.5	-6.8

Table 3.6: Δ E for ligands in first shell vs second shell. All energies are given in kJmol^{-1}.

ning hydrogen-bonds more favourable. It was conluded that MP2 would be a better choice for this type of problems.[118] To try this statement, the performance of two widely used functionals were investigated along with two wave-function based methods, Hartree-Fock and the MP2-method described in the theory section. The functionals were the BP86 and the hybrid B3LYP functionals described in the theory chapter. Table 3.6 shows the difference in energy when the ligands are coordinated in the first shell vs. having ligands coordinated in a second solvation shell. Notation for the complexes is as follows: (*N*+*P*), where *N* denotes the ligands in the first shell and *P* denotes the hydrogen bonded ligands in the second shell. As can be seen from table 3.6, both HF and MP2 predict a lower energy for complexes having ligands in a first shell. Many structures calculated with the DFT methods predict the opposite, but both functionals predicts a lower energy for the 4+0 structure than the 3+1 structure. B3LYP produced energies closer to the wave-function based methods than the pure DFT based functional BP86, since B3LYP includes Hartree-Fock exchange. Although the results reported here are not in any way is a complete study, it can serve as an indication of expected trends. Just like the effects in hydrogen-bonded systems that were pointed out by Rotzinger,[118] these effects can also be expected to appear in the systems under investigation in this thesis when using the BP86 or B3LYP functionals. Three questions are to be answered in this investigation. Firstly, since gas-phase experiments show that methanol is more strongly bound to the metal ion is there any preferential up-take or coordination of methanol or water to a doubly charged Mn^{2+}-ion? Secondly, will ligand coordination directly to the Mn^{2+} ion in a first shell configuration be more favourable than having additional ligands hydrogen bonded in a second solvation shell? And the last question will deal with stabilization against proton transfer i.e. which physical factors for the ligands determine the stability against proton transfer? The choice of computational method is based on two factors; previous conclusion from theoretical studies[88] on ligand coordination to a Mn^{2+} ions in the gas phase best replicate experimental results if the Mn^{2+} ion is treated as high-spin with five unpaired electrons. And secondly, in a system

with five unpaired d-electrons, dynamic electron correlation should be more dominant over static electron correlation in the systems under observation. To avoid any preferred structure such as the second shell structure described before, calculations at the MP2 level would thus be a suitable choice of method since the MP2-method accounts for approximately 80-90 percent of the correlation energy.[26] All structures were first optimized at the HF/6-31G(d)-level of theory to get a decent starting structure, vibrational frequencies were then calculated to ensure that structures were at a minimum on the potential energy surface. After this, optimization at the MP2/6-311(d,p) level were performed. All the structures were optimized without any symmetry constraints, and the final symmetry for all optimized structures were C_1 except for the $[Mn(L)_1]^{2+}$ complex which had the C_S symmetry.

3.17 Geometry, spin and structure of $[Mn(L)_N]^{2+}(L)_P$-complexes N=1-6, P=0-2

Based on previous calculations,[88] the most energetically stable structures were found for high-spin complexes i.e. five unpaired electrons. This is also in agreement with what has been reported in literature,[1,119] where only high-spin manganese compounds and complexes are found for tetrahedral structures, and high-spin (and a few low-spin cases) are known for octahedral complexes. The high-spin configuration and tetrahedral structure can be understood in the context of the absence of ligand-field stabilization energy, since the repulsion between the ligands is a very important factor and the tetrahedral structure is the most favourable with respect to ligand repulsion. Several of the complexes with solvent molecules in a second solvation shell $[Mn(L)_N]^{2+}(L)_P$ adopt a distorted tetrahedral structure. In the following discussion, complexes of the form $[Mn(L)_N]^{2+}(L)_P$ will be shown. N denotes the number of ligands in the first solvation shell which spans from 1-6, P is the number of ligands in the second solvation shell, which spans 0-2, but always resulting in a total ligand number of six. Bond lengths are shown in Å and angles in degrees ($^\circ$). Colours are as follows: manganese is shown in purple, hydrogen-white, oxygen-red and carbon-black. The first figures show bond lengths and angles of $[Mn(H_2O)_N]^{2+}$ complexes with water molecules in the first solvation shell. As stated before, symmetry for the $[Mn(H_2O)]^{2+}$ complex was C_S in comparison to all the other structures. When N=1, the Mn-O bond length is 1.52 Å, which differs from figure 3.8, where the energy minimum is located around 1.85-1.9 Å. This difference is due to the choice of method for the scan, in which no relaxation for each step was performed. A relaxation for each step would have resulted in a better agreement between the energy minimum for the scan and the actual bond length in the $[Mn(H_2O)]^{2+}$ complex shown in figure 3.18. For the same

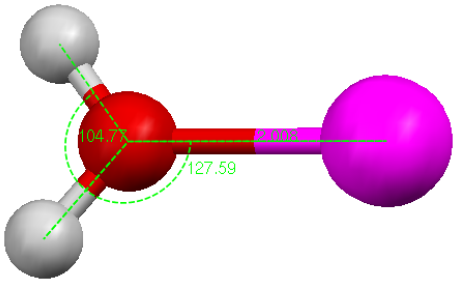

Figure 3.18: $[Mn(H_2O)]^{2+}$ (1+0)

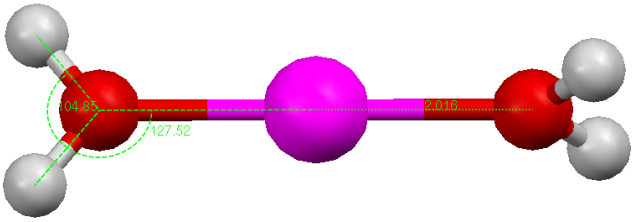

Figure 3.19: $[Mn(H_2O)_2]^{2+}$ (2+0)

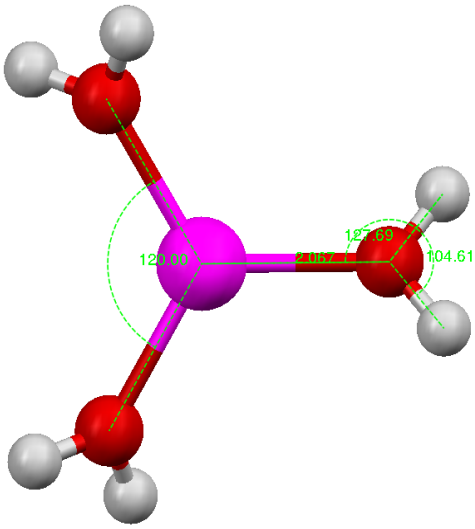

Figure 3.20: $[Mn(H_2O)_3]^{2+}$ (3+0)

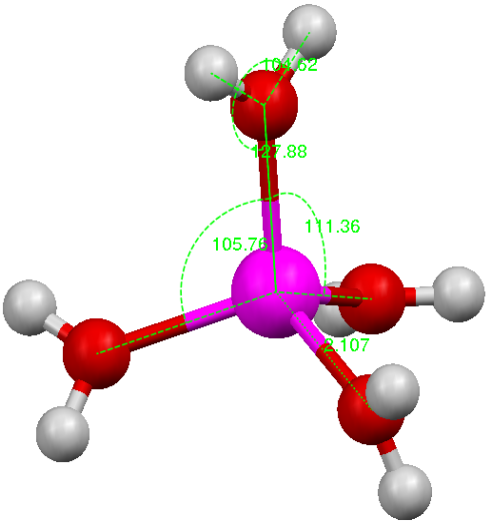

Figure 3.21: $[Mn(H_2O)_4]^{2+}$ (4+0)

reason, the Mn-O bond length in the $[Mn(CH_3OH)]^{2+}$ complex differs from the energy minimum obtained from the corresponding scan in figure 3.9. When N=2 the structure is linear, with the hydrogens of the two water molecules pointing in a perpendicular direction. For N=3, the average dihedral H-O-Mn-O angle formed between two H_2O molecules is 142.51° i.e. all hydrogen are not lying in the Mn-O plane. Average Mn-O bond lengths for the $[Mn(H_2O)_3]^{2+}$ complex is 2.07 Å. A ligand with four water molecules ends up in the tetrahedral arrangement around the manganese ion. Two different O-Mn-O angles can be found with an average of 111.36 and 105.76°. The average Mn-O bond lengths for the tetrahedral complex is 2.11 Å.

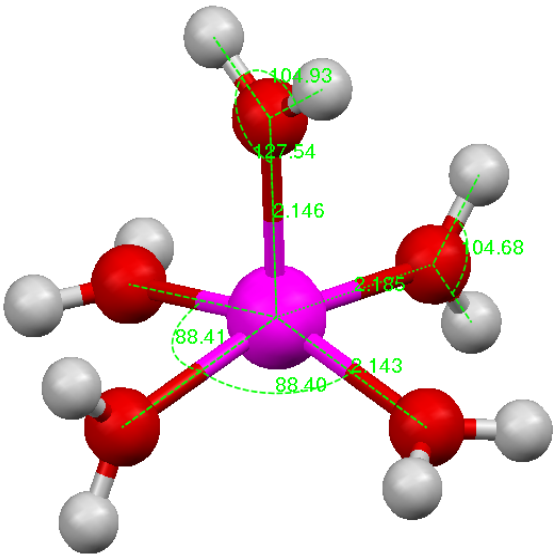

Figure 3.22: $[Mn(H_2O)_5]^{2+}$ (5+0)

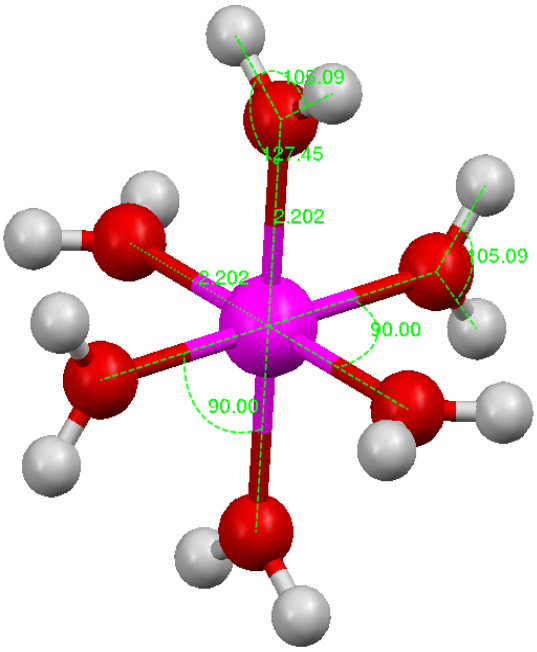

Figure 3.23: $[Mn(H_2O)_6]^{2+}$ (6+0)

The five-coordinated Mn-ion adopts a structure which is best described as a distorted square-pyramidal. Interestingly, this is the most stable structure even when starting from a trigonal bi-pyramidal geometry. The average Mn-O bond length in the plane of the square for Mn-O is 2.16 Å, and the two O-Mn-O angles formed between two opposite oxygen atoms have an average of 160.59°. The six-coordinated complex forms a completely symmetric structure with O-Mn-O angles of 90° and an average Mn-O bond length of 2.20 Å.

3.18 Second Shell Structures

A distorted trigonal structure is obtained if a water molecule is placed in the second solvation shell in the "3+1"-complex, with an average Mn-O bond length of 2.05 Å. For a four-coordinated complex with one water molecule in the second solvation shell, the tetrahedral structure is also preserved although slightly distorted in order for two of the water molecules to hydrogen-bond to the second shell. Average Mn-O bond length in this complex is 2.10 Å. A water ligand in a second shell does not affect the overall geometry for the five coordinated complex dramatically, the angle between the two water molecules that form hydrogen bonds to the second shell is reduced to approximately 84° and the average Mn-O bond lengths is 2.16 Å. When two water ligands occupy the second solvation shell according to figure 3.27, a completely symmetric tetrahedral structure

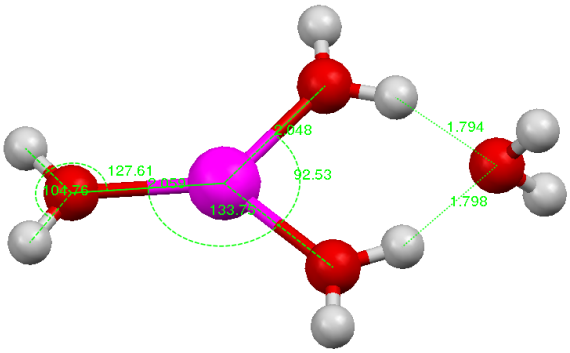

Figure 3.24: $[Mn(H_2O)_3(H_2O)]^{2+}$ (3+1)

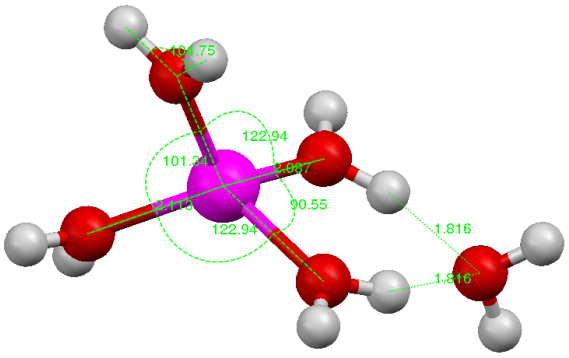

Figure 3.25: $[Mn(H_2O)_4(H_2O)]^{2+}$ (4+1)

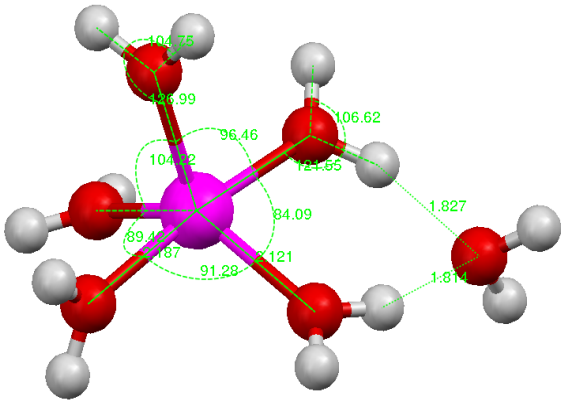

Figure 3.26: $[Mn(H_2O)_5(H_2O]^{2+}$ (5+1)

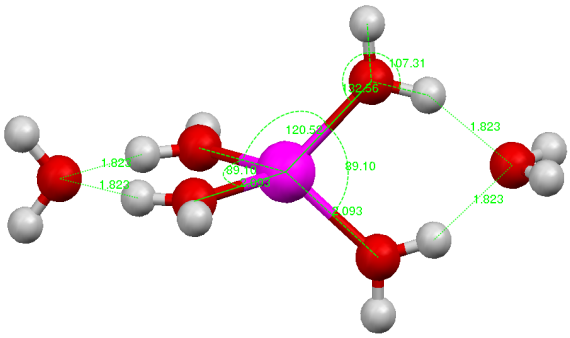

Figure 3.27: $[Mn(H_2O)_4(H_2O)_2]^{2+}$ (4+2)

is obtained with an average Mn-O bond length of 2.09 Å. These two water molecules can be placed in a "cis" position to each other resulting in the structure shown in 3.28. The geometry remains a distorted tetrahedron with a Mn-O distance of 2.09 Å on average. Comparison between the Mn-O bond lengths and the O-Mn-O angles for "3+0"- "3+1", "4+0"-"4+1"-"4+2" and the "5+0"-"5+1" complexes shows that the bond lengths are changed only slightly when introducing water molecules into the second solvation shell, whereas the O-Mn-O angles displays much more flexibility. The more rigid bond lengths are the first indication that the charge transfer between the manganese ion and the water molecules might be relatively small.

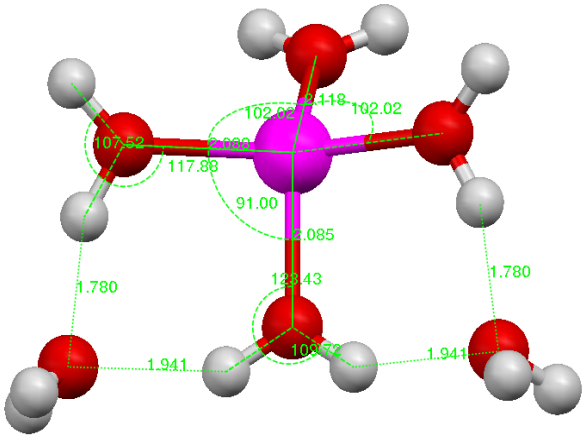

Figure 3.28: $[Mn(H_2O)_4(H_2O)_2]^{2+}$ (4+2)

3.18.1 Methanol Complexes

The complexes with methanol instead of water adopt almost the same structures as in the manganese-water cases, for example the linear O-Mn-O geometry is also adopted when two methanol molecules are coordinated to the manganese ion. The average Mn-O bond length for the $[Mn(L)_2]^{2+}$ complex is 1.99 Å. The roughly trigonal geometry is preserved for a three-coordinated complex, although all three O-Mn-O angles are different; Mn-O bond length is 2.05 Å on average. Furthermore, the tetrahedral geometry is also preserved in the four coordinated complex. All the O-Mn-O angles span from 105.1 - 109.2° and the average Mn-O bond length is 2.09 Å. Distorted square pyramidal and octahedral geometries are also preserved in the five- and six coordinated manganese-methanol complexes respectively. The last four complexes with one or two methanol complexes in a second solvation shell show the same basic structure as their water containing counterparts. The O-Mn-O angle between the two methanol molecules that are hydrogen-bonded to the second solvation shell is reduced to 94° in the "3+1" complex. Tetrahedral geometry was also observed for the "4+1" and "4+2" structures and the "5+1" structure displays a distorted square pyramidal geometry. Average Mn-O bond lengths for these last four complexes are: 2.03, 2.09, 2.14 and 2.08 Å respectively. This shows two very important aspects in comparison to the corresponding water complexes. Firstly, the Mn-O bond length stays approximately constant when a ligand is added to a second solvation shell for a given complex i.e. the Mn-O bond length "3+0" and "3+1" only differs to a small extent.

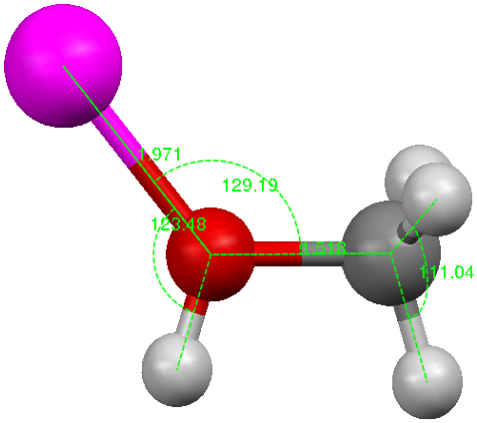

Figure 3.29: $[Mn(CH_3OH)]^{2+}$ (1+0)

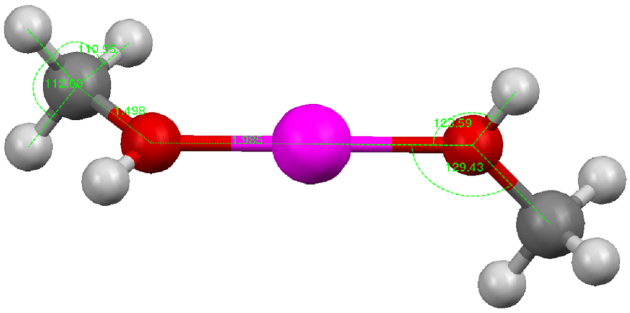

Figure 3.30: $[Mn(CH_3OH)_2]^{2+}$ (2+0)

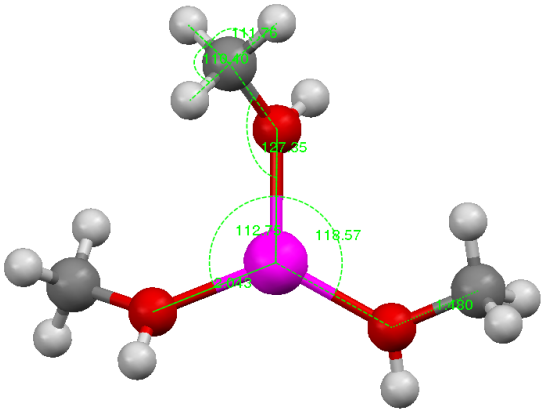

Figure 3.31: $[Mn(CH_3OH)_3]^{2+}$ (3+0)

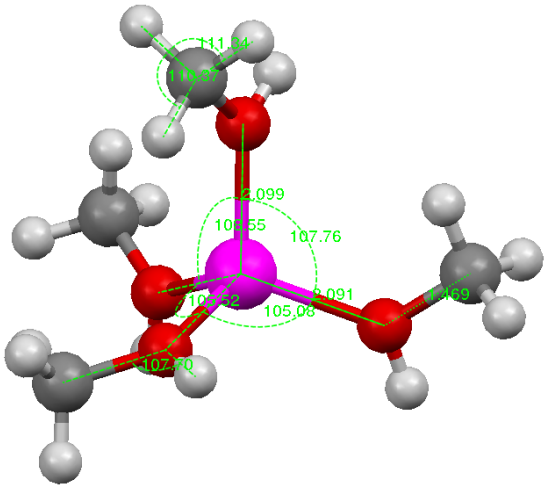

Figure 3.32: $[Mn(CH_3OH)_4]^{2+}$ (4+0)

Secondly, the Mn-O bond lengths are always shorter for the methanol comprising complexes when comparing the manganese-water and manganese-methanol complexes with the same number of ligands. This is an indication that the bond strength between the manganese ion and methanol is stronger than the interaction between the Mn ion and water molecules.

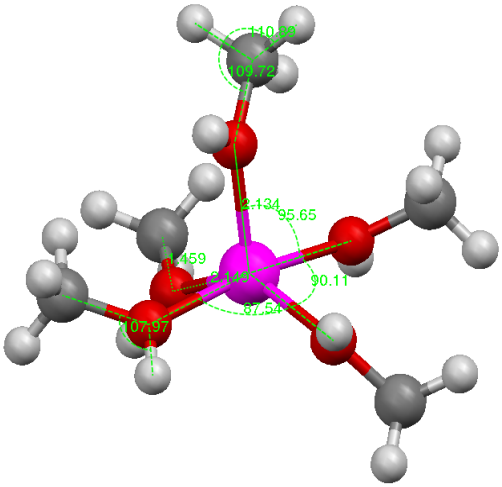

Figure 3.33: $[Mn(CH_3OH)_5]^{2+}$ (5+0)

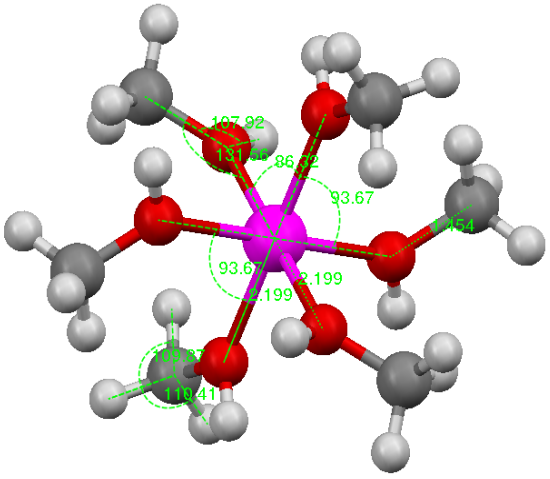

Figure 3.34: $[Mn(CH_3OH)_6]^{2+}$ (6+0)

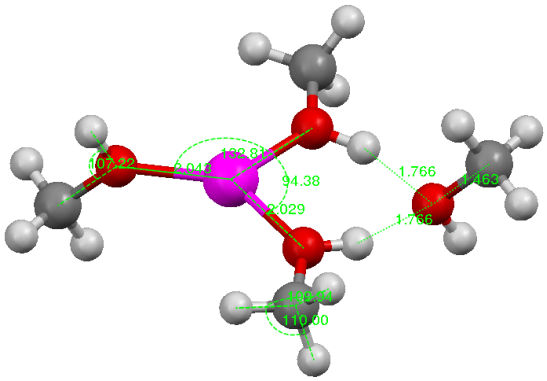

Figure 3.35: $[Mn(CH_3OH)_3(CH_3OH)]^{2+}$ (3+1)

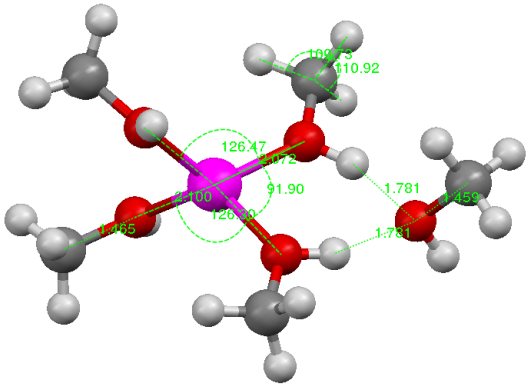

Figure 3.36: $[Mn(CH_3OH)_4(CH_3OH)]^{2+}$ (4+1)

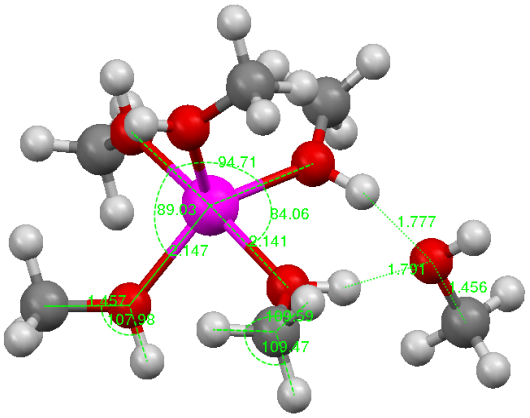

Figure 3.37: $[Mn(CH_3OH)_5(CH_3OH)]^{2+}$ (5+1)

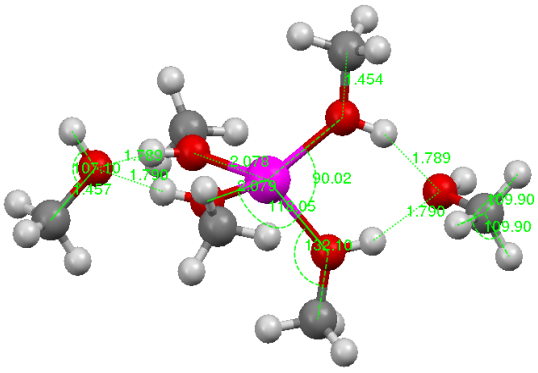

Figure 3.38: $[Mn(CH_3OH)_4(CH_3OH)_2]^{2+}$ (4+2)

3.19 Energetics for $[Mn(L)_N]^{2+}(L)_P$-complexes N=1-6, P=0-2

The binding energies for the previously described manganese-water and manganese-methanol complexes with N number of ligands of type L were analysed in two different ways. Firstly, the average binding energy is defined as the heat of reaction (or more strictly the internal energy change) for the reaction:

$$[Mn(L)_N]^{2+} \rightarrow Mn^{2+} + NL \tag{3.19.1}$$

This type of energy description gives the average energy for a total number of N ligands to be coordinated to the manganese-ion. The second is the successive or incremental binding energy, which describes the energy change for performing the step:

$$[Mn(L)_N]^{2+} \rightarrow [Mn(L)_{N-1}]^{2+} + L \tag{3.19.2}$$

Tables 3.7 and 3.8 show both types of energies for the Mn-water and the Mn-methanol complexes respectively. For all complexes, the average binding energy is always greater for the Mn-methanol complexes than the corresponding Mn-water complexes. This difference in average binding energy is almost constant at approximately 64 $kJmol^{-1}$. It can also be seen for both manganese-water and manganese-methanol complexes, that adding a ligand for a complex with N >2 results in a small and similar energy difference ranging from 0-6 $kJmol^{-1}$. Tables 3.7 and 3.8 show an interesting feature in the context of the previous discussion regarding preference for a first shell or second shell coordination.

N+*P*	Complex	Average BE $kJmol^{-1}$	Δ E Isomer $kJmol^{-1}$	Incremental BE $kJmol^{-1}$
1+0	$[Mn(H_2O)]^{2+}$	325.0		
2+0	$[Mn(H_2O)_2]^{2+}$	622.7		297.7
3+0	$[Mn(H_2O)_3]^{2+}$	850.7		228.0
4+0	$[Mn(H_2O)_4]^{2+}$	1045.3	0	194.6
3+1	$[Mn(H_2O)_3]^{2+}(H_2O)$	992.15	53.2	141.4
5+0	$[Mn(H_2O)_5]^{2+}$	1199.8	0	154.5
4+1	$[Mn(H_2O)_4]^{2+}(H_2O)$	1175.3	24.5	130.0
6+0	$[Mn(H_2O)_6]^{2+}$	1340.2	0	140.3
trans 4+0	$[Mn(H_2O)_4]^{2+}(H_2O)_2$	1302.0	38.1	102.2
cis 4+2	$[Mn(H_2O)_4]^{2+}(H_2O)_2$	1292.4	47.7	92.6

Table 3.7: Average and incremental binding energies of $[Mn(H_2O)_N]^{2+}$-complexes, where N ranges from 1-6. *N*+*P* denotes the number of *N* molecules in the first and *P* molecules second solvation shell.

N+*P*	Complex	Average BE $kJmol^{-1}$	Δ E Isomer $kJmol^{-1}$	Incremental BE $kJmol^{-1}$
1+0	$[Mn(CH_3OH)]^{2+}$	363.1		
2+0	$[Mn(CH_3OH)_2]^{2+}$	685.9		322.8
3+0	$[Mn(CH_3OH)_3]^{2+}$	918.9		233.0
4+0	$[Mn(CH_3OH)_4]^{2+}$	1114.3	0	195.4
3+1	$[Mn(CH_3OH)_3]^{2+}(H_2O)$	1057.4	56.9	138.5
5+0	$[Mn(CH_3OH)_5]^{2+}$	1263.2	0	148.8
4+1	$[Mn(CH_3OH)_4]^{2+}(H_2O)$	1241.1	22.1	126.8
6+0	$[Mn(CH_3OH)_6]^{2+}$	1397.8	0	134.7
trans 4+0	$[Mn(CH_3OH)_4]^{2+}(CH_3OH)_2$	1365.5	32.3	102.4

Table 3.8: Average and incremental binding energies of $[Mn(CH_3OH)_N]^{2+}$-complexes, where N ranges from 1-6. *N*+*P* denotes the number of *N* molecules in the first and *P* molecules second solvation shell.

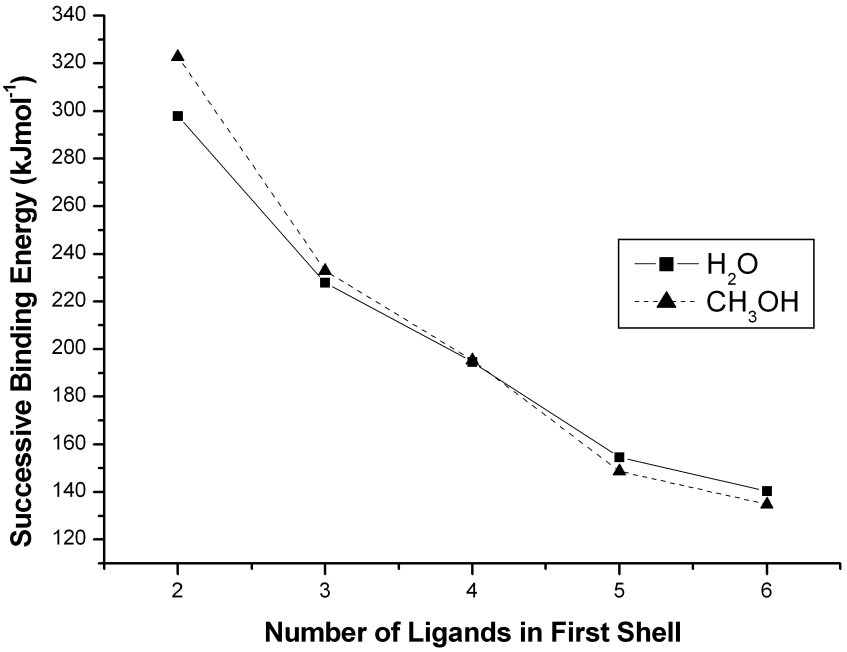

Figure 3.39: Successive binding energies for ligands in the first shell. The total number of ligands N goes from 2-6.

The average binding energies in table 3.7 and 3.8 shows that first-shell coordination is preferred over coordination in a second-shell geometry. This is in contrast to previous results by Stace and co-workers.[88] Due to the small isomer energy difference for "5+0" and "4+1" complexes, which is less than 25 $kJmol^{-1}$ for both water and methanol, both first shell and second shell coordination are possible. Two types of second shell structure are possible for a complex containing six water ligands, the trans and cis-configurations. Due to ligand repulsion in the cis-complex, this structure is destabilized by approximately 10 $kJmol^{-1}$ compared to the trans-configuration. The cis-configuration is not accessible for methanol containing complexes, despite attempts to obtain that structure. Previous work on solvation of metal cations has shown a decline in the successive binding energies when going from small to larger complexes, which agrees with the decline shown in tables 3.7 and 3.8. This decline can be attributed to an increased ligand repulsion and/or electronic effects on the metal d-orbitals when more ligands are coordinated to the metal ion. The electronic effects will be dealt with later in the chapter. Graph 3.39 shows the successive binding energies for ligands N in the first shell, where N spans from two to six.

Complex	Dominant Unimolecular pathway	CID Pathway neutral ligand loss
$[Mn(CH_3OH)_3(H_2O)]^{2+}$	H_2O	$H_2O > CH_3OH$
$[Mn(CH_3OH)_4(H_2O)]^{2+}$	H_2O	$H_2O > CH_3OH + H_2O) > CH_3OH$
$[Mn(CH_3OH)_5(H_2O)]^{2+}$	H_2O	$H_2O > CH_3OH + H_2O) > CH_3OH$
$[Mn(CH_3OH)_3(H_2O)_2]^{2+}$	H_2O	$H_2O >$(CH3OH + $2H_2O$)
$[Mn(CH_3OH)_4(H_2O)_2]^{2+}$	H_2O	$H_2O > 2H_2O >$(CH3OH + H_2O) >(CH3OH + $2H_2O$) >CH3OH

Table 3.9: Observed fragmentation pathways for unimolecular and collision-induced dissociation for $[Mn(CH_3OH)_N(H_2O)_P]^{2+}$-complexes, where N=3,4 or 5 and P=1 or 2. From 46.

As can be seen from figure 3.39, the successive binding energy is slightly larger for a methanol containing complex when N <3, but are equivalent at N=4. The steric repulsion and electronic effects from the ligands become more important when N >4. Clearly, there is an subtle interplay between the ligand abilities of donating electron density to the metal-ion and repulsion between ligands. Another interesting feature from figure 3.39 is the anomalous value for N=4, which indicates that the metal-ion complex is particularly stable at N=4. This stability is in perfect agreement with the experimental findings shown in figure 3.10 to 3.14.

3.20 Mixed Ligand Systems $[Mn(CH_3OH)_N]^{2+}(H_2O)$ N=1-5 and $[Mn(CH_3OH)_N]^{2+}(H_2O)_2$ N=1-4

The main purpose of this study is to investigate a suspected preferential take-up/coordination between water and methanol molecules to a manganese-ion. A stronger coordination between the Mn ion and methanol molecules than the interaction between Mn and water molecules is expected, because of the higher polarizability of methanol. An increasing importance of the dipole moment can also be expected with increasing complex size, due to the $1/r^4$ distance dependence from the polarizability term compared to the $1/r^2$ dependence of the dipole moment. As mentioned earlier, CID-studies show that loss of a neutral water molecule is preferred over loss of one neutral methanol molecule, which can be interpreted as a stronger Mn-methanol bond compared to the Mn-water bond. In context with the possible reaction pathways for ligand loss shown in equations 3.15.1 and 3.15.2, table 3.9 shows a summary of observed pathways for complexes of type $[Mn(CH_3OH)_N(H_2O)_P]^{2+}$- N=3-5, P=1 or 2.

3.21 Geometry and structure of $[Mn(CH_3OH)_N(H_2O)]^{2+}$, $[Mn(CH_3OH)_N(H_2O)_2]^{2+}$ and $[Mn(H_2O)_N(CH_3OH)]^{2+}$ with N=1-5

The structures for the mixed-ligand complexes follow the same pattern as the complexes in the Mn-water and Mn-methanol cases, with linear complex for two molecules, trigonal planar geometry for a complex with three ligands. The tetrahedral geometry is found when four ligands are coordinated to the metal ion and is also preserved when ligands are placed in a second solvation shell. Five coordinated complexes give a square based pyramidal structure, and six-coordinated structures give the octahedral arrangement, these structures are maintained when ligands are hydrogen bonded in a second solvation shell.

3.22 Energetics of mixed ligand complexes

The energetics for the $[Mn(CH_3OH)_N(H_2O)]^{2+}$-complexes are shown in table 3.10. Average binding energy were calculated according to equation 3.19.1 and successive binding energy according to equation 3.19.2.

N+*P*	Complex	Average BE $kJmol^{-1}$	Successive BE (CH_3OH) $kJmol^{-1}$	Successive BE (H_2O) $kJmol^{-1}$
2+0	$[Mn(CH_3OH)(H_2O)]^{2+}$	655.2	330.2	292.1
3+0	$[Mn(CH_3OH)_2(H_2O)]^{2+}$	897.4	242.2	211.5
4+0	$[Mn(CH_3OH)_3(H_2O)]^{2+}$	1097.2	199.8	178.3
3+1	$[Mn(CH_3OH)_3(H_2O)]^{2+}$	1046.1	154.4	130.4
5+0	$[Mn(CH_3OH)_4(H_2O)]^{2+}$	1251.1	153.8	136.7
4+1	$[Mn(CH_3OH)_4(H_2O)]^{2+}$	1231.1	133.9	116.8
6+0	$[Mn(CH_3OH)_5(H_2O)]^{2+}$	1388.8	137.8	125.7
5+1	$[Mn(CH_3OH)_5(H_2O)]^{2+}$	1361.8	110.8	98.6
trans 4+2	$[Mn(CH_3OH)_4(H_2O)_2]^{2+}$	1357.7	106.8	94.6
6+1	$[Mn(CH_3OH)_6(H_2O)]^{2+}$	1498.0	109.2	100.2

Table 3.10: Average and incremental binding energies of $[Mn(CH_3OH)_N(H_2O)]^{2+}$-complexes, where N ranges from 1-6. *N*+*P* denotes the number of *N* molecules in the first and *P* molecules second solvation shell.

The data presented in table 3.10 clearly shows a number of interesting features. Firstly, the average binding energy reveals that it is more favourable to have the ligands in a first solvation shell than coordinated via hydrogen-bonds in a second solvation shell. This is in accordance with the "only-water" and "only-methanol" ligand systems described earlier. A small reduction of the isomer difference compared to the "only-methanol" is observed. In the latter case the isomer difference between complexes of size 4,5 and 6 are 57,22, and 32 $kJmol^{-1}$, respectively, which in the table 3.10 have been reduced to 51, 20 and 27 $kJmol^{-1}$. The second feature that can be seen from table 3.10, involves the successive binding energy for water and methanol. For all complexes, it takes more energy to remove a methanol molecule than the energy required to perform the same reaction step for a water molecule, the reverse is seen when a methanol molecule is added. This goes for complexes with all ligands in a first shell and for complexes with one water molecule in a second coordination shell. From the findings described earlier, where coordination in a first shell was found to be more favourable, it is assumed that removing a methanol molecule from any of the complexes with a water in the second shell results in a re-arrangement of the complex to a "first-shell" structure. However, the energy difference between "first-shell" and "second-shell" structures after removal of one methanol molecule is only 20 $kJmol^{-1}$, which implies that a second shell structure might be possible.

The energy difference between the successive binding energies for methanol and water varies between 12 and 38 $kJmol^{-1}$ for first shell structures. As can be seen from table 3.10, the energy decreases for larger complexes which is a consequence of ligand repulsion and electronic effects when more ligands are coordinated to the metal ion.

The third aspect from the data presented concerns the stability of specific complex sizes. Strong indications both computationally and experimentally show that a complex size with four ligands is particularly stable in the "only-methanol" and "only-water" cases. Thus, a complex size with a total number of four ligands is expected to be more stable than a complex with three or five ligands. Figure 3.15 shows the ion-intensity distribution for $[Mn(CH_3OH)_N(H_2O)]^{2+}$ complexes before fragmentation and strong peaks can be seen for N=4 and N=6.

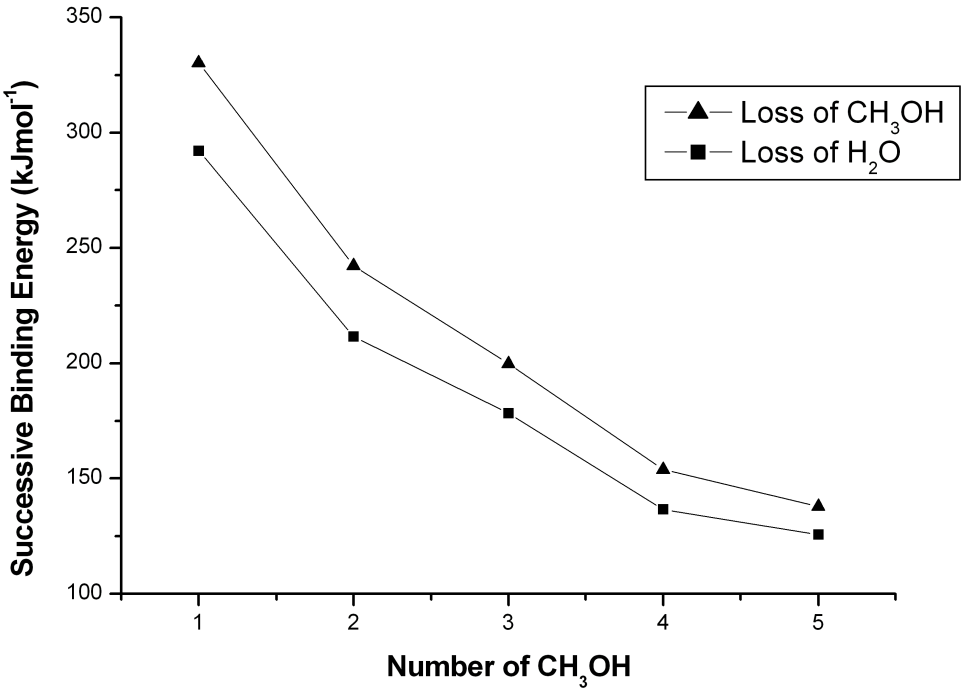

Figure 3.40: Successive binding energies for complexes of the form $[Mn(CH_3OH)_N(H_2O)]^{2+}$. Only first shell structures are considered.

Figure 3.40 shows the successive binding energies for methanol and water when complexes have the composition $[Mn(CH_3OH)_N(H_2O)]^{2+}$. As the data in the table indicates, successive binding energies are higher for methanol than water which is proof of a stronger interaction between the manganese ion and methanol compared to the corresponding interaction for water. Thus, the higher binding energy for methanol agrees with the unimolecular loss of a single water molecule (table 3.9). Furthermore, the anomalous feature on the curve for N=3 and N=5 is indicative of stable structures. This is also in agreement with the experimental findings shown in figure 3.15, where total numbers of four and six ligands constitute particularly stable structures. Table 3.11 shows the successive binding energies for mixed ligand complexes with two water molecules.

The binding energies correspond to the two reactions:

$$[\mathrm{Mn(CH_3OH)}_N\mathrm{(H_2O)_2}]^{2+} \rightarrow [\mathrm{Mn(CH_3OH)}_{N-1}\mathrm{(H_2O)_2}]^{2+} + \mathrm{CH_3OH} \quad (3.22.1)$$

and

$$[\mathrm{Mn(CH_3OH)}_N\mathrm{(H_2O)_2}]^{2+} \rightarrow [\mathrm{Mn(CH_3OH)}_N\mathrm{(H_2O)}]^{2+} + \mathrm{H_2O} \quad (3.22.2)$$

Experimental findings show that collisional activation can support loss of two water molecules simultaneously, these energies for loss of two water molecules are also shown in the table. The corresponding reaction is:

$$[\mathrm{Mn(CH_3OH)}_N\mathrm{(H_2O)_2}]^{2+} \rightarrow [\mathrm{Mn(CH_3OH)}_N]^{2+} + 2\mathrm{H_2O} \quad (3.22.3)$$

N+*P*	Complex	Average BE $kJmol^{-1}$	Successive BE (W) $kJmol^{-1}$	Successive BE (M) $kJmol^{-1}$	Successive BE 2×(W) $kJmol^{-1}$
3+0	$[Mn(M)(W)_2]^{2+}$	874.7	219.4	251.9	511.5 (255.8)
4+0	$[Mn(M)_2(W)_2]^{2+}$	1080.4	182.9	205.7	394.4 (197.2)
5+0	$[Mn(M)_3(W)_2]^{2+}$	1239.5	142.4	159.2	320.6 (160.3)
4+1	$[Mn(M)_3(W)_2]^{2+}$	1216.8			
3+2	$[Mn(M)_3(W)_2]^{2+}$	1216.8			
6+0	$[Mn(M)_4(W)_2]^{2+}$	1379.0	128.0	139.5	264.7 (132.4)
5+1	$[Mn(M)_4(W)_2]^{2+}$	1350.5			
4+2	$[Mn(M)_4(W)_2]^{2+}$	1347.2			

Table 3.11: Average and incremental binding energies of $[\mathrm{Mn(CH_3OH)}_N\mathrm{(H_2O)_2}]^{2+}$-complexes, where N ranges from 1-4. M=CH_3OH, W=H_2O and *N*+*P* denotes the number of *N* molecules in the first and *P* molecules second solvation shell.

The data presented for average binding energies in table 3.11, exhibit some interesting features. Coordination in the first shell is always more favourable, compared with having the same total number of ligands with some in a second solvation shell. This difference between the structural isomers ranges from 20-30 $kJmol^{-1}$. Interestingly, there is no energetic difference between the "4+1" and the "3+2" isomers, which gives a hint about the accessibility of different isomers having ligands in the second shell. The successive energy is shown only for complexes in the first shell, and clearly, performing the reaction step 3.22.1 is more expensive than the reaction

3.22.2. This is further evidence for a stronger binding and hence a preferential coordination of methanol molecules to the metal ion. When comparing the energy for performing reactions 3.22.1 and 3.22.2, it can be seen that it takes approximately the same amount of energy as performing the same steps for mixed ligand complexes with one water molecule. Table 3.11 also shows the successive binding energy for losing two water molecules, which obviously requires considerably more energy. However, if the energy per molecule is considered, the numbers in brackets, the energy required is comparable to the reaction step of losing (or adding) one methanol molecule.

The last table concerning the energetics of mixed ligand complexes, deals with complexes of composition $[Mn(H_2O)_N(CH_3OH)]^{2+}$. The first two complexes have been shown in previous tables, but are included in this table for completeness. The data in table 3.12 follow the trends shown for complexes with an excess of methanol. The successive binding energies are larger for methanol than the corresponding energies for water. Even with water molecules in excess, the successive binding energies indicate a stronger coordination for the methanol molecules. When comparing the successive energies for mixed ligand complexes with those for the "water-only" or "methanol-only," it can be seen that the binding energies for methanol increase whereas those for water decline. In table 3.12, differences in energetics for structural isomers are displayed. As for the previously shown mixed ligand complexes as well as the "water-only" and "methanol-only" complexes, coordination to the first shell is preferred over having ligands hydrogen-bonded in a second solvation shell. The graph in figure 3.41 shows the successive binding energies for the "first-shell"-complexes in table 3.12 and corresponds to the successive binding energies for $[Mn(CH_3OH)_N(H_2O)]^{2+}$ shown in figure 3.40. The curve is almost identical to the one in figure 3.40, it displays a small stability for a complex with a total number of four ligands even if the stability is less pronounced for loss (or addition) of a methanol molecule. This stability can also be expected for a total number of six ligands due to the shallow shape of the curve for that number of ligands. The more ligands that are coordinated, energies seem to converge to similar values, a behaviour in close agreement with figure 3.40. As a result from the different complex compositions presented, it is clear that a stronger bond is obtained between the Mn^{2+} ion and methanol than between the Mn^{2+} ion and water. The stronger interaction for methanol does not seem to be affected or weakened as the number of water molecules coordinated to the Mn^{2+}-ion increases.

The computational results obtained for the "water-only," "methanol-only" and for the mixed ligand systems follow trends that are in general agreement with earlier charged metal-ion studies.[88] For example, the decreasing successive binding energies have been reported in the literature,[113] and a number of explanations have been proposed to account for the non-linear decrease of binding energies[120]. These include electrostatic, dative and covalent mechanisms as well as $s-p$-polarization, $s-d\sigma$-mixing and various orientations of the metal d-orbitals. Siegbahn[113] et al. obtained the following successive binding energies in a study of hydration of four metal ions Be^{2+}, Mg^{2+}, Ca^{2+} and Zn^{2+}. As can be seen in figure 3.42, the binding energy for the first ligand varies to a large extent, this variation has been attributed to the differences in ion-radii. The successive binding energies of adding the fourth ligand decrease and converge to a similar value for all four complexes. As pointed out by Siegbahn et al., employing only equation 3.11.1 is not enough in order to explain all calculated results and trends, charge-transfer effects clearly have to be included as well.[121] Increasing Pauli repulsion between ligands and core polarization effects have been used to explain trends in binding energies for singly charged ions.[83] In contrast, according to Siegbahn et al., the dominating effect for doubly charged ions consists of charge transfer from ligands (H_2O) to the s and p orbitals on the metal ion.[113]

Orbital mixing[119] can occur between orbitals of appropriate symmetry and with similar energies,[54] which can affect both bonding, magnetic and spectroscopic properties. Investigations of

N+*P*	Complex	Average BE $kJmol^{-1}$	Successive BE (CH3OH) $kJmol^{-1}$	Successive BE (H_2O) $kJmol^{-1}$
2+0	$[Mn(H_2O)(CH_3OH)]^{2+}$	655.2	330.2	292.1
3+0	$[Mn(H_2O)_2(CH_3OH)]^{2+}$	874.6	251.9	219.4
4+0	$[Mn(H_2O)_3(CH_3OH)]^{2+}$	1063.3	212.6	188.6
3+1	$[Mn(H_2O)_3(CH_3OH)]^{2+}$	1005.1		
5+0	$[Mn(H_2O)_4(CH_3OH)]^{2+}$	1212.9	167.6	149.6
4+1	$[Mn(H_2O)_4(CH_3OH)]^{2+}$	1186.7		
6+0	$[Mn(H_2O)_5(CH_3OH)]^{2+}$	1350.3	112.7	99.6
5+1	$[Mn(H_2O)_5(H_2O)]^{2+}$	1331.2		
trans 4+2	$[Mn(H_2O)_5(CH_3OH)]^{2+}$	1312.5		

Table 3.12: Average and incremental binding energies of $[Mn(H_2O)_N(CH_3OH)]^{2+}$-complexes, where N ranges from 1-5. *N*+*P* denotes the number of *N* molecules in the first and *P* molecules second solvation shell.

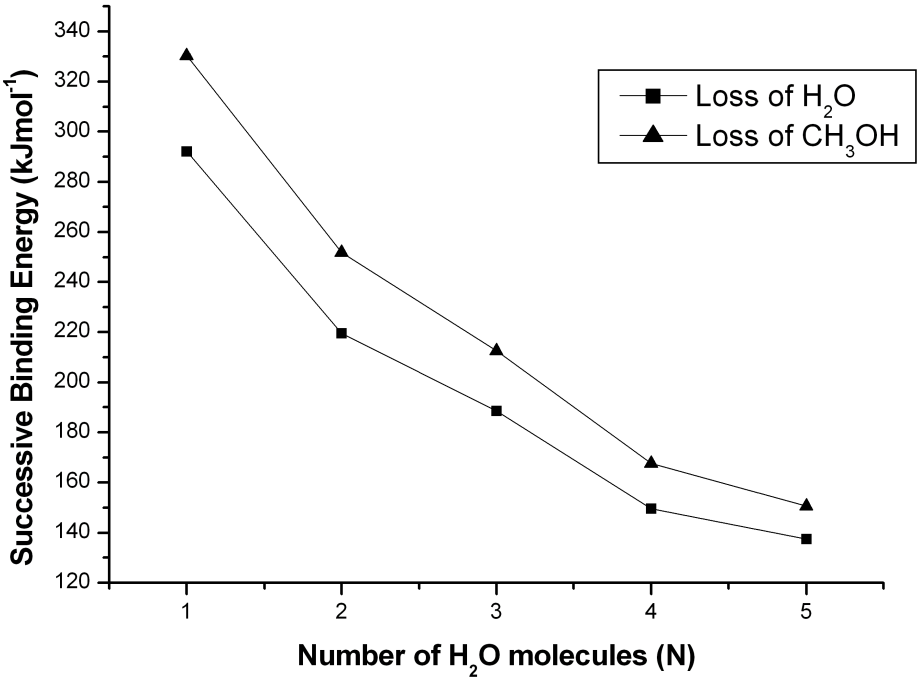

Figure 3.41: Successive binding energies for complexes of the form $[Mn(H_2O)_N(CH_3OH)]^{2+}$. Only first shell structures are considered.

successive binding energies for $[Cu(NH_3)_N]^+$ and $[Cu(H_2O)_N]^+$ complexes N=1-4 were made by Bauschlicher and co-workers.[84] A non-linear behaviour for the successive binding energies was observed, which was partly explained by the ability of transition metal ions to mix the $4s$ with the $3d$-orbital, this mixing could in turn affect the ligand repulsion as well. This orbital mixing can make the second binding energy to be higher than the first one, something that also has been observed in experiments.[122–125] El-Nahas[79] performed a similar study consisting of electronic structure calculations of $[Cu(NH_3)_N]^+$ and $[Cu(H_2O)_N]^+$ complexes and also found a non-linear decrease in the successive binding energies, which is shown if figure 3.43.

As can be seen in figure 3.43, the second binding energy is higher than that of the first ligand, a large drop then appears for the third and fourth ligand and no linearity for the successive binding energy for $[Cu(NH_3)_N]^+$ or $[Cu(H_2O)_N]^+$ was observed. The conclusion from these studies was that the electron density was minimized along the metal ion-ligand axis *via* the possibility of $4s$-$3d\sigma$ mixing. As a result, the metal ion-ligand repulsion decreases and also caused an induced quadrupole moment on the metal ion which, in turn, can interact with the dipole moment of the H_2O molecule. It was also found that a second ligand will have a higher binding energy than the first ligand, due to the energetic cost for the mixing made by the first ligand. The successive

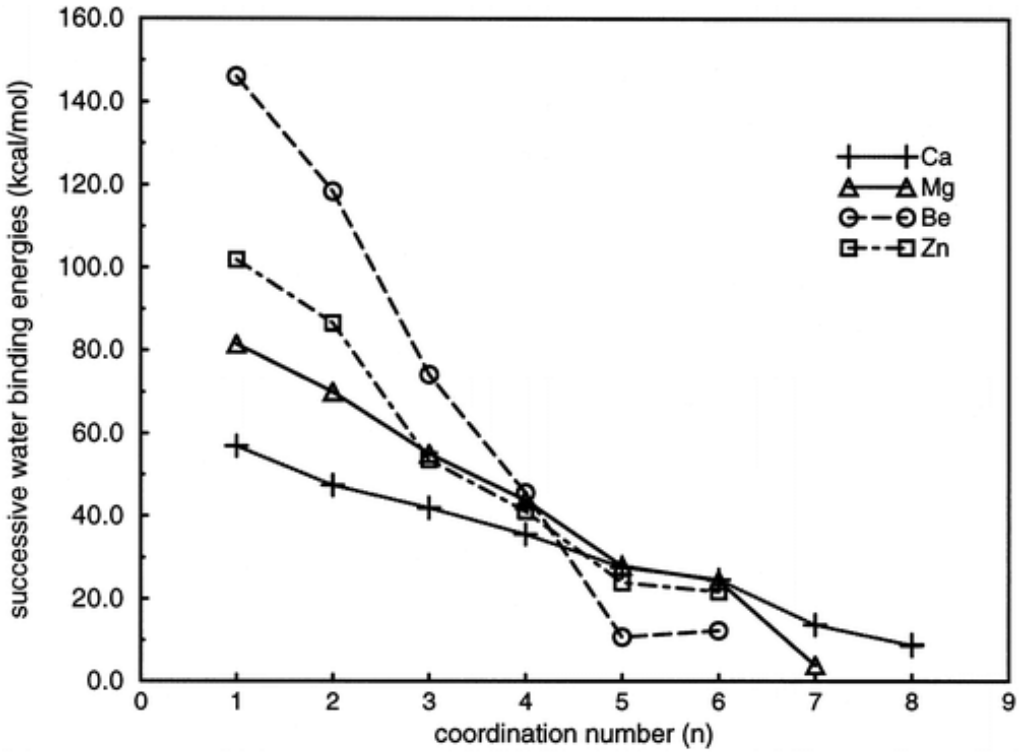

Figure 3.42: Successive binding energies for complexes of the form $[M(H_2O)_N]^{2+}$. M=Be^{2+}, Mg^{2+}, Ca^{2+} and Zn^{2+}. Image taken from reference 113.

binding energy for the third ligand drops considerably because of a large weakening of the $4s$-$3d$ orbital mixing. Upon this weakening, ligand-ligand repulsion and metal-ion ligand repulsion increases, followed by an increased metal ion-ligand bond length, in order to reduce the electrostatic repulsion. The mixing of $4s$-$3d\sigma$-orbitals has also been reported by Pettersson et al.[85] when investigating the ligand field effect of hydrated first and second row transition metal ions. Computational and experimental studies show that especially stable structures exist for coordination numbers of four and six ligands,[88,113] and that having the ligands in a first coordination shell is preferred, although coordination through hydrogen bond to a second solvation shell is energetically accessible. Kebarle *et al.*[63] studied the preferential take-up of water and methanol molecules by alkali metal ions, and found that replacing a water molecule with methanol is an exothermic reaction. This group also reported a preferential take-up of methanol in small proton clusters, but for larger proton clusters (N>9), water was the preferred coordinating species.[64] The authors explained these results by the simple electrostatic model shown in equation3.11.1. As the findings show in the current study, a more advanced analysis method needs to be employed in order to understand the results regarding the successive binding energies.

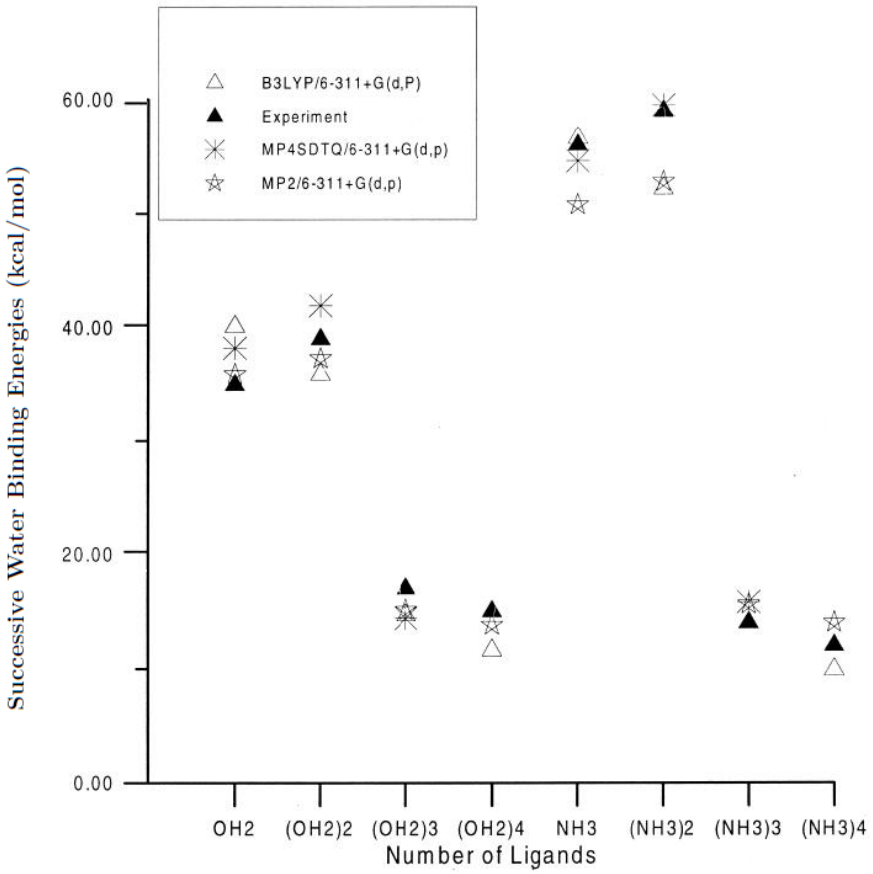

Figure 3.43: Successive binding energies for complexes of type $[Cu(NH_3)_N]^+$ and $[Cu(H_2O)_N]^+$ where N=1-4. Non-linear relationship appears for the successive binding energy partly as a consequence of s-d orbital mixing. From reference 79.

3.23 Orbital Analysis, $3d$-$4s$-Orbital mixing

Although the non-linearity of the successive binding energies shown in figures 3.39, 3.40 and 3.41 is small and not as prominent as in figure 3.42 and 3.43, the existence of orbital mixing for complexes in the current study have to be investigated. A number of different analysis methods for electron population of atomic and molecular orbitals are available, for example Mulliken population analysis,[126] but more useful methods such as the Natural Population Analysis (NPA) and Natural Bond Orbital (NBO) will be dealt with later in the chapter. The individual atomic orbital coefficients of the molecule show how much a particular atomic orbital participates to the overall molecular orbital. Hence, it is possible to investigate any orbital mixing described previously by looking at the atomic orbital coefficients from a molecular optimization, which was the method of investigation by El-Nahas.[79] Molecular coefficients are printed out as a unit-less value in a Gaussian03[41] output file. The effect of $4s$-$3d$ mixing have been discussed by Figgs,[119] regarding $[Cu(NH_3)_N]^{2+}$ complexes. For the square-planar $[Cu(NH_3)_4]^{2+}$ complex, the $4s$-$3d$ interaction

results in an energy change for the d_{z^2} until it approximately correspond in energy to the d_{xy}, d_{xz} and d_{yz} orbitals, and can be considered to be non-bonding. This non-bonding character of the d_{z^2} is also found in the current work for the $[Mn(H_2O)_N]^{2+}$ and $[Mn(CH_3OH)_N]^{2+}$-complexes, especially for higher molecular orbitals close to the HOMO-LUMO gap. Although the mixing in the current work is not particularly strong, it clearly has an impact on the successive binding energies for the complexes considered. Spin up and spin down electrons are treated separately, both α and β spins are shown in the figures for the manganese-ion that follow. Figures 3.44, 3.45, 3.46 and 3.47 show the coefficients from the $4s$ and $3d$-orbitals on the Mn^{2+} ion that are involved in particularly relevant bonding orbitals in $[Mn(H_2O)_N]^{2+}$ and $[Mn(CH_3OH)_N]^{2+}$ complexes (N=1-5). These orbitals are the highest lying bonding orbitals found in the complexes that are considered. No mixing could be found for $[Mn(H_2O)_N]$ or $[Mn(CH_3OH)_N]$ complexes when N=6. As can be seen from the α-spins in figure 3.44, a small $4s$ and $3d$ mixing is possible for N=1, 2, 3 and also for N=5. For $[Mn(H_2O)]^{2+}$, the orbital coefficients confirm possibility of $4s$ and d_{z^2} orbital mixing to form a σ bond between the oxygen and the manganese-ion. When a second ligand is coordinated to the Mn ion, the $4s$ contribution stays approximately constant whereas the d_{z^2} orbital contribution increases slightly and gives a smaller amount of $s - d\sigma$ mixing as a result, since the relative amount of d_{z^2} orbital has increased. As pointed out by El-Nahas,[79] linear structures are favoured in the presence of $s - d\sigma$-mixing, which also can explain the lower binding energy for the second water molecule. For a complex with three water molecules, a minor increase from the d_{z^2}-orbital is displayed although the $4s$ participation is approximately the same as for the $[Mn(H_2O)_2]^{2+}$ complex. Obviously, there is no significant weakening of the mixing when going from N=2 to N=3. The involvement from the $4s$ orbital has almost vanished entirely for a $[Mn(H_2O)_4]^{2+}$ complex, which indicates a loss of the $4s$-$3d$ mixing. This fact was also reported by El-Nahas.[79] Hence, the successive binding energy for the four-coordinated complex is affected by this loss, which is manifested as the humped curve in figure 3.39. A small amount of $4s$-$3d$ mixing is present in the five-coordinated manganese-water complex, which again causes the successive binding energy to decrease. Values for the coefficients of the β-spin orbitals are lower in magnitude than those for α-spin orbitals. A more pronounced participation of the β $4s$-orbitals can be found for N=1, 2 and 3. A complex with just one water molecule displays an even contribution from the $4s$ and d_{z^2} orbitals. The amount of $4s$-$3d$ mixing increases slightly for a $[Mn(H_2O)_2]^{2+}$ complex, but drops for N=3 due to a loss of d_{z^2} participation. Interestingly, the $4s$-$3d$ mixing almost disappears for the complex with four ligands, just like the α-spin orbitals, but now the d_{z^2} has almost completely vanished. A small amount of mixing is present for the $[Mn(H_2O)_5]^{2+}$ complex, as was observed for the α-spins.

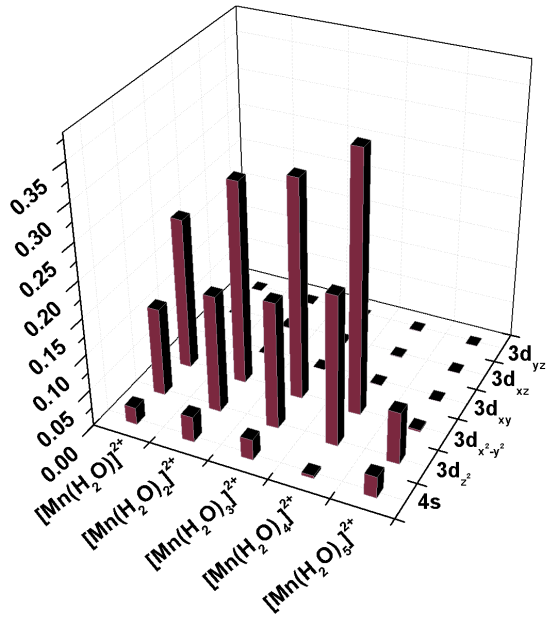

Figure 3.44: Orbital coefficients for a Mn^{2+}-ion and α-spin in $[Mn(H_2O)_N]^{2+}$-complexes where N=1-5. Orbital mixing is present for N=1, 2, 3 and 5.

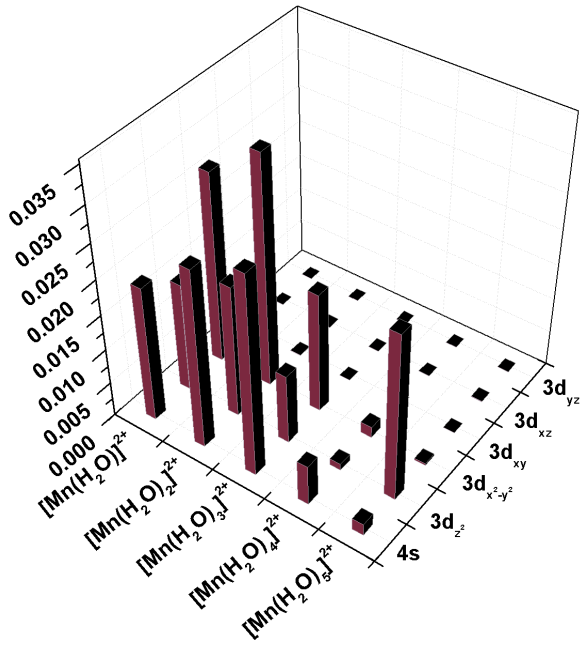

Figure 3.45: Orbital coefficients for a Mn^{2+}-ion and β-spin in $[Mn(H_2O)_N]^{2+}$-complexes where N=1-5. Orbital mixing is present for N=1, 2, 3 and 5.

Altogether, the trends for both α and β-spins are similar (with a more enhanced $4s$ contribution for β-spins) and with a very small amount of or, lack of, mixing for the four and six-coordinated complexes, which serves as further evidence for how the successive binding energies are affected by the $4s$-$3d$-mixing. Figures 3.46 and 3.47 shows the $4s$-$3d$-coefficients for α and β spin orbitals in the $[Mn(CH_3OH)_N]^{2+}$ complex, where N goes from 1-5. For α-spin orbitals, a small amount of mixing could be found for N=1-3, with a large increase of the d_{z^2} orbital for N=3, resulting in a relatively smaller amount of mixing for this coordination number, which in turn explains the smaller binding energy. The involvement from the $4s$-orbital has almost disappeared for the four-coordinated complex, indicating a loss of the mixing, similar to the $[Mn(H_2O)_4]^{2+}$ complex. A small mixing is present for the five-coordinated complex, although this mixing is weaker than its corresponding water containing complex. For β spin orbitals, the presence of the $4s$-orbital is almost constant when N goes from 1-3, as can be seen in figure 3.47. The participation from the d_{z^2} orbital has almost disappeared for the four-coordinated complex, resulting in the loss of $4s$-$3d$-mixing. For N=5, coefficients confirm orbital mixing to be present to a small extent. Clearly, the extremely small $4s$-$3d$ mixing that occurs for a four-coordinated complex and the complete absence of mixing for a six-coordinated complex is a strong indication of how the successive binding energies are affected in the current study. On the contrary to the $[Mn(H_2O)_N]^{2+}$ complexes, orbital coefficients for the methanol containing complexes also confirm participation of the d_{xy}, d_{xz} and d_{yz}-orbitals. These orbitals take part in the bonding to the oxygen atom on the methanol molecule.

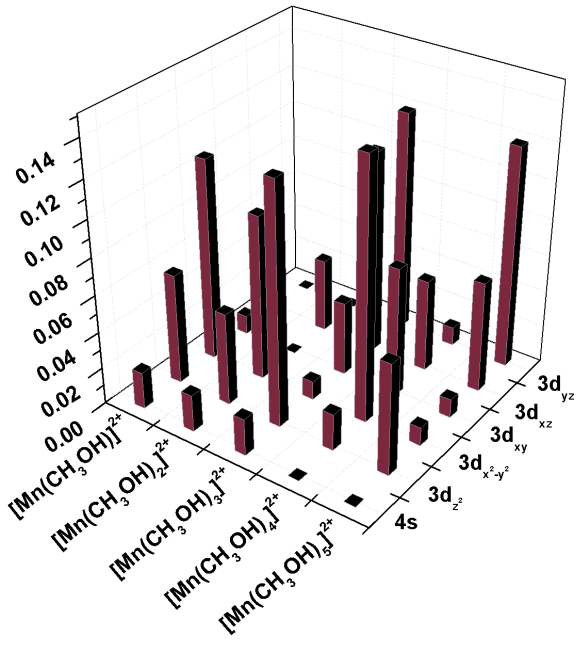

Figure 3.46: Orbital coefficients for a Mn^{2+}-ion and α-spin in $[Mn(CH_3OH)_N]^{2+}$-complexes where N=1-5. Orbital mixing is present for N=1, 2, 3 and 5.

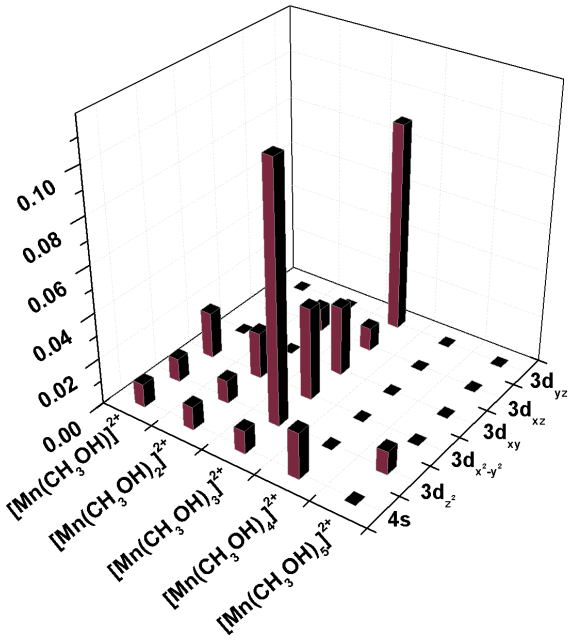

Figure 3.47: Orbital coefficients for a Mn^{2+}-ion and β-spin in $[Mn(CH_3OH)_N]^{2+}$-complexes where N=1-5. Orbital mixing is present for N=1, 2, 3 and 5.

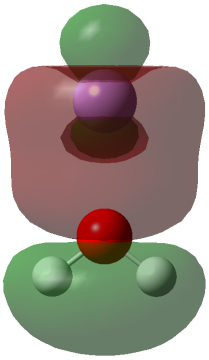

Figure 3.48: Orbital mixing (HOMO-1) for α-spin in a $[Mn(H_2O)]^{2+}$-complex.

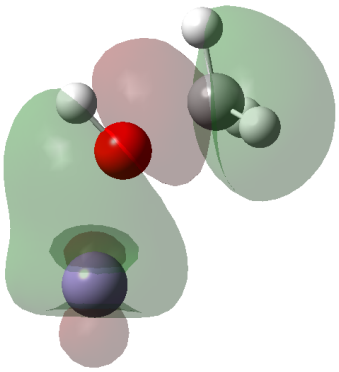

Figure 3.49: Orbital mixing (HOMO-2) for α-spin in a $[Mn(CH_3OH)]^{2+}$-complex.

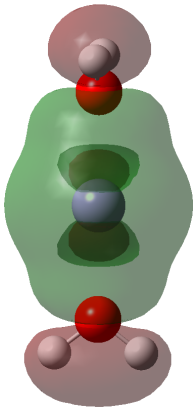

Figure 3.50: Orbital mixing (HOMO-2) for α-spin in a $[Mn(H_2O)_2]^{2+}$-complex.

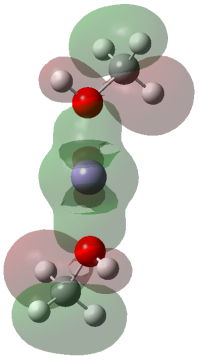

Figure 3.51: Orbital mixing (HOMO-2) for α-spin in a $[Mn(CH_3OH)_2]^{2+}$-complex.

The figures show the molecular orbitals for $[Mn(H_2O)_N]^{2+}$ and $[Mn(CH_3OH)_N]^{2+}$ complexes, where N=1 and 2, in which 4s-3d-mixing occurs, as well as p-orbitals from the oxygen atom(s). Dark areas in close proximity to the manganese atom, represent the d_{z^2} orbital.

For mixed ligand complexes, the $4s$-$3d$ mixing is expected to follow the pattern from the previous series. A complex of type $[Mn(CH_3OH)_N(H_2O)]^{2+}$ will display properties similar to a $[Mn(CH_3OH)_N]^{2+}$ complex, and if water ligands are in excess, the properties are expected to follow the trends for $[Mn(H_2O)_N]^{2+}$ complexes. Figure 3.52 and 3.53 show the coefficients for complexes of type $[Mn(CH_3OH)_N(H_2O)]^{2+}$, where N goes from 1-5. Just like the $[Mn(CH_3OH)_N]^{2+}$ and $[Mn(H_2O)_N]^{2+}$ complexes, a small dip for the $4s$ and/or $3d$-orbital occurs when N is equal to 4 and 6. The partial loss of $4s$-$3d$ mixing for these complex sizes provides a possible explanation of the humped curve representing the binding energy, shown in figure 3.40. Just like the "pure" $[Mn(CH_3OH)_N]^{2+}$ complexes, involvement of all d-orbitals occur for the mixed-ligand complexes, these orbitals are involved in bonding to the methanol molecule(s). As pointed out by Bauschlicher,[83,120,127,128] electrostatic repulsion also plays an important role in the coordination of ligands to a singly charged metal ion. The importance of electrostatic interaction has not been investigated in the current study, nevertheless, the existence of $4s$-$3d$-mixing been shown in the figures. Electrostatic repulsion is believed to play an important role especially for complexes with a coordination number N>4. As shown in the orbital coefficient diagrams, the $4s$-$3d$-mixing is largely reduced or even disappears for complexes with N>4. Since no ligand field stabilization energy exists for the Mn^{2+} ion, the geometry of larger complexes are determined mainly by the electrostatic repulsion of the ligands, which is reflected in the tetrahedral and octahedral geometry for a coordination number of 4 and 6.

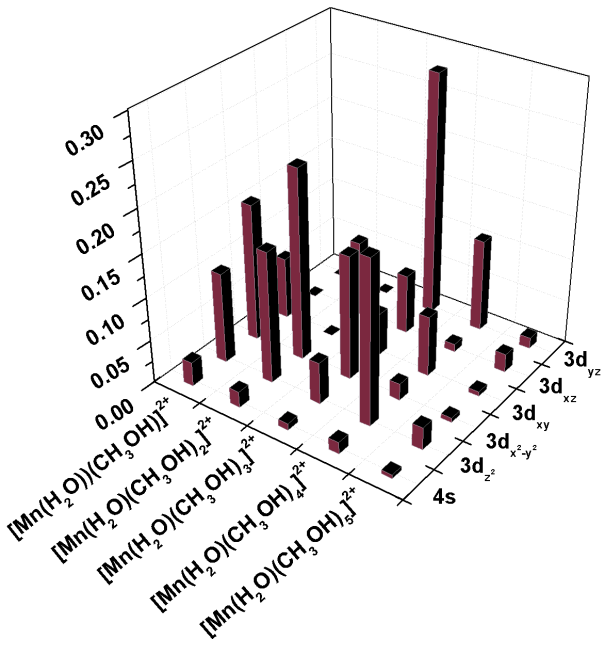

Figure 3.52: Orbital coefficients for a Mn^{2+}-ion and α-spin orbitals in $[Mn(CH_3OH)_N(H_2O)]^{2+}$-complexes where N=1-5.

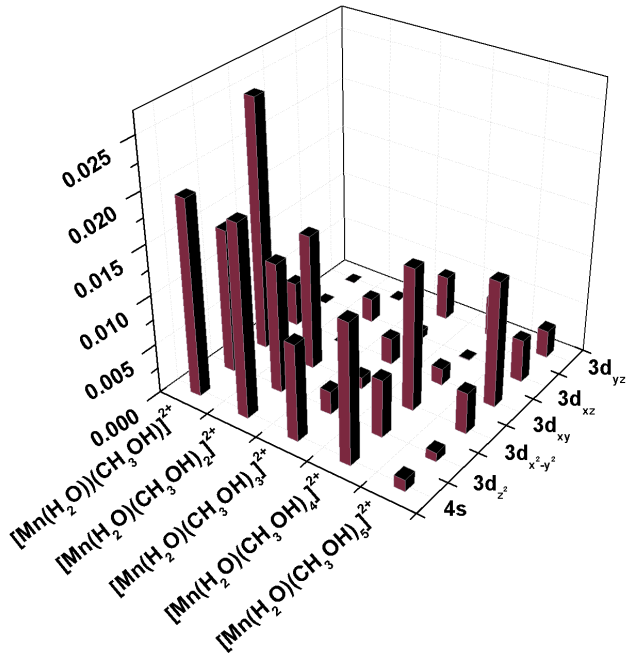

Figure 3.53: Orbital coefficients for a Mn^{2+}-ion and β-spin orbitals in $[Mn(CH_3OH)_N(H_2O)]^{2+}$-complexes where N=1-5.

3.24 Mulliken Population

One of the questions dealt with in this thesis is why methanol molecules binds more strongly to the Mn^{2+} ion than water molecules. As could be seen from the molecular orbital images in the last section regarding the methanol containing complexes, bonding can occur between d-orbitals of the Mn^{2+} ion and and p-orbitals of the oxygen atom, but can also be extended to include the p-orbitals on the carbon atom. If anti-bonding orbitals on the ligand are available, there is a possibility for back-bonding and the ability of pushing electron density from the metal-ion back to anti-bonding ligand orbitals will be one of the key factors for the overall stability of the complex.[54] Examples of ligands with this possibility include the CO and C_2H_2 molecules. When anti-bonding orbitals in the ligand are populated, a weakening of the bond within the ligand occurs and the bonding interaction between the ligand and the metal ion gets stronger.

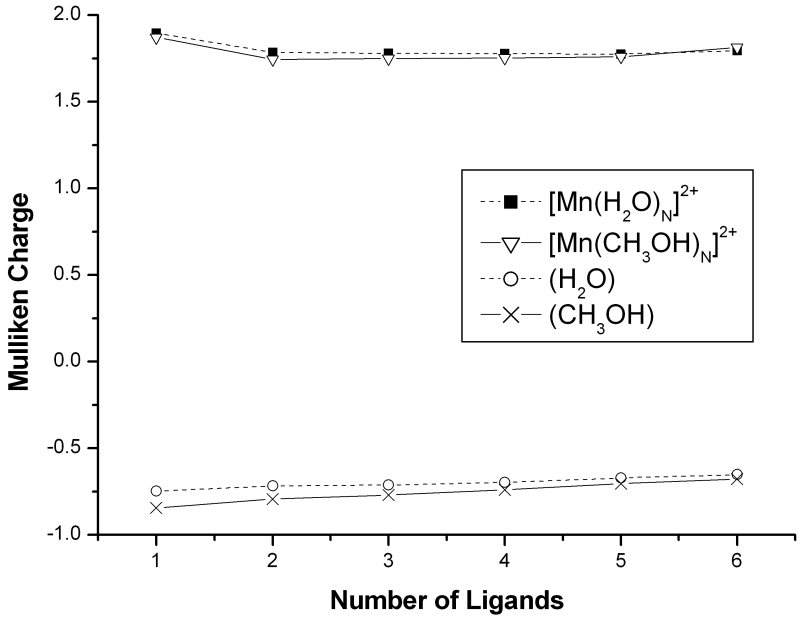

Figure 3.54: Mulliken charge for Mn^{2+}-ions in both $[Mn(H_2O)_N]^{2+}$ and $[Mn(CH_3OH)_N]^{2+}$ complexes, as well as the Mulliken charge on the oxygen atom in both H_2O and in CH_3OH when coordinated to the Mn^{2+} ion.

Figure 3.54 shows the Mulliken charge on the Mn^{2+} ion and the average Mulliken charge on the oxygen atoms in the different complexes. As can be seen from the graph, the Mulliken charge on the Mn^{2+} ion is approximately the same for both types of ligand and for all complex sizes, whereas a slightly larger difference is displayed for the oxygen atoms in the ligands. Although this difference decreases with an increasing complex size, it is clear that the oxygen atom in methanol holds a higher negative charge than the oxygen atom in water. The difference between CH_3OH and H_2O, as well as an overall decreasing negative charge, can be described as a result of ligand-ligand repulsion. A more complete picture can be seen when all atoms in the ligands are taken into account. Tables 3.13 and 3.14 shows the average Mulliken charge on the atom types in the methanol and water containing complexes. In table 3.13, the average Mulliken charge on the hydrogen atoms is shown in addition to the Mulliken charge on the Mn^{2+} ion and the free unbound water molecule.

Complex/Molecule	Mn^{2+}	O	H
H_2O	- -	-0.49	0.25
$[Mn(H_2O)]^{2+}$	1.9	-0.75	0.43
$[Mn(H_2O)_2]^{2+}$	1.79	-0.72	0.41
$[Mn(H_2O)_3]^{2+}$	1.78	-0.71	0.39
$[Mn(H_2O)_4]^{2+}$	1.78	-0.7	0.38
$[Mn(H_2O)_5]^{2+}$	1.78	-0.67	0.36
$[Mn(H_2O)_6]^{2+}$	1.8	-0.65	0.34

Table 3.13: Average Mulliken charge on each atom type in a $[Mn(H_2O)_N]^{2+}$ complex. The charge is given in units of the elementary charge e. Mulliken charge is also shown for an uncoordinated H_2O molecule as a comparison.

An interesting feature can be seen regarding the hydrogen atom in the water molecules. Upon coordination, the positive charge increases strongly. These hydrogen atoms donate electron density to the oxygen atoms and the Mn^{2+} ion. The strongest electron re-distribution from the hydrogen atoms is displayed when adding the first water molecule, the charge per hydrogen atom is $0.43e$, this re-distribution is then lowered to give a charge of $0.34e$ for the $[Mn(H_2O)_6]^{2+}$ complex. The negative charge on the oxygen atom changes approximately to the same amount from -0.75e for the first water molecule to -0.65e for the $[Mn(H_2O)_6]^{2+}$ complex. After the addition of the first water molecule, the charge on the Mn^{2+} ion stays approximately constant at $1.8e$, it clearly shows the

Complex/Molecule	Mn^{2+}	O	C	O **H**	C**H**$_3$
CH_3OH	- -	-0.46	-0.01	0.24	0.08
$[Mn(CH_3OH)]^{2+}$	1.87	-0.84	0.01	0.41	0.18
$[Mn(CH_3OH)_2]^{2+}$	1.75	-0.79	0.02	0.39	0.17
$[Mn(CH_3OH)_3]^{2+}$	1.75	-0.77	0.01	0.37	0.16
$[Mn(CH_3OH)_4]^{2+}$	1.75	-0.74	0	0.36	0.15
$[Mn(CH_3OH)_5]^{2+}$	1.76	-0.71	-0.01	0.34	0.14
$[Mn(CH_3OH)_6]^{2+}$	1.81	-0.68	-0.01	0.32	0.13

Table 3.14: Average Mulliken charge on each atom type in a $[Mn(CH_3OH)_N]^{2+}$-complex. The charge is given in units of the elementary charge e. Bold text indicates charge on that atom species in a particular functional group. Mulliken charge is also shown for an uncoordinated methanol molecule as a comparison.

interplay between the hydrogen and oxygen atoms. Obviously, only 0.20 - 022e can be donated to the Mn^{2+} ion, any excess charge are likely to be re-distributed to the coordinating atoms on the ligands. The differences and similarities between water and methanol regarding the Mulliken charge, can be seen in table 3.14. When considering the hydrogen in the $-OH$ group, electron re-distribution follows the same pattern as the hydrogen atoms in the water molecule occurs for the first ligand, but decreases when more ligands are coordinated to the metal ion. In addition, more electron transfer also occurs from the hydrogen atoms in the hydroxyl group via the C-O π-bonding in the methanol molecule to the metal-ion. The electron transfer is not as enhanced as the electron transfer from the hydroxyl group, but displays a similar pattern with a decreasing ability of electron transfer with more ligands coordinated in the complex. In comparison to the oxygen atom and the central Mn^{2+} ion, the charge on the carbon atom remains almost constant, whereas the charge on the Mn^{2+} ion and on the oxygen atoms are very similar to the ones in the $[Mn(H_2O)_N]^{2+}$ complexes. However, a slightly bigger charge is accumulated in the oxygen atoms in the $[Mn(CH_3OH)_N]^{2+}$ complexes. Since the negative charge on the oxygen atoms in the $[Mn(CH_3OH)_N]^{2+}$-complexes are larger than the corresponding charges for the $[Mn(H_2O)_N]^{2+}$-complexes, this indicates that the ability for electron transfer within the methanol molecule as a result of polarization effects is larger for methanol and this should be reflected when considering the average binding energies. Thus, a higher average binding energy for methanol can be explained by a better ability for polarization and hence electron transfer. Gross orbital population for the complexes can confirm population of higher atomic orbitals on the oxygen atoms, and reveal lost

electron density on the central metal ion. Figure 3.55 shows the gross orbital $3d$ population for a Mn^{2+} ion before and after coordination to a single water or a methanol molecule respectively.

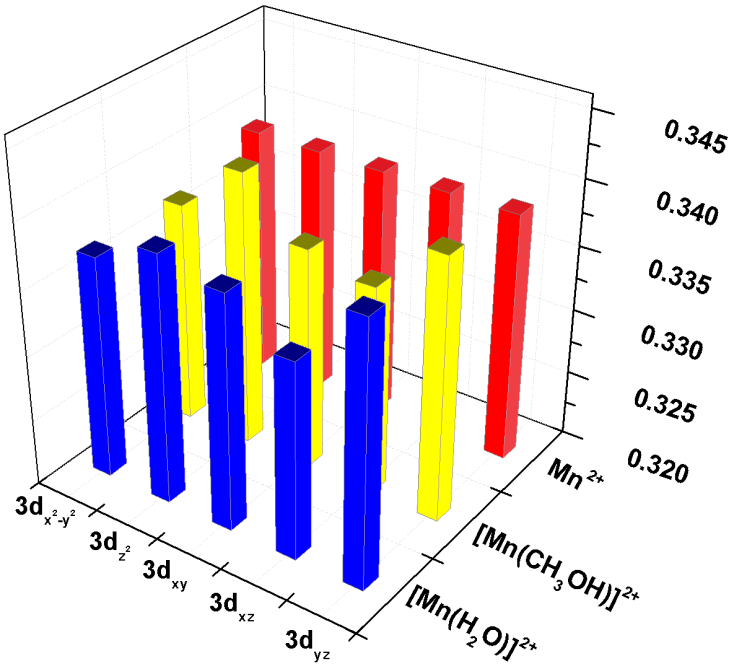

Figure 3.55: $3d$ orbital population for a free Mn^{2+} ion (red), when coordinated to a H_2O molecule (blue), and a CH_3OH molecule (yellow).

The population on the Mn^{2+} ion is approximately equal upon coordination of either water or methanol. Similarly, figure 3.56 shows population of the $4s$ and the $4p$ atomic orbitals on both free and coordinated water/methanol molecules. Since the electrons are given a high degree of freedom in the basis set used, population of high lying orbitals such as $4s$ and $4p$ are possible. As can be seen from figure 3.56, the $4s$ atomic orbital are relatively unaffected upon coordination for both methanol and water, $4p_x$ population decreases in magnitude for methanol, whereas the other two $4p$ orbitals increases. For water, population of all $4p$ orbital increases in magnitude, but a further analysis show that the population increase of the $4p$ orbitals on methanol is $0.34e$ and only $0.22e$ on water. Hence, it is reasonable to suspect that these atomic orbitals participate in anti bonding molecular orbitals and that the population of anti bonding orbitals is stronger for methanol. However, further investigations have to be made. Even if figures 3.55 and 3.56 only deal with one single ligand, it clearly shows the effect of electronic re-distribution between the metal-ion and the oxygen atom. This effect is expected to be weaker with more ligands coordinated to the Mn^{2+} ion in accordance with the Mulliken charge shown in table 3.13 and 3.14. The

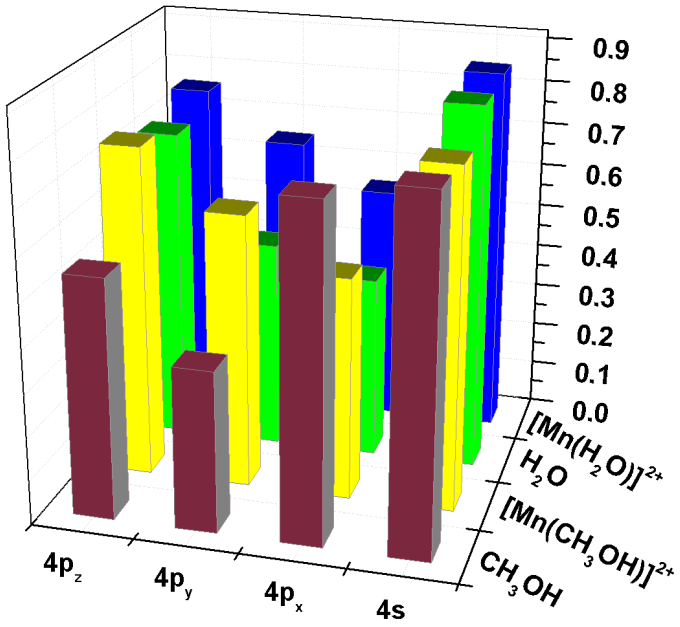

Figure 3.56: $4s$ and $4p$ orbital population for a free H_2O molecule (green) and when coordinated to a a Mn^{2+} ion (blue). Also shown is a free CH_3OH molecule (dashed grey lines), and when coordinated to a Mn^{2+} ion (yellow).

same type of analysis for the hydrogen atoms in the water and methanol molecules reveal a loss of electron population from the hydrogen atoms, and if the carbon atom is considered in the methanol molecule, it shows a very small change in electron population when coordinated to the Mn^{2+} ion.

3.25 NBO Analysis

In order to investigate the strength of bonding and back-bonding, Natural Bonding Orbital analysis is employed.[129–131] The process of creating natural bonding orbitals involves the process of finding Natural Atomic Orbitals, (NAO:s) as defined by Löwdin.[132] In the NBO analysis, the second-order perturbation stabilization energy E^2 between a donor and an acceptor orbital, is calculated according to:

$$E^2 = q_i \frac{F(i,j)^2}{\varepsilon_j - \varepsilon_i} \tag{3.25.1}$$

where q_i is the donor orbital occupancy, ε_j - ε_i is the energy difference between the donor orbital, ε_j, and an acceptor orbital, ε_i, and finally $F(i,j)$ is the off-diagonal Fock matrix elements. Figure 3.57 shows the stabilization energy E^2. Figure 3.58 and 3.59 show the stabilization energy for

water and methanol complexes, for both donor and acceptor interactions.

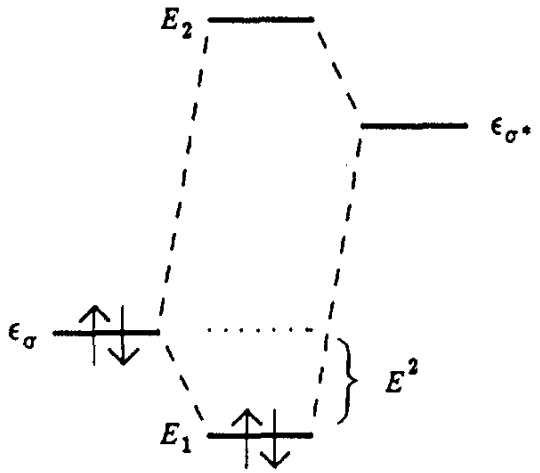

Figure 3.57: Stabilization energy between a donor and an acceptor orbital as defined in equation 3.25.1. Stabilization energy from the Gaussian package 41 is given in $kcalmol^1$.

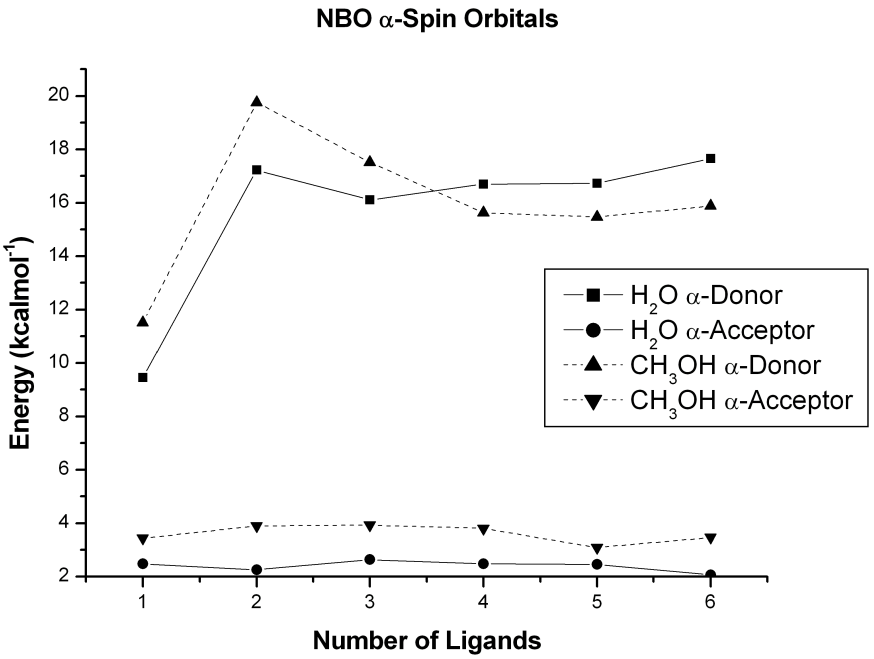

Figure 3.58: Stabilization energy (alpha-spin orbitals) for bonding and back-bonding in complexes of type $[Mn(H_2O)_N]^{2+}$ and $[Mn(CH_3OH)_N]^{2+}$, where N=1-6. Stabilization energy from the Gaussian package 41 is given in $kcalmol^1$.

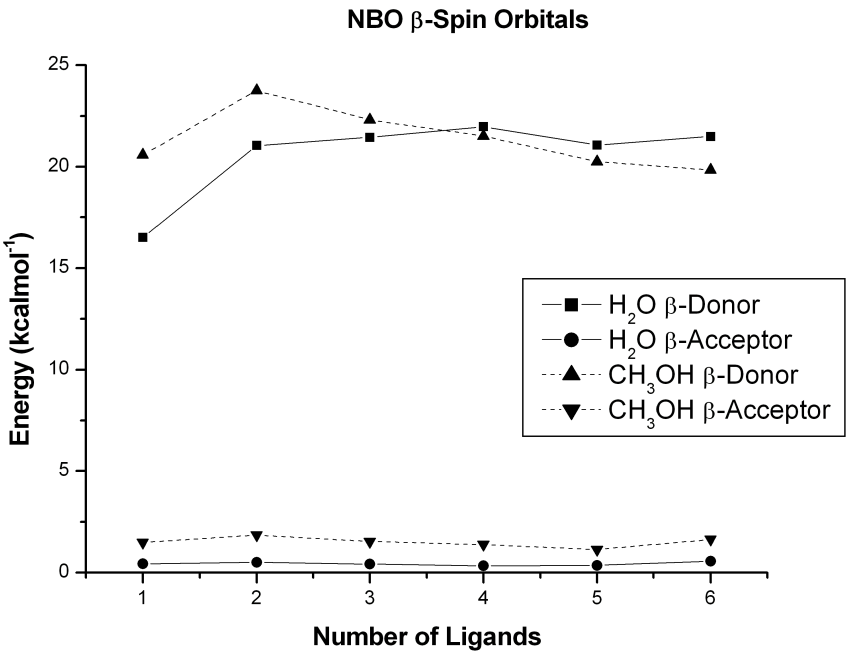

Figure 3.59: Stabilization energy (beta-spin orbitals) for bonding and back-bonding in complexes of type $[Mn(H_2O)_N]^{2+}$ and $[Mn(CH_3OH)_N]^{2+}$, where N=1-6.

Figures 3.58 and 3.59 show the stabilization energy as defined in equation 3.57 for both donor (ligand-to-metal) and acceptor (metal-to-ligand) interactions in complex types $[Mn(H_2O)_N]^{2+}$ and $[Mn(CH_3OH)_N]^{2+}$, where N=1-6. Only ligands in the first shell is considered here. The stabilization energy is calculated as the average interaction energy per water/methanol molecule. For both alpha and beta spin interactions, methanol complexes show a stronger donor interaction when N=1-3. For larger structures, in both α and β-spin cases, there is a crossover in energy which makes the donor interaction from the water ligands more favourable than the corresponding interactions from the methanol molecules. This crossover is most likely due to the increased ligand-ligand repulsion. However, the back-donation is always stronger for the methanol containing complexes, which can explain the overall stability (average binding energy). Back-donation obviously plays a crucial role for the stability of the complexes in the current work. Further analysis using the NBO-model, confirms the suggested mechanism, the oxygen atom in the water or methanol molecules donates electron density from a molecular orbital best described as a "lone-pair," and is accepted by an orbital on the Mn^{2+} ion which displays a mix of s and d atomic orbitals. This mixing decreases with increasing complex size and the trend for s-d-mixing with a larger number of ligands is in accordance with the previous findings for the orbital coefficients in the complex. Thus, no s-d-mixing could be found for the $[Mn(H_2O)_6]^{2+}$-complex.

Back-donation occurs from the Mn^{2+}-ion including core and higher orbitals to anti-bonding O−H and C−O orbitals on the water and methanol molecules respectively. A similar back-donation was found by Bock et al.[75] when investigating mono-amines and mono-hydrates for main group and transition metal ions. This back-donation weakened the N−H and O−H bond when the anti-bonding orbitals of the ligands were occupied. Also, Bock[75] found a strong ion-dipole interaction between the ligand and the metal ion, which aligns the lone-pair orbital of ammonia and water to the metal ion. Electron transfer from the water molecule to unoccupied orbitals on the metal ion was considerably weaker than the corresponding electron transfer via σ-bonding from the water molecule to the metal ion. The population of anti-bonding orbitals on the ligands results in an increase in the C−O and O−H bond lengths. This can also be found in the data for the structures shown earlier in the chapter. Table 3.15 shows a summary of how the C−O and O−H bond lengths vary with an increasing number of ligands in the complex. In comparison to the data shown in table 3.15, the C−O and O−H bond lengths for the free isolated methanol and water molecule are 1.41 and 0.94 Å respectively. Bond lengths in the coordinated systems were found to be longer than those found in the uncoordinated methanol and water molecules, giving strong support to the idea that back-donation to the anti-bonding orbitals in the ligand takes place.

Bond	$[M(L)]^{2+}$	$[M(L)_2]^{2+}$	$[M(L)_3]^{2+}$	$[M(L)_4]^{2+}$	$[M(L)_5]^{2+}$	$[M(L)_6]^{2+}$
C-O	1.5177	1.49870	1.4801	1.4697	1.45954	1.45428
O-H	0.97472	0.97212	0.96887	0.96668	0.964902	0.96350

Table 3.15: Lengths in Å for C-O and O-H bond in the $[Mn(H_2O)_N]^{2+}$ and $[Mn(CH_3OH)_N]^{2+}$-complexes when N=1-6. The bond lengths are considerably longer than for a free and uncoordinated methanol and water molecule.

3.26 First Shell-Second Shell Coordination

Since experiments for which the calculations in the current work are based on, do not directly reveal the geometry of the complexes, only theoretical results are available to make predictions and interpretations of the most stable structures. Coordination directly to the metal ion has already been shown to be energetically more favourable than ligands coordinated in a second coordination shell via hydrogen-bonds to ligands in the first shell. The choice of computational method has proven to be crucial for the outcome of geometry regarding hydrogen-bonds,[118] and the MP2 method is believed to describe the electron correlation accurately.[118] As pointed out by Morokuma,[133] the largest energy contribution for hydrogen-bonding is of electrostatic nature, but a small, although significant and important, component also comes from charge transfer. This charge transfer can, in turn, if being sufficiently strong, affect the stability of the complex which should be reflected in the overall energetics. As a first step, Mulliken charges were investigated in order to reveal the contribution from charge transfer in the structures that contain hydrogen-bonds.

Complex/Molecule	Mn^{2+}	O First Shell	H First Shell	O Second Shell	H Second Shell
H_2O	- -	-0.49	0.25		
$[Mn(H_2O)_3]^{2+}$	1.78	-0.71	0.39	-	-
$[Mn(H_2O)_3(H_2O)]^{2+}$	1.76	-0.74	0.39	-0.62	0.35
$[Mn(H_2O)_4]^{2+}$	1.78	-0.7	0.38	-	-
$[Mn(H_2O)_4(H_2O)_2]^{2+}$	1.76	-0.73	0.38	-0.60	0.34

Table 3.16: Average Mulliken charge for selected atom species in Mn^{2+}-H_2O complexes for a total coordination number of 4 and 6. Comparisons are made between oxygen and hydrogen in the first shell and the second shell.

In table 3.16, the average Mulliken charge are given on selected atoms in complexes of type $[Mn(H_2O)_N]^{2+}$ and $[Mn(H_2O)_N(H_2O)]^{2+}$, when N=3 and 4. As can be seen from table 3.16, there is a small increase of negative charge on the Mn^{2+} ion when one of the water ligands are coordinated in the second shell. Interestingly, a small increase of negative charge can also be observed on the oxygen atoms in the first shell for both $[Mn(H_2O)_3(H_2O)]^{2+}$ and $[Mn(H_2O)_4(H_2O)_2]^{2+}$. Based on this data, it can be expected that the Coulomb repulsion increases between the Mn^{2+} ion and the surrounding oxygen atoms in the first shell water ligands.

A corresponding table is shown for methanol containing complexes of the same size and structure. Table 3.17 shows the Mulliken charge for $[Mn(CH_3OH)_N]^{2+}$ and $[Mn(CH_3OH)_N(CH_3OH)]^{2+}$ complexes when N=3 and 4. For simplicity, only the charge on the Mn^{2+}-ion, as well as the charge on oxygen and hydrogen atoms in the OH-group are shown. As can be seen in the table, a small increase of negative charge can be observed on the Mn^{2+} ion and on the oxygen atoms in the first shell when methanol molecules are placed in the second coordination sphere. Thus, an increased Coulomb repulsion between the Mn^{2+} ion and the oxygen atoms in the first coordination shell can be expected. Since the complexes with ligands in the second coordination shell have proven to be less stable with respect to complexes with all ligands in the first coordination shell, a greater population of anti-bonding orbitals in "second shell complexes" is a probable reason for this destabilization. The orbitals in question are anti-bonding O−H for water containing complexes and C−O anti-bonding orbitals for the methanol containing complexes. To confirm and investigate the magnitude of anti-bonding population, Natural Bonding Orbital analyses were performed on the optimized structures.

Complex/Molecule	Mn^{2+}	O First Shell	O Second Shell	O **H** First Shell	O **H** Second Shell
CH_3OH	-	-0.46	-	0.24	-
$[Mn(CH_3OH)_3]^{2+}$	1.75	-0.77	-	0.37	-
$[Mn(CH_3OH)_3(CH_3OH)]^{2+}$	1.74	-0.79	-0.65	0.39	0.33
$[Mn(CH_3OH)_4]^{2+}$	1.75	-0.74	-	0.36	-
$[Mn(CH_3OH)_4(CH_3OH)_2]^{2+}$	1.74	-0.77	-0.63	0.39	0.32

Table 3.17: Average Mulliken charge for selected atom species in Mn^{2+}-CH_3OH complexes for a total coordination number of 4 and 6. Bold text indicates the H atom in the OH-group.

Tables 3.18 and 3.19 show a summary of the stabilization energy as defined in equation 3.25.1 from ligands in a first shell (denoted L_1) to the Mn^{2+}-ion. Also shown are the stabilization energies between a ligand in the second shell (denoted L_2) and the ligands in the first shell. The energy is taken as the average energy including all bonding interaction i.e. all orbitals that participate in a particular interaction are included. NBO analysis confirms that the electron density donated from ligands in the second shell end up in anti-bonding O−H or C−O orbitals on ligands in the first shell. As can be seen from tables 3.18 and 3.19, the energetic contribution between the first and second shell ligands can be as much as half of the energetic interaction between the first shell ligands and the Mn^{2+} ion. Comparing this bonding energy with the back-bonding energy in figure 3.58 and 3.59, it is obvious that the interaction between first and second shell ligands is much stronger than the back-bonding interaction shown for "first shell only complexes." This interaction energy explains the lower stability for complexes with ligands coordinated in a second shell. Electron transfer from ligands in the second shell populate anti-bonding orbitals on the first shell ligands, which destabilizes the complex.

Complex/Molecule	$L_1 \rightarrow Mn^{2+}$ $(kJmol^{-1})$ α-spin	$L_1 \rightarrow Mn^{2+}$ $(kJmol^{-1})$ β-spin	$L_2 \rightarrow L_1$ $(kJmol^{-1})$ α-spin	$L_2 \rightarrow L_1$ $(kJmol^{-1})$ β-spin
$[Mn(H_2O)_3(H_2O)]^{2+}$	75.2	104.3	35.4	35.4
$[Mn(H_2O)_4(H_2O)_2]^{2+}$	81.8	109.0	30.6	30.5

Table 3.18: Stabilization energy between first shell ligands L_1 and the Mn^{2+}-ion as well as the stabilization energy between second shell ligands L_2 and first shell ligands. The latter energy only describes electron transfer to anti-bonding or non-bonding O−H orbitals.

Even if table 3.18 and 3.19 only include two complex sizes "3+1" and "4+2", the trend of less stable complexes when ligands are coordinated in a second shell has been shown in table 3.7 and 3.8. The reason for the deceased stability of the "4+1" and "5+1" complexes compared to a "5+0" and a "6+0" complex is believed to have the same origin with population of anti-bonding ligand orbitals, as shown in table 3.18 and 3.19.

3.27 Proton transfer reactions

The purpose of the following study was to investigate the physical properties of water and methanol molecules to determine the factors that govern the proton transfer reaction. The requirements for stabilization of gas phase clusters has been the focus of a large number of experimental and theoretical studies.[62,87,92,94,134] Most studies have dealt with hydration of metal ions and the work generally includes the number of water molecules for stabilization and different reaction pathways for proton transfer reactions. Some of the ideas regarding proton transfer reactions have already been presented in section 3.12, where the difference in the second ionization energy of the metal ion and the first ionization energy of the ligand is believed to play a critical role in the stability of the complex. In one experimental study by Stace et al.[94] different fragmentation pathways for $[Mg(CH_3OH)_N^+]$ and $[Mg(CH_3OH)_N^{2+}]$ complexes were investigated. These fragmentation pathways included numerous reactions of charge-transfer, proton transfer and neutral ligand loss. A large variety of different reactions is not to be dealt with in the current study, only proton transfer reactions and properties of ligands that make a proton transfer reaction feasible will be discussed. Using the technique of electrospray ionization, Kebarle and co-workers[65] investigated the ions of Mg, Ca, Sr, Ba and many ions of the first-row transition metals. Despite the large number of ions investigated, the only hydroxide species detected were for ions of Be and Cu. Two specific

Complex/Molecule	$L_1 \rightarrow Mn^{2+}$ $(kJmol^{-1})$ α-spin	$L_1 \rightarrow Mn^{2+}$ $(kJmol^{-1})$ β-spin	$L_2 \rightarrow L_1$ $(kJmol^{-1})$ α-spin	$L_2 \rightarrow L_1$ $(kJmol^{-1})$ β-spin
$[Mn(CH_3OH)_3(CH_3OH)]^{2+}$	71.8	100.9	38.9	39.0
$[Mn(CH_3OH)_4(CH_3OH)_2]^{2+}$	71.6	97.5	34.2	34.2

Table 3.19: Stabilization energy between first shell ligands L_1 and the Mn^{2+} ion as well as the stabilization energy between second shell ligands L_2 and first shell ligands. The latter energy only describes electron transfer to anti-bonding or non-bonding $C-O$ orbitals.

reaction pathways were observed; proton transfer, reaction 3.12.4, and neutral ligand loss, 3.12.5. From these studies, it was concluded that the maximum number of water molecules for which the proton transfer reaction occurred, decreased with a decreasing second ionization energy of the metal. It was also suggested that two important factors for the proton transfer to occur, were the second ionisation energy of the metal and the bond dissociation energy, E_D, between the metal ion and the hydroxyl group, $E_D(M^+{-}OH)$. The analysis of Kebarle et al. was later revised in a computational study by Beyer et al.[134] In this study, proton transfer reactions of $[M(H_2O)_2]^{2+}$-system, where M=Be, Mg, Ca, Sr and Ba, were investigated. Beyer discussed the concept and the implications of an ionic bond between the metal ion and the hydroxyl group, rather than a covalent bond considered in earlier studies. The bond dissociation energy between the metal-ion and the hydroxyl group $E_D(M^{2+} - OH^-)$ was expressed as a result of three different energetic contributions:

$$E(M^{2+}{-}OH^-) = IE(M^+) + E_D(M^+{-}OH){-}EA(OH) \tag{3.27.1}$$

where $IE(M^+)$ is the second ionization energy of the metal ion, $E_D(M^+{-}OH)$ defined as previously and EA(OH) is the electron affinity of the $-OH$ group. Accordingly, the total energy for the proton transfer reaction E_{Tot} for a metal ion-complex can be expressed as:

$$E_{Tot} = E_{Ave}[M(H_2O)_N]^{2+} - E(M^{2+} - OH^-) - E_{Ave}[M(OH)(H_2O)_{N-2}]^+ + E_{PT} \tag{3.27.2}$$

where $E_{Ave}[M(H_2O)_N]^{2+}$ and $E_{Ave}[M(OH)(H_2O)_{N-2}]^+$ represents the average binding energy of N water molecules to the metal ion before and after the proton reaction respectively, and E_{PT} consists of two terms, one of them that includes the energy for performing the reaction:

$$2H_2O \rightarrow H_3O^+ + OH^+ \tag{3.27.3}$$

and one additional term $E_{Coulomb}$, which is the energy released by the Coulomb explosion. It was found that the proton transfer reaction proceeded *via* a second shell intermediate, with one water molecule hydrogen bonded in the second shell in order to facilitate the proton transfer. Two transition states were located on the potential energy surface for all ions except Be. The second transition state was found to lower the energy barrier for the proton transfer reaction and thus acted as a loophole for the release of H_3O^+. In a similar study,[92] the doubly charged ions of Sn, Pb and Hg were considered for metal ion complexes of type $[M(H_2O)_2]^{2+}$ and $[M(H_2O)_4]^{2+}$. A second transition state connected by a second shell intermediate preceding the proton transfer, was also found for the $[M(H_2O)_2]^{2+}$-complexes of the work of Stace[92] and Beyer.[134] Figure 3.60 shows the structures in the reaction sequence in the current work i.e. for a $[Mn(H_2O)_2]^{2+}$-complex. Based on the work of Beyer et al., only $[Mn(H_2O)_2]^{2+}$ and $[Mn(CH_3OH)_2]^{2+}$ are considered. All

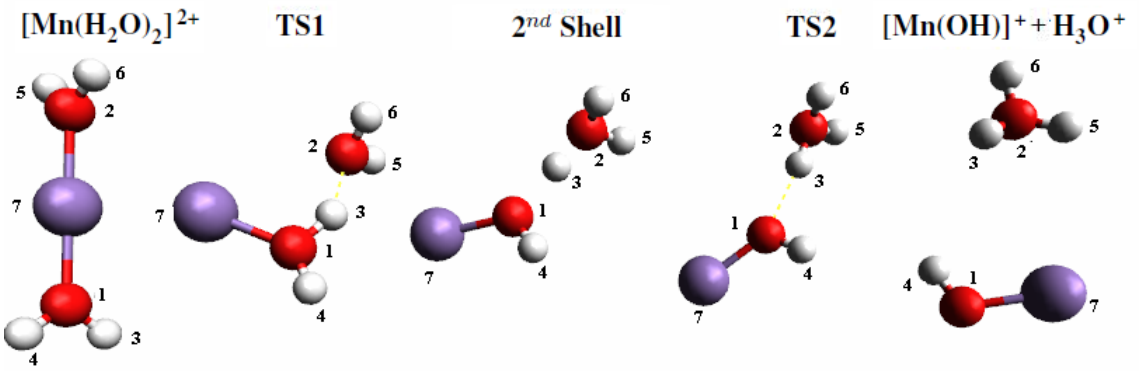

Figure 3.60: Proton transfer reaction for a $[M(H_2O)_2]^{2+}$-complex. These are the different structures during the proton transfer reaction $[Mn(H_2O)_2]^{2+} \longrightarrow [MnOH]^+ + H_3O^+$.

calculations were done with the Gaussian03[41] package, employing the B3LYP[34–36]-functional with a triple-zeta basis set equipped with (3df,3pd) polarization functions in order to model the hydrogen bonded system adequately. Frequency calculations were performed on all structures to ensure minima of the potential energy surface. Initial starting geometries for the transition state search with the quasi-Newton synchronous transit-guided method (QST3) in Gaussian03, were found *via* a relaxed potential energy scan for the complexes. The scan was performed decreasing the O-Mn-O angle in 20 steps. Intrinsic reaction coordinate calculations (IRC) and an additional structure relaxation confirmed the connection between a minimum and an obtained transition state on the potential energy surface. As already pointed out, a second transition state could be found for the $[Mn(H_2O)_2]^{2+}$-complex, but only one transition state that connects the reactants and the products could be located for the $[Mn(CH_3OH)_2]^{2+}$ and the $[Mn(H_2O)(CH_3OH)]^{2+}$-complexes. Despite numerous attempts, no complete proton transfer reaction could be obtained for the H_3O^+-loss from the $[Mn(H_2O)(CH_3OH)]^{2+}$-complex. Tables 3.20,3.21 and 3.22 show important bond lengths and distances between atoms, in structures that correspond to stationary states on the potential energy surface during the proton transfer reaction.

Bond	$[Mn(H_2O)_2]^{2+}$(Å)	TS1 (Å)	2nd Shell(Å)	TS2(Å)	Products(Å)
Mn(7)-O(1)	1.984	1.912	1.860	1.811	1.757
Mn(7)-O(2)	1.984	3.063	4.062	5.242	∞
O(1)-H(3)	0.974	1.035	1.442	2.669	∞
O(2)-H(3)	4.617	1.517	1.066	0.983	0.979

Table 3.20: Atomic distances for the reaction $[Mn(H_2O)_2]^{2+} \longrightarrow [MnOH]^+ + H_3O^+$.

Bond	$[Mn(CH_3OH)_2]^{2+}$(Å)	TS (Å)	Products(Å)
Mn(13)-O(1)	1.948	1.871	1.746
Mn(13)-O(2)	1.948	3.075	∞
O(1)-H(5)	0.970	1.082	∞
O(2)-H(5)	4.498	1.387	0.975

Table 3.21: Atomic distances for the reaction $[Mn(CH_3OH)_2]^{2+} \longrightarrow [MnOH]^+ + CH_3OH_2^+$.

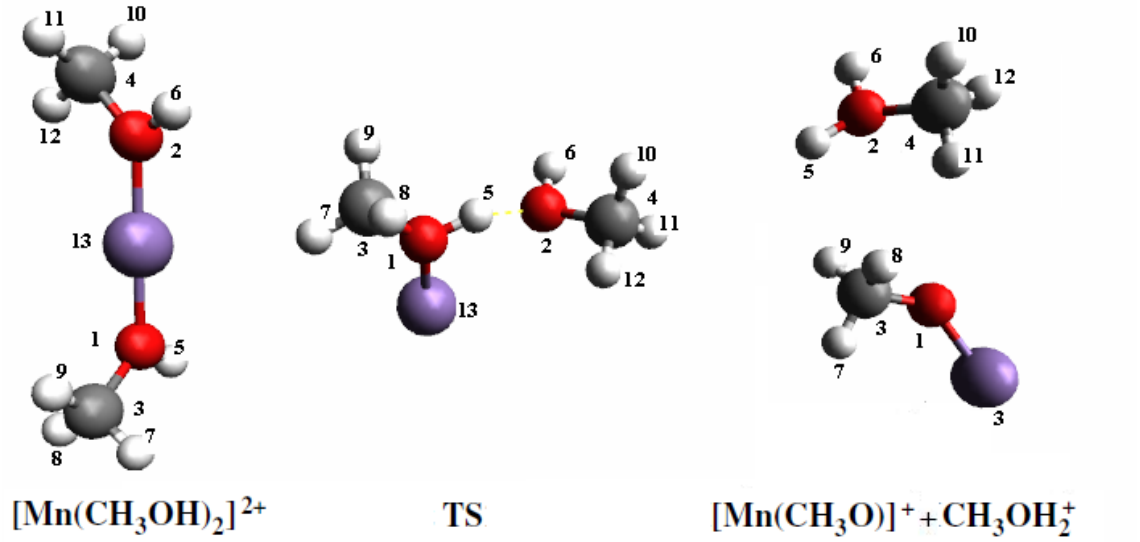

Figure 3.61: Proton transfer reaction for a $[M(CH_3OH)_2]^{2+}$-complex. These are the different structures during the proton transfer reaction $[Mn(CH_3OH)_2]^{2+} \longrightarrow [Mn(CH_3O)]^+ + CH_3OH_2^+$.

Bond	$[Mn(CH_3OH)(H_2O)]^{2+}$(Å)	TS (Å)	Products(Å)
Mn(10)-O(1)	1.989	1.888	1.757
Mn(10)-O(2)	1.940	2.936	∞
O(1)-H(5)	0.973	1.102	∞
O(2)-H(5)	4.579	1.354	0.975

Table 3.22: Atomic distances for the reaction $[Mn(CH_3OH)(H_2O)]^{2+} \longrightarrow [MnOH]^+ + CH_3OH_2^+$.

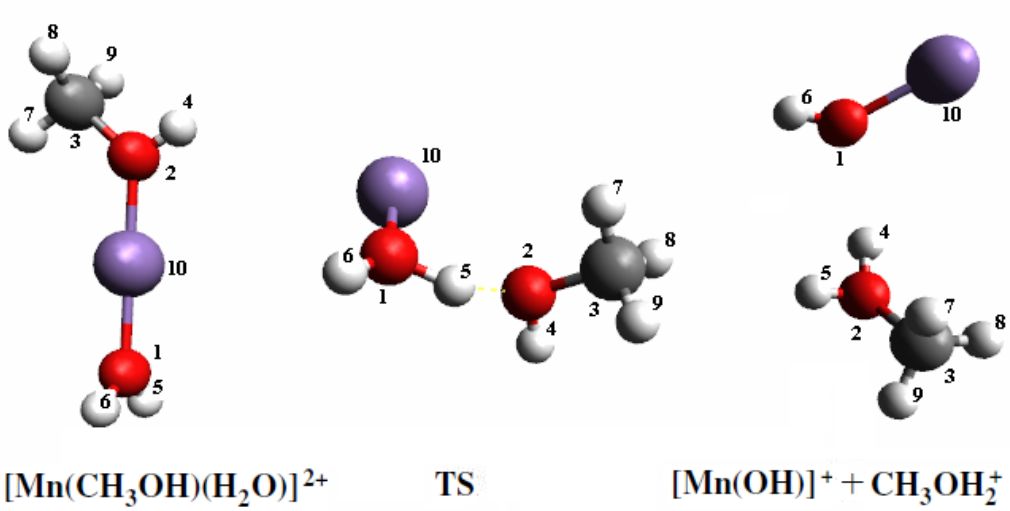

Figure 3.62: Proton transfer reaction for a $[Mn(CH_3OH)(H_2O)]^{2+}$-complex. These are the different structures during the proton transfer reaction $[Mn(CH_3OH)(H_2O)]^{2+} \longrightarrow [Mn(OH)]^{+} + CH_3OH_2^{+}$.

3.28 Energetics of proton transfer reactions

Three energy reaction profiles have been calculated, including proton transfer reactions and neutral ligand loss for the "water only" and "methanol only" complexes, $[Mn(H_2O)_2]^{2+}$, $[Mn(CH_3OH)_2]^{2+}$. In addition, energetics for proton transfer and neutral ligand loss have been calculated for the simplest mixed ligand complex possible, $[Mn(H_2O)(CH_3OH)]^{2+}$. In all reactions, proton transfer is always exothermic and thus favourable over neutral ligand loss which is endothermic. Table 3.23 shows different physical properties in the gas phase, for the water and methanol molecules. In addition to table 3.4, the proton affinity, PA, is also shown. The corresponding energy profile for the proton transfer reaction and neutral ligand loss for the $[Mn(H_2O)_2]^{2+}$-complex is shown in figure 3.63. This energy profile agrees very well with the energy profile for $[Mg(H_2O)_2]^{2+}$ shown in figure 3.64 and taken from Beyer 134. Taking the initial complex $[M(H_2O)_2]^{2+}$ as a zero point, the first transition point, TS1, lies higher for $[Mg(H_2O)_2]^{2+}$ at $(152.9) kJmol^{-1}$, than that for the $[Mn(H_2O)_2]^{2+}$ complex (115.7) $kJmol^{-1}$. The second shell intermediate structure lie 131.9 and 83.6 $kJmol^{-1}$ above the zero-point for $[Mg(H_2O)_2]^{2+}$ and $[Mn(H_2O)_2]^{2+}$ respectively. Finally, the last transition structure, TS2, displays a reversed behaviour compared to TS1, which stays at 165.0 $kJmol^{-1}$ for $[Mg(H_2O)_2]^{2+}$, and 102.6 $kJmol^{-1}$ for $[Mn(H_2O)_2]^{2+}$. This is surprising since the second ionization energy for Mg is slightly lower than that of Mn (table 3.5) i.e. the energy difference for Mg and H_2O is larger than that of Mn and H_2O. Previous studies[87] suggested that a large energy difference between the second ionization energy of the metal ion and the

first ionization energy of the ligand would result in a spontaneous charge transfer reaction. Hence a larger difference should result in lower energy barriers which is not in accordance with the date presented here, where the transition states for the $[Mg(H_2O)_2]^{2+}$-complex lies higher above the zero-point than the $[Mn(H_2O)_2]^{2+}$-complex. One of the conclusions from the study of Beyer et al.,[134] was that the transition states are correlated to the ionic radius, rather than to differences in ionization energies between the metal ion and the ligand. This correlation can also be found in this study since the data can be better understood when the ionic radii for Mg^{2+} and Mn^{2+} are taken into account. These radii are shown in table 3.24. The similarities between the energetic curves for the proton transfer reaction of the Mn^{2+} and Mg^{2+}-ions shown in figure 3.63 and 3.64 should be noted.

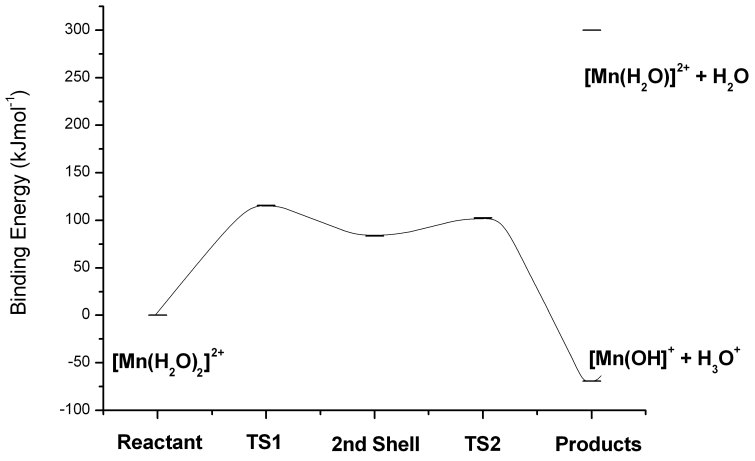

Figure 3.63: Energy profile for the reaction $[Mn(H_2O)_2]^{2+} \longrightarrow [MnOH]^{+} + H_3O^{+}$.

Molecule	α (Å^3)	$\mu(D)$	IE (eV)	PA ($kJmol^{-1}$)	E_D (RO-H) ($kJmol^{-1}$)
H_2O	1.48	1.85	12.6	691	498
CH_3OH	3.23	1.71	10.8	754	437

Table 3.23: Physical properties (polarizability α, dipole moment μ, first ionization energy IE, proton affinity PA and bond dissociation energy) E_D for the H_2O and the CH_3OH in the gas phase. From 135.

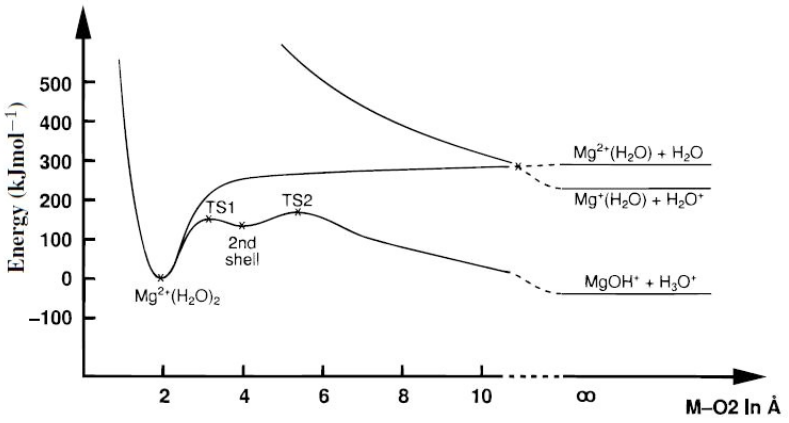

Figure 3.64: Energy profile for the reaction $[Mg(H_2O)_2]^{2+} \longrightarrow [MgOH]^+ + H_3O^+$. Figure taken from Beyer and co-workers 134.

Ion	Radii (pm) Coordination Number 4	Radii (pm) Coordination Number 6
Mg^{2+}	71	86
Mn^{2+}	80	97

Table 3.24: Ionic radii for the H_2O and the CH_3OH-ions with coordination number 4 and 6. Values taken from reference 136.

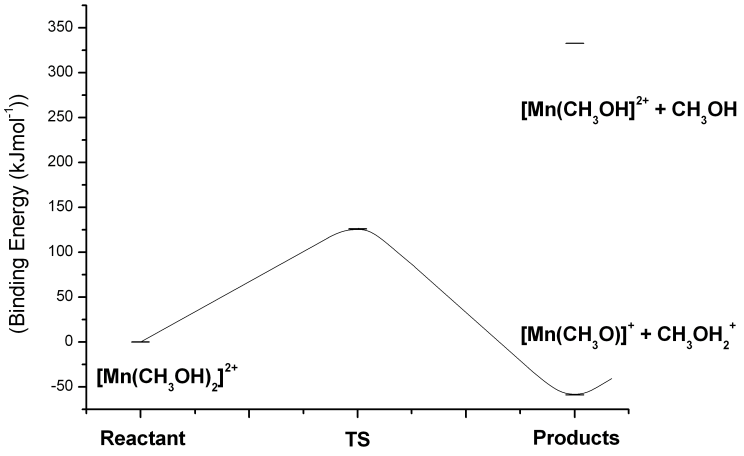

Figure 3.65: Energy profile for the reaction $[Mn(CH_3OH)_2]^{2+} \rightarrow [Mn(CH_3O)]^+ + CH_3OH_2^+$.

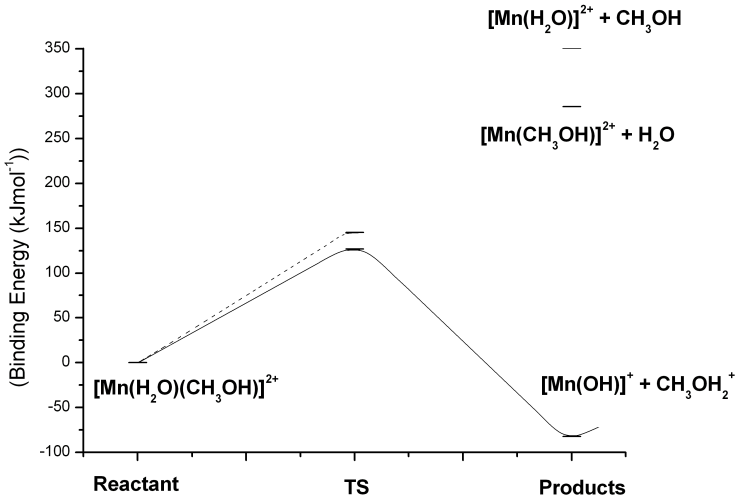

Figure 3.66: Energy profile for the reactions $[Mn(CH_3OH)(H_2O)]^{2+} \rightarrow [Mn(CH_3O)]^{+} + H_3O^{+}$ and $[Mn(CH_3OH)(H_2O)]^{2+} \rightarrow [Mn(OH)]^{+} + CH_3OH_2^{+}$

As can be seen in the two energy profiles in figures 3.65 and 3.66, neutral ligand loss is always unfavourable from an energetic point of view. The energy profile for the proton transfer reaction of manganese water complex is shown in 3.65. The transition state is approximately 11 $kJmol^{-1}$ higher than the corresponding transition state for the "water only" complex. Similarly, the products for the latter reaction are 13 $kJmol^{-1}$ more stable than the products formed in the proton transfer for $[Mn(H_2O)_2]^{2+}$-complex. The data presented in table 3.23 show that the proton affinity is higher for the methanol molecule than that of a water molecule, which can explain the higher energy barrier for the proton transfer reaction of the "methanol only" complex. On the other hand, the first ionization energy, IE, is considerably lower for methanol than for water. As a consequence, this implies a larger difference between the ionization energy of the ligand and the second ionization energy of the metal ion, and this energy difference gives a higher possibility for electron transfer within the complex. It is therefore reasonable to suspect that the hydrogen in the O−H-group in the methanol molecule is more acidic than the hydrogen atoms in the $[Mn(H_2O)_2]^{2+}$-complex. If electron density is withdrawn from the hydrogen atom on the hydroxyl group it can undergo the proton transfer more readily, and therefore the energy barrier is lowered to some extent. The net effect is shown in figure 3.65, where a small increase of the energy barrier can be seen. However, this increase is damped by the re-distribution of charge in the complex. The energy barrier for the mixed ligand complex is in line with the other observations in this study. The transition state for loss of H_3O^{+} from the $[Mn(H_2O)(CH_3OH)]^{2+}$ complex lies approximately 19 $kJmol^{-1}$ above the transition state for loss of $CH_3OH_2^{+}$. This is a manifestation of the higher proton affinity in

combination with a higher bond dissociation energy $E_D(RO - H)$ of the methanol molecule, which makes loss of $CH_3OH_2^+$ more favourable than loss of H_3O^+. Two transition states were located for loss of H_3O^+. However, no successful IRC calculation could connect the products with any of the two transition states found, and hence, this reaction pathway were ruled out. Three transition states could be found for $CH_3OH_2^+$, but only one of them proved to be a true transition state for the reaction considered. In the study of Stace et al.,[94] one of the distinct signals in the MIKES spectra could be attributed to $[Mg(OH)(CH_3OH)]^+$, which is a result of charge transfer rather than a proton transfer reaction. Forming the $[Mg(OH)(CH_3OH)]^+$-complex from a pure methanol containing complex, includes loss of the CH_3^+ fragment, a reaction that has not been considered here. Since the formation of $[Mn(OH)(CH_3OH)]^+$ is accessible through proton transfer, it is also likely that this complex shows a particular stability. Hence, it can be assumed that this complex is more likely to be found experimentally than any fragment arising from H_3O^+ loss.

3.29 Mulliken Charges

In order to analyse the importance of charge transfer during the proton transfer reaction, Mulliken charges on all atoms in the complexes for the reactions explored, have been investigated and are shown in tables 3.25, 3.26 and 3.27 respectively. Beyer et al. made a similar investigation with natural population analysis, and found that the charge on the metal ion only changed by $0.1e$ for Ca and the other metal ions. The conclusion was that charge transfer was not the driving force for the proton transfer reaction.

Atom	$[Mn(H_2O)_2]^{2+}$	TS1	2nd Shell	TS2	$[Mn(OH)]^+ + H_3O^+$
O(1)	-0.64	-0.67	-0.87	-0.89	-0.82
O(2)	-0.64	-0.64	-0.45	-0.42	-0.42
H(3)	0.39	0.41	0.47	0.44	0.47
H(4)	0.39	0.38	0.32	0.36	0.35
H(5)	0.39	0.38	0.42	0.47	0.47
H(6)	0.39	0.38	0.42	0.47	0.47
Mn(7)	1.72	1.77	1.69	1.57	1.47

Table 3.25: Mulliken charge on the different atoms for reaction 3.12.4. Atom labels can be found in figure 3.60.

Atom	$[Mn(CH_3OH)_2]^{2+}$	TS	$[Mn(CH_3O)]^+ + CH_3OH_2^+$
O(1)	-0.73	-0.51	-0.73
O(2)	-0.73	-0.52	-0.53
C(3)	0.31	0.21	0.25
C(4)	0.31	0.25	0.44
H(5)	0.37	0.36	0.43
H(6)	0.37	0.31	0.43
H(7),(8)	0.09	0.04,0.08	0.02
H(9)	0.06	0.08	0.02
H(10),(11)	0.09		0.074
H(12)	0.06	0.02	0.09
Mn(13)	1.64	1.57	1.41

Table 3.26: Mulliken charge on the different atoms in the $[Mn(CH_3OH)_2]^{2+}$-complex. Atom labels can be found in figure 3.61.

Atom	$[Mn(CH_3OH)(H_2O)]^{2+}$	TS	$[Mn(OH)]^+ + CH_3OH_2^+$
O(1)	-0.63	-0.51	-0.82
O(2)	-0.74	-0.52	-0.53
C(3)	0.31	0.25	0.44
H(4)	0.37	0.32	0.43
H(5)	0.39	0.37	0.43
H(6)	0.39	0.31	0.35
H(7)	0.06	0.03	0.09
H(8),(9)	0.09	0.08,0.06	0.074
Mn(10)	1.68	1.62	1.47

Table 3.27: Mulliken charge on the different atoms in the $[Mn(CH_3OH)(H_2O)]^{2+}$-complex. Atom labels can be found in figure 3.62.

The charges on the atoms in table 3.25, 3.26 and 3.27 reveal that the biggest change in charges occurs for the two oxygen atoms and the manganese atom. Although a larger change can be observed in the current study in comparison to the values reported by Beyer et al.,[134] the charge transfer is relatively small and hence, the difference in second and first ionization energies of the

metal ion and the ligand play a minor role for the proton transfer reaction. However, the ionization energies might have a crucial impact on charge transfer reactions, which have not been considered here. As a consequence of the minor change in Mulliken charge on the atoms, the two most important factors that determine if a proton transfer reaction will occur are the proton affinity, PA, and the bond dissociation energy E_D of the O−H-bond. Furthermore, no conclusion or prediction can be made here if the factors change their importance or influence with a changing number of ligands in the complex.

3.30 Conclusions

A number of questions based on experimental observations regarding competitive solvation of a Mn^{2+} have been dealt with in this chapter, such as average and successive binding energies, orbital mixing, second solvation shell structure and proton transfer reactions. The average binding energy of methanol and water to the Mn^{2+} ion show that methanol molecules bind more strongly to the Mn^{2+} ion than water molecules, which is in agreement with experiments. This is due to a more efficient charge transfer between the methanol molecules and the Mn^{2+} ion than the corresponding charge transfer between the Mn^{2+} ion and water molecules. This trend is seen in both in first-shell coordination of the ligands and second-shell coordination, where the ligands in the second coordination sphere are hydrogen bonded to the ligands in the first shell.

Coordination to a first shell is always more favourable for both methanol and water molecules, due to an increased occupation of anti-bonding orbitals between the metal ion and the first shell ligands when additional ligands are coordinated in the second coordination shell. This in turn, affects the overall stability of the complex. The irregular pattern of the successive binding energies is caused, at least to some extent, by $3d$-$4s$ orbital mixing of the orbitals on the metal-ion. This effect is reduced as more ligands are coordinated to the metal-ion, and the orbital mixing explains the higher binding energies for just one or two ligands compared to five or six ligands. The loss of this orbital mixing can also explain why complexes of both methanol and water of size 4 and 6 are particularly stable. Proton transfer reactions have been investigated for the smallest possible of ligands size, and proton affinity and dissociation energy of the O−H-bond are believed to be more important for the overall reaction than are differences in the first ionization energy of the ligand and the second ionization energy of the metal ion. Hence, in the current work, methanol containing complexes display a slightly higher reaction barrier than water containing complexes. Finally, proton transfer from a "water-only" complex are facilitated by two reaction barriers or transition states.

Chapter 4

Manganese Doping Of Graphene

Introduction *Due to the quest and search for new efficient materials that can be used in electronics and spintronics, several research-groups turned their interest towards graphene and the possibility of doping graphene with metal atoms. Transition metals in general, and manganese in particular, with a high magnetic moment in its free state, $5\mu_B$ which is expected to preserve a high magnetic moment when coordinated to a graphene layer, constitute very interesting dopants. A number of theoretical studies have been published in this area,*[137–145] *and these studies have dealt with the implications of different coordination sites and the magnetic and electronic properties. A few papers have used periodic structures in order to replicate a macroscopic system, other studies have employed graphite or graphene as a cluster or a small molecule. The aim with the current study is to bridge the gap between a few of the structures dealt with in previous studies, and consider structures bigger than considered with before. Different coordination sites, magnetic and electronic properties will be discussed for a number of cases in this study.*

Since the first successful manufacturing of a single layer of graphene in 2004[146,147], the interest in doping a single or double layer of graphene with various metal atoms has grown steadily. Expected applications in this field of research are for example semi-conductors with various band gaps[148] and sensors.[149] The magnetic properties discovered has been explained by defects in the graphene structure. Various doping agents are expected to increase and change the magnetic and electronic properties of graphene, making it to a potential candidate for future electronic devices. The aim with this study is to investigate graphene systems doped with manganese atoms and compare the results with smaller systems of the same kind, to see the impact on the magnetic moment for the Mn atoms. Four different coordination sites will be considered and discussed in the light of magnetic and band structure properties.

Relaxations of the dopant were performed as spin-unrestricted calculations using periodic structures in the Aimpro code[150] employing the Density Functional Theory with the PW92 functional.[37] In order to examine the number of unpaired electrons, an initial spin configuration of 5 unpaired electrons was given to the manganese atom. Spin optimization was then allowed to occur during the geometry relaxation. Energy convergence criterion for the optimizations was set to 10^{-5} Hartrees, and the convergence criterion for symmetry was set to a factor of 10^{-5}. Pseudopotentials as described by Hartwigsen, Goedecker and Hutter[151] were used on both carbon and manganese atoms. The energy was sampled with a 4×4×4-grid according to the Monkhorst-Pack scheme[152], and a small electronic temperature of kT=0.04 eV was used together with a smearing of the occupancy according to M. Methfessel and A. Paxton.[153] The 4×4×4 grid was also used for Mulliken analysis which are reported here as the average of the k-points of a specific band. An kinetic-energy' cutoff of 600 eV was used for the Fourier analysis of charge density in all calculations. Simple hexagonal graphite, which normally is denoted AA-stacking, has been reported to be unstable[154], and therefore only so-called AB-stacking has been considered in the current work. Figure 4.1 shows the graphite AB-stacking principle[155], which can be described as a carbon atom α in one of the graphene planes lies above the carbon atoms in all other neighbouring planes, and that carbon atoms denoted β lies at centre of the hexagonal ring formed of the carbon atoms in the next/nearest layer. The band structure for the hexagonal cell was obtained using a path of symmetry points (A, K, G, M and L) according to figure 4.2.

Magnetic properties were investigated through calculating the total magnetic moment for the system in terms of the Bohr magneton μ_B, which is defined as:

$$\mu_B = \frac{e\hbar}{2m_e} \tag{4.0.1}$$

where e is the elementary charge and m_e is the electron rest mass. This magnetic moment equates roughly to a number of unpaired electrons in the system, and further analysis such as Mulliken population is necessary in order to investigate which orbital or orbitals that contribute to spin polarization on any atom.

Choice of doping sites in the current work will be following the work of Mao et al., where coordination above center of a hexagon in the graphene layer is denoted H-doping, coordination directly above a carbon atom will be denoted T-site doping. In two of the systems investigated here, the manganese atom replaces one carbon atom and that coordination mode or site will be denoted substitutional doping.

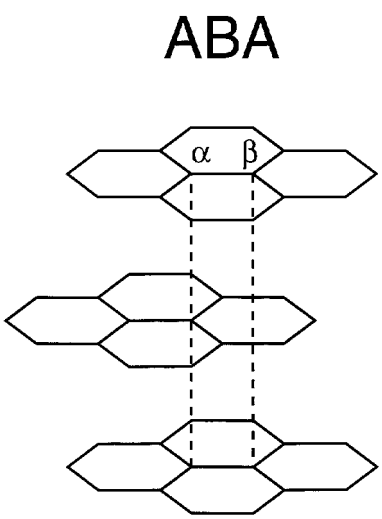

Figure 4.1: AB-stacking of graphite sheets. Atoms denoted α lie "on top" of another α atom, and atoms denoted β lie above the centre of the hexagonal rings formed of 6 carbon atoms in the nearest layer. Reproduced from 155.

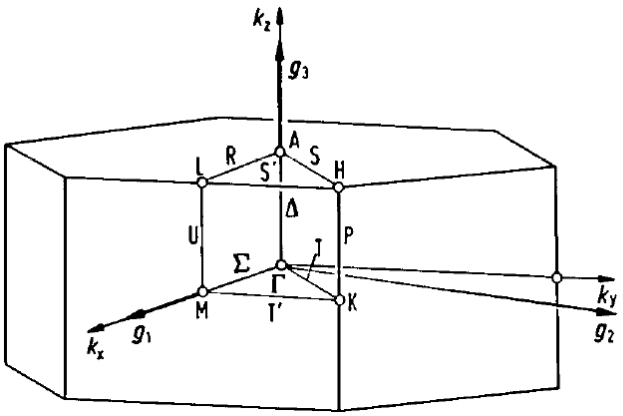

Figure 4.2: Symmetry points for the hexagonal lattice considered in the current work was A, K, Γ, M and L. Brillouin zon diagram reproduced from 156.

4.1 Pristine Double Layer of Graphene

In order to compare the change in physical properties occurring when a double layer of graphene is doped with a Mn-atom, a pure graphene system has to be investigated at first. Figure 4.3 shows a fraction of the supercell of 144 carbon atoms, with a carbon-carbon bond length of 1.412 Å which is close to the carbon-carbon bond length found in the relaxed structure of Mao.[143] The distance between the graphene layers was 3.32 Å which is close to experimentally obtained results for graphite[157] which was 3.35 Å, and the magnetic moment was found to be 0 μ_B. To ensure

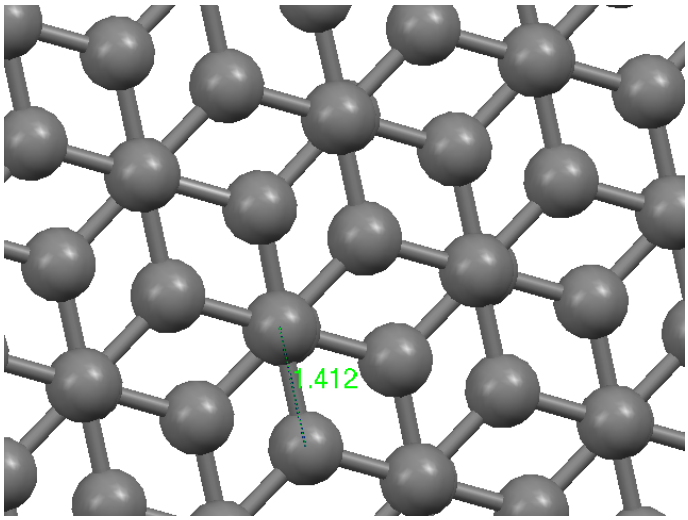

Figure 4.3: Part of the pure graphene double layer with a C-C distance of 1.412 Å.

that no interaction occurred between the graphene double layer slabs, these were separated by a distance of approximately 25 Å. Figure 4.4 shows the band structure for a 4 atom system of pure graphene. Three points were considered, the gamma point Γ, K and M according to figure 4.2. Comparing this band structure with the figure 4.5 taken from the work of Mao et al.[143], shows the band structure for a double layer of graphene including 32 carbon atoms. Although the three symmetry points are taken in a different order, the band structures exhibit a similar behaviour for the these points. Obviously, the band gap becomes zero at the K point since the conduction and valence band meet at that point. This meeting leads to a finite value for the density of states (right part of figure 4.5) for graphene, and it can be considered to be semi-metallic which is consistent to what has been found in earlier studies. In the case of the bilayer, the density of the states at the Fermi level is zero. In order to cover a bigger part of the Brillouin zone of the hexagonal cell when an adatom is coordinated to the graphene double layer, more symmetry points were included in the current study for the band structure calculations. Figure 4.6 shows the band structure for α and β spin orbitals including the 10 highest bands for a 36-atom unit cell. As can be seen in the figure, there is a perfect match between the α and β spins. This band structure displays a different behaviour for similar points as in figure 4.4 and 4.5, with a corresponding valence band maximum and conduction band minimum at the Γ and A point. The Fermi level lies at -1.78 eV as indicated in the figure, in comparison to the work of Mao et al., where the Fermi level was set to be zero. The band structure of the 144-atom graphene system in figure 4.6 can be considered to be semi-metallic, but due to the coarse k-point sampling a very small band gap opens at the Γ and A point.

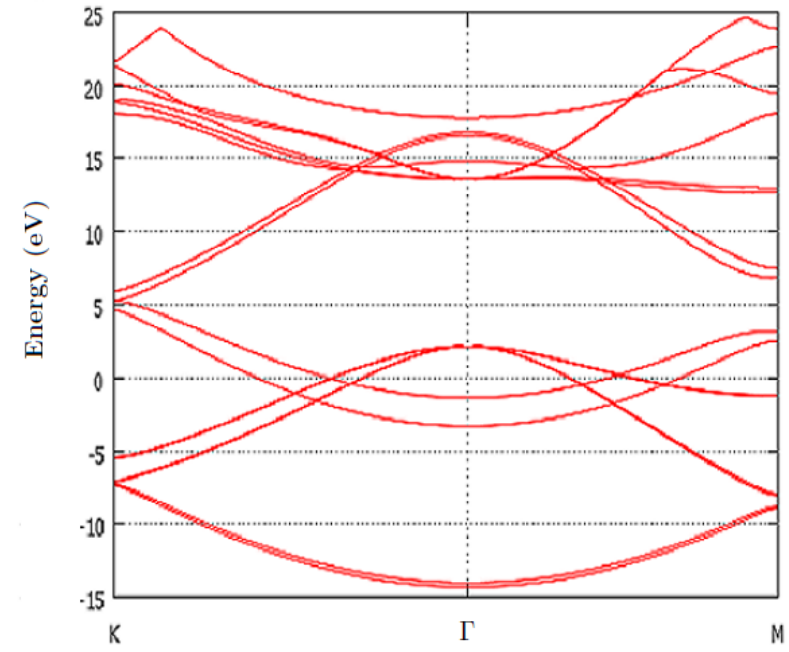

Figure 4.4: Band structure for a four C-atom bilayer graphene cell.

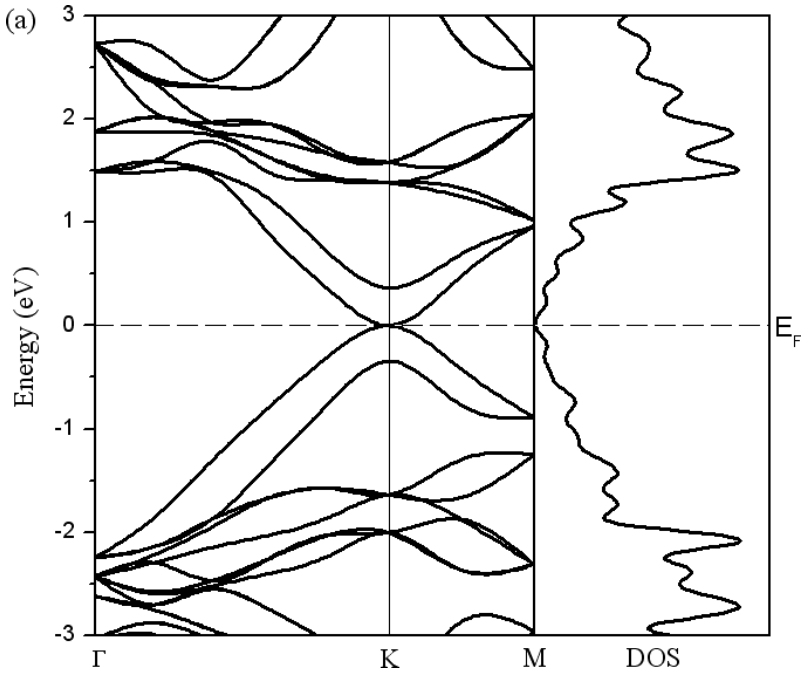

Figure 4.5: Band structure for a bi-layer of graphene. From 143.

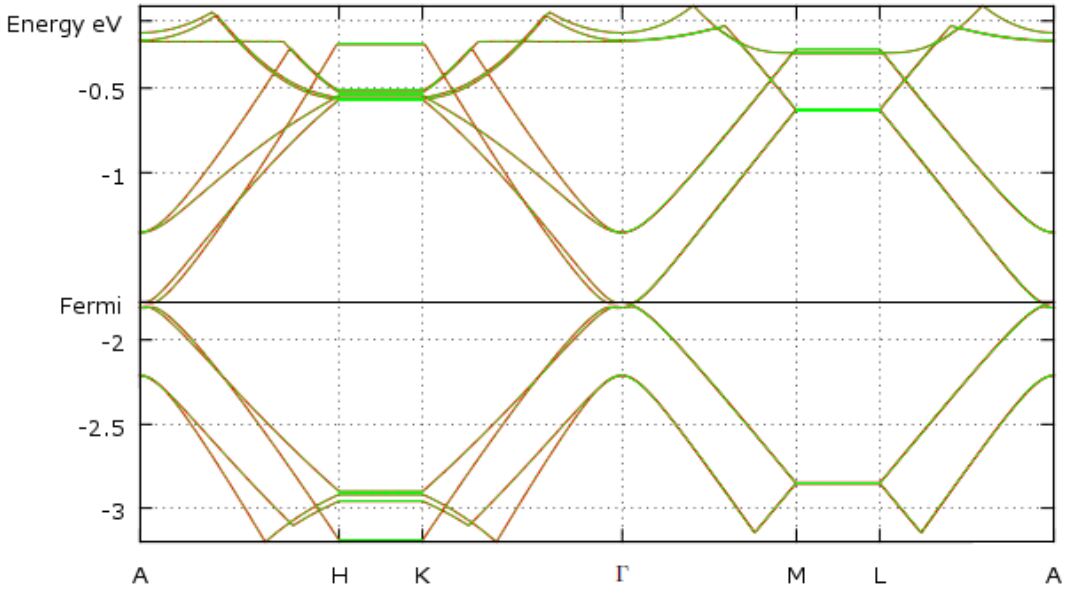

Figure 4.6: Band structure for α (red) and β (green) spin in the graphene supercell containing 144 atoms. Valence band maximum and conduction band minima occur at the Γ and A point.

4.2 Manganese H-Coordinated

The first coordination site investigated in the current work is shown in figure 4.7. The manganese atom is coordinated above the double layer of graphene, at the centre of a hexagonal ring formed by six carbon atoms (denoted 1-6 in figure 4.7) in the graphene layer. The height above the graphene layer was 1.985 Å, and the average Mn-C bond length as 2.11 Å, which is close to the values obtained for the same coordination site in the work of Mao et al[140] when investigating coordination of Mn, Fe and Co on a single layer of graphene. This was the preferred coordination site for all the adatoms investigated. However, different values for the magnetic moment and spin properties have been reported in the literature. Mao et al. reported a magnetic moment of the Mn atom (local magnetic moment) increased to to $5.56\mu_B$. For Fe and Co, the magnetic moment decreased to 2.20 and $1.10\mu_B$ respectively. Sevincli et al.[139] also investigated transition metals adsorbed on a graphene surface and concluded that the overall magnetic moment for Mn doping was zero, due to antiferromagnetic coupling in the system. For adsorption of transition metals on both sides of the graphene sheet, Mn atoms displayed a total magnetic moment of $10.49\mu_B$ per pair due to ferromagnetic coupling, which indicates a small increase of the moment for each of the manganese atoms compared to the free atom. In the current work the total magnetic moment for the system is calculated and for the H-site coordination, the magnetic moment for the total

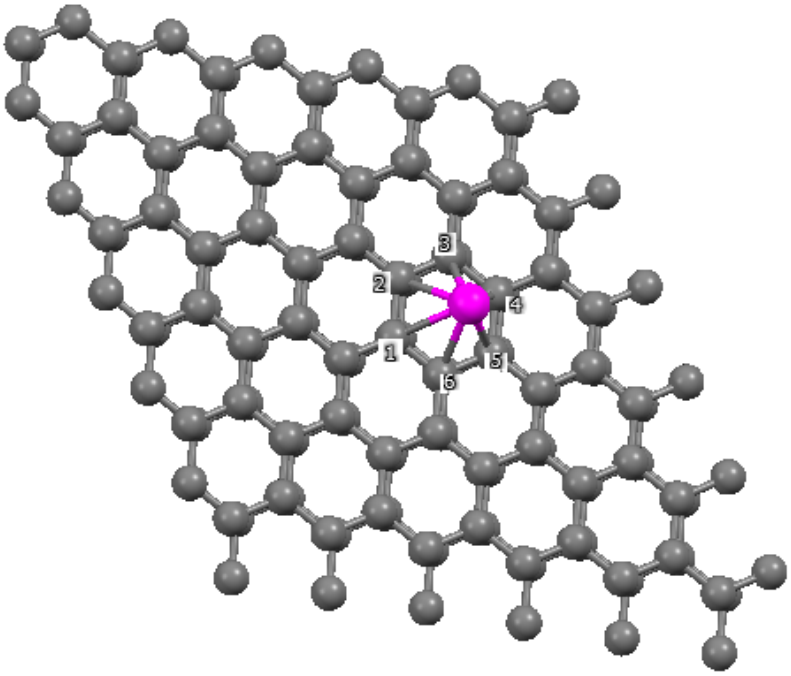

Figure 4.7: H-site coordination of a Mn atom on a double layer of graphene to six carbon atoms.

system has decreased to $3.0\mu_B$. The coupling is mediated by the number and phase of intervening π bonds between the Mn atoms, and so depends on the shape and size of the supercell used. The band structure for the H-site coordinated manganese atom, which is displayed in figure 4.8, is modified compared to the pure graphene system. The Fermi level is now shifted to a higher level, (-1.32 eV). This shift of the Fermi level into the conduction band was also reported by Mao et al. There is a clear separation of the α spin orbitals at the Γ point, whereas all β spin orbitals lies above the Γ point. As a representation of the different bands shown in figure 4.8, the valence band was further investigated by Mulliken analysis. In figure 4.9, the Mulliken charge for the manganese atom is shown as the sum of all the k-points for that particular band, (this goes for all the following Mulliken graphs in the chapter). The α and β (or spin-up/spin-down) electrons are divided in completely different ways. α electrons are almost entirely occupying the 4s-orbital, whereas the β electrons are occupying mainly the $3d_{xy}$, $3d_{x^2-y^2}$ and $3d_{z^2}$-orbitals. This is what was found in the study of Mao et al., where the band structure and density of states for the majority of spins consisted mainly of the $4s$-orbital and the minority spins consisted mainly of orbitals of $3d$ character near the Fermi level. Figure 4.10 shows the resulting β spins orbitals on the coordinated manganese atom, with a clear d-orbital contribution. As can be seen in the figure, this orbital takes no participation in the bonding between the graphene layer and the manganese atom. The lobes on the carbon atoms in the graphene layers consist of the $3p_z$ orbitals, confirmed by the Mulliken analysis.

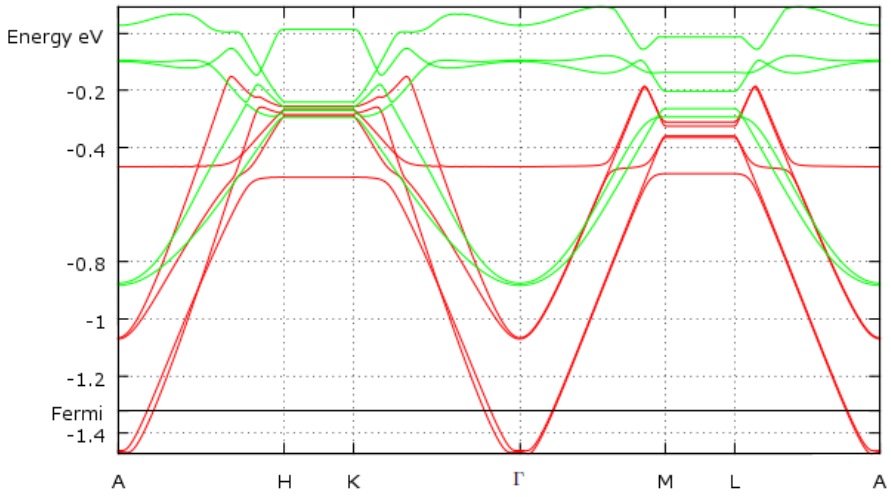

Figure 4.8: Band structure for the α and β spin orbitals for the Mn H-site coordination.

As pointed out earlier, the magnetic moment for a coordinated manganese atom decreases upon coordination to a graphene surface compared to an isolated manganese atom. The largest remaining spin for the system occurs for the T-coordinated manganese atom, with a magnetic moment of $4.3\mu_B$. The three other systems investigated showed a larger decrease of the total magnetic moment, approximately down to $3\mu_B$. Clearly, and also indicated by the band structure for the systems, the graphene layer is affected by the doping of the manganese atom. One of the important things to answer is how many of the carbon atoms in the graphene layer that are affected and contribute to the overall magnetic moment, and what orbitals on the manganese atom and the carbon atoms that are involved in the spin polarization. In the case of majority of spin, Mao et al. found a large contribution from the manganese $4s$-orbital in a band just below the Fermi level for H-site doping. On the other hand, the $3d$ orbitals from the manganese atom were found to contribute to the minority of spin. This is also what can be seen from the Mulliken analysis of the manganese atom in figure 4.9 where the α spin orbitals are almost entirely represented by the manganese $4s$ orbital, and for the β spin orbitals, the contribution comes from the $3d_{yz}$, $3d_{x^2-y^2}$ and $3d_{z^2}$ orbitals. A Mulliken analysis of the carbon atoms in the system reveal that only the six carbon atoms that are bonded to the manganese atom needs to be taken into account regarding the induced magnetic moment, since the influence on the other carbon atoms is negligible. Figure 4.11 shows the Mulliken analysis of the H-coordinated manganese graphite system, including the valence orbitals for all the carbon atoms (C1-C6) that are bonded to the manganese atom.

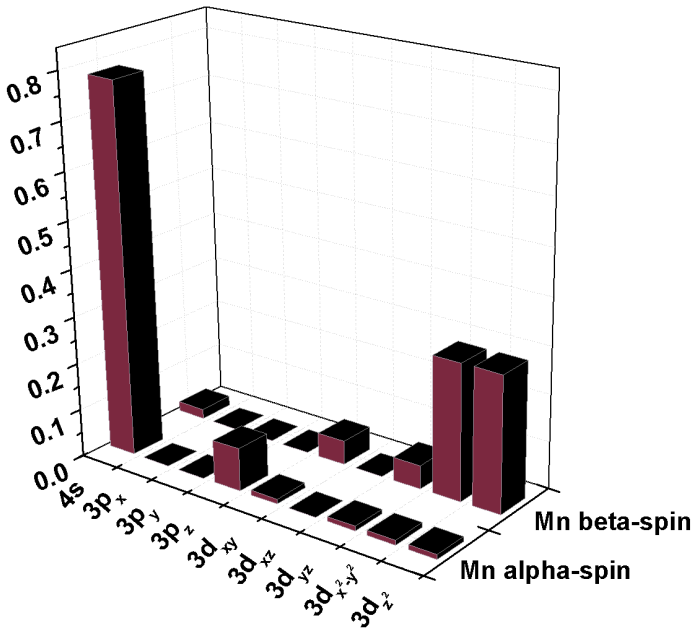

Figure 4.9: Mulliken charge for different orbitals in the valence band for the H-coordinated manganese atom. α spin electrons occupies mainly the 4s-orbital, in comparison to the β-spin electrons which occupies the higher d-orbitals. The results are in agreement with the results of Mao et al.

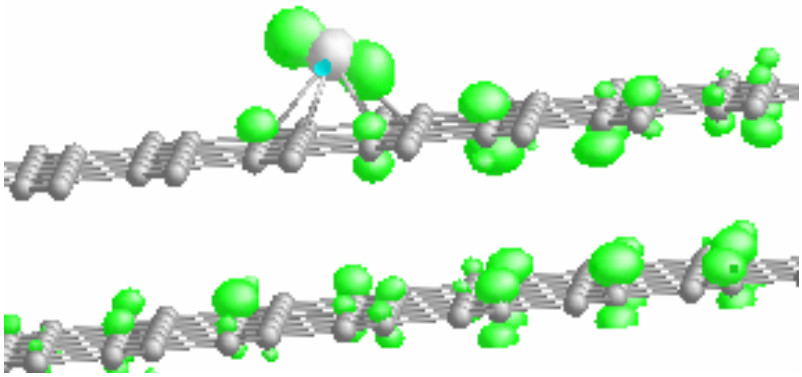

Figure 4.10: Orbital on the manganese atom has a very distinct d-character mainly from the $d_{x^2-y^2}$ and the lobes on the graphene layers consists of the $3p_z$ orbital.

It is obvious that the induced magnetic moment on these atoms are localized mainly on the $2p_z$ orbitals. Minor populations of the $2s$ α and $2p_z$ β orbitals do also occur, but as a result of the large population on manganese $4s$ and carbon $2p_z$ α orbitals, it can be concluded that the spin polarization in the system is located on these atoms and orbitals.

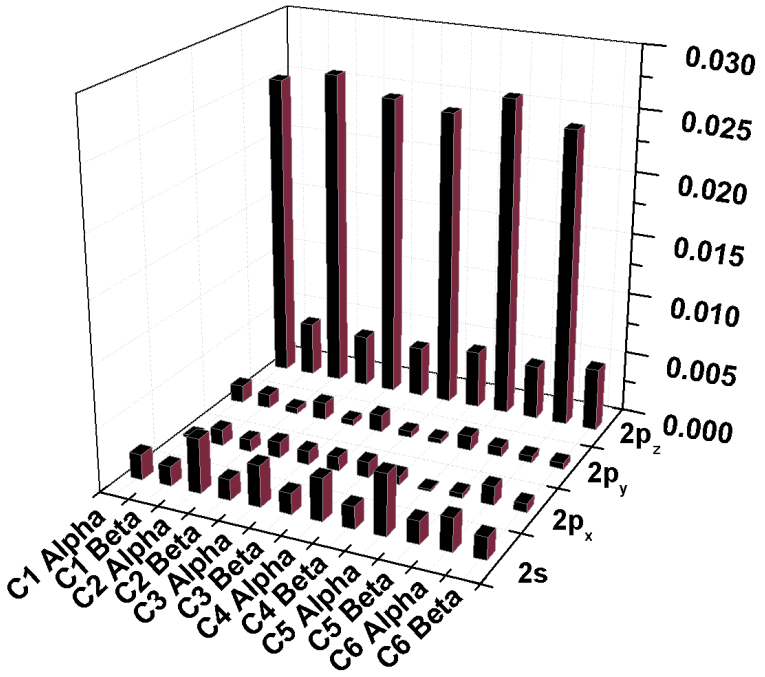

Figure 4.11: Mulliken population of the six carbon atoms in the H-doped system, which are denoted C1 to C6, that are bonded to the manganese atom, with a large contribution from the $2p_z$ α orbitals.

4.3 T-site coordination of manganese

Coordination of the manganese atom just above a carbon atom in the graphene layer leads to dramatic changes in the physical properties of the system. The coordination mode is shown in figure 4.12, with a height of the manganese atom above the carbon atom just beneath of 1.967 Å. Three other carbon atoms that surrounds this carbon atom which are placed just below the manganese atom, are involved in the bonding to the manganese atom and the average bond length to these carbon atoms is 2.35 Å. In the work of Sevincli,[139] this coordination site was not the lowest in energy, therefore little discussion was provided for this coordination mode. Interestingly, the magnetic moment of the system is not reduced to more than 4.3 μ_B. Thus, if this coordination site could be stabilized, it might be interesting from a spintronic point of view. Figure 4.13 shows the band structure for the coordination site with a manganese atom coordinated directly above a carbon atom. In this case, the valence band is constant and lies just along the Fermi level (-1.46 eV) in all directions and for all symmetry points.

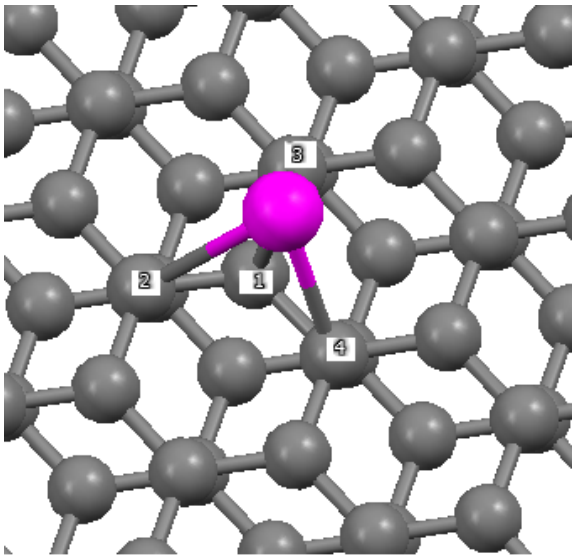

Figure 4.12: Coordination mode for a manganese atom just on top of a carbon atom, T-site coordination. Carbon atoms involved in bonding are denoted 1-4.

The Fermi level is now lowered compared to the H-site coordination, and the both α and β spin orbitals show a perfect agreement for all points. The conduction band displays a minimum for the Γ and A point, almost touching the valence band. A more enhanced metallic character can thus be expected for this coordination site as well. Mulliken analysis for the manganese atom in the valence band is shown in figure 4.14. Especially the α spin orbitals occupy the d-orbitals to a larger extent than the p-orbitals, which is reflected in figure 4.16 and 4.17, which shows the resulting orbital on the manganese atom with larger occupation of the $3d_{z^2}$-orbital for the α spin electrons. As can be seen from the Mulliken analysis, there is almost no occupation of the $4s$ α spin orbitals for this coordination site. On the other hand, Mulliken analysis confirm that the $4s$ contributes the almost entirely to β spin. This effect have been observed by Duffy et al[158] when calculating coordination of transition metals on a graphite. Although using a different technique with an isolated graphite cluster instead of periodic structures, this group observed an increase of the $3d$ orbital population at the expense of the $4s$ orbital, for which some transition metals did increase the magnetic moment.

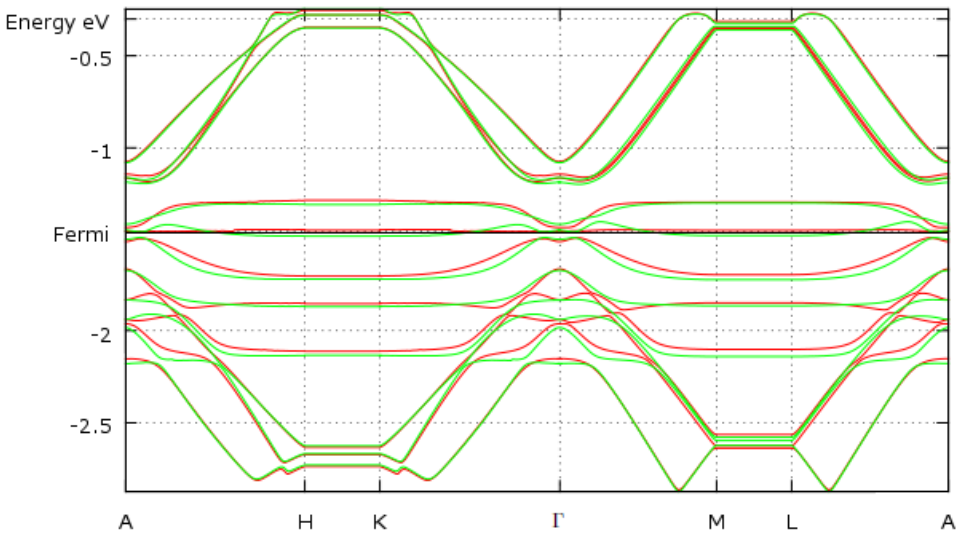

Figure 4.13: Band structure for α (red) and β (green) spin orbitals for T-site coordination with a constant valence band.

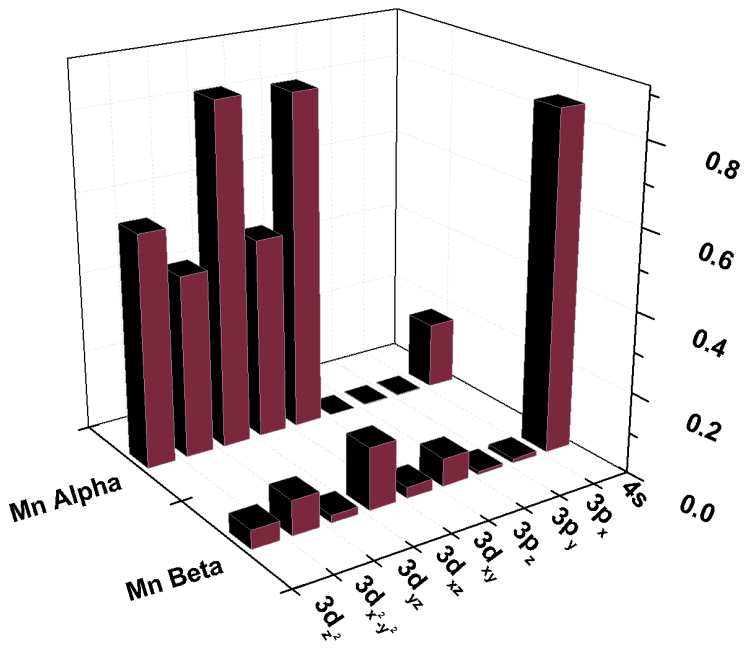

Figure 4.14: Mulliken population for the T-coordinated manganese atom. Most of the population is situated in the 3d α orbitals.

Four carbon atoms are involved in the bonding to the manganese atom for the T-site coordination, one of them is placed just beneath the manganese atom and the remaining three are surrounding the first one according to figure 4.12. In figure 4.15, the Mulliken population of the four carbon atoms is shown. The carbon atom just beneath the manganese atom is denoted C1 and reveals an uneven population on the α and β spin orbitals. Interestingly, one of the remaining carbon atoms in the graphene layer, C2, shows an even population for the α and β spin orbitals, whereas the the other two carbon atoms have a larger population on the $2p_z$ orbital. Although a net population on the β orbitals exists, the magnitude relative to the population on the manganese atom is small. The population on the $3d$ α orbitals are thus the determining factor for the overall magnetic moment.

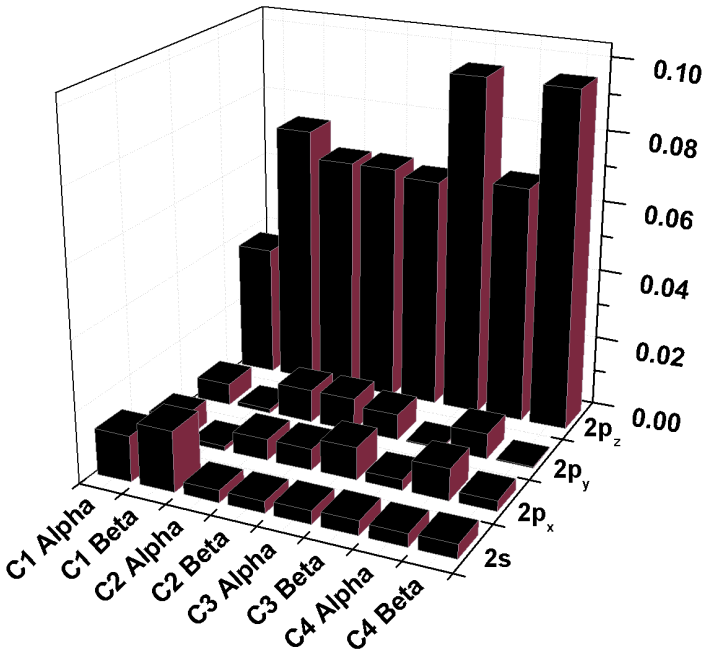

Figure 4.15: Mulliken population of the four carbon atoms in the T-doped system. C1 is the carbon atom just beneath the manganese atom.

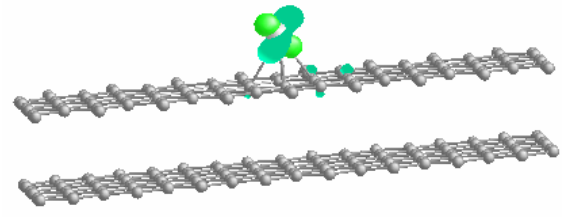

Figure 4.16: α orbitals for the highest occupied band for the T-coordinated manganese atom. Orbitals are shown as the sum over all k-points in the Brillouin zone.

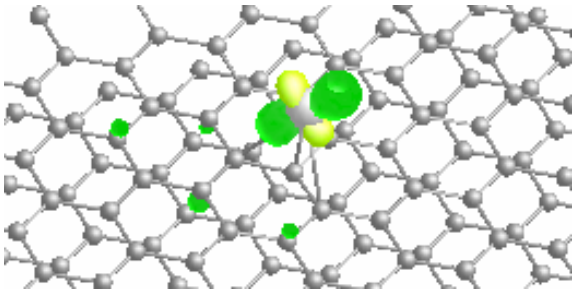

Figure 4.17: β orbitals for the highest occupied band for the T-coordinated manganese atom. Orbitals are shown as the sum over all k-points in the Brillouin zone.

4.4 Manganese atom substitutionally above graphene layer

The next coordination mode considered in the current study can be described as replacing one carbon atom in the layer with a manganese atom i.e. the manganese atom substitutes the carbon atom. The manganese atom is placed above the graphene layer according to figure 4.18. A number of theoretical studies have dealt with substitutional coordination rather than the two previous coordination modes. In substitutional coordination, the manganese atom can be considered to occupy a vacancy in the graphene layer, which would lead to a more stable coordination and less possibility for migration of the manganese atom. The average Mn-C bond length was 1.80 Å, resulting in a height of 1.40 Å for the manganese atom above the graphene layer, which is considerably smaller than for the two previous coordination sites. In one study by Wu et al. the Mn-C bond lengths for the same coordination mode were 1.834 and 1.826 Å and the height over the graphene layer was found to be 1.37 and 1.39 Å when using two different computer codes. This is also in good agreement with previous studies for the same coordination site.

The magnetic moment for this coordination site in the current work was reduced to 3.0 μ_B, which also was reported by both groups. This could be a consequence of the symmetry for this coordination site, which allows for a strong interaction with the orbitals on the manganese atom and the graphene bi-layer. The Fermi level lies at -1.527 eV, which is slightly lower than for the H and T-site coordination. Interestingly, the conduction band for both α and β spin orbitals crosses the Fermi level and overlaps with the valence band at the Γ and A point, which indicates a strong possibility for electron movement into the conduction band since the band gap is zero at these points. Thus, the semi-metallic property is still maintained for this coordination mode.

The Mulliken analysis for the substitutional coordination site reveals that the participation

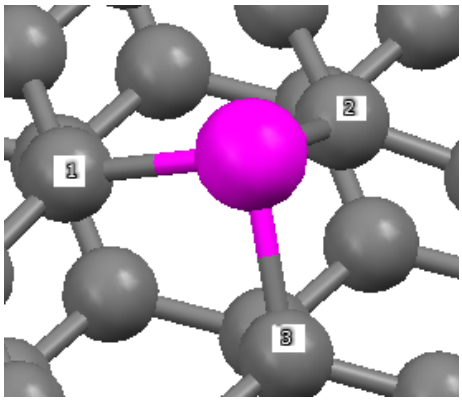

Figure 4.18: Substitution of a carbon atom with manganese. Height of manganese atom above the graphene layer is 1.40 Å and the magnetic moment is reduced to $3.0\mu_B$. Carbon atoms involved in bonding are denoted 1-3.

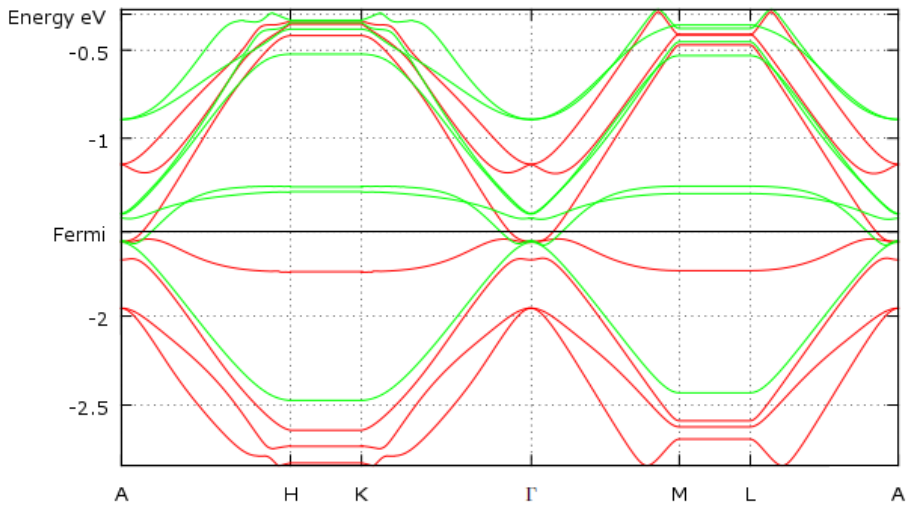

Figure 4.19: Band structure for α (red) and β (green) spin orbitals for the substitutional coordination site.

from the α electrons in the valence band is almost negligible, whereas the participation from the β electrons includes all the five d-orbitals, especially the $3d_{xz}$.

The current coordination site for the substitutionally doped system has a magnetic moment of $3.0\mu_B$, which indicates a substantial lowering of the magnetic moment for the free manganese atom in accordance with Mao[142] and Santos.[159] A consequence of the replacement of one carbon atom for a manganese atom, is that a stronger covalent character of the Mn-C bond can be expected. The Mulliken population analysis for the manganese atom in this system reveals that a large proportion of the spin polarization is caused by population of the $3d$ β orbitals. A small popula-

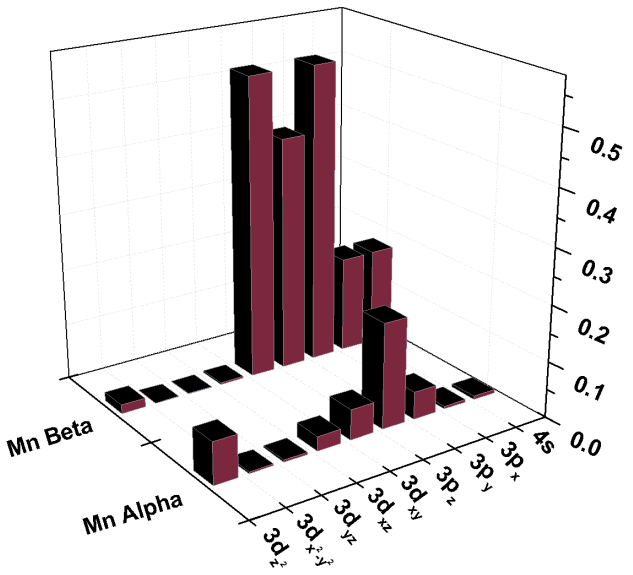

Figure 4.20: Mulliken charge for the substitutional coordination site.

tion of the $4s$ orbitals can be seen, especially for the α spin orbital. Just like the observation by Duffy et al., it can be assumed that population of the $3d$ orbitals and suppression of the $4s$ orbitals can increase the magnetic moment for some transition metals. In this case though, a simultaneous population of other orbitals of the opposite spin causes the total magnetic moment to decrease. Three carbon atoms are involved in the bonding to the manganese atom and these are the crucial ones when considering the total magnetic moment. Figure 4.21 shows the Mulliken population of these three carbon atoms, labelled C1-C3. Due to the large population of the graphene $2p_z$ α orbitals, there is a lowering of the total magnetic moment for the system.

4.5 Substitutional manganese atom between graphene layers

The last system investigated in this study comprise a manganese atom between the two graphene layers, a coordination mode which also was investigated by Mao et al.[143] Just like in the previous substitutional coordination mode, one carbon atom is substituted for a manganese atom, but points down between the layers instead of up from the upper layer as in the first three coordination modes. This coordination mode lies 1.20 eV lower in energy compared to the previous substitutional coordination mode. Figure 4.22 and 4.23 shows how the manganese atom is coordinated between the graphene layers, where the distance between the sheets is 3.245 Å. Average Mn-C bond length was found to be 1.82 Å and the distance from the manganese atom down to the hexagonal ring

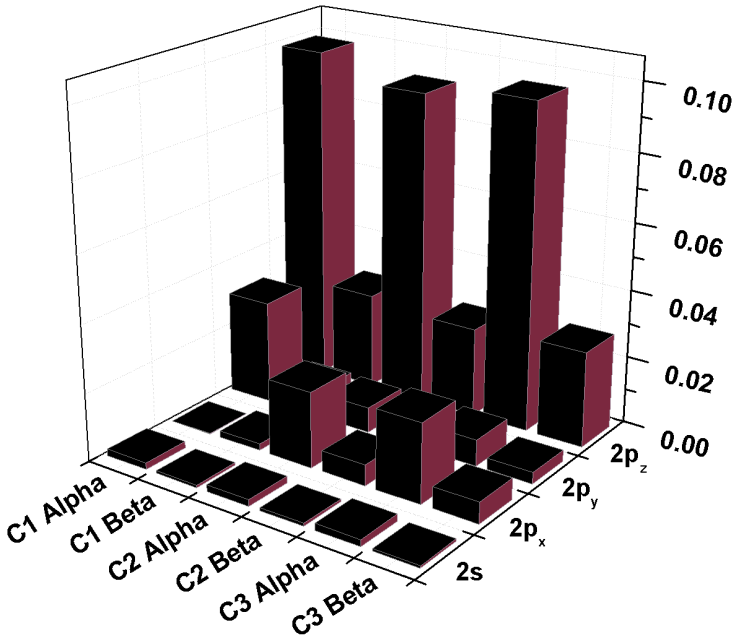

Figure 4.21: Mulliken population of the three carbon atoms denoted C1 to C3, in the first substitutional system that are bonded to the manganese atom.

formed by carbon atoms in the lower layer as indicated by the thin black lines in figure 4.23 was 2.38 Å on average. Interestingly, the magnetic moment is hugely reduced to 1.26 μ_B. Hence, interaction between the manganese atom and the lower graphene layer cannot be ruled out despite the distance of 2.38 Å. In their study, Mao et al. also found a large reduction of the local magnetic moment for the manganese atom down to 1.76 μ_B, which was explained by a large re-distribution of charge on both the manganese and the carbon atoms involved in bonding to the manganese atom. The band structure for this system is similar to the previous system, although no overlap of the valence and conduction band can be found. For this system, the Fermi level has shifted to -1.611 eV, which compared to pure graphene is a shift towards the conduction band and this is in agreement with previous studies. For both α and β spins, the bands are always separated, but approaching each other in the Γ and A point, in a similar way that has been seen for the other three systems. The β spins have two bands that lies very close to the Fermi level and gives this coordination mode a more metallic behaviour. Mulliken analysis for the manganese atom in figure 4.25 reveals a large spin polarization for the β electrons, which occupies all the five d-orbitals, especially $3d_{xy}$, $3d_{xz}$ and $3d_{yz}$. For this coordination mode, the manganese atom binds to three carbon atoms in the upper layer of graphene in which it substitutes a carbon atom. Interaction to

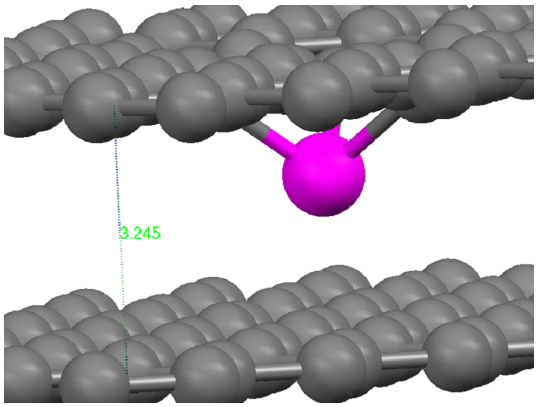

Figure 4.22: Coordination mode with the substitutional manganese atom between the layers.

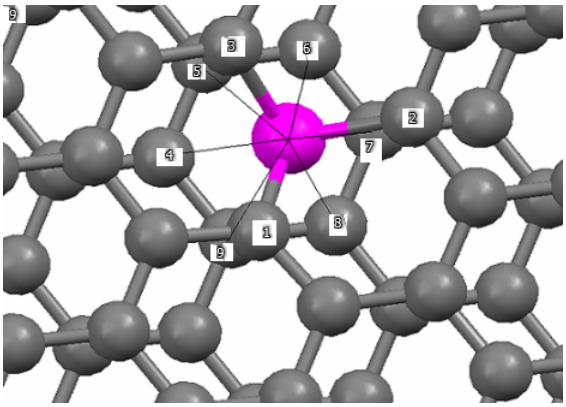

Figure 4.23: Thin black lines indicate the distance of 2.38 Å from the Mn atom to the next layer of graphene. Carbon atoms involved in bonding are labelled 1-3, carbon 4-9 belong to the next graphene layer.

six other carbon atom in the lower layer cannot be ruled out despite the larger distance to these carbon atoms. The Mulliken population for this coordination site is shown in figure 4.26 in which the three first carbon atoms C1-C3 are the carbon atoms that binds directly to the manganese atom. The remaining six are the carbon atoms in the lower layer. As can been seen in the figure, spin polarization occurs on the three carbon atoms which are directly coordinated to the manganese atom. A small spin polarization can also be found on the other six carbon atoms denoted C4-C9, but since an only slightly unequal population of both α and β spin orbitals occur on these atoms, the resulting spin polarization is very small. For the carbon atoms C1-C3, the Mulliken population is small in magnitude compared to the Mulliken population for the manganese atom, which reveals that population on the 3d β orbitals on the manganese atom contribute to the overall spin polarization for this system.

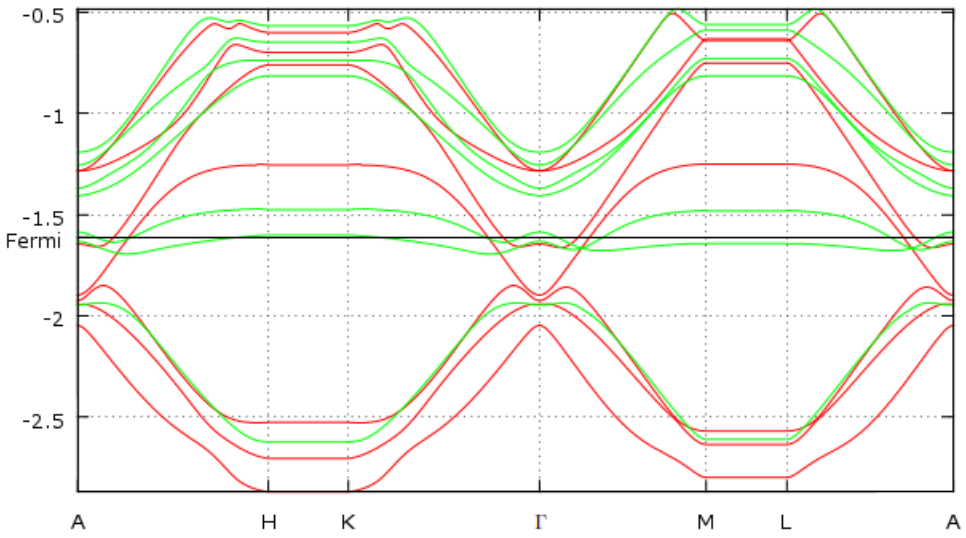

Figure 4.24: Band structure for α (red) and β (green) spin for the substitutional coordination site with a manganese atom between the two graphene layers.

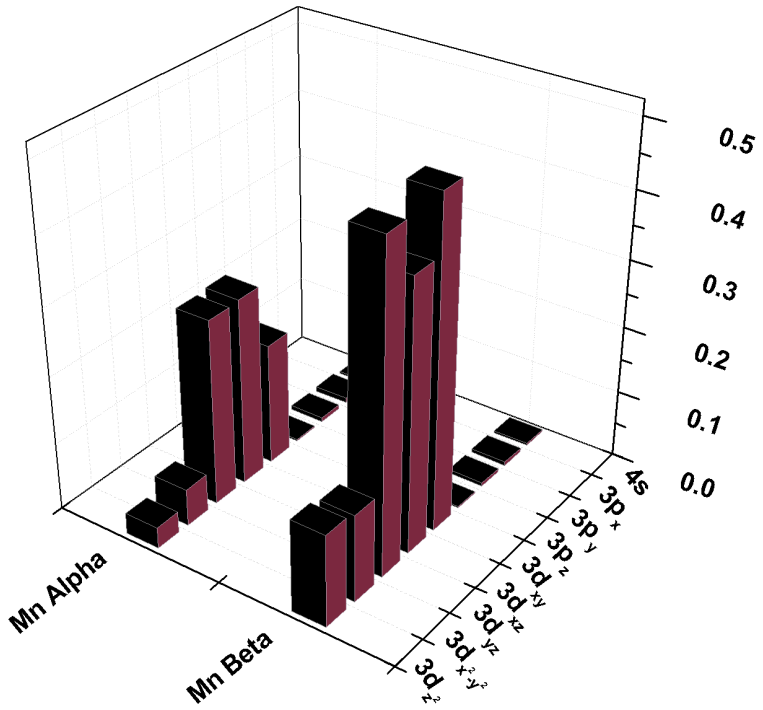

Figure 4.25: Mulliken charge for the substitutional coordination site with the manganese atom between the two graphene layers.

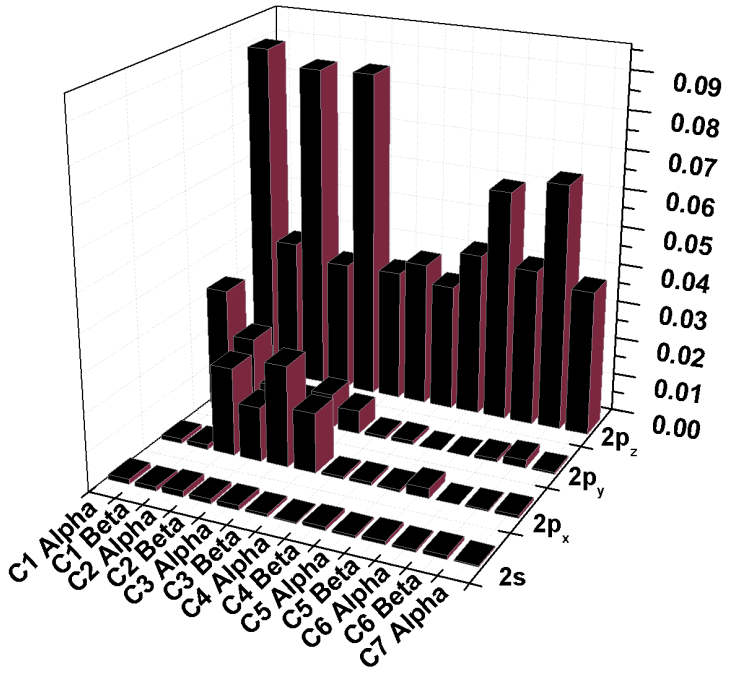

Figure 4.26: Mulliken populations of the nine carbon atoms denoted C1 to C9, which are involved in bonding or interaction with the manganese atom.

4.6 Conclusions

In summary, this investigation has dealt with four different coordination or doping sites for a manganese atom in a double layer on graphene. Two of the doping sites consider a manganese atom above a pure graphene layer (i.e. adatoms), and for the other two doping sites, one carbon atom is replaced with the manganese atom.

Band structure calculations confirm that coordination of a manganese atom to a graphene layer results in a modification of the band structure for the system. The band structures resulting from the doping indicates a change towards a more metallic or semi-metallic behaviour. Doping of a manganese atom results in a shift of the Fermi level upwards towards the conduction band. The Fermi level coincides with the valence band for T-site doping. This coordination site also displays the largest preserved magnetic moment $4.3\mu_B$. The spin polarization for T-site coordination is a result of population of $3d\ \alpha$ orbitals on the manganese atom. Thus, T-site doping might be important in spintronics.

For H-site and substitutional doping, the magnetic moment decreases to $3.0\mu_B$. Band structures for these two systems shows a semi-metallic behaviour with an overlap of conduction and valence

band at the A and Γ points. Several studies have found a similar reduction for the same coordination sites. For the last coordination mode, the magnetic moment has decreased to $1.26\mu_B$. Charge transfer to the six carbon atoms in the lower layer of graphene is a probable reason for this large reduction of the magnetic moment.

It has been suggested[142] that a larger doping concentration than 3-5% of manganese atom on graphene will result in an anti-ferromagnetic system with a small overall magnetic moment although individual manganese atoms might have a large magnetic moment.

These calculation have been performed at a very low temperature, and the structures investigated here might be found experimentally to be stable at low temperatures. However, problems that possibly would occur for adatoms doped on a graphene surface at elevated temperatures, include diffusion of the adatoms. If the structures could be stabilized, the T-site doping would be the most promising for spintronics.

Chapter 5

Manganese Based Metal-Organic Frameworks

Introduction *Metal Organic frameworks belong to a relatively new class of compounds with an extremely high surface to volume ratio, which make them as suitable candidates in various fields such as gas storage, sensors, gas separation, catalysis and optoelectronic devices. A lot of effort has been put into synthesis of these structures and their potential applications. Metal-organic frameworks provide most fascinating structures, consisting of inorganic clusters or parts connected via organic linkers into a one, two or three dimensional network with possible coordination sites for different molecules. One possible application for metal organic frameworks would be hydrogen storage since the binding strength to the various coordination sites in the structure might be tunable depending on the metals or linkers involved. The aim with this study is to theoretically investigate one specific metal-organic structure containing manganese atoms, with the Aimpro code. Physical properties are discussed in the light of adsorption/coordination of molecules to the structure and the possibility for hydrogen storage is analysed.*

In the search for new materials suitable for gas storage, gas separation and catalysis, a new class of materials has been developed and earned a lot of attention the last 10-15 years.[160–166] Sometimes in literature called "iso-reticular frameworks", with the meaning of a network-like structure extending in one, two or three dimensions, they can be considered to be inorganic building blocks connected via organic molecules or "linkers". One of the first metal-organic frameworks successfully synthesized was reported by Yaghi et al[167] in 1999. Many structures follows a similar underlying topology, in which the inorganic part consists of a metal-oxide cluster and the linker is a benzene based molecule. Providing pores with a very well defined size, which can be altered when changing the metal atoms in the inorganic part or changing the linker, the MOF structure

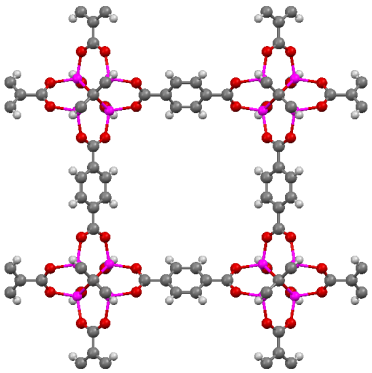

Figure 5.1: The Zn based cubic IR-MOF5 with a pore diameter of 8Å, possible coordination can occur to the inorganic part or to the benzene based linker.

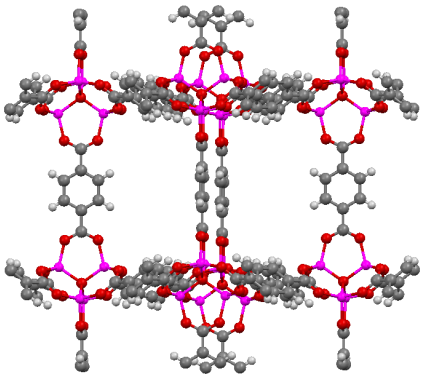

Figure 5.2: IR-MOF5, with zinc-oxide clusters (Zn_4O) in each corner, connected via 1,4-benzenedicarboxylate linkers.

can be "tuned" for selection of specific molecules for adsorption/coordination to the structure. This in turn can be used for gas purification or gas storage depending on intrinsic physical properties of coordinating species or properties of the MOF structure.[167–181] One the most widely investigated MOF structures is the MOF structure reported by Yaghi et al.[167] which is commonly denoted MOF1 or IR-MOF5, where IR stands for "Iso-Reticular". It can be described as units of oxygen based Zn_4O clusters, connected via 1,4-benzenedicarboxylate units, which extends into a three dimensional network with a very well defined pore size. Figure 5.1 and 5.2 shows the minimum cubic cell (No. 221 *Pm-3m*) containing 424 atoms in total. The cell has the parameters of the side length a=25.832 Å. The colours on the atoms is as follows: black=carbon, red=oxygen, white=hydrogen and purple=zinc. IR-MOF5 has been under experimental and theoretical consideration for a number of studies, for example hydrogen or methane storage.[170–173] Experimental studies from Eddaoudi et al.[173] have also modified the structure, with larger linkers, a larger pore size as a result. A number of different linkers and modified MOF structures from the work of Eddaoudi are shown in figures 5.3 and 5.4. For IR-MOF2 to IR-MOF7, benzendicarboxylate with functional groups such as bromo, amino, n-propoxy, n-pentoxy, cyclobutyl or benzene rings constitutes the "new" linkers. Successive longer linkers are used in IR-MOF8 to IR-MOF16, in which the pore size is dramatically increased. The yellow spheres constitute the largest van der Waals spheres that would fit into the cubic structure without touching the framework. By just changing the linker many different MOF:s with the same underlying topology can be made.

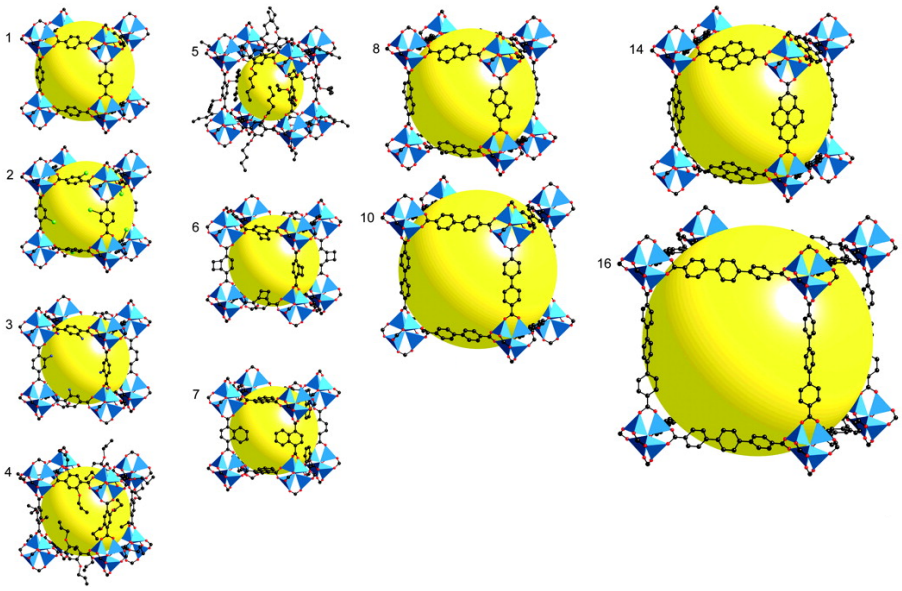

Figure 5.3: MOF structures with different linkers. Yellow spheres=largest van der Waals radius, blue polyhedra=zinc atoms. From 173.

In figure 5.3, different MOF structures based on the IR-MOF5 structure are shown, as a result of different linkers. The colour scheme is as follows: Zn=blue polyhedra, O=red, C=black, Br=green) (in stucture 2), amino-groups=blue (in stucture 3). All hydrogen atoms been omitted for clarity. The variety of different linkers is shown in figure 5.4, where BDC=Benzene DiCarboxylate, NBC=Naphtalene DiCarboxylate, BPDC=BiPhenyl DiCarboxylate, HPDC=HPhenyl Dixarboxylate, PDC=Pyrene DiCarboxylate and TPDC=TerPhenyl DiCarboxylate.

As already pointed out, metal-organic frameworks are easily made structures, a solvo-thermal reaction where a metal oxide and its carboxylic acid in a common solvent are heated to a few hundred degrees. The surface to weight ratio for metal-organic frameworks is extremely high, for IR-MOF5 and its derivatives 2500-3000 m^2. But limitations do exist, metal-organic frameworks are only thermally stable up to approximately $300 - 400°$C. At more elevated temperatures, the structures collapses.

Coordination of different gas or solvent molecules might occur both to the linker or the metal atom in the inorganic part. Known problems with coordination/adsorption of different molecules to the structure is due to the binding strength of the molecule. Upon binding, a lot of energy is released as heat, and this energy must be provided back to the system if the molecules are to be released again. This can be a technical problem for practical use of a specific metal-organic framework structure, for example in hydrogen storage. Heating up the structure for release of adsorbed molecules might

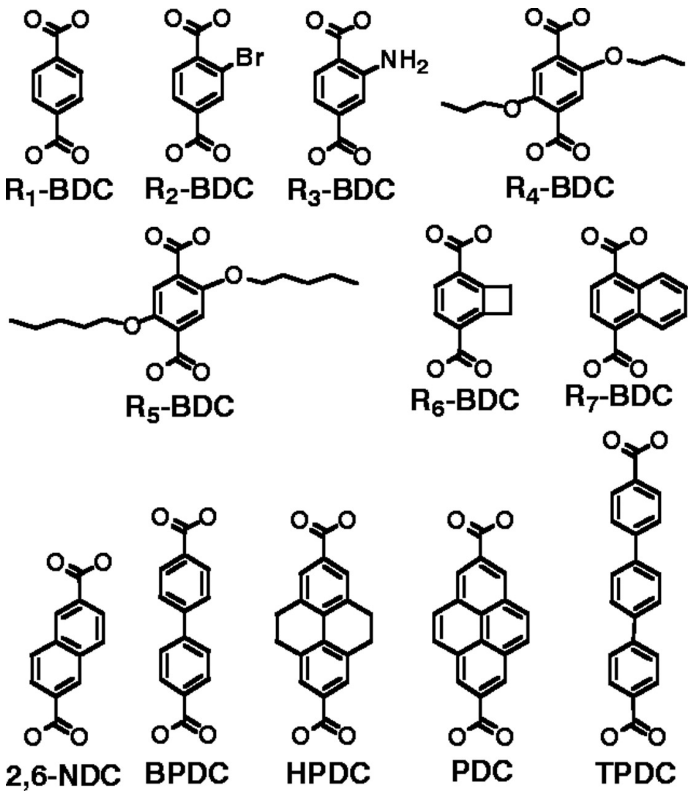

Figure 5.4: Different linkers used for the zinc-based MOF structures. From reference 173.

result in a collapse of the entire MOF structure.

The aim of this study is to consider one specific MOF structure which contains manganese atoms in its inorganic parts, and investigate its physical properties and abilities for adsorption of a few selected molecules. Due to its many possible spin states, a manganese based MOF-73 structure provides many interesting coordinating features to investigate.

The metal-organic structure in the current work was reported by Eddaoudi et al.[182] under the name MOF-73 when using the solvent DEF, Diethyl-formamide and the structure was collected from the Cambridge Data Base. This structure was also reported when replacing DEF with DMF, Dimethyl-formamide by Luo et al.[183] MOF-73 crystallises in the monoclinic space group (C2/c No.15) and the unit cell reported contained 85 atoms and has the empirical formula $C_{34}H_{34}Mn_3NO_{14}$. Other important cell parameters given from Eddaoudi were; a = 24.7821(16) Å, b = 10.5842(7)Å, c = 17.4219(11) Å, α= 90°, β= 129.9320(10)°, γ = 90° and with a total volume of V=3504.1(4) Å^3.

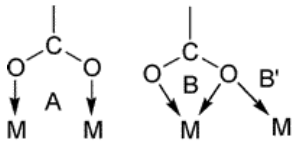

Figure 5.5: The two different alternating coordination modes in MOF-73, O=oxygen, C=carbon and M=manganese. From reference 182.

The super cell used in the current study contained 348 atoms if solvent molecules were included, without any solvent molecules, the number of atoms was 204. Figure 5.6 which is taken from Eddaoudi[182] shows the principal structure of this MOF structure. The "back-bone" of MOF-73 is shown to the left in the sequence, with manganese atoms as light-blue spheres, oxygen as red spheres and carbon as black spheres. Manganese atoms bind to the carboxylate groups in two different ways i.e. two different manganese centres can be found. One of the manganese atoms binds to two carboxyl groups according to mode A, one as in mode B, and the last one as in mode B'. Furthermore, one DEF molecule is also bound to each of these Mn A centres, and when removing this molecule leaves an open site free for coordination of other molecules. These "open" sites might also facilitate different reactions, which can be useful in organic synthesis. This will be discussed later. The second type of manganese atom is located next to the first manganese atom and holds six carboxyl groups, with four of them as in mode A, and two as in mode B'. Thus, this rod-like back-bone linked at their corners and edges, comprises MnO_6 octahedra. Each "rod" in the structure is connected to four neighbouring rods, which gives the resulting structure to the right in figure 5.6. All the channels formed are rhombic with the dimensions of 11.2×5.9 Å^2. In figure 5.6, the solvent DEF molecules are omitted for clarity, they reside in the rhombic channels after the synthesis, but can be removed under a combined vacuum and heating process. When performing a de-gassing experiment of the MOF-73 structure, Eddaoudi et al. observed a weight loss of 22.9% when the temperature was elevated from 115 to 350°C, and this corresponds to one solvent molecule per formula unit. Furthermore, the structure starts decomposing at a temperature of 400°C.

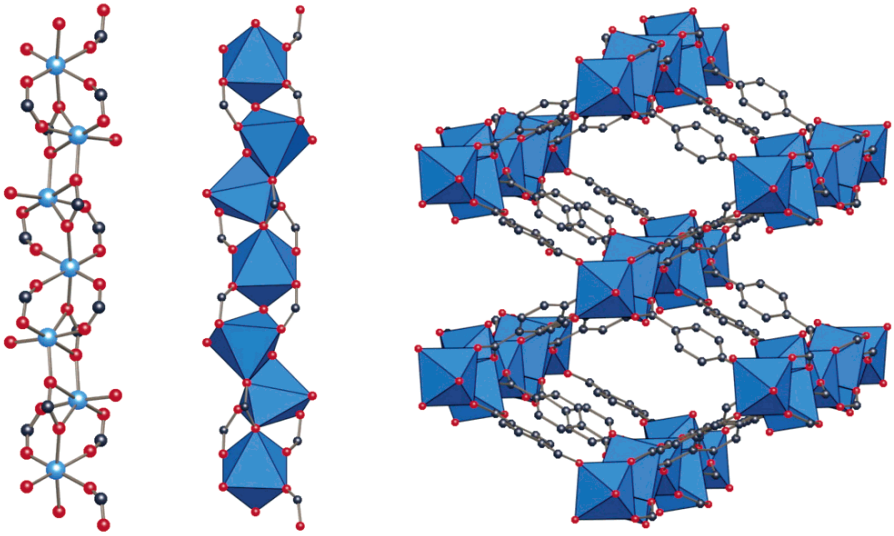

Figure 5.6: Left: Rod-like back-bone structure of MOF-73 where blue spheres=manganese, red spheres=oxygen, black spheres=carbon. Middle: Simplified back-bone structure with manganese as shown as polyhedra. Right: Structure of de-solvated MOF-73, with the solvent molecules omitted 182.

Only adsorption to the exposed manganese sites after solvent desorption will be considered in the current work, despite the possibility for the same molecules to be adsorbed elsewhere in the structure. It has been argued that adsorption will occur to these open metal-atom sites before occupation of any other possible site in the structure, and the main purpose with the current study is to investigate the change in electronic and magnetic properties upon coordination to the open manganese sites. As already mentioned the open metal-atom sites might facilitate chemical reactions and act as a catalyst, not only in metal-organic frameworks.[184] Experimental investigations of similar sites in metal-organic frameworks have been performed by Long et al.[185] This group investigated a manganese based MOF structure with exposed Mn^{2+} sites, which can act as a Lewis acid and they reported successful results for cyanosilylation reactions with yields up to 80%. In another study by Yaghi et al.[186] ring opening reactions were studied, and the reactions were believed to take place with the aid of the linker.

Several groups have shown interest in the synthesis of new manganese containing MOF structures[163,164,166,187–194], due to the interesting properties of manganese. In a paper from Jiang et al.[187] magnetic properties of a manganese containing MOF structure were investigated, and the result indicated an antiferromagnetic behaviour between the neighbouring manganese atoms. The same conclusion was made by Qi et al.[188], and Bai et al.[191] when performing magnetic susceptibility measurements in manganese containing MOFs. Thus, occurrence of antiferromagnetic

interaction in the MOF-73 structure in the current work cannot be ruled out. One of the few theoretical studies on metal-organic frameworks based on Sc, Ti, Cr and Mn was carried out by Sun et al.[195] Adsorption of hydrogen molecules to the structure was studied by this group, and physical properties like binding energies, magnetic moment and bond length/separation from the transition metal center were investigated for these metals. The binding energy varied from almost 50 kJmol^{-1} down to less the 10 kJmol^{-1}, with the lowest binding energy for manganese based MOF. Despite the low binding energy for hydrogen molecules to this MOF structure, it clearly shows the ability to tune the binding energy when changing the element in the structure. Both experimental as well as theoretical studies have been performed regarding hydrogen storage in several MOF structures.[170–172,175–178,196] Two of the most promising metal-organic frameworks (MOF-20 and MOF-177) are zinc-based structures according to figure 5.3, although constructed with larger linkers. At 77 K, the H_2 uptake reached 6.7 and 7.5 wt % respectively. Some manganese based metal-organic frameworks also demonstrate a similar capability for hydrogen uptake, Long et al.[175] achieved an uptake of 6.9 wt % in one study. Hence, investigation of hydrogen uptake for the MOF-73 structure could reveal very interesting possibilities.

5.1 Computational Details

Two relaxations (with and without DEF-molecules) were performed as spin unrestricted calculations, whereas the remaining two relaxations, MOF-73/carbon monoxide and MOF73/hydrogen molecules, were performed as spin-averaged calculations using periodic structures in the Aimpro code[150] and employing Density Functional Theory with the PW92-functional.[37] An initial spin configuration of 5 unpaired electrons was given to the manganese atom. Spin optimization was then allowed to occur during the geometry relaxation. Energy convergence criteria for the optimizations were set to 10^{-5} Hartrees, and the convergence criteria for symmetry were set to a factor of 10^{-5}. Pseudo-potentials as described by Hartwigsen, Goedecker and Hutter[151] were used on all oxygen, carbon, hydrogen and manganese atoms. Due to the dimensions of the monoclinic supercell, the energy was only sampled in the Γ point, and a small electronic temperature of kT=0.12 eV was used together with a smearing of the occupancy according to M. Methfessel and A. Paxton.[153] A 4×4×4 grid was used for band structure and Mulliken analyses which are reported here as the average of the k-points of a specific band. All band structure calculations were performed as spin averaged calculations. Figure 5.7 shows the Brillouin zone for the monoclinic cell[197] and high symmetry points which are used in band structure calculations in the current work; Γ, X, Y, Z and T. Four different cases will be considered. Firstly, the "pure" structure when the solvent molecules have been removed will be discussed. In close connection to this case, the structure as

collected from the Cambridge Database as adsorbed i.e. including solvent molecules coordinated to the structure will be considered. Two new molecules will then be investigated in turn, CO and H_2. Despite their simplicity, these molecules provide many interesting physical properties in adsorption to the MOF-73 structure.

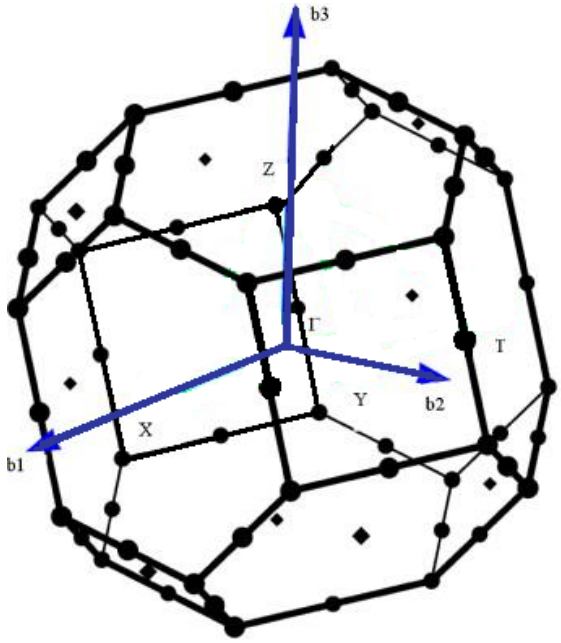

Figure 5.7: Brillouin zone for the monoclinic cell with the high-symmetry points Γ, X, Y, Z and T. Taken from reference 197.

In order to investigate the binding energies of the molecules, their atomic reference states were considered using periodic conditions, the molecules being put in a box with length of 20Å and the energy was obtained using a 4×4×4 grid according to the Monkhorst-Pack scheme.[152]

5.2 Confirmation of Computational Methods

As previously mentioned, when dealing with large unit cells, energy sampling from just the Γ-point might be enough, instead of using a grid of k-points, since the sampling occurs in a small part of reciprocal space. To confirm if sampling in the Γ-point is a suitable choice, comparison between a Γ-point calculation and a multi k-point calculation was made. A grid of 2×2×2 k-points was used for sampling of the energy in one calculation and compared with the same system considered only with the Γ-point. The cell under consideration was the 348-atom MOF-73 unit cell with all solvent molecules adsorbed on the available manganese atoms. As a result, when employing only the Γ-point, the energy lies 1.86 $kJmol^{-1}$ lower, compared with the k-point calculation. Thus,

dealing with these systems when only considering the Γ-point is a perfectly adequate choice of energy sampling.

As a reference bond type, the Mn-O bond was chosen, because of its role in the rod-like backbone and coordination to different molecules. For example, the solvent molecule DEF coordinates via its oxygen atom to the manganese atom in the structure, and release of this molecule from the MOF structure might affect the other Mn-O bonds for this particular Mn atom. Several forms of Mn-O bond lengths are available in the literature depending on the space group of the MnO-type under consideration. The mean distance for the Mn-O bond in the rutile type of MnO_2-type has been reported[198] as 1.89 Å where two of the bonds were found to be a bit elongated. Approximately the same bond lengths were reported by Kohler and Armbruster[199] with four bond lengths of 1.882 Å and two of 1.894 Å. With the chosen basis set in the current work, Mn-O bond lengths were 1.890 Å on average for rutile. From these results, it can be concluded that the chosen basis sets for manganese and oxygen are adequately.

5.3 MOF-73 Structure With And Without Diethylformamide

The first case considering MOF-73, was the structure as it was reported by Eddaoudi et al., which is the structure with solvent molecules adsorbed to the structure. Solvent molecules are residues from the synthesis and was also reported to be successfully removed during heating of the structure under vacuum. In each super cell, 8 solvent molecules are present. Figure 5.8 show parts of the MOF-73 structure with and without solvent molecules. Figures to upper and lower left are the structures with solvent molecules from above and from the side in which the rhombic channels in the structure can be seen. Solvent molecules are filling almost the entire channel. Images to the right show the MOF-73 structure without any solvent molecules present. The rhombic channels are completely free for adsorption of new molecules, which can be seen in the lower image to the right. Binding energies E_{Bind} per solvent molecule are calculated according to the principle:

$$E_{Bind} = \frac{E_{(MOF73+molecules)} - [E_{(MOF73-molecules)} + N \times E_{(molecules)}]}{N} \tag{5.3.1}$$

where (MOF73 + molecules) and (MOF73 - molecules) is the MOF-73 structure with and without adsorbed molecules respectively. In this particular case, the molecule in question is the solvent molecule DEF and the number N is 8.

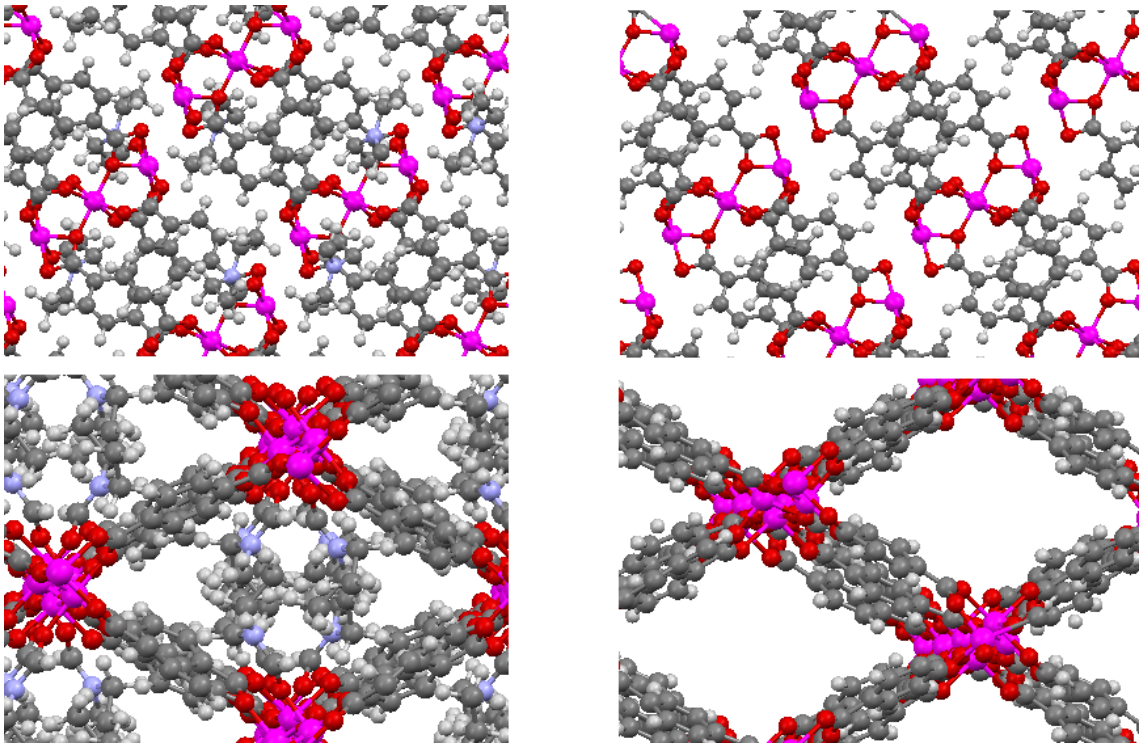

Figure 5.8: Image showing the MOF-73 structure with (upper and lower left), and without (upper and lower right) solvent molecules. Purple spheres=manganese, black spheres=carbon, red spheres=oxygen, blue spheres=nitrogen and white spheres=hydrogen.

Table 5.1 shows change in the average bond lengths when the DEF molecules are removed from the MOF-73 structure. Two bond lengths are reported for Mn-O, in which the first value denoted (1), refers to the manganese bond lengths in the host structure, whereas the second value denoted (2) refers to the bond between a manganese atom and the oxygen in the solvent molecule. All other bond lengths are also reported as average bond lengths. The values from table 5.1 clearly shows an increase in the bond lengths when the solvent molecules are removed. For all but the C-H bond lengths, the increase should be detectable. For example, the C-O bond lengths range between 1.271 and 1.322 Å, and the Mn-O bond lengths range between 1.793 and 2.492 Å. A deviation this large can be interpreted as a destabilisation of the entire structure which occurs especially between manganese and oxygen atoms. Binding energy as defined from equation 5.3.1, gives a binding energy of 213 kJmol^{-1} per solvent molecule for diethylformamide, which can be considered to be reasonable since removal of the solvent molecules had to be performed under vacuum and heating to a temperature of 350°C. The magnetic moment for the total system including solvent molecules is $0.0\mu_B$. When the solvent molecules are removed, a very small increase of the total magnetic moment to $0.004\mu_B$ is observed. Bandstructures for MOF-73 with and without DEF molecules are shown in figures 5.9 and 5.10.

Bond	MOF-73 with DEF molecules Bond Length Å	MOF-73 without DEF molecules Bond Length Å
Mn-O (1)	1.938	2.006
Mn-O (2)	1.907	-
C-O	1.285	1.294
C-C	1.440	1.457
C-H	1.095	1.096

Table 5.1: Bond lengths for different bond types regarding the MOF-73 structure with and without the solvent molecules DEF. All the bond lengths are average values and some differences do occur for bonds of the same kind. Differences are larger for the uncoordinated or de-adsorbed structure, is a sign of a more destabilized structure.

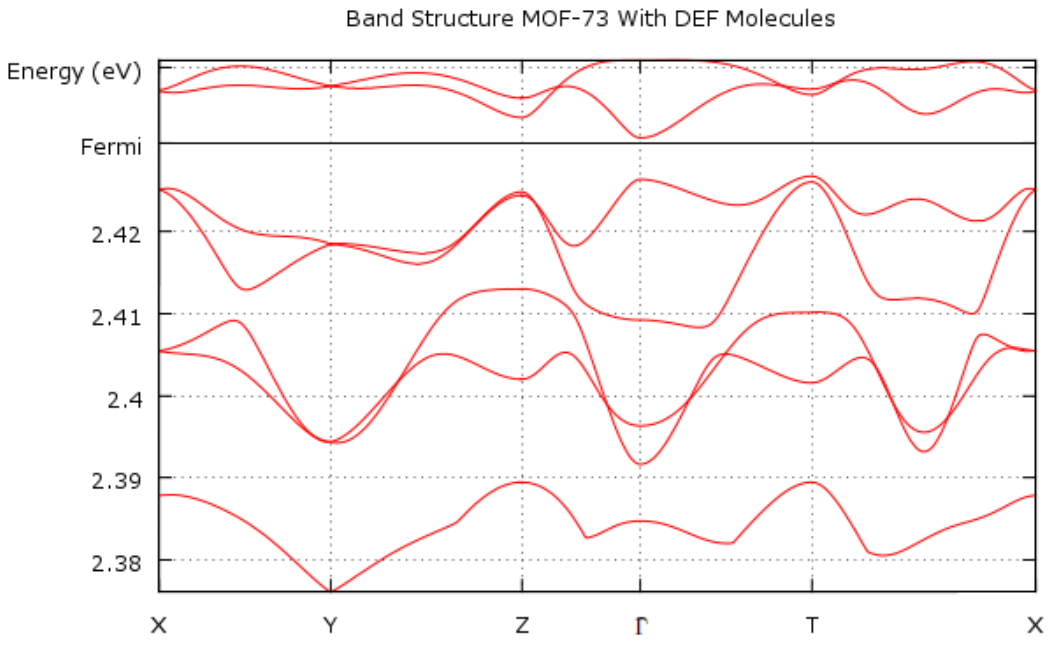

Figure 5.9: Band structure for MOF-73 with DEF. Five occupied and two unoccupied bands are shown.

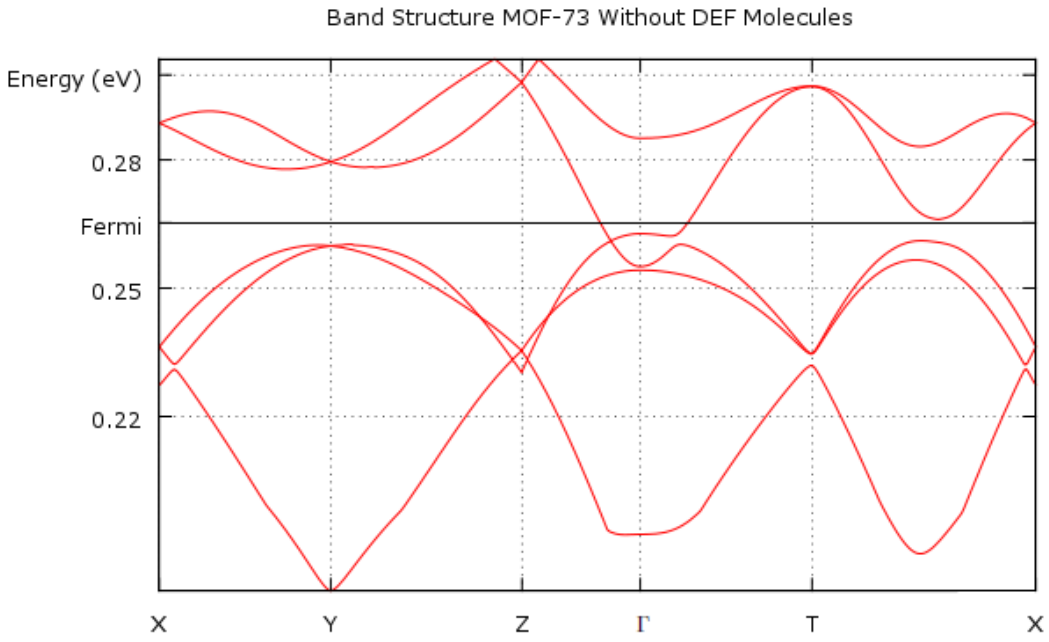

Figure 5.10: Band structure for MOF-73 without DEF molecules present. Three occupied and two unoccupied bands are shown.

The band structure for the MOF-73 structure is changed dramatically when the DEF molecules are removed. When the DEF molecules are present, the Fermi level lies at 2.43 eV and the valence band and conduction band are separated by 0.01-0.02 eV except for the Γ point in which the separation is approximately 0.005 eV. No overlap of the conduction band and the valence band occurs, but the small band gap could be unreliable in DFT. A completely different band structure is displayed for the de-adsorbed MOF-73 structure. The Fermi level is now shifted down to approximately 0.265 eV. Clearly, the band structure is heavily affected by desorption of solvent molecules. This behaviour can be expected for any kind of molecule that is coordinated to the exposed manganese sites. Crossing of the valence band and conduction band occurs in the proximity of the Γ point which indicates metallic behaviour. Coordination of diethylformamide will shift the Fermi level up in energy and make the bands around the Fermi level more separated from each other. Upon coordination of the DEF molecules, the MOF-73 structure approaches a more semi-conductor like behaviour. Mulliken analyses for the MOF-73 structure with and without DEF molecules are shown on the following next two pages. Two interesting features can be observed in the bar diagrams for the Mulliken population. Firstly, the difference between the α and β spin electrons, a difference that is prominent for these two systems. Secondly, a difference between manganese atoms is also present.

All manganese atoms are not equally occupied, depending on which coordination the manganese atom in question has. As discussed in the previous section, manganese atoms in the MOF-73 structure can be distinguished into two types according to their coordination to surrounding atoms. In the unit cell used in the current work, four of the manganese atoms have a permanent six-fold coordination, and the remaining eight manganese atoms are coordinated to the diethylformamide molecules. Hence, these atoms have a five-fold coordination in the desorbed case, and are the manganese atoms which can be open for coordination of external molecules. As can be seen from figure 5.11 and 5.12, the α electrons are mainly occupying the d_{xy} and d_{z^2} orbitals, whereas a larger occupation of all d-orbitals can be observed for the β electrons. For both α and β electrons, four atoms have a much larger occupation compared to the other atoms, and these are the manganese atoms with a permanent six-fold coordination. Since the calculated spin polarization was 0 for this system, the occupation for both α and β spins are equal, although occupying different orbitals to a different extent. The difference between different types of manganese atoms remain, when the DEF molecules are removed, although an almost perfectly even population of the d-orbitals for α and β spins can be seen in figure 5.13 and 5.14.

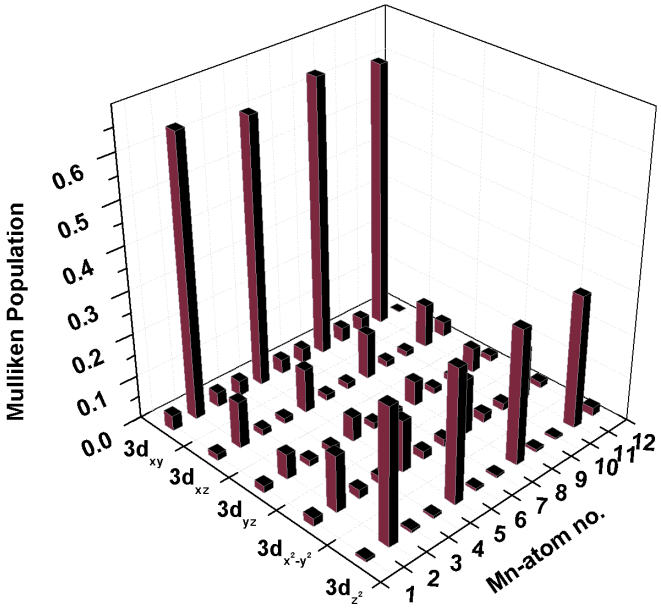

Figure 5.11: Mulliken population for the α spin orbitals for MOF-73 with DEF molecules. Atom no. 2, 5, 8 and 11 are holding DEF.

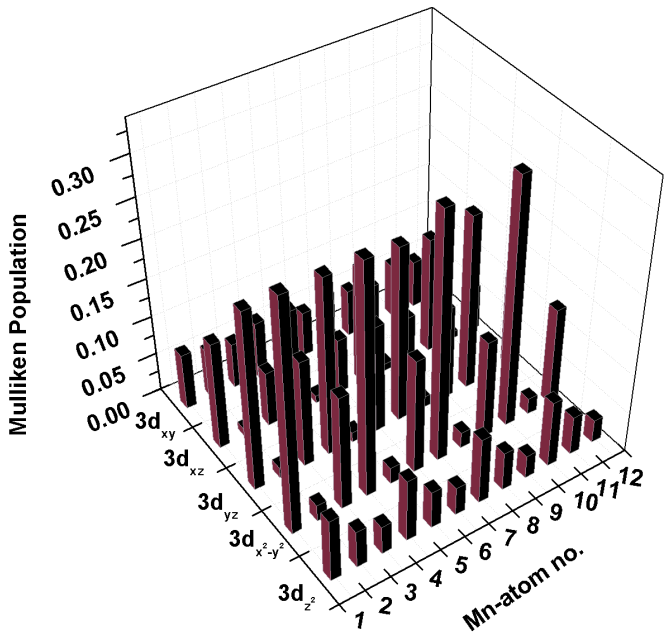

Figure 5.12: Mulliken population for the β spin orbitals for MOF-73 with DEF molecules. Atom no. 2, 5, 8 and 11 are holding DEF.

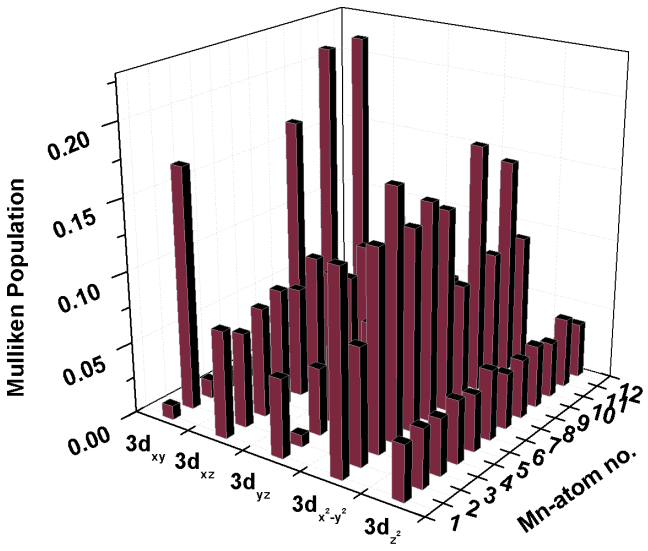

Figure 5.13: Mulliken population for the α spin orbitals for MOF-73 without DEF. Atom no. 2, 8, 10 and 12 are open sites.

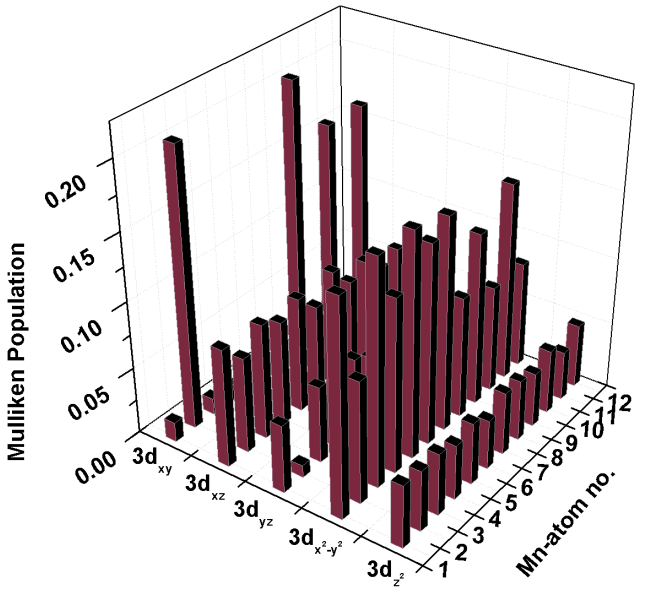

Figure 5.14: Mulliken population for the β spin orbitals for MOF-73 without DEF. Atom no. 2, 8, 10 and 12 are open sites.

Spin	$2s$	$2p_x$	$2p_y$	$2p_z$
α	1.20132	0.82036	0.77600	0.79816
β	1.20145	0.82035	0.77599	0.79811

Table 5.2: Mulliken population for the oxygen atom on the uncoordinated solvent molecule. Even population for all orbitals.

Spin	$2s$	$2p_x$	$2p_y$	$2p_z$
α	0.00035	0.00007	0.00042	0.00113
β	0.00099	0.00064	0.00007	0.00481

Table 5.3: Mulliken population for the oxygen atom on the coordinated solvent molecule. Significant loss of charge occurs for all orbitals.

Mulliken analysis were also performed for the free and adsorbed solvent molecule. Table 5.2 and 5.3 shows the α and β spin orbitals for oxygen atom on the free and the adsorbed solvent molecule respectively. As can be seen from table 5.2, the population for α and β spin orbitals is almost exactly even, with most of the electronic charge placed on the $2s$-orbital. Upon adsorption, the charge distribution on the oxygen atom is dramatically changed, with a large drop in the electronic charge for all orbitals. For the $2s$-orbital this loss of charge is as large as approximately 1.2 electrons, which supports the high bonding energy. A strong interaction can thus be concluded for the solvent molecules remaining from the synthesis. The large loss of charge on the oxygen atom might also accounts for the reduction of the net magnetic moment for the system.

5.4 CO Adsorbed In The MOF-73 Structure

Carbon monoxide constitutes a very interesting molecule when adsorbed or coordinated to a transition metal atom. According to simple electronegativity rules, bonding occurs via the the oxygen atom, which is not what is found in reality. Bonding to a transition metal atom occurs via the carbon atom since the highest occupied molecular orbital (HOMO) on carbon monoxide is the 3σ, which has a larger electron density than other orbitals in the molecule.[54] This orbital is found to be the one to coordinate to an appropriate orbital on the transition metal, this is shown in figure 5.15.

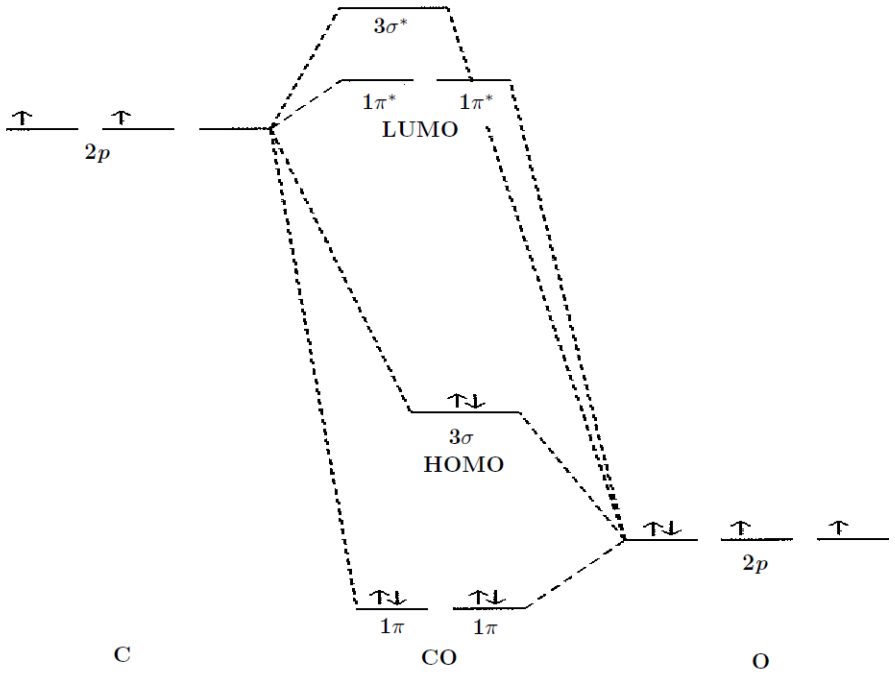

Figure 5.15: Molecular orbitals on the CO, with the 3σ HOMO orbital that forms the bonding orbital to transition metals. From reference 54.

Attempts trying to coordinate the CO molecule via the oxygen atom were made in the current work, without success. Thus, it was concluded that adsorption to the manganese atom takes place via the carbon atom. Figure 5.16 shows important bond lengths when the CO molecule is adsorbed to the manganese atom, with a slight modification of the C-O bond length. Literature value[200] of the C-O bond length is 1.128 Å and this bond a elongated to approximately 1.165 Å. Four CO molecules in total were placed on the open manganese sites in the 204-atom unit cell and the binding energy is calculated to 255 kJmol^{-1} per CO molecule, which is in accordance with the much smaller bond length for the carbon monoxide molecule. Bond lengths for Mn-C was determined to be 1.75 Å, which is approximately 0.2 Å longer than reported in literature.[201] All attempts to perform a spin optimization of this system and start with an initial spin of $5\mu_B$ were unsuccessful and might be a sign of a magnetic moment of $0\mu_B$ for each manganese atom, or possibly an antiferromagnetic system. The average Mn-O bond length is increased to 2.210 Å which is an indication of an overall weakening of the MOF-73 structure. Other bond lengths are comparable to the values reported in table 5.1. The band structure for the MOF-73 structure containing carbon monoxide is shown in figure 5.17. Clearly, the band structure is affected by the CO adsorption and the highest valence band crosses and lies above the Fermi level to a large extent, and the system can be expected to be metallic.

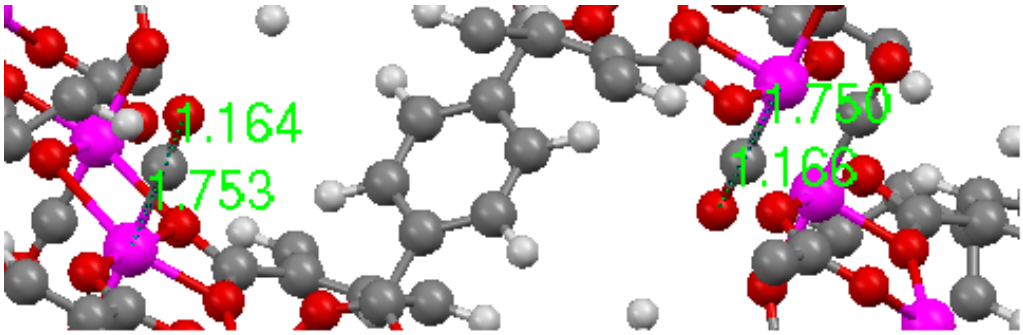

Figure 5.16: Bond lengths for the CO molecule when coordinated to the exposed manganese site in the MOF-73 structure. Purple spheres=manganese atoms, black spheres=carbon atoms, red spheres=oxygen atoms and white spheres=hydrogen atoms.

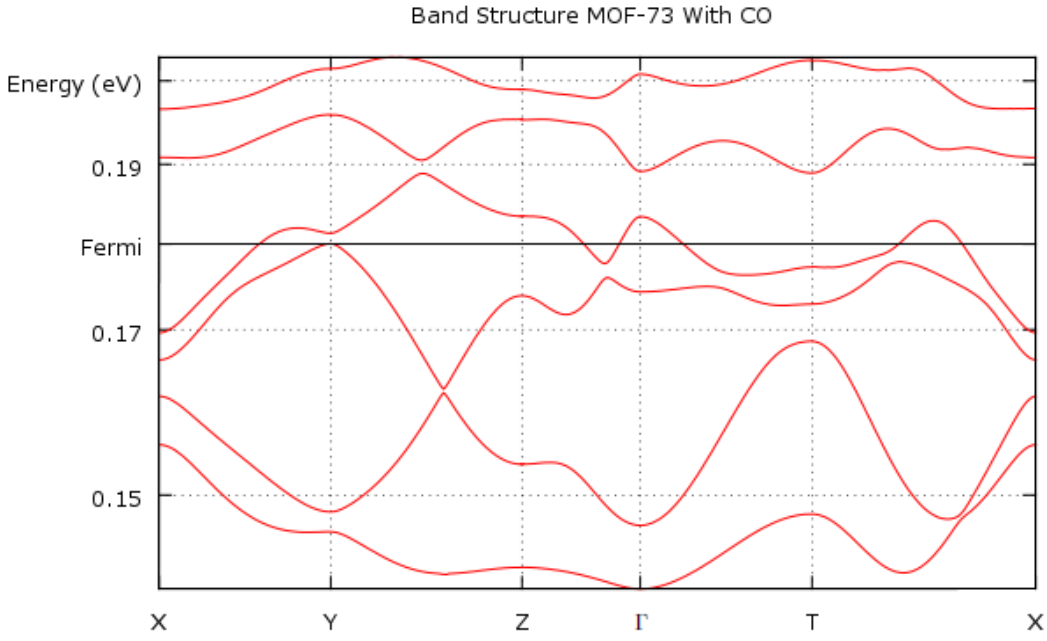

Figure 5.17: Band structure for the MOF-73 structure with 4 adsorbed CO molecules.

The Mulliken populations of manganese atoms are displayed in figures 5.18 and 5.19. Manganese atoms with a six-fold coordination are shown as light grey bars and manganese atoms occupied with CO molecules are shown as dark grey bars. Occupation of α and β orbitals occurs to an equal extent, and covers the entire range of d-orbitals. A very small difference between the light grey bars can be observed, since only four of the eight "open" manganese atoms sites are occupied with CO molecules.

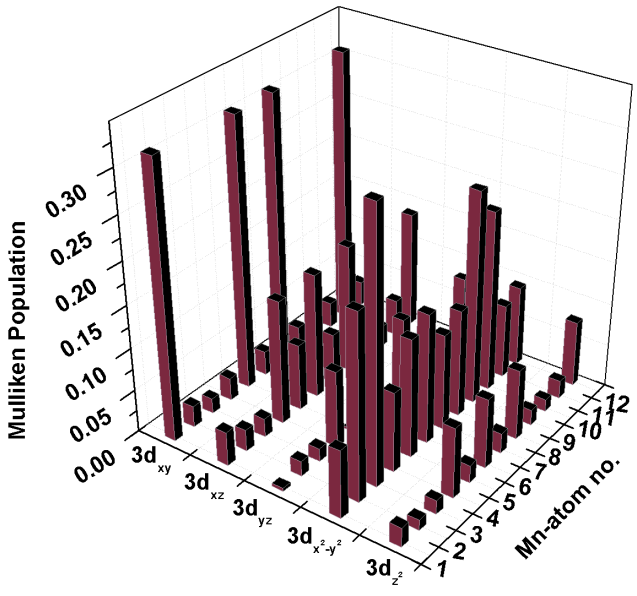

Figure 5.18: Mulliken population for the α spin orbitals with CO molecules. Manganese atom no. 1, 5, 7 and 11 are holding CO.

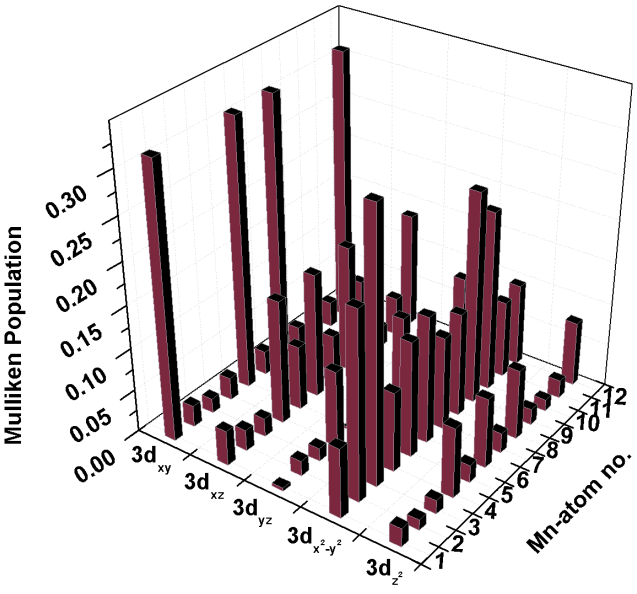

Figure 5.19: Mulliken population for the β spin orbitals with CO. Manganese atom no. 1, 5, 7 and 11 are holding CO.

Spin	$2s$	$2p_x$	$2p_y$	$2p_z$
α	0.92459	0.25059	0.25059	0.35138
β	0.92458	0.25065	0.25065	0.35140

Table 5.4: Mulliken population for α spin orbitals in CO.

Spin	$2s$	$2p_x$	$2p_y$	$2p_z$
α	0.00082	0.00011	0.00028	0.00324
β	0.00079	0.00011	0.00029	0.00323

Table 5.5: Mulliken population for β spin orbitals in CO.

Table 5.4 and 5.5 show the Mulliken population for the carbon atom in the uncoordinated as well as the coordinated CO-molecule, with an equal Mulliken population for α and β spin electrons. For the uncoordinated CO molecule, population almost reaches one electron on the $2s$-orbital, $2p_x$ and $2p_y$ orbitals displays similar occupation of approximately 0.25 electrons whereas the $2p_z$ orbital have a slightly higher population of 0.35 electrons. Just like the DEF molecules, the carbon atom displays a large flux of electron density from the carbon atom to the manganese atom. This gives a further support for the stronger binding to the manganese atom compared to the DEF molecule. Carbon monoxide provides an interesting feature to the bonding to transition metals, due to its ability for back-bonding to the C-O anti-bonding orbitals.[54] However, it is not possible in the current study to directly analyse the existence and/or magnitude of back-bonding for the MOF-73 structure with adsorbed CO-molecules. In one combined experimental and computational study of CO adsorption on Cu and Ni surfaces, the importance of bond elongation for the C≡O bond were discussed. Theoretical values for the bond in free CO were 1.146 Å and when adsorbed and fully relaxed on a Cu-cluster, the bond length was increased to 1.161 Å. These values are close to the bond lengths in the current study, in which the free CO has a bond length of 1.132 Å and 1.164-1.166 Å for a CO molecule when adsorbed to the MOF-73 structure. Thus, back bonding can not be ruled out as a consequence to the adsorption.

5.5 H_2 Adsorbed In The MOF-73 Structure

One of the most interesting molecules for adsorption in metal-organic frameworks is the hydrogen molecule. Adsorption studies has been under investigation both experimentally and theoretically in a number of studies.[170–172,175,177,178,195,196] Metal-organic frameworks are expected to play an important role in hydrogen storage, although a number of difficulties still exist, such as too strong binding interaction between the metal-organic framework structure and the hydrogen molecule. This results in an unreasonable release of energy upon binding and similarly, an unreasonable amount of energy has to be provided to release the hydrogen molecules. If the binding interaction between the metal-organic framework and the hydrogen molecule is too weak, unexpected migration of the hydrogen molecules might occur. Previous studies have shown that the most favourable adsorption mode of hydrogen molecules in metal-organic frameworks is the η_2 coordination. Both hydrogen atoms are bonded to the adsorbent, which in this case is the manganese atom. Figure 5.20 shows the coordination mode and important bond lengths for hydrogen molecules adsorbed in the MOF-73 structure. As can be seen from the image, the bond length between each manganese and hydrogen atom is 1.627 Å. A small elongation of the H-H bond length can be seen, from the literature value of 0.74 Å to 0.876 Å. Hence, the distance from the manganese atom to the centre of the H-H bond is 1.371 Å. Equation 5.3.1 gives a binding energy of approximately 58.4 kJmol^{-1} per H_2 molecule. This is significantly higher than reported for manganese containing MOF:s in earlier studies, although the binding energy reported in the current work seems to be promising for storage of hydrogen molecules in the MOF-73 structure.

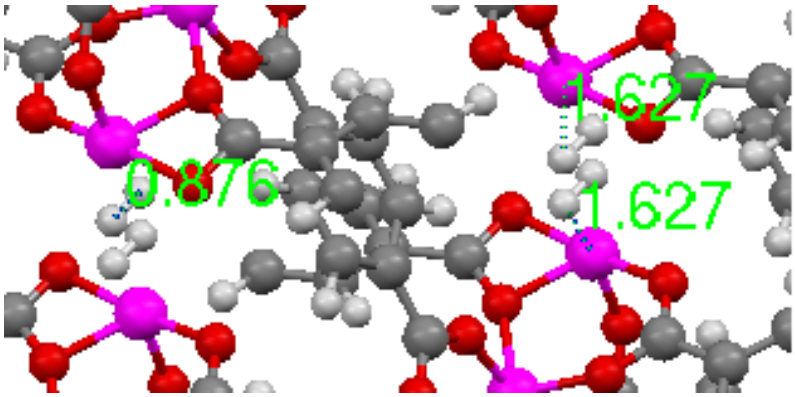

Figure 5.20: Coordination mode and bond lengths for the MOF-73 structure with adsorbed H_2 molecules.

The MOF-73 structure with adsorbed hydrogen molecules shows dramatic change in the band structure according to figure 5.21, where the Fermi level now lies approximately right between the conduction and valence band. These bands are relatively even throughout the whole Brillouin zone and never touch each other or overlap at any point, clearly adopting a behaviour of a small gap semi-conductor. However, since the band gap only varies between 0.04-0.06 eV, it would be possible for electrons to move from valence to the conduction band at elevated temperatures. Sun and co-workers [195] explained their low binding energy between the MOF structure and hydrogen molecule by two mechanisms: The first one is an energy-gaining mechanism which is due to shift downward of the bonding energy levels. The second mechanism is competing with the first one and is an energy-consuming mechanism which comes from the shift upwards of anti-bonding levels if occupied. As previously stated, this group also found a magnetic moment of 3.25μ_B per manganese atom, whereas the magnetic moment for the MOF-73 with hydrogen molecules adsorbed, only displays a magnetic moment of -0.011μ_B. Thus, this argument does not hold in the current work. It is also reflected in the binding energy for hydrogen molecules since the binding energy in this work is much larger compared to the work of Sun et al. The local density of states from the work of Sun et el. is shown in figure 5.22, where the upper diagram represents the "uncoordinated" system and the lower diagram is the system after adsorption. In the upper diagram, the sharp blue peak is the H_2 molecule which is moved to a lower energy after adsorption. The only d-orbitals that were found to be changed in energy were determined to be the d_{z^2} orbitals, which interacts with the hydrogen σ molecular orbital.

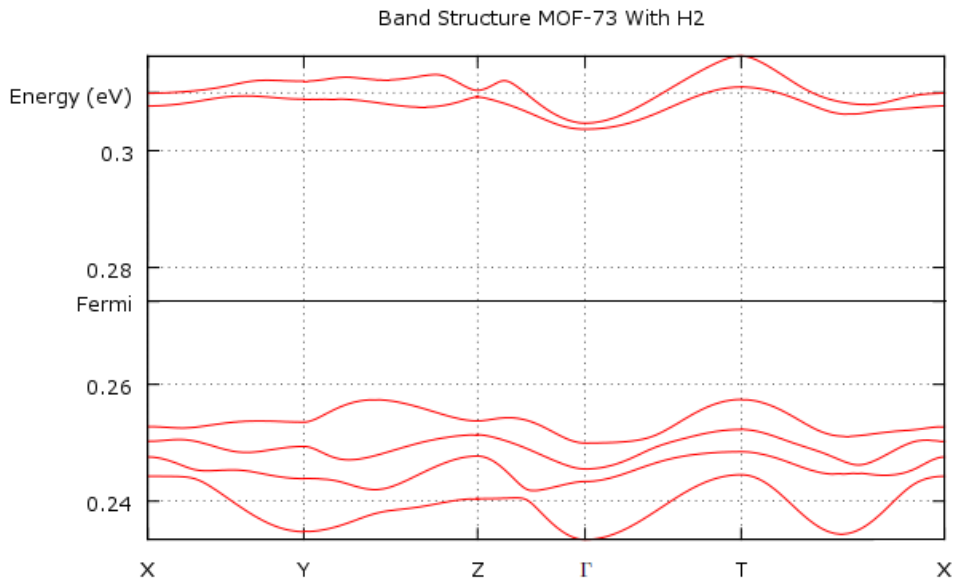

Figure 5.21: Band structure for the MOF-73 structure with 4 adsorbed H_2 molecules.

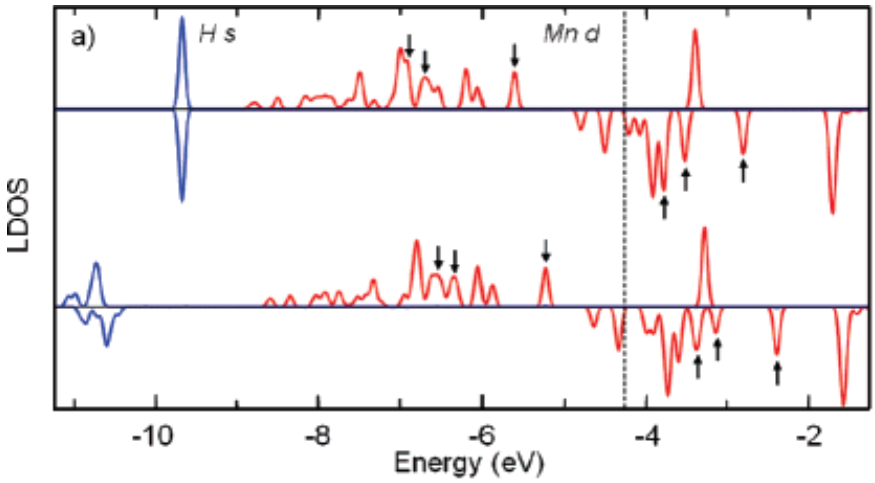

Figure 5.22: Local density of states of manganese d-orbitals and hydrogen s-orbitals before (upper curve) and after (lower curve) which show the change of LDOS upon binding of hydrogen molecules in the MOF structure. Black arrows represent the positions of the d_{z^2} orbitals of the four Mn atoms in the unit cell. The dotted line is the limit between occupied and unoccupied states. Image taken from the work of Sun et al [195] and the MOF structure considered was reported by [176].

Figure 5.23 and 5.24 shows the Mulliken analysis for α and β spin orbitals for the MOF-73 structure with adsorbed hydrogen molecules. These diagrams clearly show an even population of α and β spin orbitals which is not in agreement with previous studies. A very low spin polarization could be found from this Mulliken analysis, but it is not possible to see a difference that small from these bar diagrams. An interesting difference between the light grey bars which include both "open-site" manganese atoms as well as manganese atoms with adsorbed hydrogen molecules, can be seen. Four of these atoms have a higher population of the d_{xy} orbitals, and these atoms "carry" the adsorbed hydrogen molecules. Re-distribution of charge can also be seen for the remaining "open-site" manganese atoms, compared to figure 5.13 and 5.14, although it is not that big. A large change can also be seen for the four six-folded manganese atoms, which is a sign of a charge transfer through the back-bone structure including all manganese atoms. Thus, a very important difference between the orbitals involved in bonding of the hydrogen molecules in the current work and the work of Sun et al.[195] can be observed. In the current work, bonding to hydrogen molecules occurs via the d_{xy} orbital on the manganese atom, in the work of Sun et al. the bonding involves the d_{z^2} orbital due to the local symmetry of the manganese atom. Accessibility to the d_{z^2} orbital is easier in the square-plane environment for the unit cell in the work of Sun but since the coordination is different in the unit cell in the current work, other orbitals such as the d_{xy} might play a more important role in adsorption processes.

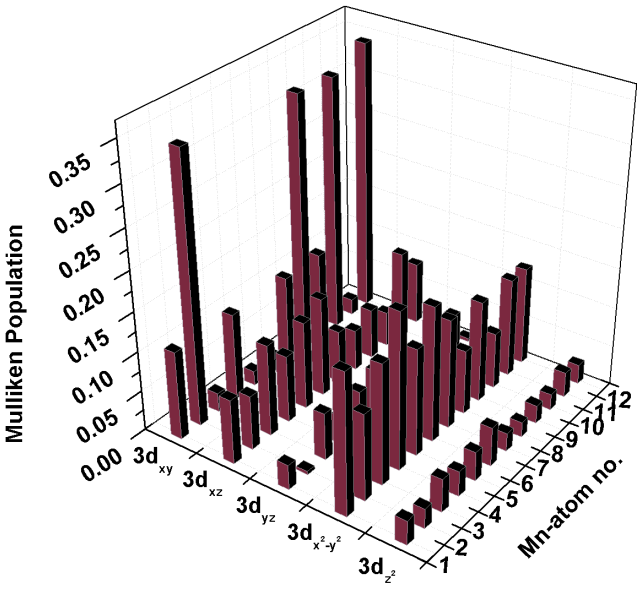

Figure 5.23: Mulliken population for the α spin orbitals for MOF-73 with H_2. Manganese atom no. 2, 8, 10 and 12 are holding H_2.

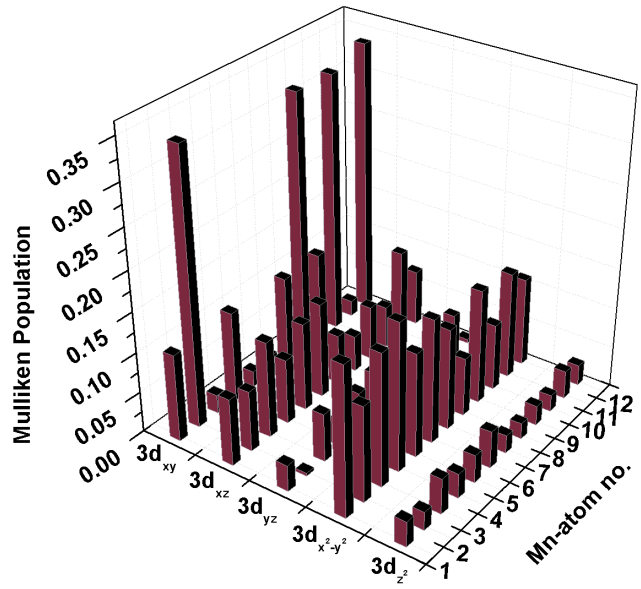

Figure 5.24: Mulliken population for the β spin orbitals for MOF-73 structure with H_2. Manganese atom no. 2, 8, 10 and 12 are holding H_2.

5.6 Conclusions

Despite the lack of experimental results for the MOF-73 structure, a number of theoretical results have been obtained and analysed in this study. Solvent is used during the synthesis, and some molecules are still adsorbed to the structure. When these molecules are removed from the structure, a radical change in the band structure was found. Band structure of the desorbed MOF-73 structure has a metallic or semi-metallic behaviour with overlap of the valence and conduction band. When solvent molecules from the synthesis are present in the structure, which in the current study means coordination to some of the manganese atoms, a small but complete separation of the valence and conduction band occurs. All the bands considered in the band structure analysis lose their strong curvature and the bands become more constant throughout the entire Brillouin zone. Mulliken analysis reveals that the bonding to the solvent molecules include the d_{xz}, d_{yz}, $d_{x^2-y^2}$ and d_{z^2} orbitals. A large difference between the α and β spin orbitals can be seen when the solvent molecules are present in the structure. However, due to a net magnetic moment of $0\mu_B$, the total occupation of α and β spin orbitals are equal, however this does not rule out the antiferromagnetic coupling. Coordination of CO molecules to the MOF-73 structure was investigated through adsorption via the carbon atom. The binding energy is found to be larger than that for the solvent molecule by approximately 40 $kJmol^{-1}$ per molecule. Upon adsorption of CO, a modification of the band structure also occur. A complete separation of the valence and conduction band being observed, although the highest occupied band lies above the Fermi level to a large extent in the Brillouin zone. Mulliken analysis confirms the modification of the band structure and bonding to the CO molecule involves d_{xz}, d_{yz}, $d_{x^2-y^2}$ and d_{z^2} orbitals which are occupied to a larger extent compared to the desorbed MOF-73 structure. No significant difference between occupation of α and β spin orbitals occurs which supports the finding of a net magnetic moment of $0\mu_B$. Adsorption of the hydrogen molecule was investigated through η_2 coordination in which the hydrogen molecule is bonded to the manganese atom via its H-H σ bond. The bond strength was found to be almost 60 $kJmol^{-1}$ per molecule, which is much larger than previous findings. This makes the MOF-73 structure interesting for hydrogen storage. Upon coordination of the hydrogen molecule, modification of the band structure occurs through a complete and distinct if small separation of the occupied and unoccupied bands. Thus, a more semi-conductor behaviour of the system can be expected, although movement of electrons to the conductions band can be expected at elevated temperatures. Magnetic moment for this system was determined to -0.011μ_B, which might be a consequence of an incomplete spin optimization. The low spin state is confirmed by an even occupation of the α and β spin orbitals. Bonding to the hydrogen molecule occurs via the d_{xy} orbitals, probably due to the local coordination environment of the manganese atom which makes

this interaction particularly favourable. In summary, coordination of molecules to the MOF-73 structure provides interesting modification of the band structure due to the bonding interaction.

Bibliography

[1] Cotton, F.; Wilkinson, G. *Advanced Inorganic Chemistry. A Comprehensive Text, 4th ed.*; John Wiley and Sons, New York, 1980.

[2] Weeks, M. *Journal of Chemical Education* **1932**, *9*, 22.

[3] Frieden, E. *J. Chem. Ed.* **1985**, *65*, 917.

[4] Einstein, A. *Ann. Physik* **1905**, *17*, 132–148.

[5] Compton, A. *Phys. Rev* **1923**, *21*, 483–502.

[6] Balmer, J. *Ann. Phys.* **1885**, *25*, 80–85.

[7] Rydberg, J. *Ann. Phys.* **1908**, *25*, 660–696.

[8] Bohr, N. *Philosophical Magazine* **1913**, *26*, 1–24.

[9] de Broglie, L. *Phil. Mag* **1924**, *47*, 446.

[10] Heisenberg, W. *Zeitschrift für Physik* **1925**, *33*, 879–893.

[11] Born, M.; Heisenberg, W. *Zeitschrift für Physik* **1925**, *34*, 858–888.

[12] M. Born, W. H.; Jordan, P. *Zeitschrift für Physik* **1925**, *35*, 557–615.

[13] Schrodinger, E. *Phys. Rev.* **1926**, *28*, 1049–1070.

[14] Born, M.; Oppenheimer, J. *Ann. Physik* **1927**, *84*, 457.

[15] Heisenberg, W. *Zeitschrift für Physik* **1927**, *43*, 172.

[16] Gerlach, W.; Stern, O. *Zeitschrift für Physik* **1922**, *9*, 353–355.

[17] Uhlenbeck, G.; Goudsmit, S. *Naturwissenschaften* **1925**, *47*, 953.

[18] Pauli, W. *Zeitschrift fur Physik* **1925**, *31*, 765.

[19] Hund, F. *Zeitschrift fur Physik* **1925**, *33*, 345.

[20] Hartree, D. *Proc. Comb. Phil. Soc.* **1928**, *24*, 89–132.

[21] Fock, V. *Zeitschrift für Physik* **1930**, *61*, 126–148.

[22] Slater, J. *Phys. Rev.* **1929**, *34*, 1293.

[23] Slater, J. *Phys. Rev.* **1930**, *35*, 509.

[24] Roothaan, C. *Reviews of Modern Physics* **1951**, *23*, 69.

[25] Hall, G. *Proceedings of the Royal Society, London* **1951**, *A205*, 541.

[26] Jensen, F. *Introduction to Computational Chemistry*; John Wiley and Sons, 2001.

[27] Möller, C.; Plesset, M. *Phys. Rev. B* **1934**, *46*, 0618–0622.

[28] Dirac, P. *Proc. Cambridge Phil. Soc.* **1930**, *26*, 376.

[29] Hohenberg, P.; Kohn, W. *Phys. Rev. B* **1964**, *136*, B846–B871.

[30] Kohn, W.; Sham, L. *Phys. Rev* **1965**, *140*, 1133–1138.

[31] Hedin, L.; Lundqvist, B. *J. Phys. C. Solid State Phys.* **1971**, *4*, 2064–2083.

[32] Vosko, S.; Wilk, L.; Nusair, M. *Canad. J. Phys* **1980**, *58*, 1200–1211.

[33] Perdew, J. *Phys. Rev B* **1986**, *33*, 8822–8824.

[34] Becke, A. D. *J. Chem. Phys.* **1993**, *98*, 5648–5652.

[35] Miehlich, B.; Savin, A.; Stoll, H.; Preuss, H. *Chem. Phys. Lett.* **1989**, *157*, 200–206.

[36] Lee, C.; Yang, W.; Parr, R. *Phys. Rev. B* **1988**, *37*, 785–789.

[37] Perdew,; Wang, *Phys. Rev. B* **1992**, *45*, 13244.

[38] Cramer, C. *Essentials of Computational, Chemistry Theory and Models*; John Wiley and Sons, 2002.

[39] Leach, A. *Molecular Modelling, Principles and Applications*, 2nd ed.; Prentice Hall, 2001.

[40] Bloch, F. *Z. Phys* **1928**, *52*, 555–560.

[41] Frisch, M. J. et al. *Gaussian 03, Revision C.02*, Gaussian, Inc., Wallingford, CT, 2004.

[42] Schlegel, H. *J. Comp. Chem* **1982**, *3*, 214–218.

[43] Fletcher, R. *Practical Methods of Optimization*; Wiley, New York, 1980.

[44] Bofill, J. *J. Comp. Chem* **1994**, *15*, 1–11.

[45] Bofill, J.; Comajuan, M. *J. Comp. Chem* **1995**, *16*, 1326–1338.

[46] Duncombe, B.; Rydén, J.; Puskar, L.; Cox, H.; Stace, A. **2008**, *19*, 520–530.

[47] Griffith, J.; Orgel, L. *Quarterly Reviews* **1957**, *11*, 381.

[48] Berthe, H. *Ann. Phys.* **1929**, *3*, 133.

[49] Vleck, J. V. *J. Chem. Phys.* **1935**, *3*, 807.

[50] Dr. John Turner, U. o. S.; 2009.

[51] Pauling, L. *The Chemical Bond*; Cornell University Press, 1967.

[52] Scläfer, H.; Gliemann, G. *Basic Principles Of Ligand Field Theory*; Wiley-Interscience, 1969.

[53] Murell, J.; Kettle, S.; Tedder, J. *The Chemical Bond*; John Wiley and Sons, 1979.

[54] Miessler, G.; Tarr, D. A. *Inorganic Chemistry, Third Edition*; Prentice Hall, 2003.

[55] Atkins, P.; Friedman, R. *Molecular Quantum Mechanics 4th ed.*; Oxford University Press, 2004.

[56] Bransden, B.; Joachain, C. *Introduction to Quantum Mechanics*; Longman Scientific and Technical, 1989.

[57] Huheey, J.; Keiter, E.; Keiter, R. *Inorganic Chemistry: Principles of Structure and Reactivity*, 4th ed.; HarperCollins College Publishers, 1993.

[58] George, D.; McClure, D. *Prog. Inorg. Chem.* **1959**, *1*, 381.

[59] Orgel, L. *J. Chem. Soc.* **1952**, 4756.

[60] Larsen, E.; Mar, G. L. *J. Chem. Educ.* **1974**, *51*, 633.

[61] Burdett, J. *Molecular Shapes*; Wiley-Interscience, New York, 1980.

[62] Shvartsburg, A.; Siu, M. *J. Am. Chem. Soc.* **2001**, *123*, 10071–10075.

[63] Nielsen, S.; Masella, M.; Kebarle, P. *J. Phys. Chem. A* **1999**, *103*, 9891–9898.

[64] Kebarle, P.; Searles, S.; Zolla, A.; Scarboro, J.; Arshadi, M. *J. Am. Chem. Soc.* **1967**, *89*, 6393–&.

[65] Jayaweera, P.; Blades, A.; Ikonomou, M.; Kebarle, P. *J. Am. Chem. Soc.* **1990**, *112*, 2452–2454.

[66] Peschke, M.; Blades, A.; Kebarle, P. *Int. J. Mass. Spec.* **1999**, *187*, 685–699.

[67] Deng, H.; Kebarle, P. *J. Am. Chem. Soc.* **1998**, *120*, 2925–2931.

[68] Klassen, J.; Anderson, S.; Blades, A.; Kebarle, P. *J. Phys. Chem.* **1996**, *100*, 14218–14227.

[69] Blades, A.; Jayaweera, P.; Ikonomou, M.; Kebarle, P. *Int. J. Mass. Spec. Ion. Proc.* **1990**, *102*, 251–267.

[70] Blades, A.; Ikonomou, M.; Kebarle, P. *Anal. Chem.* **1991**, *63*, 2109–2114.

[71] Bock, C.; Katz, A.; Glusker, J. *J. Am. Chem. Soc.* **1995**, *117*, 3754–3763.

[72] Trachtman, M.; Markham, G.; Glusker, J.; George, P.; Bock, C. *Inorg. Chem.* **1998**, *37*, 4421–4431.

[73] Markham, G.; Glusker, J.; Bock, C. *J. Phys. Chem. B* **2002**, *106*, 5118–5134.

[74] George, P.; Glusker, J.; Trachtman, M.; Bock, C. *Chem. Phys. Lett.* **2002**, *351*, 454–458.

[75] George, P.; Glusker, J.; Markham, G.; Trachtman, M.; Bock, C. *Mol. Phys.* **2003**, *101*, 2451–2467.

[76] Trachtman, M.; Markham, G.; Glusker, J.; George, P.; Bock, C. *Inorg. Chem.* **2001**, *40*, 4230–4241.

[77] Trachtman, M.; Bock, C. *J. Mol. Struc. Theochem* **2004**, *672*, 75–96.

[78] Bock, C.; Trachtman, M. *Inorg. Chem.* **2002**, *41*, 4680–4688.

[79] El-Nahas, A.; Tajima, N.; Hirao, K. *J. Mol. Struct. Theochem* **1999**, *469*, 201–213.

[80] El-Nahas, A. *Chem. Phys. Lett.* **2000**, *329*, 176–178.

[81] El-Nahas, A. *Chem. Phys. Lett.* **2001**, *345*, 325–330.

[82] Xiao, C.; Walker, K.; Hagelberg, F.; El-Nahas, A. *Int. J. Mass Spec.* **2004**, *233*, 87–98.

[83] Jr., C. B.; Langhoff, S.; Partridge, H.; Rice, J.; Komornicki, A. *J. Chem. Phys.* **1991**, *95*, 5142–5148.

[84] Jr., C. B.; Langhoff, S.; Partridge, H. *J. Chem. Phys.* **1991**, *94*, 2068–2072.

[85] Akesson, R.; Pettersson, L.; Sandstrom, M.; Wahlgren, U. *J. Am. Chem. Soc.* **1994**, *116*, 8705–8713.

[86] Akesson, R.; Pettersson, L.; Sandstom, M.; Siegbahn, P.; Wahlgren, U. *J. Phys. Chem.* **1993**, *97*, 3765–3774.

[87] Walker, N.; Dobson, M.; Wright, R.; Barran, P.; Murrell, J.; Stace, A. *J. Am. Chem. Soc.* **2000**, *122*, 11138–11145.

[88] Cox, H.; Akibo-Betts, G.; Wright, R.; Walker, N.; Curtis, S.; Duncombe, B.; Stace, A. *J. Am. Chem. Soc.* **2003**, *125*, 233–242.

[89] Stace, A.; Shukla, A. *J. Am. Chem. Soc.* **1982**, *104*, 5314–5318.

[90] Stace, A.; Moore, C. *J. Am. Chem. Soc.* **1983**, *105*, 1814–1819.

[91] Walker, N.; Wright, R.; Barran, P.; Cox, H.; Stace, A. *J. Chem. Phys.* **2001**, *114*, 5562–5567.

[92] Cox, H.; Stace, A. *J. Am. Chem. Soc.* **2004**, *126*, 3939–3947.

[93] Puskar, L.; Tomlins, K.; Duncombe, B.; Cox, H.; Stace, A. *J. Am. Chem. Soc.* **2005**, *127*, 7559–7569.

[94] Woodward, C.; A.J., M. D.; Stace, *J. Phys. Chem. A* **1997**, *101*, 2279–2287.

[95] Barran, P.; Walker, N.; Stace, A. *J. Chem. Phys.* **2000**, *112*, 6173–6177.

[96] Wu, B.; Duncombe, B.; Stace, A. *J. Phys. Chem. A* **2008**, *112*, 2182–2191, PMID: 18275172.

[97] Duncombe, B.; Duale, K.; Buchanan-Smith, A.; Stace, A. *J. Phys. Chem. A* **2007**, *111*, 5158–5165.

[98] Akibo-Betts, G.; Barran, P.; Puskar, L.; Duncombe, B.; Cox, H.; Stace, A. *J. Am. Chem. Soc.* **2002**, *124*, 9257–9264, PMID: 12149032.

[99] Wu, B.; Duncombe, B.; Stace, A. *J. Phys. Chem. A* **2006**, *110*, 8423–8432.

[100] Wu, G.; Stace, A. *Int. J. Mass Spec.* **2006**, *249*, 289–295.

[101] Duncombe, B.; Puskar, L.; Wu, B.; Stace, A. *Can. J. Chem.-Revue Canadienne de Chimie* **2005**, *83*, 1994–2004.

[102] Puskar, L.; Barran, P.; Duncombe, B.; Chapman, D.; Stace, A. *J. Phys. Chem. A* **2005**, *109*, 273–282.

[103] Stace, A. *J. Phys. Chem. A* **2002**, *106*, 7993–8005.

[104] Stace, A. *Phys. Chem. Chem. Phys.* **2001**, *3*, 1935–1941.

[105] Walker, N.; Wright, R.; Barran, P.; Murrell, J.; Stace, A. *J. Am. Chem. Soc.* **2001**, *123*, 4223–4227.

[106] Wright, R.; Walker, N.; Firth, S.; Stace, A. *J. Phys. Chem. A* **2001**, *105*, 54–64.

[107] Akibo-Betts, G.; Barran, P.; Stace, A. *Chem. Phys. Lett.* **2000**, *329*, 431–436.

[108] Barran, P.; Mikhailov, V.; Stace, A. *J. Phys. Chem. A* **1999**, *103*, 8792–8798.

[109] Dobson, M.; Stace, A. *Int. J. Mass Spec.* **1997**, *165*, 5–12.

[110] Dobson, M.; Stace, A. *Chem. Comm.* **1996**, 1533–1534.

[111] Murrell, J.; Jenkins, A. *Properties of Liquids and Solutions*; John Wiley and Sons: Chichester, 1994.

[112] Asthagiri, D.; Pratt, L.; Paulaitis, M.; Rempe, S. *J. Am. Chem. Soc.* **2004**, *126*, 1285–1289.

[113] Pavlov, M.; Siegbahn, P.; Sandström, M. *J. Phys. Chem. A* **1998**, *102*, 219–228.

[114] Marcus, J. *Annu. Rev. Phys. Chem.* **1964**, *15*, 155.

[115] Corongiu, G.; Clementi, E. *J. Chem. Phys.* **1978**, *69*, 4485.

[116] Tonkyn, R.; Weisshaar, J. *J. Am. Chem. Soc.* **1986**, *108*, 7128.

[117] Yamashita, M.; Fenn, J. *J. Phys. Chem.* **1984**, *88*, 4451.

[118] Rotzinger, F. *J. Am. Chem. Soc.* **2005**, *109(4)*, 1510–1527.

[119] Figgs, B.; Hitchman, M. *Ligand Field Theory and Its Applications*; Wiley-VCH, 2000.

[120] Jr., C. B.; Langhoff, S.; Partridge, H. *Modern Electronic Structure Theory*; World Scientific, Singapore, 1995.

[121] Maye, P.; Mezei, M. *J. Mol. Struct. Theochem.* **1996**, *362*, 317.

[122] Holland, P.; Castleman, A. *J. Chem. Phys.* **1982**, *76*, 4195.

[123] Marinelli, P.; Squires, R. *J. Am. Chem. Soc.* **1989**, *111*, 4101.

[124] Magnera, P.; David, D.; Michl, J. *J. Am. Chem. Soc.* **1989**, *111*, 4100.

[125] Magnera, P.; David, D.; Stulik, D.; Orth, R.; Jonkman, H.; Michl, J. *J. Am. Chem. Soc.* **1989**, *111*, 5036.

[126] Mulliken, R. *J. Chem. Phys.* **1962**, *36*, 3428.

[127] Rosi, M.; Bauschlicher, C. *J. Chem. Phys.* **1989**, *90*, 7264–7272.

[128] Rosi, M.; Bauschlicher, C. *J. Chem. Phys.* **1990**, *92*, 1876–1878.

[129] Reed, A.; Curtiss, L.; Weinhold, F. *Chem. Rev.* **1988**, *88*, 899–926.

[130] Reed, A. E.; Weinhold, F. *J. Chem. Phys.* **1985**, *83*, 1736–1740.

[131] Reed, A. E.; Weinhold, F. *J. Chem. Phys.* **1983**, *78*, 4066–4073.

[132] Löwdin, P.-O. *J. Chem. Phys.* **1955**, *97*, 1474–1489.

[133] Morokuma, K. *Acc. Chem. Research* **1977**, *10*, 294–300.

[134] Beyer, M.; Williams, E.; Bondybey, V. *J. Am. Chem. Soc.* **1999**, *121*, 1565–1573.

[135] Lide, D. *CRC Handbook of Chemistry and Physics, Internet Version 2005, http://www.hbcpnetbase.com*; CRC Press, Boca Raton, FL, 2005.

[136] Shannon, R. *Acta Cryst.* **1976**, *32*, 751.

[137] Medeiros, P.; de Brito Mota, F.; Mascarenhas, A.; de Castilho, C. *Nanotechnology* **2010**, *21*, year.

[138] Johll, H.; Kang, H.; Tok, E. *Phys. Rev. B* **2009**, *79*, year.

[139] Sevincli, H.; Topsakal, M.; Durgun, E.; Ciraci, S. *Phys. Rev. B* **2008**, *77*, year.

[140] Mao, Y.; Yuan, J.; Zhong, J. *J. Phys. Cond. Matt.* **2008**, *20*, year, 13th Conference on Liquid and Amorphous Metals, Ekaterinburg, RUSSIA, JUL 08-14, 2007.

[141] Rahman, F. *Appl. Phys. A-Matt. Sci.& Proc.* **2007**, *86*, 221–224.

[142] Wu, M.; Cao, C.; Jiang, J. *New J. Phys.* **2010**, *12*, year.

[143] Mao, Y.; Zhong, J. *Nanotechnology* **2008**, *19*, year.

[144] Uchoa, B.; Lin, C.; Neto, A. *Phys. Rev. B* **2008**, *77*, year.

[145] Krasheninnikov, A.; Lehtinen, P.; Foster, A.; Pyykkö, P.; Nieminen, R. *Phys. Rev. Lett.* **2009**, *102*, 126807.

[146] Novoselov, K.; Geim, A.; Morozov, S.; Jiang, D.; Zhang, Y.; Dubonos, S.; Grigorieva, I.; Firsov, A. *Science* **2004**, *306*, 666–669.

[147] Berger, C.; Song, Z.; Li, T.; Li, X.; Ogbazghi, A.; Feng, R.; Dai, Z.; Marchenkov, A.; Conrad, E.; First, P.; de Heer, W. *J. Phys. Chem. B* **2004**, *108*, 19912–19916.

[148] McCann, E.; Fal'ko, V. *Phys. Rev. Lett.* **2006**, *96*, 086805.

[149] Schedin, F.; Geim, A.; Morozov, S.; Hill, E.; Blake, P.; Katsnelson, M.; Novoselove, K. *Nat. Mat.* **2007**, *6*, 652–655.

[150] Jones, R.; Briddon, P. Chapter 6 The Ab Initio Cluster Method and the Dynamics of Defects in Semiconductors. In *Identification of Defects in Semiconductors*; Stavola, M., Ed.; Elsevier, 1998; Vol. 51, Part 1, pp 287 – 349.

[151] Hartwigsen, C.; Goedecker, S.; Hutter, J. *Phys. Rev. B* **1998**, *58*, 3641–3662.

[152] Monkhorst, H.; Pack, J. *Phys. Rev. B* **1976**, *13*, 5188–5192.

[153] Methfessel, M.; Paxton, A. *Phys. Rev. B* **1989**, *40*, 3616–3621.

[154] Khantha, M.; Cordero, N.; Molina, L.; Alonso, J.; Girifalco, L. *Phys. Rev. B* **2004**, *70*, 125422.

[155] Palser, A. *Phys. Chem. Chem. Phys.* **1999**, *1*, 4459–4464.

[156] Sellmyer, D. *Appendix - Bravais and reciprocal lattices, unit cells, first Brillouin zones: Part of Landolt-Bornstein - Group III Condensed Matter Numerical Data and Functional Relationships in Science and Technology, Volume 13a, Phonon States of Elements. Electron States and Fermi Surfaces of Alloys*; Springer-Verlag, 1981.

[157] Girifalco, L.; Lad, R. *J. Chem. Phys.* **1956**, *25*, 693–697.

[158] Duffy, D.; Blackman, J. *Phys. Rev. B* **1998**, *58*, 7443–7449.

[159] Santos, E.; Ayuela, A.; Sanchez-Portal, D. *New J. Phys.* **2010**, *12*, year.

[160] Yaghi, O.; O'Keeffe, M.; Ockwig, N.; Chae, H.; Eddaoudi, M.; Kim, J. *Nature* **2003**, *423*, 705–714.

[161] Yaghi, O.; Li, G.; Li., H. *Nature* **1995**, *378*, 703–706.

[162] Eddaoudi, M.; Li, H.; Reineke, T.; Fehr, M.; Kelley, D.; Groy, T.; Yaghi, O. *Top. Catal.* **1999**, *9*, 105–111.

[163] Kim, K. Y. K. Y. K. S.-J., S. *Inorg. Chim. Acta* **2007**, *360*, 1870–1874.

[164] Dinca, M.; Dailly, A.; Long, J. *Chem.-A Eur. J.* **2008**, *14*, 10280–10285.

[165] Liu, Y.; Kravtsov, V.; Larsen, R.; Eddaoudi, M. *Chem. Comm.* **2006**, 1488–1490.

[166] Wang, S. *Cryst. Res. Tech.* **2008**, *43*, 894–898.

[167] Li, H.; Eddaoudi, M.; O'Keeffe, M.; Yaghi, O. *Nature* **1999**, *402*, 276–279.

[168] Li, J.-R.; Kuppler, R.; Zhou, H.-C. *Chem. Soc. Rev.* **2009**, *38*, 1477–1504.

[169] Samsonenko, D.; Kim, H.; Sun, Y.; Kim, G.-H.; Lee, H.-S.; Kim, K. *Chem. Asian J.* **2007**, *2*, 484–488.

[170] Rosi, N.; Eckert, J.; Eddaoudi, M.; Vodak, D.; Kim, J.; O'Keeffe, M.; Yaghi, O. *Science* **2003**, *300*, 1127–1129.

[171] Mulder, F.; Dingemans, T.; Wagemaker, M.; Kearley, G. *Chem. Phys.* **2005**, *317*, 113–118, 2nd Neutrons and Numerical Methods Workshop, Grenoble, FRANCE, SEP, 2004.

[172] Bordiga, S.; Vitillo, J.; Ricchiardi, G.; Regli, L.; Cocina, D.; Zecchina, A.; Arstad, B.; Bjorgen, M.; Hafizovic, J.; Lillerud, K. *J. Phys. Chem. B* **2005**, *109*, 18237–18242.

[173] Eddaoudi, M.; Kim, J.; Rosi, N.; Vodak, D.; Wachter, J.; O'Keeffe, M.; Yaghi, O. *Science* **2002**, *295*, 469–472.

[174] Dybtsev, D.; Chun, H.; Yoon, S.; Kim, D.; Kim, K. *J. Am. Chem. Soc.* **2004**, *126*, 32–33.

[175] Dinca, M.; Long, J. *Ang. Chem.-Int. Ed.* **2008**, *47*, 6766–6779.

[176] Dinca, M.; Yu, A.; Long, J. *J. Am. Chem. Soc.* **2006**, *128*, 8904–8913.

[177] Dinca, M.; Long, J. *J. Am. Chem. Soc.* **2007**, *129*, 11172–11176.

[178] Dinca, M.; Long, J. *J. Am. Chem. Soc.* **2005**, *127*, 9376–9377.

[179] Moon, H.; Kobayashi, N.; Suh, M. *Inorg. Chem.* **2006**, *45*, 8672–8676.

[180] Eddaoudi, M.; Li, H.; Yaghi, O. *J. Am. Chem. Soc.* **2000**, *122*, 1391–1397.

[181] Rosseinsky, M. *Nat. Mat.* **2010**, *9*, 609–610.

[182] Rosi, N.; Kim, J.; Eddaoudi, M.; Chen, B.; O'Keeffe, M.; Yaghi, O. *J. Am. Chem. Soc.* **2005**, *127*, 1504–1518.

[183] Luo, F.; Che, Y.-x.; Zheng, J.-m. *Inorg. Chem. Comm.* **2008**, *11*, 358–362.

[184] Figueroa, S.; Requejo, F.; Lede, E.; Lamaita, L.; Peluso, M.; Sambeth, J. *Catal. Today* **2005**, *107-08*, 849–855, 19th Ibero American Catalysis Symposium, Merida, MEXICO, 2004.

[185] Horike, S.; Dinca,; andK. Tamaki, M. *J. Am. Chem. Soc.* **2008**, *130*, 5854–5856.

[186] Britt, D.; Lee, C.; Uribe-Romo, F.; Furukawa, H.; Yaghi, O. *Inorg. Chem.* **2010**, *49*, 6387–6389.

[187] Jiang, Y.; Yu, R.; Bai, Y.; Xie, Z.; Zheng, L. *Trans. Met. Chem.* **2008**, *33*, 1019–1026.

[188] Qi, C.; Zhang, D.; Gao, S.; Ma, H.; He, Y.; Ma, S.; Chen, Y.; Yang, X. *J. Mol. Struc.* **2008**, *891*, 357–363.

[189] Wang, F.-Q.; Zheng, X.-J.; Wan, Y.-H.; Wang, K.-Z.; Jin, L.-P. *J. Mol. Struc.* **2006**, *798*, 155–161.

[190] Manna, S.; Zangrando, E.; Drew, M.; Ribas, J.; Chaudhuri, N. *Eur. J. Inorg. Chem.* **2006**, 481–490.

[191] Bai, Z.-S.; Qi, Z.-P.; Lu, Y.; Yuan, Q.; Sun, W.-Y. *Crys. G. Des.* **2008**, *8*, 1924–1931.

[192] Dobrzynska, D.; Jerzykiewicz, L.; Jezierska, J.; Duczmal, M. *Crys. G. and Des.* **2005**, *5*, 1945–1951.

[193] Wei, Q.; Nieuwenhuyzen, M.; James, S. *Micr. Mes. Mat.* **2004**, *73*, 97–100.

[194] Choi, J.; Park, J.; Park, M.; Moon, D.; Lah, M. S. *Eur. J. Inorg. Chem.* **2008**, 5465–5470.

[195] Sun, Y.; Kim, Y.-H.; Zhang, S. *J. Am. Chem. Soc.* **2007**, *129*, 12606+.

[196] Wong-Foy, A.; Matzger, A.; Yaghi, O. *J. Am. Chem. Soc.* **2006**, *128*, 3494–3495.

[197] Bekenev, V.; Khyzhun, O. Y.; Atuchin, V. *J. All. Comp.* **2009**, *485*, 51–58.

[198] Baur, W. *Acta Crys. Sect. B-Struc. Sci.* **1976**, *32*, 2200–2204.

[199] Kohler, T.; Armbruster, T.; Libowitzky, E. *J. Sol. St. Chem.* **1997**, *133*, 486–500.

[200] Atkins, P. *Molecular Quantum Mechanics 6th ed.*; Oxford University Press, 1999.

[201] Geier, J.; Willner, H.; Lehmann, C.; Aubke, F. *Inorg. Chem.* **2007**, *46*, 7210–7214, PMID: 17616186.